

MODELING AND CONTROL OF A HYBRID-ELECTRIC  
VEHICLE FOR DRIVABILITY AND FUEL ECONOMY  
IMPROVEMENTS

DISSERTATION

Presented in Partial Fulfillment of the Requirements for  
the Degree Doctor of Philosophy in the  
Graduate School of The Ohio State University

By

Kerem Koprubasi, B.S., M.S.

\* \* \* \* \*

The Ohio State University

2008

Dissertation Committee:

Prof. Giorgio Rizzoni, Adviser

Prof. Yann Guezennec

Prof. Andrea Serrani

Prof. Steve Yurkovich

Approved by

---

Adviser

Graduate Program in  
Mechanical Engineering

© Copyright by  
Kerem Koprubasi  
2008

## ABSTRACT

The gradual decline of oil reserves and the increasing demand for energy over the past decades has resulted in automotive manufacturers seeking alternative solutions to reduce the dependency on fossil-based fuels for transportation. A viable technology that enables significant improvements in the overall tank-to-wheel vehicle energy conversion efficiencies is the hybridization of electrical and conventional drive systems.

Sophisticated hybrid powertrain configurations require careful coordination of the actuators and the onboard energy sources for optimum use of the energy saving benefits. The term optimality is often associated with fuel economy, although other measures such as drivability and exhaust emissions are also equally important. This dissertation focuses on the design of hybrid-electric vehicle (HEV) control strategies that aim to minimize fuel consumption while maintaining good vehicle drivability.

In order to facilitate the design of controllers based on mathematical models of the HEV system, a dynamic model that is capable of predicting longitudinal vehicle responses in the low-to-mid frequency region (up to 10 Hz) is developed for a parallel HEV configuration. The model is validated using experimental data from various driving modes including electric only, engine only and hybrid. The high fidelity of the model makes it possible to accurately identify critical drivability issues such as time lags, shunt, shuffle, torque holes and hesitation.

Using the information derived from the vehicle model, an energy management strategy is developed and implemented on a test vehicle. The resulting control strategy has a hybrid structure in the sense that the main mode of operation (the hybrid

mode) is occasionally interrupted by event-based rules to enable the use of the engine start-stop function. The changes in the driveline dynamics during this transition further contribute to the hybrid nature of the system.

To address the unique characteristics of the HEV drivetrain and to ensure smooth vehicle operation during mode changes, a special control method is developed. This method is generalized to a broad class of switched systems in which the switching conditions are state dependent or are supervised. The control approach involves partitioning the state-space such that the control law is modified as the state trajectory approaches a switching set and the state is steered to a location within the partition with low transition cost. Away from the partitions that contain switching sets, the controller is designed to achieve any suitable control objective. In the case of the HEV control problem, this objective generally involves minimizing fuel consumption.

Finally, the experimental verification of this control method is illustrated using the application that originally motivated the development of this approach: the control of a HEV driveline during the transition from electric only to hybrid mode.

Dedicated to my parents.

## ACKNOWLEDGMENTS

First of all, I would like to thank my advisor Prof. Giorgio Rizzoni for his continued support, encouragement and guidance. He opened the doors to many opportunities for me, both academically and professionally. Also, I am grateful to Prof. Yann Guezennec, Prof. Andrea Serrani and Prof. Steve Yurkovich who have contributed to this thesis with numerous suggestions. I feel very privileged to have had all of you in my dissertation committee.

I am indebted to my former co-advisor Dr. Eric Westervelt. He helped shape the course of my research and spent countless hours editing and improving my papers. It was a great pleasure working with you Eric!

I truly enjoyed the times I spent with many great friends here at the Center for Automotive Research. I can not possibly count all of them. Special thanks to all generations of Challenge-X team members (most of whom graduated before me!). Let's do a quick count: Jason, Kris, Mike, Joe, Courtney, John N., Bo, Marc, Leonardo, Annalisa, Enrico, Eric, Craig, John K. and many others. And a number of brilliant people whom I got the chance to meet with over the years: Ben, Nadia, Lorenzo, Marcello, Shawn, Sai and Gabriel to name only a few.. Thank you everyone for baring with me!

I am deeply thankful to my wonderful family who have always been there to support me even though they were thousands of miles away..

I saved the last spot for the person who deserved this degree as much as I did. She picked me up and helped me through my toughest times. I don't know how I could manage this without her. Eren, I can not thank you enough for everything. I am looking forward to all the great times that are yet to come!

## VITA

July 20, 1980 ..... Born - İzmir, Turkey.

June, 2002 ..... B.S. Mechanical Engineering,  
Middle East Technical University,  
Ankara, Turkey.

July, 2004 ..... M.S. Mechanical Engineering,  
University of New Hampshire,  
Durham, NH.

September, 2004 - present ..... Graduate Teaching and Research  
Associate, The Ohio State University,  
Columbus, OH.

## PUBLICATIONS

### Research Publications

K. Koprubasi, E. R. Westervelt, G. Rizzoni, E. Galvagno, and M. Velardocchia, “Experimental Validation of a Model for the Control of Drivability in a Hybrid-Electric Vehicle”, *Proceedings of the International Mechanical Engineering Congress and Exposition*, number 41489, 2007.

K. Koprubasi, E. R. Westervelt, and G. Rizzoni, “Toward the Systematic Design of Controllers for Smooth Hybrid Electric Vehicle Mode Changes”, *Proceedings of the American Control Conference*, 2007.

K. Koprubasi, J. M. Morbitzer, E. R. Westervelt, and G. Rizzoni, “Toward a Framework for the Hybrid Control of a Multi-Mode Hybrid-Electric Driveline”, *Proceedings of the American Control Conference*, 2006.

P. Pisu, K. Koprubasi, and G. Rizzoni, “Energy Management and Driveability Control Problems for Hybrid Electric Vehicles”, *Proceedings of the IEEE International Conference on Decision and Control / European Control Conference*, 2005.

## **FIELDS OF STUDY**

Major Field: Mechanical Engineering



## TABLE OF CONTENTS

	Page
Abstract . . . . .	ii
Dedication . . . . .	iv
Acknowledgments . . . . .	v
Vita . . . . .	vi
List of Tables . . . . .	xi
List of Figures . . . . .	xii
Notation and Acronyms . . . . .	xix
Chapters:	
1. Introduction . . . . .	1
1.1 Motivation . . . . .	1
1.2 Contributions of the Dissertation . . . . .	3
1.3 Organization of the Dissertation . . . . .	4
2. Literature Review . . . . .	6
2.1 Hybrid-Electric Vehicle Architectures . . . . .	6
2.2 Modeling: General Concepts and Applications to HEVs . . . . .	8
2.3 Energy Management in Hybrid-Electric Vehicles . . . . .	15
2.4 Control Techniques for Improving Drivability . . . . .	20
2.4.1 Conventional and Hybrid Vehicles . . . . .	21
2.4.2 Hybrid Vehicles . . . . .	25

2.5	Control of Systems with Mode Switching Behavior . . . . .	28
2.5.1	Hybrid and Switched Systems: An Overview . . . . .	28
2.5.2	Control of Mode Transitions . . . . .	31
3.	Dynamic Modeling of Hybrid-Electric Vehicles . . . . .	34
3.1	Experimental Platform . . . . .	34
3.2	HEV Dynamic Model . . . . .	37
3.2.1	Engine . . . . .	38
3.2.2	Transmission . . . . .	41
3.2.3	Electric Machines and Rear Drive . . . . .	50
3.2.4	Axles . . . . .	52
3.2.5	Brakes . . . . .	53
3.2.6	Tires and Vehicle . . . . .	54
3.2.7	High Voltage Battery . . . . .	57
3.2.8	Driveline Losses . . . . .	58
3.3	Summary . . . . .	59
4.	Model Validation . . . . .	60
4.1	Identification and Validation of Subsystem Models . . . . .	60
4.1.1	Engine Dynamics . . . . .	61
4.1.2	Rear Driveline Dynamics . . . . .	65
4.2	Validation of the HEV Model . . . . .	68
4.2.1	Electric Only Operation . . . . .	69
4.2.2	Engine Only Operation . . . . .	72
4.2.3	Hybrid Vehicle Operation . . . . .	75
4.3	Summary . . . . .	80
5.	Control Strategy Development . . . . .	81
5.1	Control Systems Architecture . . . . .	81
5.1.1	Hardware Architecture . . . . .	82
5.1.2	Control Software Architecture . . . . .	84
5.2	HEV Control Strategy . . . . .	86
5.2.1	Supervisory Level Controls . . . . .	88
5.2.2	Component Level Controls . . . . .	92
5.3	Summary . . . . .	124
6.	Control of Systems with Mode Switching Induced Transients . . . . .	125
6.1	Problem Formulation . . . . .	125
6.2	Proposed Solution Method . . . . .	128

6.3	Potential Applications of the Proposed Control Method . . . . .	129
6.4	An Illustrative Example: Control of HEV Launch . . . . .	130
6.4.1	Hybrid Model of HEV Launch . . . . .	131
6.4.2	Control Design . . . . .	134
6.4.3	Simulation Results . . . . .	137
6.4.4	Remarks on the Closed-Loop Stability of the Switched System	142
6.5	Summary . . . . .	144
7.	Experimental Verification of Control Strategies . . . . .	146
7.1	Electric Only Mode: Active Damping Controller . . . . .	146
7.2	HEV Control Strategy: In-Vehicle Validation . . . . .	151
7.2.1	Test 1: Investigation of Control Strategy Behavior . . . . .	151
7.2.2	Test 2: Fuel Economy Comparison . . . . .	156
7.3	Control of HEV Launch . . . . .	160
7.3.1	Control Design . . . . .	161
7.3.2	Experimental Results . . . . .	164
7.4	Summary . . . . .	169
8.	Conclusions and Future Work . . . . .	171
8.1	Conclusions . . . . .	171
8.2	Future Work . . . . .	173
Appendices:		
A.	Vehicle Control Unit Signals . . . . .	176
B.	Driving Cycle for Fuel Economy Evaluation . . . . .	178
C.	Hybrid Model of the Test Vehicle . . . . .	180
Bibliography . . . . .		184

## LIST OF TABLES

<b>Table</b>		<b>Page</b>
2.1	Advantages and disadvantages of heuristic methods and real-time optimization techniques for HEV control. . . . .	19
3.1	Schedule of friction of elements engaged in different gears. Gear ratios exclude the final drive and counter gear speed reduction ratios. . . . .	47
5.1	Some of the important transition conditions used in the supervisory controller. . . . .	89
5.2	The three-way split ECMS pseudo-code. (Some of the algorithm details are not shown here.) . . . . .	114
6.1	Numerical values of the parameter uncertainties used for controller robustness analysis. . . . .	141
7.1	A comparison of the fuel consumptions obtained from the test vehicle (using different control strategies) and the fuel consumption of the baseline vehicle over the urban driving schedule. . . . .	157
A.1	Vehicle control unit signal information. . . . .	177
B.1	Driving cycle statistics. . . . .	179

## LIST OF FIGURES

Figure	Page
2.1 Common hybrid-electric vehicle architectures (TR: transmission, R: ring gear, C: pinion gear carrier, S: sun gear) . . . . .	7
2.2 Example of a model-based development cycle used in the automotive industry. . . . .	10
2.3 Conceptual schematic of the power spectrum of the vehicle acceleration and the regions of interest for modeling. . . . .	12
2.4 Typical HEV operating modes (TC: torque coupler, BATT: battery) .	16
2.5 Typical driveline disturbances observed during gear-shifting. . . . .	22
2.6 Typical drivability issues related to pedal tip-in (experimental data from OSU hybrid vehicle). . . . .	24
2.7 A conceptual illustration of the torque chattering issue. The local minima of the value function lie in widely separated regions for consecutive engines speeds. . . . .	28
2.8 Various Hybrid Dynamical Interactions that Commonly Arise in Mechanical Systems . . . . .	29
2.9 Common bumpless transfer schemes. . . . .	31
3.1 OSU Challenge-X hybrid electric vehicle . . . . .	35
3.2 Experimental Vehicle Configuration . . . . .	36

3.3	A simplified illustration of the ECU process that converts a percentage based torque request into an actual torque request and a main fuel injection quantity. . . . .	39
3.4	A stick diagram of the 6-speed automatic transmission. . . . .	43
3.5	Geometric configurations of the transmission gear sets. . . . .	45
3.6	Variation of the clutch torques with slip speed and applied pressure. .	49
3.7	The mechanical configuration of the electrically driven rear axle of the experimental vehicle. . . . .	51
3.8	The half shaft model extended with gear backlash. Note that $\omega_{d,i}$ , the differential output speed, is equal to $\omega_{tr}$ for the front axle, and $\omega_{em}/\zeta_{gb}\zeta_{rd}$ for the rear axle. . . . .	53
3.9	A free-body diagram of the tire. . . . .	56
3.10	Driveline losses as functions of speed and torque. . . . .	58
4.1	Identification of the engine friction using dynamometer data. The approximation is only valid for nominal engine temperatures. . . . .	62
4.2	Experimental results from the engine coast down experiment. The torque converter speed ratio remains higher than the critical speed ratio during this test. . . . .	62
4.3	A comparison of the total friction and engine deceleration rate from the coast-down experiments. . . . .	64
4.4	Validation of the engine and the torque converter model combined. The simulated and experimental engine speed and torque converter speed ratio are shown. . . . .	64
4.5	The rear EM dynamics identification experiment. A sequence of short torque pulses are applied to the EM and the resulting motor speed is recorded. . . . .	66
4.6	EM internal losses as a function of the EM speed obtained from the coast down tests. . . . .	67

4.7	The impact of the rear electric machine time constant on the simulation results. . . . .	68
4.8	Validation of the rear driveline model. The simulated vehicle acceleration and EM speed are compared with the experimental results. . .	69
4.9	Details of the test shown in Figure 4.8. The gear backlash model accurately represents the transient effects in the rear driveline. . . . .	70
4.10	The simulated battery pack voltage and current are compared with experimental results for the test shown in Figure 4.8. . . . .	71
4.11	Validation of the front driveline model in engine only operation. The simulated vehicle acceleration and engine speed are compared with experimental data. . . . .	73
4.12	Validation of the front driveline model in engine only operation. The simulated transmission input-output speeds are compared with experimental data. . . . .	73
4.13	Details of the engine only operation validation test showing two gear upshifts under medium engine load. . . . .	74
4.14	Transmission on-coming and off-going clutch pressure traces used for the validation of the front driveline model. . . . .	75
4.15	Validation of the HEV model in hybrid operation. The simulated vehicle acceleration and engine speed are compared with experimental data. . . . .	76
4.16	Validation of the HEV model in hybrid operation. The simulated transmission input-output speeds are compared with experimental data. .	76
4.17	Validation of the HEV model in hybrid operation. The simulated battery pack voltage and current are compared with experimental data. .	77
4.18	Details of the hybrid operation validation test highlighting the driveline disturbance that occurs after the engine start. . . . .	78

5.1	The test vehicle's control hardware architecture. The gray-highlighted blocks represent the prototype control units that are implemented by the team while others are production control units. . . . .	83
5.2	Some of the important control signals and their communication with the vehicle control unit. Note that the wheel speeds are originally transmitted by the ABS control unit and that the battery control unit acts as a gateway for communication. . . . .	83
5.3	Control software development process. The embedded target toolbox and the target compiler differ based on the specific choice of the microcontroller. . . . .	85
5.4	Hierarchical control systems architecture in a hybrid-electric vehicle. .	87
5.5	A state machine representation of the vehicle supervisory controller. .	89
5.6	Potential issues with the implementation of control algorithms using finite state machines. . . . .	91
5.7	A typical accelerator pedal vs torque map for a diesel engine. . . . .	93
5.8	Maximum torque characteristics of an HEV. It is assumed that the transmission upshifts when the engine speed reaches 3000 rpm and that the engine is on during vehicle launch. . . . .	94
5.9	Maximum power characteristics of an HEV. The available power is calculated assuming 100% drivetrain efficiency. . . . .	95
5.10	A severe EM torque disturbance (experimental) causes oscillations in the rear driveline. The EM speed is a good indicator of rear driveline disturbances. . . . .	100
5.11	The plant-control interactions for the rear driveline active damping problem. . . . .	101
5.12	The Bode magnitude-phase plot of $H_{em}(s)$ . The targeted driveline oscillations lie in the 1-5 Hz frequency band. . . . .	102
5.13	The open-loop equivalent of the control scheme shown in Figure 5.11.	102



5.14	The Bode magnitude plots of $G_{cl}(s)$ , $G_{ol}(s)$ , and $K_{ol}(s)$ . . . . .	103
5.15	A comparison of pedal tip-in and tip-out responses with and without active driveline damping. Note that the driveline backlash causes a large overshoot in the vehicle acceleration following pedal tip-in when the controller is not used. . . . .	104
5.16	The average tank-to-battery and battery-to-tank energy conversion efficiencies take on different forms inside the numbered sections. This also requires that different equivalence factor formulations be used for different sections. . . . .	109
5.17	Variations of the proportional and integral SOC correction subfunctions with respect to SOC deviation from nominal and its weighted moving average. . . . .	111
5.18	The ECMS look-up table generation process. . . . .	113
5.19	A comparison of the conventional ECMS and the version used for real-time implementation. . . . .	115
5.20	Rapid switching between torque requests during the ECMS operation.	116
5.21	Variation of the ECMS cost function for four consecutive samples. The bold dot represents the minimum value of the cost function in each case.	117
5.22	A comparison of pedal tip-in responses at different battery SOC's. A torque hole is present for the case of SOC = 54% due to the poor calibration of the SOC correction function (5.25). . . . .	119
5.23	Poor engine idle quality resulting from the uncorrected ECMS engine torque request. . . . .	121
5.24	Engine torque reduction requested by the TCU during a 1-2 gear shift.	122
5.25	A comparison of the actual and the maximum available regenerative braking torque and power. A portion of the available regenerative braking power is discarded to achieve better drivability. . . . .	124
6.1	An abstraction of the modeling formalism that represents the switched hybrid systems of interest. . . . .	127

6.2	A block diagram representation of the controllers that are in effect inside the edge partitions. . . . .	129
6.3	Simplified driveline model for the HEV launch example. . . . .	130
6.4	A hybrid model of the mode traversals for the HEV launch problem. .	132
6.5	External torques acting on the system during the transition from electric only to parallel hybrid mode using open-loop control. Note that the ICE torque is a combination of the ISA and ICE torque requests. . . . .	137
6.6	Simulated engine and clutch speeds and vehicle acceleration during the transition from electric only to parallel hybrid mode using open-loop control. . . . .	138
6.7	Simulated engine and clutch speeds and vehicle acceleration during the transition from electric only to parallel hybrid mode using the proposed control design. . . . .	139
6.8	Simulated external torques during the transition from electric only to parallel hybrid mode using the proposed control design. . . . .	139
6.9	Top plot shows the simulated engine and clutch speeds using the revised control laws in the presence of model uncertainty. Lower plot shows a comparison of the vehicle accelerations for the three cases considered here. . . . .	142
6.10	External torques acting on the system in the presence of model uncertainty and actuator torque limitations. . . . .	143
6.11	The effect of clutch torque tolerance $\epsilon'$ (used in the control law) on the simulation result when the clutch friction coefficient is not accurately known. . . . .	143
7.1	Experimental validation of the feedback controller during pedal tip-in and tip-out. The test vehicle is in electric only operating mode. . . .	147
7.2	Controller performances when there is a change in backlash direction. .	149
7.3	Simulated backlash fill time as a function of the EM torque request. .	150

7.4	Vehicle speed and engine speed acquired during the control strategy verification test. Following the convention in Figure 5.5, test sections are labeled such that 2, 4 and 5 represent the electric only, hybrid and regenerative braking modes respectively. . . . .	152
7.5	Actuator torque requests, driver's pedal positions and vehicle acceleration obtained during the control strategy verification test. . . . .	153
7.6	Battery voltage, battery current (positive currents indicate battery discharge), estimated battery SOC, and the ECMS equivalence factor obtained during the control strategy verification test. . . . .	154
7.7	Effectiveness of the dead-band function in reducing torque chattering. . . . .	155
7.8	Operating points of the actuators on the speed-torque plane. . . . .	158
7.9	The estimated battery SOC during the fuel economy test. . . . .	159
7.10	The driveline disturbance during the mode transition using the open-loop control strategy at different vehicle speeds. . . . .	165
7.11	A comparison of driveline speeds and vehicle acceleration using the described controllers. In both cases, the mode transition sequence is triggered at $v_{veh} = 10$ mph. . . . .	166
7.12	A comparison of the actuator torque requests given by the described controllers. In both cases, the mode transition sequence is triggered at $v_{veh} = 10$ mph. . . . .	167
7.13	The driveline disturbance during the mode transition using the proposed control strategy at different vehicle speeds. . . . .	169
B.1	A real-world driving cycle used to evaluate the fuel economy of the test vehicle. . . . .	178

## NOTATION AND ACRONYMS

### Acronyms

ABCU	Anti-locking Braking system Control Unit
ABS	Anti-locking Braking System
AC	Alternating Current
AMT	Automated Manual Transmission
BCU	Battery Control Unit
BSA	Belted Starter Alternator
CAN	Controller Area Network
CX-DYN	Challenge-X Dynamic Simulator
DC	Direct Current
DOF	Degree-Of-Freedom
ECMS	Equivalent Consumption Minimization Strategy
ECU	Engine Control Unit
EESS	Electrical Energy Storage System
EM	Electric Machine
EVT	Electrically Variable Transmission
HEV	Hybrid Electric Vehicle
ICE	Internal Combustion Engine
I/O	Input/Output
ISA	Integrated Starter Alternator
MCU	(Rear Electric) Motor Control Unit
MPGGE	Miles Per Gallon Gas Equivalent
NiMH	Nickel Metal Hydride
NVH	Noise, Vibration and Harshness
NOx	Nitrogen Oxide
PGS	Planetary Gear Set
PID	Proportional-Integral-Derivative
RGS	Ravigneaux Gear Set
RTI	Real Time Interface
SACU	Starter-Alternator Control Unit
SOC	State Of Charge
TCU	Transmission Control Unit
VCU	Vehicle Control Unit

## MODELING

### Symbols

$A$	Surface area
$a$	Acceleration
$b$	Damping coefficient
$C$	Model coefficient
$F$	Force
$f$	Mapping function
$g$	Gravitational acceleration
$I$	Current
$J$	Inertia
$K$	Geometrical constant
$k$	Torsional stiffness
$M$	Mass
$n$	Number of elements
$P$	Power
$p$	Pressure
$R$	Radius
$S$	Battery state-of-charge
$T$	Torque
$u$	Longitudinal tire deflection
$V$	Voltage
$v$	Velocity
$Z$	Resistance
$\alpha_{dr}$	Accelerator pedal position
$\beta_{dr}$	Brake pedal position
$\delta$	Time delay
$\eta$	Energy conversion efficiency
$\gamma$	Road grade
$\gamma_c$	Torque converter coupling speed ratio
$\kappa$	Transient tire slip
$\mu$	Friction coefficient
$\omega$	Angular velocity
$\sigma_k$	Tire relaxation length
$\tau$	Time constant
$\rho$	Density
$\theta$	Angular position
$\zeta$	Speed reduction ratio

## Subscripts

<i>a</i>	Air
<i>acc</i>	Accessory
<i>act</i>	Actual quantity
<i>b, *</i>	Transmission brake, *
<i>bl</i>	Backlash
<i>batt</i>	High-voltage battery
<i>br</i>	Brake
<i>bsa</i>	Belted-starter alternator
<i>c, *</i>	Transmission clutch, *
<i>cg</i>	Counter gear
<i>d</i>	Vehicle drag
<i>dr</i>	Driver
<i>em</i>	Electric machine
<i>f</i>	Front (axle or wheel)
<i>f1</i>	One-way clutch
<i>fd</i>	Front differential
<i>fr</i>	Friction
<i>gb</i>	Gearbox
<i>hs</i>	Half shaft
<i>ice</i>	Internal combustion engine
<i>ice, f</i>	Engine fuel
<i>idle</i>	Engine idle condition
<i>ind</i>	Indicated quantity
<i>oc</i>	Open-circuit
<i>p</i>	Torque converter pump side
<i>pgs, c</i>	PGS carrier
<i>pgs, p</i>	PGS pinion gear
<i>pgs, r</i>	PGS ring gear
<i>pgs, s</i>	PGS sun gear
<i>r</i>	Rear (axle or wheel)
<i>rd</i>	Rear differential
<i>req</i>	Requested quantity
<i>rgs, c</i>	RGS carrier
<i>rgs, p1</i>	RGS pinion gear 1
<i>rgs, p2</i>	RGS pinion gear 2
<i>rgs, r</i>	RGS ring gear
<i>rgs, s1</i>	RGS sun gear 1
<i>rgs, s2</i>	RGS sun gear 2
<i>rr</i>	Rolling resistance
<i>s</i>	Tire slip
<i>t</i>	Torque converter turbine side

$tc$	Torque converter
$th$	Threshold value
$tr$	Transmission
$veh$	Vehicle
$x$	Longitudinal direction
$wh$	Wheel (or tire)
$z$	Vertical direction

## CONTROL

### Symbols

$A$	Linear state space representation, plant matrix
$B$	Linear state space representation, input matrix
$C$	Linear state space representation, output matrix
$\mathcal{C}^\infty$	Continuously differentiable
$\mathcal{F}$	Vector field
$G(s)$	Transfer function from system input to system output
$H$	State to performance output transformation matrix
$H(s)$	Transfer function from system output to performance output
$\mathcal{J}$	Cost function
$K$	Controller gain matrix
$K(s)$	Compensator transfer function
$\mathcal{P}$	State space partition
$Q_{lhv}$	Lower-heating value of fuel
$\mathcal{S}$	Switching set
$s$	Equivalence factor
$\mathcal{T}$	Transition map
$T$	Linear transition map
$\mathcal{U}$	Controller space
$u$	Input vector
$\mathcal{X}$	State space
$w$	Frequency
$x$	State vector
$y$	System output vector
$z$	Performance output vector
$\Delta T$	Sampling time
$\Sigma$	System mode
$\Omega$	Sensitivity function
$\bar{\eta}$	Average efficiency
$\epsilon$	Clutch tolerance at zero slip speed
$\gamma_{wc}$	Vehicle weight correction factor for fuel economy

## Subscripts

<i>act</i>	Actual
<i>aero</i>	Aerodynamic
<i>ave</i>	Average
<i>belt</i>	Belt coupling
<i>ch</i>	Charge
<i>cl</i>	Closed-loop
<i>dc</i>	Dry clutch
<i>dis</i>	Discharge
<i>drv</i>	Drivability
<i>eqf</i>	Equivalent electrical fuel
<i>hp</i>	High-pass filter
<i>lp</i>	Low-pass filter
<i>rgn</i>	Regenerative braking
<i>road</i>	Road load
<i>tank</i>	Fuel tank
<i>ol</i>	Open-loop



# CHAPTER 1

## INTRODUCTION

### 1.1 Motivation

According to a recent study conducted by the United States Energy Information Administration [1], the transportation sector used 68% of all available petroleum resources in the U.S. in 2006. 66% of these resources were imported. The study also shows that the transportation sector performed the worst overall in energy conversion efficiency estimated at only 20%. As a result, the automotive industry is increasingly pursuing alternative propulsion technologies to reduce the dependency of transportation on non-renewable fuels and to improve the efficiency of vehicles.

One of currently viable technologies is the hybridization of conventional and electric powertrains with the objective of reducing fuel consumption and harmful exhaust emissions. This class of hybrid vehicles, commonly referred to as hybrid-electric vehicles (HEVs), utilizes electrical energy storage and drive systems often in combination with internal combustion engines (ICEs). The idea of developing a hybrid drivetrain dates as far back as 1898 when Dr. Ferdinand Porsche built the first hybrid car. Porsche's hybrid used an internal combustion engine to spin a generator that provided power to electric motors located in the wheel hubs [2]. Unfortunately, hybrid vehicles have since been overlooked mainly due to the significant developments in ICE technologies and the availability of petroleum at a reasonable cost. Today, the situation is changing rapidly as the cost of petroleum continues to increase and the growing global population continues to take its toll on supply. As a result, hybrid

vehicles are rapidly entering the mainstream and are now produced in a variety of powertrain configurations<sup>1</sup> to meet the high standards of automobile consumers and the demanding requirements of government regulations.

Regardless of the selected hybrid configuration, a careful coordination of the powertrain functions is crucial to improve the energy conversion efficiency, reduce pollutant emissions and improve drivability. These goals are equally important and often conflicting from a control engineering standpoint. As an example, ICEs operate with greater efficiency at moderate speeds and loads, whereas drivability and emissions constraints generally favor low load operation. A control framework that appropriately combines these objectives by making “optimum” use of the hybrid powertrain is highly desirable. One of the main objectives of this research is the development and experimental verification of such control framework with particular focus on improved drivability and fuel economy.

In order to address the control issues related to vehicle drivability, the dynamical behavior of a hybrid vehicle should be carefully analyzed. A dynamic vehicle simulator facilitates this analysis and enables the design of model-based control strategies with the objective of reducing controller calibration effort. The simulator should be designed such that it accurately represents the vehicle behavior within the frequency bandwidth of interest and without imposing excessive complexity. Therefore, in addition to the previously discussed objective, this research also discusses the development and validation of a HEV model that predicts the dynamic behavior of the vehicle in the low-frequency range.

A thorough investigation of the drivability issues in HEVs reveals the following fact: The underlying principles of HEV operation lead to additional drivability issues in HEVs compared to conventional vehicles. This is due to *the hybrid nature of the HEV drivetrains and the control strategies* that manage them. In context of the systems theory, hybrid systems are systems that consist of interacting continuous-time and discrete-time dynamics. A subset of hybrid systems, that is relevant to

<sup>1</sup>The reader is referred to [3] for a detailed description of hybrid vehicle architectures that have been implemented by various manufacturers and research groups around the world.

this study, is the class of switched systems [4] in which the continuous phases of a system’s dynamics are interrupted by a switching signal that is either supervised by a high-level logic or is a result of the dynamics of the plant.

A relatively unexplored problem in the area of switched systems, which is of great practical interest, is the analysis and control of *mode-switching induced transients*. In the case of HEVs, the adverse effects of mode-switching induced transients are revealed through undesired drivability characteristics. Examples of automotive applications in which this problem is apparent are: the control of mode transitions in multi-mode combustion engines [5], the control of gear shifting in automated-manual transmissions [6] and the control of soft-landing in variable valve actuated engines [7]. Due to the broad applicability of this framework, the final objective of this dissertation is to study potential control solutions for systems that exhibit mode-switching induced transients. Applications to hybrid-electric vehicles are also demonstrated.

## 1.2 Contributions of the Dissertation

The primary objective of this dissertation is to investigate and find control solutions to drivability problems that arise due to the intrinsic characteristics of hybrid-electric vehicle drivetrains and the control strategies that manage them. In accordance with this objective, the first contribution of this research is the development and experimental validation of a through-the-road parallel HEV model with the purpose of predicting low-to-mid frequency vehicle dynamic behavior that has impact on longitudinal drivability. Throughout the course of this dissertation, simplified versions of this model are used for the design of control algorithms.

A second contribution is made in the area of HEV control design. Despite the presence of considerable research effort on fuel economy optimization, these works rarely consider the drivability effects of the actions taken by the energy management controllers. This dissertation attempts to address this limitation. Through experimental investigations of a fuel optimization technique called the equivalent consumption minimization strategy (ECMS) [8], critical drivability issues are identified and

solution methods are proposed as modifications to the ECMS. In fact, most of the drivability issues discussed in this dissertation are relevant to a broad class of energy management strategies rather than being specific to the ECMS.

One of the findings of this research is the importance and difficulty of maintaining good drivability in a HEV that uses a multi-mode control architecture because of the need for proper utilization of the engine start-stop function. This observation motivated the study in the area of control of systems with mode-switching induced transients. The beginnings of a mathematical approach are presented to address the problem of achieving seamless mode transitions in a special class of switched dynamical systems. The proposed framework is applied to a HEV driveline control problem during the transition from electric only to hybrid mode.

### **1.3 Organization of the Dissertation**

This dissertation is organized as follows. Chapter 2 provides an overview of the past research related to the modeling and control of hybrid-electric vehicles as well as some fundamental concepts in the area of hybrid systems. Chapter 3 describes the development of a drivability-oriented dynamic model for a parallel HEV configuration, which is also the experimental platform of this dissertation. Chapter 4 outlines the experimental procedures that are used to validate the vehicle model developed in Chapter 3. Various comparisons of model predictions and real world data are given for typical HEV driving conditions. Chapter 5 explains the control strategies implemented onboard the test vehicle that are mainly aimed at improving the fuel economy and drivability of the test vehicle. Chapter 6 provides the beginnings of a framework that addresses the problem of the control of systems with mode switching induced transients. The presented approach is also applied to a simplified HEV driveline control problem. Chapter 7 outlines the experiments that are used towards verifying the control strategies described in Chapters 5 and 6. The focus of these experiments is

on the improvement of vehicle drivability during transient events such as pedal tip-in/tip-out and operating mode transitions. In Chapter 8, some concluding remarks are made and future research directions are proposed.

Appendix A provides a comprehensive list of the signals used by the vehicle control system. Appendix B contains data from a real-world driving cycle that is used to measure the actual fuel economy obtained from the test vehicle in Chapter 7. Also, Appendix C gives the hybrid model used in Chapter 7 for the design of the HEV launch controller.

## CHAPTER 2

### LITERATURE REVIEW

#### 2.1 Hybrid-Electric Vehicle Architectures

Hybrid-electric vehicles incorporate multiple energy storage and conversion units for propulsion. As a result of the wide range of possibilities involved in integrating the elements of a hybrid propulsion system, different vehicle architectures evolved. The specific choice of a HEV configuration depends on several factors including the type of the application, cost and weight considerations and expectations of the targeted customers. Investigation of the techniques used in the design of hybrid vehicle powertrains is beyond the scope of this research. The main objective of this section is to familiarize the reader with common HEV configurations and the terminology used to classify hybrid vehicles.

A hybrid-electric vehicle propulsion system typically consists of a fuel tank, an ICE, one or more electrical energy carriers (e.g. batteries, super-capacitors), electric machines, power converters, a transmission and various driveline linkages. These elements can be combined in various ways to accomplish different objectives. The resulting configurations can be treated under the following general categories:

**Series Hybrids:** The tractive power is supplied directly by one or more electric machine(s) in series HEV architectures. An electric generator drives an ICE in an efficient operating region to charge the electrical energy storage system (EESS). Series hybrid vehicle architectures are typically used in heavy-duty vehicles such as trucks

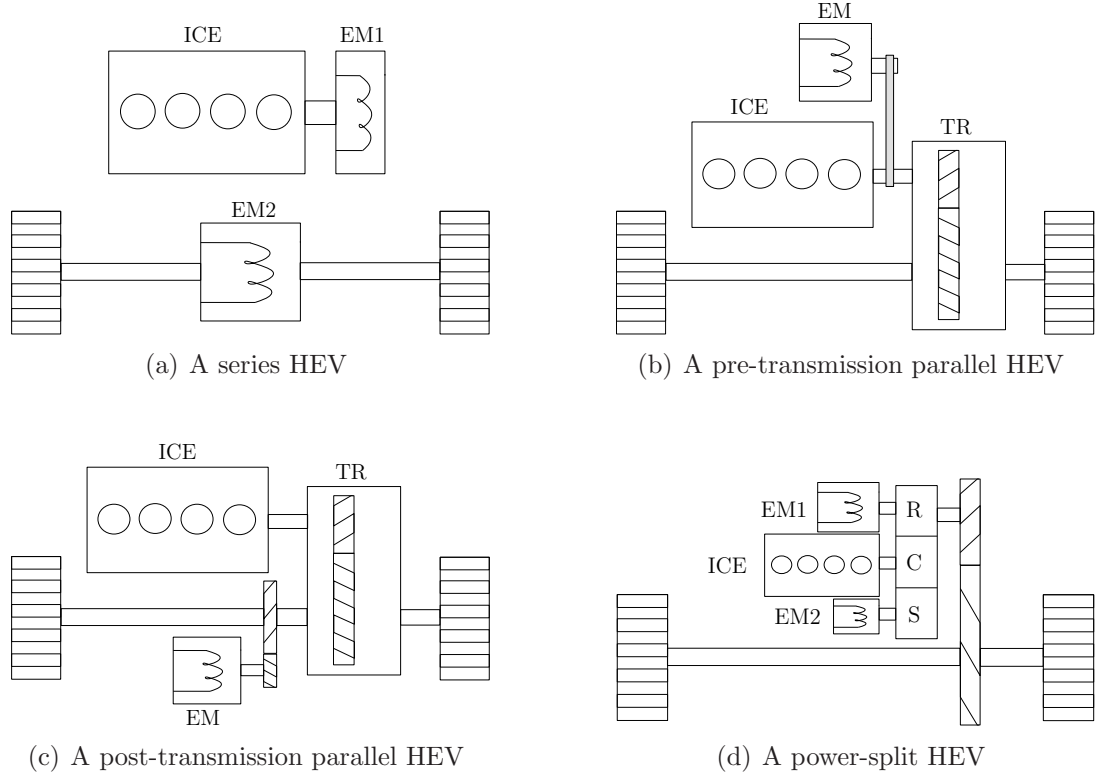


Figure 2.1: Common hybrid-electric vehicle architectures (TR: transmission, R: ring gear, C: pinion gear carrier, S: sun gear)

and locomotives [3]. Also, a vehicle that uses wheel hub motors is most suited to operate with the series hybrid principle. An example series HEV architecture is depicted in Figure 2.1(a).

**Parallel Hybrids:** In this class of hybrids, the tractive power is supplied by a proper combination of the ICE and the electric machines (EMs). A dedicated generator or a motor-generator can be used to maintain the EESS in a desired state-of-charge (SOC) range. Parallel-hybrid vehicles can be further divided into two categories according to the location of the EMs. A pre-transmission parallel hybrid has an EM connected to the ICE prior to the transmission. Mild-hybrids with integrated starter-generators

and dual-mode hybrids<sup>1</sup> fall into this category. An example pre-transmission parallel HEV architecture is depicted in Figure 2.1(b). A post-transmission parallel hybrid has a traction EM connected to either the driven axle (after the final drive) or the non-driven axle (known as a *through-the-road* hybrid). An example post-transmission parallel HEV architecture is depicted in Figure 2.1(c).

**Power-split Hybrids:** Electrically-variable transmissions (EVTs) [9] are exclusively used in power-split HEV architectures. An EVT is a single- or multiple-stage arrangement of planetary gearsets that allows the power generated by an ICE and two EMs to be distributed in a continuously variable fashion. While a portion of the generated power is delivered to the road, the excess power is stored in the battery. The simplistic design of EVT<sup>2</sup>s (less parts, very few to no friction elements) brings unique benefits to power-split hybrids in terms of the ease of packaging and the reduction of overall weight. An example power-split HEV architecture is depicted in Figure 2.1(d).

Other hybrid vehicle concepts incorporating mechanical or hydraulic storage devices have been also investigated [3]. However, the three categories listed above cover majority of the hybrid vehicle architectures available today.

## 2.2 Modeling: General Concepts and Applications to HEVs

A model is a mathematical representation of the behavior of a process, a logic concept, or the operation of a system. Mathematical models of dynamical systems, such as the system studied in this dissertation, are mostly executed in numerical simulation environments. The purpose of a numerical simulation is to mimic the actual behavior of a system under controlled operating conditions. Analyzing the model predictions allows one to improve the targeted aspects of the system in consideration.

In automotive control applications, component and system models are used to achieve the following objectives.

<sup>1</sup>Dual-mode parallel hybrids are strong-hybrids that can use the EM, the ICE, or a combination of the two for propulsion [3].

<sup>2</sup>This comment applies to single-stage EVT<sup>2</sup>s since the mechanical construction of multiple-stage EVT<sup>2</sup>s may be more complex than conventional transmissions in certain cases.



**Design Verification:** Models help determine (prior to implementation) whether a product or a system meets the desired technical specifications.

**Improved Reliability:** Models provide a means for investigating the system reliability in a computer environment. External effects such as sensor noise and actuator faults can be conveniently simulated to predict whether the system will function reliably under real life operating environments. Such a model-based testing approach reduces the need to perform costly and cumbersome experiments on a prototype of the physical system.

**Reduction in Development Time:** As a result of the discussed benefits of using system models, the time associated with the product development process can be significantly reduced.

**Reduction in Calibration:** Production-intent control systems require extensive calibration for proper operation. Accurate models can help simplify the calibration process by allowing the designer to make the initial adjustments directly on the system model.

The phrase *model-based design* is typically used to emphasize the benefits of model-aided design techniques in the product development cycle. An example product development cycle used in systems engineering (“V-chart”) is shown in Figure 2.2. The model-based design techniques used in this cycle are not limited to software-based techniques. It is common practice to include hardware prototypes of selected components in a model to test the unique physical aspects of a real system. This technique, known as hardware-in-the-loop testing [10], is used for component/system verification and validation in the second half of the development cycle. By combining hardware and software-in-the-loop design techniques, the quality and efficiency of a product development cycle can be greatly improved.

Despite their convenience, physical models are ultimately inaccurate representations of real systems. The level of accuracy usually depends on the model complexity. Unfortunately, sophisticated system models require extensive computational resources

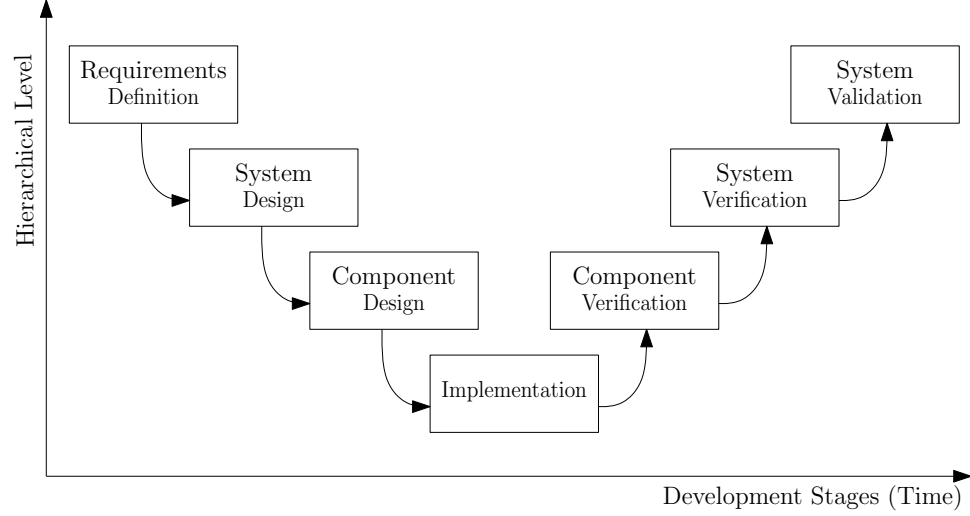


Figure 2.2: Example of a model-based development cycle used in the automotive industry.

and are time consuming to simulate. Therefore, it is often necessary to make careful judgements regarding the required detail of modeling according to the desired model accuracy and the available computational resources.

In systems engineering, a typical approach for the design of computational models is to focus on the system dynamics that have a significant impact on the behaviors of the variables of interest. As a result, the dynamics that are not relevant to the targeted application are abstracted. Following this approach for automotive systems results in the classification of vehicle models as static, quasi-static, low-frequency dynamic and high-frequency dynamic models. The primary functions of these vehicle models can be summarized as follows:

**(Quasi-) Static Models:** Static and quasi-static models are treated under the same category since both types of models serve similar purposes. The main objectives are to evaluate the performance characteristics, fuel economy and exhaust emissions of vehicles over pre-determined test cycles. The preliminary design and testing of high-level control strategies for HEVs are usually done using quasi-static vehicle models.

**Low-Frequency Dynamic Models:** In addition to the benefits of quasi-static models, low-frequency dynamic models provide further insight into driveline and vehicle dynamics that have impact on the drivability, stability and handling of a vehicle. Modeling of the longitudinal vehicle motions is sufficient to characterize drivability, however, lateral motions should also be incorporated to evaluate stability and handling. Dedicated driveline, traction or stability controls can be developed and tested using low-frequency dynamic vehicle models.

**High-Frequency Dynamic Models:** These types of models are generally developed to analyze the noise, vibration and harshness (NVH) characteristics of vehicles. Due to issues related to model scale and complexity, high-frequency dynamic models are mostly applied to individual vehicle sub-systems (e.g. transmissions, suspension systems) or components (e.g. transfer cases, engine mounts). Analytical or finite-element models are often utilized for analysis.

The modeling objectives described above are correlated to various frequency regions in Figure 2.3. A conceptual power spectrum of the vehicle acceleration is also given. This inherent *spectral separation* of the drivetrain dynamics will be further discussed in Chapter 6 in order to achieve decoupling of the control tasks.

Among the aforementioned classes of vehicle models, the low-frequency dynamic models that represent longitudinal vehicle motions are most relevant to this research. However, some of the important characteristics of quasi-static HEV models are also highlighted owing to their widespread use for vehicle architecture selection, supervisory control design and performance evaluation.

Quasi-static HEV models can be rapidly executed in a simulation environment and they are sufficiently accurate for the prediction of “slow” vehicle dynamics (as indicated by Figure 2.3). These models are usually categorized as forward- or backward-looking according to the propagation of events and power flows inside the simulators [11]:

**Backward-looking models:** These models operate based on the assumption that a predefined vehicle speed trace is met by the vehicle. Therefore, the driver behavior is

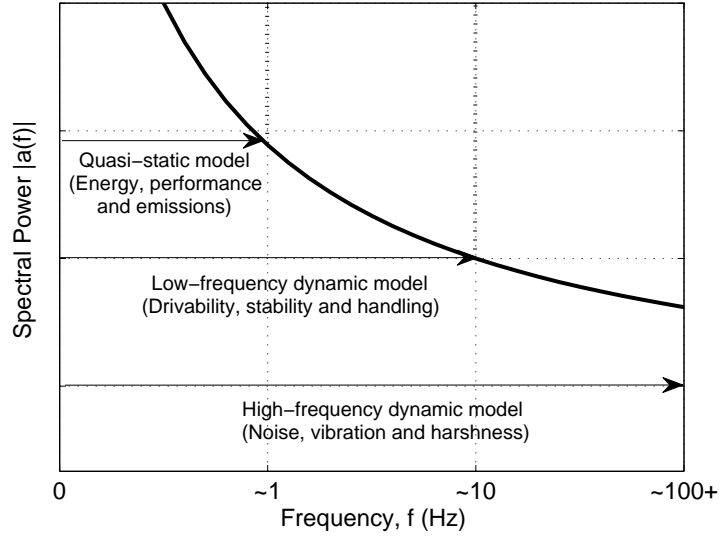


Figure 2.3: Conceptual schematic of the power spectrum of the vehicle acceleration and the regions of interest for modeling.

not modeled in the simulator. Based on the predicted road loads, the tractive power required on the road is carried backwards through the drivetrain until the energy (fuel and electricity) required to meet a given speed trace is computed. These models can be executed faster than forward-looking models, however, they pose major weaknesses as a result of the assumption that the vehicle speed trace is already met. Therefore, it is not possible to simulate events such as full throttle acceleration<sup>3</sup> in which the vehicle speed trace is not defined *a priori* and the maximum effort of the vehicle is to be determined.

**Forward-looking models:** Forward-looking models follow a more realistic chain of computations from the standpoint of the causality of events that take place in an actual vehicle. A driver model (which is usually a PID controller) compares the simulated vehicle speed with the speed trace and generates accelerator and brake

<sup>3</sup>Note that full throttle acceleration is an expression used for conventional vehicles operated by throttle controlled engines. In the context of HEVs, this simply corresponds to a maximum power request made by the driver.

commands. These commands along with other feedback variables are then received by the HEV control strategy and a power split is computed. Using this power split, the energy consumption (or generation) is calculated using look-up table data. The power provided by the actuators is then propagated downstream through the driveline by taking into account the component energy losses. The resulting tractive power and the predicted road loads are used to compute the vehicle speed which can be different from the original speed trace. Forward-looking type simulators are well-suited for the implementation and comparison of control strategies and they enable the prediction of maximum effort events and the validation of actual vehicle behavior. The main drawback is the relatively poor simulation speed. The simulator developed in this research (although not quasi-static) is also of forward-looking type.

Examples of quasi-static HEV simulators and reconfigurable simulation environments are given in [11–14]. Notably, the simulation environments developed at the Argonne National Laboratory (PSAT) [12] and the National Renewable Energy Laboratory (ADVISOR)<sup>4</sup> [11] provide excellent means for rapid simulation and evaluation of a wide variety of HEV configurations.

Regardless of the differences in the operating principles of forward- and backward-looking simulators, the simplifying assumptions employed in quasi-static models apply to both categories. Power conversion efficiencies of drivetrain components and the energy (fuel or electricity) consumption/regeneration of on-board energy carriers are typically represented in the form of static look-up table data. The only degree-of-freedom (DOF) considered is that of the vehicle.<sup>5</sup> The contributions of driveline inertias are included as part of an equivalent vehicle mass.

Low-frequency dynamic vehicle models are extensions of forward-looking quasi-static models with the objective of predicting the transient behavior of the drivetrain. As previously mentioned, these models typically have a bandwidth of up to 10-20 Hz.

<sup>4</sup>This simulation environment was originally developed at the National Renewable Energy Laboratory. However, it is currently a product of the AVL LIST GMBH.

<sup>5</sup>In certain cases where forward-looking quasi-static simulators are used, the engine dynamics are also explicitly computed.

The development of HEV low-frequency dynamic models have been reported in [15–18]. These models are well-suited for the study of low-frequency dynamics of both mechanical and electrical sub-systems in HEVs.

“Mixed-bandwidth” vehicle simulators and modeling environments that combine quasi-static and dynamic component models have also been developed. These types of models generally aim to serve specific purposes. For example, the SimDriveline™ toolbox, developed by The MathWorks Inc. [19], is a modeling environment that incorporates dynamic models of driveline components (such as the transmission and the tires) in addition to a number of quasi-static models that characterize the behavior of the components upstream from the transmission (such as the engine and the torque converter). A study by [20] describes the development of an HEV simulator with emphasis on the dynamic modeling of the power electronics. Another example of mixed-bandwidth HEV models is given in [21] where a simplified longitudinal drivetrain model of a series HEV is combined with detailed lateral dynamics to facilitate the development of a vehicle stability controller.

It is important to note that HEV drivetrains have similar operating principles as conventional drivetrains with the exception of the electrical drive systems and, in some cases, special transmission units used in HEVs. Therefore, most automotive modeling principles apply to both conventional and hybrid vehicles. However, the modeling of conventional drivetrains and subsystems (particularly engines and transmissions) is a very broad topic and only some key references on automatic transmission models are highlighted here.

Drivability-oriented dynamic modeling of automatic transmissions has been the subject of various studies [22–24]. The main purpose of these models is to investigate the transmission behavior during gear shifting. The vibrational characteristics introduced by the compliance of transmission parts are not relevant to these types of models. A study by Deur *et al.* [22] focused on park-drive engagement dynamics with an emphasis on nonlinear effects such as nonlinear friction, clutch drag and backlash. Cho [23] used a simplified model of a four-speed transmission for the development of a clutch-to-clutch shift controller during the 1-2 gear shift. Zheng *et al.* [24] described a

detailed four-speed transmission model that includes all upshift mechanical dynamics as well as a model of the hydraulic system. The common modeling approach followed by Cho and Zheng *et al.* is that each phase of operation (e.g. 1st gear, 1-2 torque phase, 1-2 inertia phase) is individually modeled and the transitions between them are enabled by logic statements. However, the work by Fujii *et al.* [25], describes the derivation of a 11 DOF transmission model which also includes sophisticated models of friction elements. This type of model is appropriate for detailed analysis and validation of transmission behavior. However, such level of complexity is not suited for an overall hybrid vehicle model.

The HEV model presented in this research focuses on the mechanical drivetrain behavior with a particular emphasis on transmission dynamics. The models for power electronics and electrical energy storage/distribution units are highly simplified since these components do not have a direct influence on vehicle drivability. In this respect, the developed simulator can be classified as a mixed-bandwidth HEV simulator. The main purpose of the simulator is to characterize the input-output interactions between the drivetrain components. Internal states that do not affect the mechanical response of the vehicle (e.g. engine manifold temperature) are not explicitly modeled.

## 2.3 Energy Management in Hybrid-Electric Vehicles

In a hybrid vehicle, an automated powertrain controller coordinates the power flows between the energy carriers (electrical or thermal), the actuators and the environment in response to the driver's power demand. The main objectives of the controller are to improve fuel economy, reduce exhaust emissions and maintain various subsystems (e.g. the battery) in their desired states while ensuring seamless operation of the drivetrain. As a result, the actions taken by the control strategy play a critical role in determining the performance and efficiency of a hybrid vehicle.

Figure 2.4 depicts the power flows and corresponding operating modes typically used in a parallel HEV. Zero-emissions mode, engine start-stop, hybrid mode and

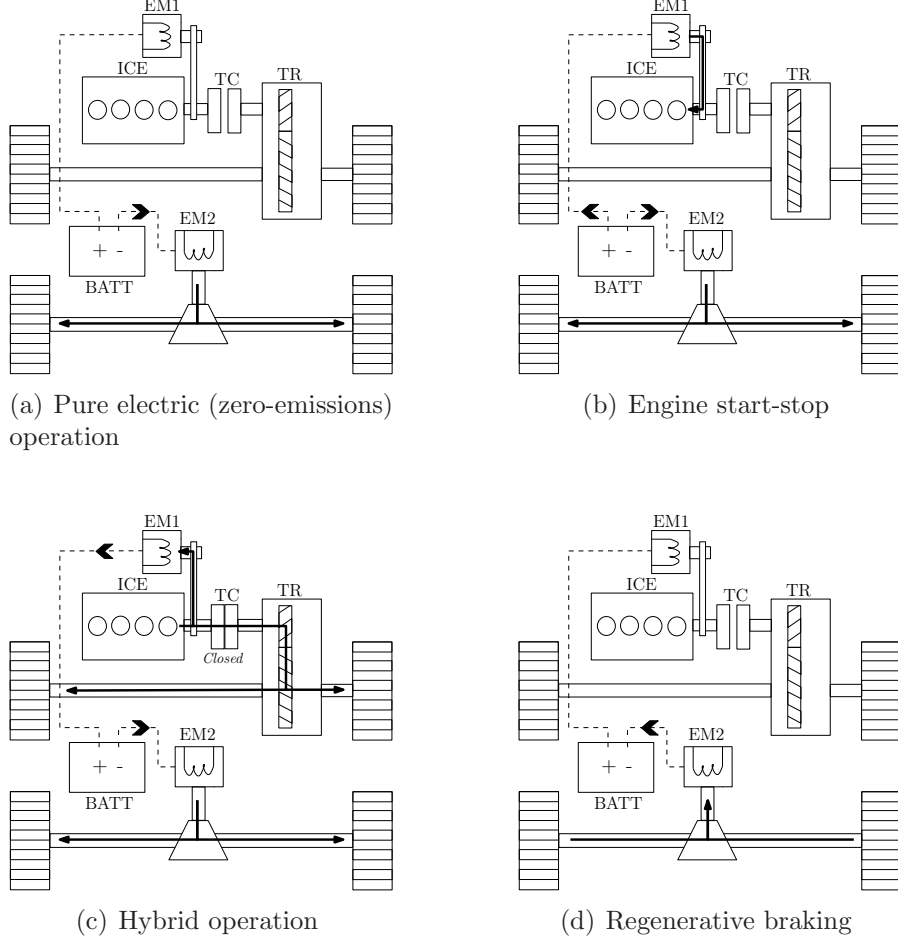


Figure 2.4: Typical HEV operating modes (TC: torque coupler, BATT: battery)

regenerative braking are a few of the strategies that are used to achieve the control objectives described above.

The current focus of controller design for HEVs is on the generation of policies that minimize the fuel consumption over an unknown driving cycle. This problem (known as the energy management problem) has been extensively studied including the managing of the state of the electrical energy buffer for charge-sustaining vehicles [26–29]. Assuming *a priori* knowledge of the driving cycle, a globally optimal solution to this problem can be obtained by dynamic programming [30,31]; however practical solutions cannot assume such knowledge of the driving cycle.



Practical approaches can be investigated under two main categories: heuristic methods and real-time optimization techniques. *Heuristic methods* are based on rules determined by the designer according to his/her knowledge of the powertrain. For example, the following basic logic statement can be used to maintain the battery charge higher than a desirable level in an HEV:

$$\text{If Battery Charge is low then Motor Traction Torque} := 0 \quad (2.1)$$

A rule-based control algorithm is comprised of a large number of logic statements similar to (2.1). When combined, these statements create a knowledge base that can be used to control the high-level functions of the hybrid powertrain. These types of algorithms are also suited to the implementation of fuzzy logic control for HEVs as discussed in [32]. The existence of a number of patents on rule-based HEV control algorithms [33–35] makes it evident that heuristics based energy management techniques are commonly used in industrial applications.

The efficacy of heuristic methods strongly relies on the calibration of rules. As a drawback of the large scale of the HEV system, developing an efficient rule-based supervisory control strategy can be fairly time consuming. However, some benefits of rule-based strategies are also worthwhile to note. For production intent systems, development and calibration of control algorithms are usually handled by different engineering groups. Therefore, the control design engineer is responsible for making tuning of the control algorithms intuitive for the calibration engineer. In this respect, heuristic methods provide benefits over mathematically involved control strategies. Another advantage comes from the flexibility of a rule-based algorithm in the sense that additional rules can be introduced into an existing strategy without requiring major changes in the algorithm structure.

*Real-time optimization techniques* result in controllers that minimize a combined metric which is generally comprised of fuel and battery use. Due to the model-based nature of these controllers, the calibration requirements are much lower than those

designed using heuristic methods. Also, optimality<sup>6</sup> of the resulting controllers can be guaranteed in a non-global sense.

Equivalent Consumption Minimization Strategy (ECMS), a model-based instantaneous fuel minimization technique, has been successfully applied to the control of hybrid vehicles [8,30,36]. This technique utilizes a weighted cost function of electrical and fuel energies. Its performance is usually improved by adaptively tuning an equivalence ratio between the two forms of energy. This ratio can be tuned according to the driving conditions and corrected as necessary to compensate for large deviations in the battery SOC [28,30]. Another real-time control strategy presented in [37] uses a principle similar to ECMS to calculate the optimal torque split. In this strategy, a target performance metric that consists of energy consumption and emissions is minimized over permissible ICE and EM torque requests. The solution is then adjusted according to battery SOC considerations.

Applications of stochastic control to the HEV energy management problem have been demonstrated in [38,39]. In their work, Lin *et al.* [38] computed an optimal energy management policy by iteratively solving a stochastic dynamic program over an infinite horizon. The resulting controller is implemented in the form a static state feedback controller. In this control scheme, the driver's power request is modeled as a random Markov process to accurately represent the nondeterministic nature of this variable. Another relevant work by Tate *et al.* [39] used the shortest path stochastic control approach for energy management. The main advantages of this method over the method presented in [38] are due to the proposed battery SOC control technique and the reduced number of tuning parameters involved in the design. Tate's method allows the battery SOC to freely vary from its nominal value until the vehicle is turned off (as opposed to penalizing SOC deviations continuously). It is also claimed that better fuel economy is obtained as a result of the relaxed SOC constraint using the method described in [39].

<sup>6</sup>Conditions for optimality can be defined in terms of fuel economy, emissions, performance etc. Here, it is assumed that fuel economy is the primary metric for design.

Heuristic Methods		Optimization Techniques	
Advantages	Disadvantages	Advantages	Disadvantages
Simple algorithm development	No guarantee for optimality	Leads to (quasi-) optimal control policies	Requires accurate component models
Intuitive calibration	Time-consuming calibration	Small number of calibration parameters	Calibration may be non-intuitive
Modest need for computational resources	Performance dependent on vehicle architecture	Easy to adapt to different architectures	Computationally burdensome

Table 2.1: Advantages and disadvantages of heuristic methods and real-time optimization techniques for HEV control.

Other techniques such as optimal sliding control [40], robust control [41] and model predictive control [42] have also been investigated for the energy management control of HEVs. Wei *et al.* [40] studied the conditions for which an optimal sliding control exists assuming a fixed (and known) power request. This work showed that, if exists, an optimal solution that also satisfies the battery SOC constraint can be obtained by fast switching between the specified operating points of the engine. Pisu *et al.* [41] presented  $H_\infty$  controllers for energy management in HEVs. Unfortunately, the algorithm complexity, computational burden and large number of tunable parameters make the design of  $H_\infty$  controllers virtually impractical for real-time HEV control applications. Koot *et al.* [42] suggested that a quadratic or dynamic programming problem can be solved within the model predictive control framework using predicted future driving conditions over a short driving horizon. However, this strategy also requires extensive computational resources since the finite horizon dynamic programming problem should be solved online at every time step.

The advantages and disadvantages of heuristic methods and real-time optimization techniques for HEV control are listed in Table 2.1. A detailed comparison of real-time HEV energy optimization techniques is also given in a recent survey paper by Sciarretta *et al.* [43].

Most practical control strategies combine heuristic methods and optimization techniques to manage the power distribution in a hybrid vehicle. In this type of control

scheme, the vehicle operating modes (such as those depicted in Figure 2.4) and the interactions between the modes are usually determined by event or time based conditions. The power split inside an operating mode is determined by either heuristic methods or by the aforementioned optimization techniques. The control strategy developed in this dissertation also follows this approach.

Another important aspect of control is the reduction of exhaust emissions. In addition to conventional engine control techniques such as exhaust gas recirculation and air-fuel ratio control [44], certain types of pollutant emissions can be further reduced in HEVs by means of engine load shifting. The resulting lack of power, if any, can be compensated using electric machines.

The most common approach for incorporating emissions into control is to assign a penalty term for pollutant emissions and treat this term as part of the energy management objective [28,37]. This approach is motivated by the spectral separation principle previously demonstrated in Figure 2.3, i.e. the dynamics associated with most types of emissions are in the same bandwidth as the dynamics associated with energy consumption. On the other hand, drivability is mostly affected by transient events. Therefore, it can not be treated similar to energy consumption and exhaust emissions from a controls standpoint.

## **2.4 Control Techniques for Improving Drivability**

One of the objectives of this research is to analyze the impacts of HEV control strategies on vehicle drivability. Therefore, it is necessary to gain an in-depth understanding of the drivability issues that occur in conventional and hybrid vehicles. This section describes these issues and reviews some of the active control techniques used to overcome drivability problems in conventional, electric and hybrid-electric vehicles.

Drivability is a subjective term associated with the driver's perception of the dynamic responses of the vehicle. It is usually evaluated by experienced drivers that analyze the vehicle behavior under specific driving conditions such as engine idling, take-off, acceleration, cruise (low/high speed), pedal tip-in/tip-out, gear shifts and

engine start/stop. The overall assessment of vehicle drivability can be time-consuming and is subject to human error. Recently, auto manufacturers moved towards the use of special software packages to evaluate drivability in an objective fashion [45]. These software packages utilize learning methods (such as neural networks) that process a combination of sensor information obtained from various driving situations.

In this work, drivability is regarded as the driver’s response to changes in the *longitudinal acceleration* of the vehicle. Events that affect the lateral or vertical dynamic behavior of a vehicle are not of interest in this study. Within the context of longitudinal motions, driveline excitations created in the low frequency range (up to 10 Hz) are perceived by the driver as physical disturbances since the human body has mechanical resonances in the range of 4 to 8 Hz [46].

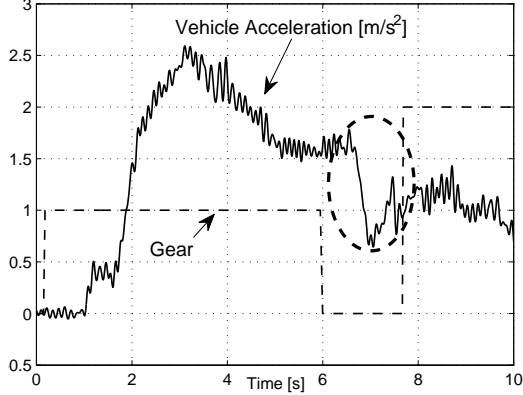
The control of a number of critical driving conditions have been studied for conventional and hybrid vehicles. These studies are briefly reviewed next according to the types of drivability problems and the classes of vehicles to which they are relevant.

#### 2.4.1 Conventional and Hybrid Vehicles

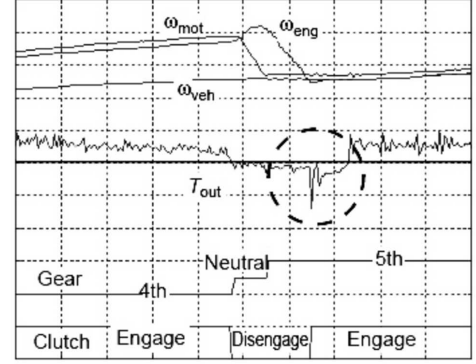
In the following, issues that typically arise in both conventional and hybrid drive-trains due to unintended power interruptions, inherent driveline characteristics (elasticity, backlash etc.) and sluggish engine response (delay, time lag etc.) are discussed.

**Gear shifting:** Gear shifting is the most commonly studied class of drivability problems. A survey paper by [47] reviews some of the recent works on the control of automatic, (automated) manual, continuously variable and electrically variable transmissions. Figure 2.5 depicts typical drivability issues observed during gear shifting. The vehicle acceleration obtained from an automatic transmission<sup>7</sup> (Figure 2.5(a)) and the shaft torque obtained from an automated manual transmission (Figure 2.5(b)) confirm that significant torque losses occur during gear shifting in both types of transmissions.

<sup>7</sup>The acceleration data is acquired from the experimental hybrid vehicle during a test when the vehicle is propelled solely by the diesel engine.



(a) Automatic transmission (experimental data from OSU hybrid vehicle)



(b) Automated manual transmission [50]

Figure 2.5: Typical driveline disturbances observed during gear-shifting.

In automatic transmissions, gear shifting is typically managed by hydraulic actuation mechanisms via line pressure and clutch/band pressure control. The major issues are the loss of transmission output torque during torque synchronization and the overshoot of transmission torque during speed synchronization [24]. Accurately specifying the pressure profiles and timing for on-coming and off-going clutches is crucial for achieving a smooth power transfer from the engine to the wheels. Reducing engine torque during gear shifts is also necessary to achieve further improvements [48]. Various control schemes have been proposed for gear shifting in automatic transmissions using sliding mode control [23], model referenced adaptive control [49] and explicit model following control combined with linear quadratic regulator design [24].

The control of automated manual transmissions (AMTs) is another active research field. The main control issue in AMTs is the smooth engagement of a dry clutch that synchronizes the engine crankshaft and transmission input shaft speeds. An electrohydraulic actuation mechanism controls the clutch slip during gear engagements. To achieve a smooth vehicle launch, Slicker *et al.* [51] designed a robust controller using quantitative feedback theory for an AMT operated heavy-duty truck. Dolcini *et al.* [52] designed an observer-based optimal controller to enable smooth dry clutch

engagements. Glielmo *et al.* [6] recently developed a strategy for AMT clutch control using a hybrid model of clutch engagement with dedicated controllers for each phase. An interesting approach to gear shifting in manual transmissions is proposed by Pettersson *et al.* [53] where the function of an automatic clutch is replaced by engine torque control. In this system, the neutral gear is directly engaged by moving the gear lever to the appropriate position after the transmission input is controlled to zero torque by means of fuel injection.

Additional opportunities for gear shifting arise in hybrid vehicles by proper control of electric machines. Baraszu *et al.* [54] proposed an open-loop torque fill-in strategy to improve shift quality for a post-transmission parallel HEV using an AMT. Lee *et al.* [50] developed a gear shifting method based on speed synchronization of the actuators (a diesel engine and an induction machine) for a pre-transmission parallel HEV also equipped with an AMT. Despite these developments, electrically assisted gear shifting is still a promising research area considering the wide array of HEV configurations available today.

**Pedal tip-in/tip-out:** For vehicles equipped with (automated) manual transmissions, driveline damping is not sufficient to quickly dissipate the transient effects of abrupt torque changes in the absence of torque converters. Even in automatic and continuously variable transmissions, pedal tip-in/tip-out may lead to noticeable disturbances when the torque converter by-pass clutch is locked up. Similar issues also occur in electric and hybrid-electric vehicles if the electric machines are rigidly coupled to the driveline.

Driveline torsional resonance frequencies are excited by quick changes in torque demand. The oscillations that correspond to the fundamental driveline resonance frequency are often referred to as *shuffle* vibrations. These low-frequency vibrations are mainly caused by the compliances of the half-shafts that connect the final drive to the wheels [55]. Another undesired response characteristic, generally referred to as *shunt*, arises upon initial pedal application due the high rate of change of driveline torque. This phenomenon is typically seen in drivelines with large gear backlash and

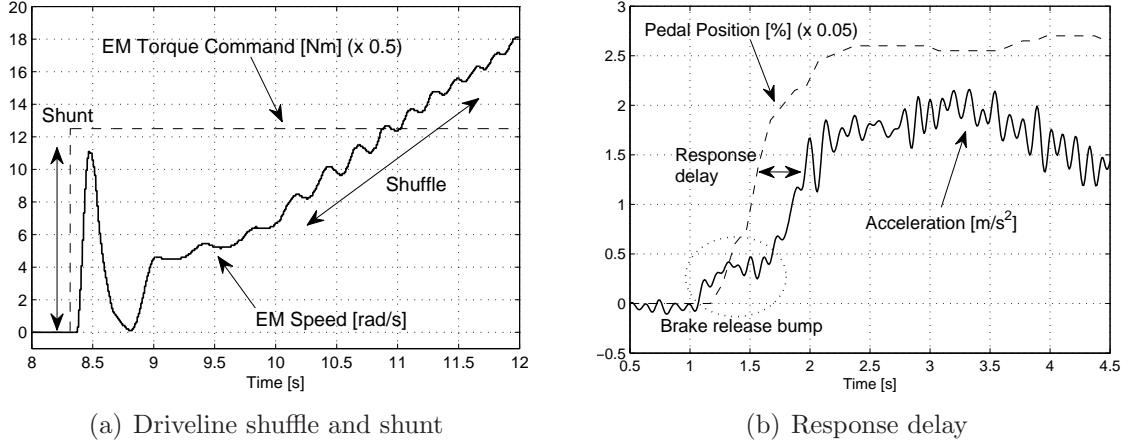


Figure 2.6: Typical drivability issues related to pedal tip-in (experimental data from OSU hybrid vehicle).

it is characterized by an initial jerk which then leads to shuffle vibrations [56]. In conventional vehicles, pedal response delays pose further issues caused by the slow dynamics of the ICE. Response delays become more important in vehicles that use diesel engines since the turbocharger loop introduces a considerable lag during torque build-up.

Typical pedal tip-in/tip-out related drivability issues are demonstrated in Figure 2.6. Figure 2.6(a) depicts the shunt and shuffle observed in the test vehicle when operated in pure electric mode with no torque compensation. A typical response delay experienced during diesel only operation is shown in Figure 2.6(b).<sup>8</sup> This figure also illustrates the brake release bump phenomenon that commonly occurs in automatic transmission equipped vehicles.

Various control strategies have been proposed for the closed-loop control of pedal tip-in/tip-out response. Ha *et al.* [57] used the feedback linearization method to maintain a desired acceleration trace for a vehicle that is equipped with an automatic

<sup>8</sup>The oscillations in the acceleration trace are primarily due to sensor noise.



transmission and a spark-ignited engine. Lefebvre *et al.* [58] proposed an  $H_\infty$  controller for the active damping of driveline shuffle using engine speed measurements. Baumann *et al.* [59] proposed an anti-jerk controller using the root-locus technique. In their work, the speed difference between the engine speed and the wheel speeds is used as feedback to the controller. The control of driveline vibrations in electric drivetrains is also studied by Amann *et al.* [60]. In this work, the driveline vibrations are compensated by an induction machine using an observer-based linear control scheme.

**Pedal feel:** Another type of drivability considerations arise during low/high speed cruising and “part throttle” accelerations due to inconsistencies in the power delivered to the wheels in response to a driver demand. This problem is not transient in nature, hence, improvements are generally realized by calibration of static maps and parameters. For conventional vehicles, the control problem is that of properly tuning the engine pedal-torque maps and determining transmission gear shift points [61]. However, the problem is more involved in HEVs since the driver’s demand for power (or acceleration) can be met using different actuators through different paths [34]. This problem will be discussed in more detail in Chapter 5.

### 2.4.2 Hybrid Vehicles

Additional drivability considerations may arise in hybrid vehicles due to the presence of multiple (often redundant) actuators and as a result of the operating principles of supervisory control strategies. This section provides a brief description of these considerations. More detail will be given in Chapter 5.

**Mode transitions:** Due to the complex nature of hybrid drivetrains, HEVs are usually operated in fully or partially mode-based control schemes as discussed in Section 2.3. Such a mode-based control architecture is almost inevitable due to the engine start-stop function that is a unique characteristic of most HEVs. In conventional vehicles, engine start and stop only occur at the start and stop of the actual vehicle. Therefore, it does not pose a major drivability problem. However, since the

start-stop function is frequently used in hybrid vehicles, its seamless implementation is crucial for consumer acceptability.

The types of drivability issues that result from engine start-stop largely depend on the HEV architecture. In some power-split HEVs, the engine can not be fully decoupled from the driveline. Therefore, vibrations resulting from the initial cranking of the engine are transmitted to the driveline in the absence of a preemptive control action. However, the situation is different in HEVs that use manual or automatic transmissions since a torque decoupling device (a dry clutch or a torque converter<sup>9</sup>) allows the engine to be physically separated from the driveline during the start event. In this case, the control objective is to smoothly engage the engine to the driveline immediately after the first ignition (or the first fuel injection in the case of a diesel engine). A detailed discussion of engine start-stop related drivability and NVH issues is given in [62, 63].

In summary, the essence of the problem involves quickly and smoothly starting the engine, and carefully synchronizing the speeds and torques of the transmission and the engine after the start event. In this dissertation, this problem is referred to as the *HEV launch problem*. A related reference in this area is the work by Beck *et al.* [64], where a model predictive control approach is used to regulate the mode transitions in a power-split HEV during vehicle launch. Another approach, which is one of the contributions of this dissertation, is published in [65] where a control design method is described for systems that exhibit state-dependent mode transitions. The proposed design method is accompanied by a simulation example that focuses on achieving smooth mode transitions for a parallel HEV.

Mode transitions that affect drivability in HEVs are not limited to the engine start and stop events. For example, a mode change from hybrid operation to regenerative braking may excite driveline vibrations when the gear backlash reverses direction. Another mode change that may result in poor drivability is the one in which a traction

<sup>9</sup>This is only valid in the case in which an electrically actuated hydraulic system controls the torque converter fluid pressure such that vibrations are not transmitted to the driveline during engine start.

controller is activated while the HEV is operating in hybrid mode. Note that this example is also relevant to conventional vehicles that utilize automatic traction control systems. From a systems theoretic viewpoint, these two examples differ from the HEV launch problem in the sense that only controller discontinuities are present in the former case (as opposed to discontinuities in the plant dynamics). These theoretical concepts will be further discussed in Section 2.5.

**Control allocation:** The policies generated by the control strategies described in Section 2.3 may result in poor drivability due to the potential for chattering or abrupt transitions between actuator torque requests. These types of issues can be observed even when the control system fully respects the driver’s power/torque demand. This situation arises since an energy optimal power distribution to the actuators does not necessarily assure good drivability. As an example, an instantaneous fuel minimization strategy (such as ECMS) may chatter between the two local minima of its cost function, thus generating significantly distinct torque splits for consecutive operating points. This phenomenon is conceptually illustrated on the engine speed-torque plane in Figure 2.7. The value function has two local minima that are widely separated on the torque axis although the corresponding engine speeds are relatively close to each other. In this case, torque chattering is the resulting effect of the repetitive acceleration and decelerations of the engine crankshaft.

In an attempt to address the drivability issues that result from the control actions, some studies proposed adding an anti-jerk term into the energy minimization function [28,66]. However, it is questionable whether such modifications would help circumvent the types of issues discussed here. A detailed experimental investigation of the energy optimization methods such as ECMS is necessary to reveal the intrinsic drivability problems that may otherwise be overlooked by numerical simulations conducted over long periods of driving data. This topic will be further discussed in the following chapters.

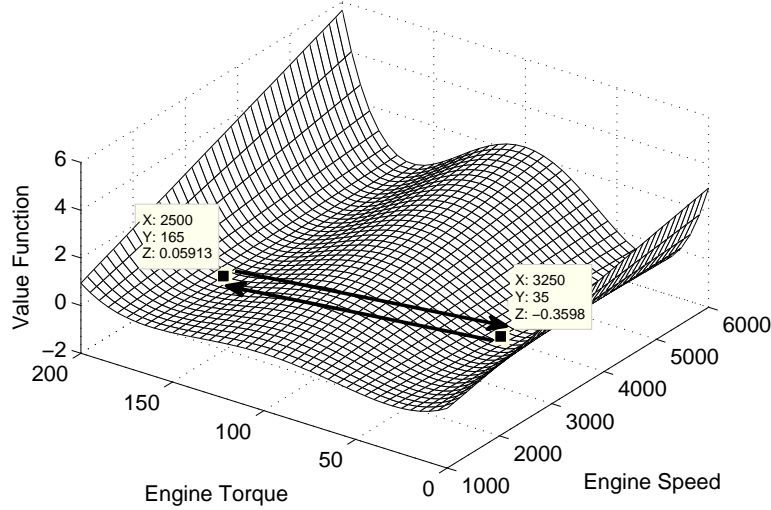


Figure 2.7: A conceptual illustration of the torque chattering issue. The local minima of the value function lie in widely separated regions for consecutive engines speeds.

## 2.5 Control of Systems with Mode Switching Behavior

### 2.5.1 Hybrid and Switched Systems: An Overview

Systems that consist of interacting continuous-time and discrete-time dynamics are referred to as *hybrid systems*. These interactions may arise at the plant level due to the switching between the internal dynamics of a system or they may arise at the controller level as a result of supervisory control decisions. In certain cases, a hybrid plant may also be interacting with a hybrid controller. These possible interactions are illustrated in Figure 2.8.

Hybrid systems continue to be actively studied by the computer science and control systems communities. Issues of current research interest are the development of analytical and computational tools to help study fundamental issues such as the existence and uniqueness of solutions [67], conditions for stability [68,69] and optimality [70], and methods to synthesize controllers to meet these specifications [71]. The proposed method in this research is relevant to the modeling and control of a family

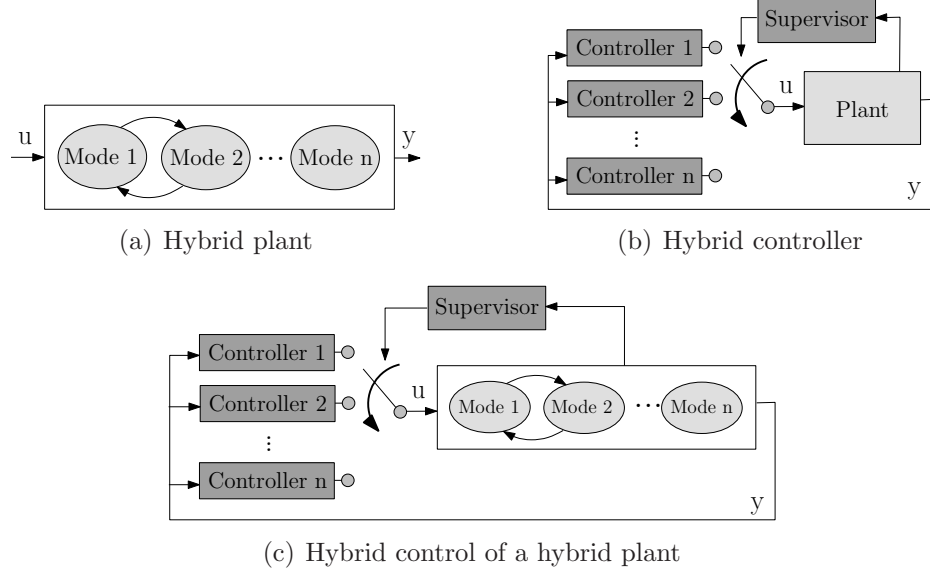


Figure 2.8: Various Hybrid Dynamical Interactions that Commonly Arise in Mechanical Systems

of continuous-time systems known as *switched systems*. The most commonly studied class of switched systems [72] is described by the following differential equation

$$\dot{x} = f_{\sigma}(x) \quad (2.2)$$

where  $x \in \mathbb{R}^n$ ,  $f_{\sigma} : \mathbb{R}^n \rightarrow \mathbb{R}^n$  is a family of smooth vector fields and  $\sigma : [0, \infty) \rightarrow \{1, 2, \dots, M\}$  is the switching signal. Another important class of switched systems that give rise to state discontinuities at the switching instances are *systems with impulse effects* [69, 72].

Considerable research has been conducted on the stability analysis of (2.2) under an arbitrary or supervised switching signal. Most stability conditions are developed for linear switched systems and differential inclusions using common/multiple Lyapunov functions [73], linear matrix inequalities [74], Lie-algebraic methods [75],

LaSalle’s invariance principle [76], and stable convex combinations of constituent linear systems [77]. Other stability conditions based on average switching rates (dwell-time) are also proposed [78]. Some of these tools are generalized to certain classes of nonlinear switched systems [79].

The importance of stability analysis of switched systems is without question. However, satisfying other specifications such as closed-loop performance and optimality are also essential for switched systems with inputs. In this context, controllers that are non-hybrid, or perhaps are themselves hybrid (consider a supervisory controller interaction with lower-level continuous controllers), can be applied to two distinct areas: (i) synthesizing (hybrid or non-hybrid) controllers for switched hybrid systems and (ii) designing hybrid controllers for systems that are not necessarily hybrid to achieve multiple control objectives or to improve closed-loop performance by appropriately changing the control action. This research aims to address issues in these two areas.

Within hybrid system science, control synthesis is a growing field with many problems still unsolved. Some of the previous works investigated the problem of constructing a stabilizing switching law by selecting from a family of controllers [72, 80, 81]; while others focused on finding an optimal control for systems with switched dynamic models [82]. Sufficient optimality conditions (verification theorems) are developed for some relaxed problems in hybrid systems [70, 83]. The optimal control of hybrid systems has been addressed using extensions of Pontryagin’s maximum principle [82, 84] and Bellman’s dynamic programming [70] with additional extensions to stochastic hybrid systems [85, 86]. An automated synthesis method is proposed for the model predictive control of constrained hybrid systems using multi-parametric programming [87]. Also, the performance benefits of designing hybrid controllers for linear and nonlinear systems are discussed [88]. Applications of these methods to automotive control have been proposed for traction control [89], energy management of hybrid electric vehicles [90], electronic throttle control [91], idle-speed control [92], and the control of valves for camless engines [7].

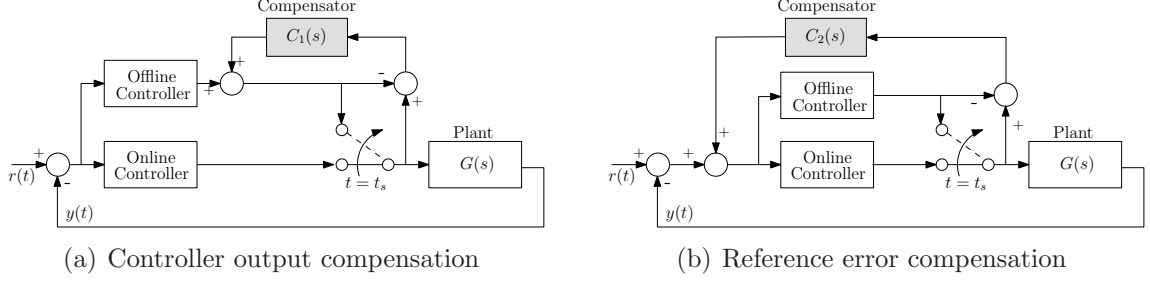


Figure 2.9: Common bumpless transfer schemes.

### 2.5.2 Control of Mode Transitions

As discussed earlier, the HEV system has a hybrid dynamical nature as a result of the operating principles of supervisory control strategies and the intrinsic dynamical properties of hybrid vehicles due to functions such as engine start-stop. One of the topics of interest in this dissertation is the design of controllers that effect seamless mode changes in switched dynamical systems (an example being the HEV system). Such a control framework is desired to avoid mode switching related drivability issues in HEVs, while also achieving the primary objective of supervisory control strategies, that is, minimizing fuel consumption.

This problem is similar in principle to the problem of *bumpless transfer* in classical control [93–99]. The objective of bumpless transfer is to combine multiple controllers for the control of a linear plant such that the undesired output transients during a controller transfer (or as a result of another input nonlinearity such as saturation) are minimized. Relevant applications involve switching from a manual operation to an automatic operation such as in an aircraft autopilot system.

Example bumpless transfer architectures are shown in Figure 2.9. In Figure 2.9(a), a bumpless transfer compensator,  $C_1(s)$ , is introduced to the output channel of the offline controller. The control signal is modified by an additive correction term such that the plant,  $G(s)$ , receives a continuous input at the switching time,  $t = t_s$ .

Another bumpless transfer scheme is shown in Figure 2.9(b) where the common controller reference is subjected to a correction signal generated by  $C_2(s)$ , which uses the difference between the online and offline controller outputs as feedback.

Methods of synthesizing bumpless transfer compensators are discussed in various publications. Due to the similar nature with the anti-windup problem<sup>10</sup>, mathematical frameworks that address both classes of problems are generally sought. One of the earlier works in this area by Hanus *et al.* [93] proposed the so-called conditioning technique that follows a reference signal manipulation approach (also termed as the realizable reference in [93]) similar to Figure 2.9(b). Kothare *et al.* [95] proposed a unified anti-windup bumpless transfer framework that included all traditional compensator schemes as special cases of this general framework. In this parametrization, two constant design matrices are shown to be sufficient to represent any linear time invariant anti-windup bumpless transfer compensator structure. Turner *et al.* [97] adapted the common LQR framework to synthesize bumpless transfer compensators using a reference signal manipulation scheme. Zaccarian *et al.* [98] presented a design method that guarantees a  $\mathcal{L}_2$  bound on the mismatch between the actual plant output and a predefined ideal response at the switching instant,  $t = t_s$ . In this sense, this formulation is different than the conventional bumpless transfer schemes. Another recent work by Zheng *et al.* [99] extended the method developed in [97] by adding a mismatch compensator to a LQR bumpless compensator for the purpose of handling controller uncertainty, i.e. the discrepancy between the dynamics of the controller model and the actual controller.

Current methods of bumpless transfer, however, do not directly apply to switched dynamic systems, since the changes in plant dynamics also result in undesired output transients even if the controller itself does not experience a discontinuity. Note that hybrid vehicle drivetrains experience changes in both plant and controller structures during operating mode transitions.

<sup>10</sup>Controller windup refers to the insensitivity of the input of a plant to changes in the reference signal due to magnitude or rate limitations at the controller output.



This dissertation extends some of the underlying principles of bumpless transfer to the case of systems that exhibit state-dependent switching. The problem of achieving a “bumpless transfer” is formulated as an output regulation problem where the control law is modified as the state trajectory approaches a known switching set. A preliminary illustration of this control technique was given in our previous work [65]. Further details of this method are described in Chapter 6, and the experimental verification is given in Chapter 7.

## CHAPTER 3

# DYNAMIC MODELING OF HYBRID-ELECTRIC VEHICLES

This chapter describes the development of a low-frequency dynamic model for a through-the-road parallel hybrid electric vehicle. The model is capable of identifying the longitudinal dynamic behaviors of the vehicle that affect drivability and fuel consumption. An extension of this model can be used to predict certain types of exhaust emissions, however this aspect is not considered in this research.

### 3.1 Experimental Platform

The experimental test vehicle used for modeling and control development in this dissertation is the hybridized version of a commercially available mid-sized sport utility vehicle (Chevrolet Equinox<sup>®</sup>). The conversion to a hybrid-electric powertrain was carried out by a student team at the Center for Automotive Research at The Ohio State University.<sup>1</sup> A picture of the experimental vehicle is shown in Figure 3.1. The hybridized version of this vehicle includes the following components.

**Diesel internal combustion engine (ICE):** A 1.9L turbocharged diesel engine that uses a common-rail injection system is the main power plant of the vehicle. The engine is capable of generating 110 kW of peak power (at 4000 rpm) and 325 Nm of peak torque (at 2000 rpm).

<sup>1</sup>This project is part of the Challenge-X competition [100], a program sponsored by General Motors and by the United States Department of Energy with the aim of exploring means of achieving better fuel economy and lower emissions while maintaining safety, performance and utility through the use of advanced powertrain technologies.



Figure 3.1: OSU Challenge-X hybrid electric vehicle

**Belted starter-alternator (BSA):** A permanent magnet brushless DC machine capable of delivering 10 kW of continuous power performs the starter and alternator functions. This machine is belted to the engine crankshaft. The BSA is capable of generating 80 Nm of peak torque at low operating speeds.

**Automatic transmission:** A front-wheel drive type 6-speed automatic transaxle that has a 450 Nm torque capacity transfers the power generated by the ICE and the BSA to the front axle.

**Traction electric machine (EM):** An asynchronous AC induction machine capable of delivering 32 kW of continuous power is directly coupled to the rear differential through a driveshaft. The EM generates 185 Nm of peak torque at low speeds.

**High-voltage battery pack:** A 300V nominal Nickel-Metal Hydride (Ni-MH) battery pack with a 6.5 Ah energy capacity powers the electric machines and the electrical accessories. The battery pack is capable of delivering 35 kW power at nominal state-of-charge. The overall capacity of the electric powertrain is thus limited by the power rating of the high-voltage battery pack.



## 3.2 HEV Dynamic Model

A low-frequency dynamic model of the experimental hybrid vehicle is developed to facilitate the evaluation of control strategies in terms of drivability, fuel economy and performance. An earlier phase of this dynamic model is given in [101]. The dynamic vehicle model evolved from a forward quasi-static simulator previously developed at The Ohio State University as part of the Challenge-X project.

The dynamic HEV model, CX-DYN, can be configured in a variety of ways according to the objectives of the simulation. If the objective is to follow a desired velocity profile to predict the vehicle performance and fuel economy, the simulator can be executed using driver feedback.<sup>2</sup> If the objective is to verify correct operation of a control strategy, the simulator can be executed using only the control strategy in the feedback loop. In this scheme, actual accelerator and brake pedal commands are fed to the simulator and the corresponding vehicle states are obtained. A third possibility involves executing the vehicle simulator in an open-loop fashion using torque commands obtained from actual driving conditions. This scheme is most suited for model validation using experimental data. Note that the last two cases involve no driver feedback. Therefore, modeling errors may accumulate over time and possibly lead to inaccurate results for long term simulations.

CX-DYN simulator uses the MATLAB *ode23tb* routine for numerical integration of differential equations. This routine implements a variable-step solver that is suited for stiff dynamic systems. A particular case where the model stiffness becomes an issue is the event of gear shifting. The frictional behavior of a clutch changes abruptly in a small neighborhood of zero slip speed during the clutch engagement phase. A stiff numerical solver is necessary to achieve good accuracy and acceptable simulation speed during these types of events. On the other hand, the control strategy runs using a fixed step time as this is consistent with its real-time implementation. However, different segments of the control strategy are updated using different sampling times that range from 0.001 s to 1 s.

<sup>2</sup>Driver feedback is generated by a driver model which is a PID-type controller.

The following fundamental assumptions are made regarding the vehicle model:

1. Only longitudinal dynamics are included. Indirect coupling effects due to vertical and lateral motions are neglected.
2. The transient characteristics of the powertrain actuators are represented with highly simplified models. This is necessary since the actuators' internal controls that have a considerable impact on the transient behaviors of the actuators are not accurately known.
3. The torsional flexibilities of all the shafts and gears, except for the rear and front half-shafts, are assumed to be infinitely large.
4. The frictional properties of the road surface are assumed to be acting uniformly on all tires.
5. The drivetrain losses are represented by lumped efficiency and friction models. Frictional losses of driveline components due to effects such as gear meshing and bearing friction are not modeled individually.
6. The impacts of environmental factors such as temperature are not taken into consideration in the component models.

As a result of the assumptions 1 and 4, a half car model is deemed sufficient to represent the components downstream from the front and rear differentials. This approach assumes that the right and left halves of a particular axle exhibit the same dynamic behavior.

Mathematical models of the vehicle subsystems and components are described next.

### **3.2.1 Engine**

The detailed fluid-thermodynamic models [44] often used to describe diesel engine dynamics do not provide a substantial amount of additional information for the validation of a drivability-oriented vehicle model. In this work, a simplified mean-value

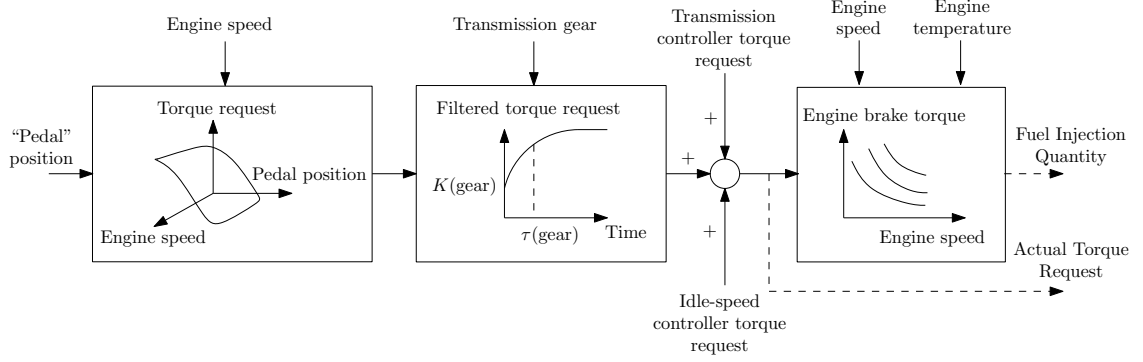


Figure 3.3: A simplified illustration of the ECU process that converts a percentage based torque request into an actual torque request and a main fuel injection quantity.

engine model is used to represent the dynamics between the torque request and the resulting crankshaft speed.

In the experimental vehicle, the engine control unit (ECU) receives a percentage based torque request as an input that corresponds to the accelerator pedal position in a conventional vehicle. The ECU then converts this percentage into an actual torque request via static look-up tables. Furthermore, the torque request calculated by the ECU is modified according to the torque requests generated by the transmission control unit (TCU) and the idle-speed controller. This process is briefly illustrated in Figure 3.3.

To represent the aforementioned effects, those that significantly impact the engine behavior are implemented in the vehicle model. The engine torque request ( $T_{ice,req}$ ) is calculated as a function of the percentage based torque request ( $T_{ice,per}$ ), the engine speed ( $\omega_{ice}$ ), and other modifications resulting from the idle speed controller ( $T_{ice,idle}$ ) and the transmission controller ( $T_{ice,tr}$ ):

$$T_{ice,req} = f_{ice,trq}(\omega_{ice}, T_{ice,per}) + T_{ice,idle} + T_{ice,tr} \quad (3.1)$$

Here,  $f_{ice,trq}$  is a 2-D look-up table that is used by the ECU to convert the percentage based torque request into the actual torque request. The idle-speed controller is modeled as a PI controller combined with a feedforward term that compensates for

the engine friction. The TCU torque request ( $T_{ice,tr}$ ) is difficult to model and is only taken into consideration for the experimental validation of gear shifts as described in Chapter 4.

The relationship between the engine torque request and the indicated torque is given by

$$\dot{T}_{ice,ind} = \frac{1}{\tau_{ice}} (-T_{ice,ind}(t) + T_{ice,req}(t - \delta_{ice})) \quad (3.2)$$

where  $T_{ice,ind}$  is the indicated engine torque,  $\tau_{ice}$  is the engine time constant due to turbocharger dynamics, and  $\delta_{ice} = \pi/\omega_{ice}$  is the power stroke to induction transport delay (180 deg in the crank angle domain). The resulting crankshaft dynamics are given by

$$\dot{\omega}_{ice} = \frac{1}{J_{ice} + J_{bsa} + J_p} (T_{ice,ind} + T_{bsa} - T_{ice,fr} - T_p) \quad (3.3)$$

where  $J_{ice}$  is the engine inertia,  $J_p$  is the torque converter pump inertia, and  $J_{bsa}$  is the combined inertia of the belt, the pulley and the BSA rotor. The mathematical expressions for  $T_{bsa}$  and  $T_p$  are provided in the following sections. The engine friction is approximated as a quadratic function of the engine speed based on the available engine data:

$$T_{ice,fr} = b_{ice,2}\omega_{ice}^2 + b_{ice,1}\omega_{ice} + b_{ice,0} \quad (3.4)$$

where  $b_{ice,i}$  are engine friction coefficients. All engine accessory loads are also lumped into the engine friction. The engine friction also has a strong dependence on the engine temperature. This dependence, which results in a higher friction at low engine temperatures, is not taken into consideration in the engine model. As described in the next chapter, the vehicle model is validated by means of experiments conducted under moderate engine coolant temperatures.

The engine fuel consumption ( $\dot{m}_{ice,f}$ ) and the energy conversion efficiency ( $\eta_{ice}$ ) are calculated using static maps as functions the engine speed and engine brake torque.<sup>3</sup> The fuel economy map is extrapolated using the manufacturer's friction torque data such that  $T_{ice,ind} = 0$  corresponds to zero fuel consumption. This accurately represents

<sup>3</sup>Engine brake torque is approximately given as  $T_{ice,br} = T_{ice,ind} - T_{ice,fr}$ .



the case in which the vehicle operates in pure electric mode (engine off) or the case in which engine “fuel cut-off” is active.

### 3.2.2 Transmission

The accuracy of the transmission model is crucial for the prediction of vehicle drivability. Most of the driveline transients during events such as engine start and gear shifts originate from the transmission. Owing to the transmission’s critical role in determining the dynamic behavior of the drivetrain, this dissertation discusses the transmission dynamics in detail.

The transmission model is developed as a result of a collaborative work with Politecnico di Milano and is discussed in our joint publication [101]. The governing kinematic and dynamic equations are given in the remainder of this section without illustrating the derivation of the equations. Note that the transmission model is revised by the author after this publication.

#### Torque Converter

The torque converter model is adapted from the empirical quasi-static model developed in [102]. The dynamics due to fluid inertial effects become more pronounced at frequencies higher than 10 Hz [103]. Therefore, these effects are neglected in the torque converter model. The torque converter pump and turbine torques are given as functions of the engine and turbine speeds:

$$T_p(\omega_{ice}, \omega_t) = \begin{cases} C_{tc,1}\omega_{ice}^2 + C_{tc,2}\omega_{ice}\omega_t + C_{tc,3}\omega_t^2 & 0 \leq \omega_t/\omega_{ice} < \gamma_c \\ C_{tc,4}\omega_{ice}^2 + C_{tc,5}\omega_{ice}\omega_t + C_{tc,6}\omega_t^2 & \gamma_c \leq \omega_t/\omega_{ice} \leq 1 \\ -C_{tc,4}\omega_{ice}^2 - C_{tc,5}\omega_{ice}\omega_t - C_{tc,6}\omega_t^2 & \omega_t/\omega_{ice} > 1 \end{cases} \quad (3.5)$$

$$T_t(\omega_{ice}, \omega_t) = \begin{cases} C_{tc,7}\omega_{ice}^2 + C_{tc,8}\omega_{ice}\omega_t + C_{tc,9}\omega_t^2 & 0 \leq \omega_t/\omega_{ice} < \gamma_c \\ C_{tc,4}\omega_{ice}^2 + C_{tc,5}\omega_{ice}\omega_t + C_{tc,6}\omega_t^2 & \gamma_c \leq \omega_t/\omega_{ice} \leq 1 \\ -C_{tc,4}\omega_{ice}^2 - C_{tc,5}\omega_{ice}\omega_t - C_{tc,6}\omega_t^2 & \omega_t/\omega_{ice} > 1 \end{cases} \quad (3.6)$$

Here,  $T_p$  and  $T_t$  represent the torque converter pump and turbine torques. Also,  $C_{tc,i}$

(where  $i = 1, \dots, 9$ ) are empirical coefficients,  $\gamma_c$  is the torque coupling speed ratio, and  $\omega_t$  is the turbine speed. If the torque converter lock-up clutch is engaged then the torque converter acts as a rigid coupling, i.e,  $T_p = T_t$  and  $\omega_{ice} = \omega_t$ . However, this effect is not modeled in the simulator since the TCU strategy for torque converter lock-up control is not known.

The torque converter (mechanical) inertial effects are taken into consideration by adding the pump inertia ( $J_p$ ) to the engine side and the turbine inertia ( $J_t$ ) to the transmission input side. This is a reasonable assumption since the transmission input shaft and the engine crankshaft can be assumed as rigid shafts.

### Transmission: Mechanics

The 6-speed automatic transmission is composed of a series arrangement of a 2-stage compound gear set called a Ravigneaux gear set (RGS) and a simple planetary gear set (PGS). This arrangement is also known as the LePelletier arrangement [104]. The power-flow between the input and output shafts is coordinated by the proper engagement of 3 wet clutches, 2 brakes (a band brake and a multi-disc brake) and a one-way clutch. A layout of the gears, the friction elements and the torque converter is given in Figure 3.4 [105]. This figure also shows the acronyms that are used to refer to the gears and clutches inside the transmission.

The sun gear of the PGS (referred to as PGS,S) is mechanically fixed to the transmission housing. Therefore, the configuration of the PGS imposes the following kinematic constraints:

$$\omega_{pgs,r} = \frac{2R_{pgs,p}}{R_{pgs,r}} \omega_{pgs,p} \quad (3.7)$$

$$\omega_{pgs,c} = \frac{R_{pgs,r}}{R_{pgs,r} + R_{pgs,s}} \omega_{pgs,r} \quad (3.8)$$

$R_{pgs,*}$  are the effective radii of the PGS gears where the subscript  $* = \{p, r, s, c\}$  represents the pinion set, the ring gear, the sun gear and the carrier, respectively. The angular speeds of the PGS gears are denoted as  $\omega_{pgs,*}$ .

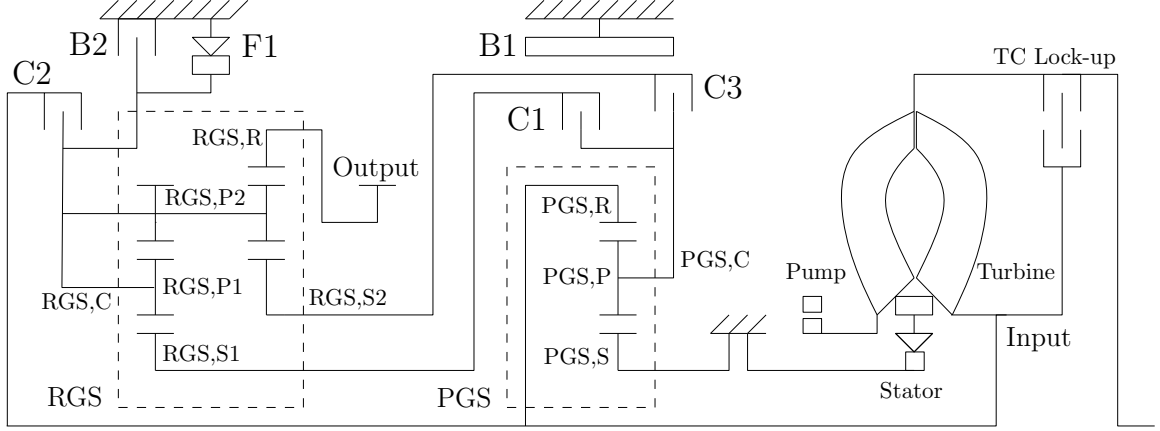


Figure 3.4: A stick diagram of the 6-speed automatic transmission.

Similarly, the RGS kinematic constraints can be written as

$$\omega_{rgs,c} = \frac{R_{rgs,p1}}{R_{rgs,c1}K_{rgs,c1} + R_{rgs,c2}K_{rgs,c2}} \omega_{rgs,p1} + \frac{R_{rgs,p2}}{R_{rgs,c1}K_{rgs,c1} + R_{rgs,c2}K_{rgs,c2}} \omega_{rgs,p2} \quad (3.9)$$

$$\omega_{rgs,s1} = \frac{R_{rgs,c1}}{R_{rgs,s1}} \omega_{rgs,c} - \frac{R_{rgs,p1}}{R_{rgs,s1}} \omega_{rgs,p1} \quad (3.10)$$

$$\omega_{rgs,s2} = \frac{R_{rgs,c2}}{R_{rgs,s2}} \omega_{rgs,c} - \frac{R_{rgs,p2}}{R_{rgs,s2}} \omega_{rgs,p2} \quad (3.11)$$

$$\omega_{rgs,r} = \frac{R_{rgs,c2}}{R_{rgs,r}} \omega_{rgs,c} + \frac{R_{rgs,p2}}{R_{rgs,r}} \omega_{rgs,p2} \quad (3.12)$$

where  $R_{rgs,\star}$  represent the effective radii of the RGS gears. The subscript  $\star = \{p1, p2, r, s1, s2, c\}$  denotes the pinion set 1, the pinion set 2, the ring gear, the sun gear 1, the sun gear 2, and the carrier, respectively. Similarly,  $\omega_{pgs,\star}$  are the angular speeds of the RGS gears. Note that the subscripts  $c1$  and  $c2$  represent the effective radii of the PGS carrier extending from its axis of rotation to the pinion set 1 and pinion set 2. Also,  $K_{rgs,c1}$  and  $K_{rgs,c2}$  are constants resulting from the geometric configurations of the pinion set 1 and pinion set 2.

The following kinematic relationships also apply at the transmission input and output shafts:

$$\omega_t = \omega_{pgs,r} \quad (3.13)$$

$$\omega_{tr} = \left( \frac{1}{\zeta_{cg}\zeta_{fd}} \right) \omega_{rgs,r} \quad (3.14)$$

where  $\omega_{tr}$  is the transmission output speed, and  $\zeta_{cg}$  and  $\zeta_{fd}$  are the speed reduction ratios of the counter gear and the final drive. Equations (3.7–3.12) impose 6 algebraic constraints (excluding the sun gear constraint,  $\omega_{pgs,s} = 0$ ) on the transmission gear sets, thus resulting in a total of 3 DOFs. In order to realize a specific gear ratio, 2 of these DOFs are constrained by a proper combination of clutches and brakes.

The geometric configurations of the PGS and the RGS are demonstrated in further detail in Figure 3.5. The pinion arrangement used in the RGS is obtained from [106]. The RGS has two pinion sets (a short pinion set, P1, and a long pinion set, P2) that are connected to a common carrier. The rotational directions that correspond to the 1st gear are also shown in Figure 3.5. In this configuration, the disc clutch C1 connects the PGS carrier to the RGS sun gear 1. Also, the one-way clutch F1 grounds the RGS carrier to the transmission housing resulting in  $\omega_{rgs,c} = 0$ .

The following PGS dynamic equations are obtained by computing the net torques about the corresponding gears axes:

$$\dot{\omega}_t = \frac{1}{J_{pgs,1}} (T_t \eta_{tr} \eta_{fd} - T_{tr,fr} - n_{pgs,p} R_{pgs,r} F_{pgs,pr} - T_{c,2}) \quad (3.15)$$

$$\dot{\omega}_{pgs,p} = \frac{1}{J_{pgs,p}} (R_{pgs,p} (F_{pgs,pr} - F_{pgs,ps})) \quad (3.16)$$

$$\dot{\omega}_{pgs,c} = \frac{1}{J_{pgs,c}} (n_{pgs,p} R_{pgs,c} (F_{pgs,pr} + F_{pgs,ps}) - T_{c,1} - T_{c,3}) \quad (3.17)$$

Here,  $T_{c,j}$  (where  $j = \{1, 2, 3\}$ ) represent the clutch torques,  $J_{pgs,p}$  is the inertia of a single PGS pinion,  $J_{pgs,c}$  is the PGS carrier inertia,  $n_{pgs,p}$  is the number of gears in the PGS pinion set,  $F_{pgs,pr}$  is the reaction force between the pinion and the ring gear, and  $F_{pgs,ps}$  is the reaction force between the pinion and the sun gear. The inertia at the turbine shaft,  $J_{pgs,1}$ , can be written as

$$J_{pgs,1} = J_t + J_{pgs,r} + J_{c,2} \quad (3.18)$$

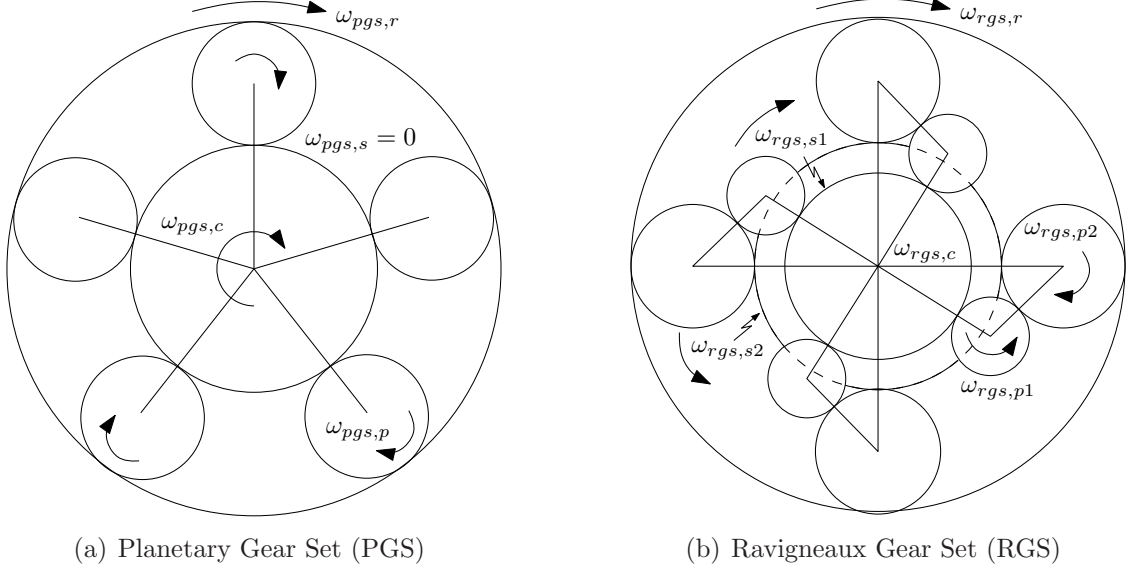


Figure 3.5: Geometric configurations of the transmission gear sets.

where  $J_{pgs,r}$  is the inertia of the PGS ring gear and  $J_{c,2}$  is the combined inertia of the rotating clutch 2 components.  $\eta_{tr}$  and  $\eta_{fd}$  denote the transmission and final drive mechanical efficiencies. The transmission friction,  $T_{tr,fr}$  is lumped into the transmission input shaft and it can be approximately represented as:

$$T_{tr,fr} = b_{tr,1}\omega_t + b_{tr,0} \quad (3.19)$$

where  $b_{tr,0}$ ,  $b_{tr,1}$  are friction coefficients. This simplified approach to modeling driveline losses is discussed in more detail in Section 3.2.8.

The dynamic equations that describe the motion of the RGS elements are obtained through calculations similar to the PGS:

$$\dot{\omega}_{rgs,s1} = \frac{1}{J_{rgs,2}}(T_{c,1} - n_{rgs,p1}R_{rgs,s1}F_{rgs,s1}) \quad (3.20)$$

$$\dot{\omega}_{rgs,s2} = \frac{1}{J_{rgs,3}}(T_{c,3} - T_{b,1} - n_{rgs,p2}R_{rgs,s2}F_{rgs,s2}) \quad (3.21)$$

$$\dot{\omega}_{rgs,p1} = \frac{1}{J_{rgs,p1}}(R_{rgs,p1}(F_{rgs,p2} - F_{rgs,s1})) \quad (3.22)$$

$$\dot{\omega}_{rgs,p2} = \frac{1}{J_{rgs,p2}}(R_{rgs,p2}(F_{rgs,p2} - F_{rgs,s2} - F_{rgs,r})) \quad (3.23)$$

$$\begin{aligned} \dot{\omega}_{rgs,c} = & \frac{1}{J_{rgs,c}}(R_{rgs,c1}F_{rgs,s1} + R_{rgs,c2}(F_{rgs,s2} - F_{rgs,r}) \\ & + K_{rgs,p2}F_{rgs,p2} + T_{c,2} - T_{b,2} + T_{c,f1}) \end{aligned} \quad (3.24)$$

$$\dot{\omega}_{rgs,r} = \frac{1}{J_{rgs,4}}(n_{rgs,p2}R_{rgs,r}F_{rgs,r} - \frac{2}{\zeta_{cg}\zeta_{fd}}T_{hs,f}) \quad (3.25)$$

$T_{b,k}$  (where  $k = \{1, 2\}$ ) are the brake torques for friction elements B1 and B2,  $T_{c,f1}$  is the one-way clutch torque,  $J_{rgs,p1}$  is the inertia of a single gear in the RGS pinion set 1,  $J_{rgs,p2}$  is the inertia of a single gear in the RGS pinion set 2,  $n_{rgs,p1}$  is the number of gears in the RGS pinion set 1,  $n_{rgs,p2}$  is the number of gears in the RGS pinion set 2,  $F_{rgs,*}$  (where  $* = \{s1, s2, p2, r\}$ ) are reaction forces acting on various gears,  $K_{rgs,p2}$  is a constant resulting from the relative geometric configurations of the pinion set 1 and pinion set 2, and  $T_{hs,f}$  is the reaction torque of a single half shaft on the front axle. The remaining inertias given in (3.20–3.25) are the following

$$J_{rgs,2} = J_{rgs,s1} + J_{c,1} \quad (3.26)$$

$$J_{rgs,3} = J_{rgs,s2} + J_{c,3} \quad (3.27)$$

$$J_{rgs,4} = J_{rgs,r} + \frac{J_{cg}}{\zeta_{cg}^2} + \frac{J_{fd}}{\zeta_{cg}^2\zeta_{fd}^2} \quad (3.28)$$

where  $J_{rgs,s1}$  is the RGS sun gear 1 inertia,  $J_{rgs,s2}$  is the RGS sun gear 2 inertia,  $J_{rgs,r}$  is the RGS ring gear inertia,  $J_{cg}$  is the output reflected inertia of the counter gear pair,  $J_{fd}$  is the output reflected inertia of the final drive gear set,  $J_{c,1}$  is the combined inertia of the rotating clutch 1 components, and  $J_{c,3}$  is the combined inertia of the rotating clutch 3 components.

The dynamic equations (3.15–3.17) and (3.20–3.25) can be solved together with the kinematic constraints (3.7–3.12) to obtain the transmission gear speeds and reaction torques.

### Transmission: Hydraulics

Figure 3.4 shows the configuration of hydraulically operated friction clutches and brakes as well as the mechanical one-way clutch. These friction elements are activated according to the clutch schedule given in Table 3.1 [105]. Note that only sequential gear shifts are considered in the vehicle model while neglecting skip shifts such as a 4-6 gear shift. As Table 3.1 indicates, every upshift or downshift requires the engagement of an “on-coming” clutch as well as the disengagement of an “off-going” clutch. A selected friction element is always maintained as engaged during the gear shift. For example, during a 3-4 upshift, friction element C2 becomes engaged, C1 remains engaged, and C3 is gradually disengaged.

Gear	C1	C2	C3	B1	B2	F1	Gear Ratio
1	X					X	4.148
2	X			X			2.370
3	X		X				1.556
4	X	X					1.115
5		X	X				0.859
6		X		X			0.686
R			X		X		3.394

Table 3.1: Schedule of friction of elements engaged in different gears. Gear ratios exclude the final drive and counter gear speed reduction ratios.

The dynamics between the pressure commands that are given to the clutch solenoids and the reaction torques generated by the friction elements are quite complex [24]. In this work, these dynamics are represented by highly simplified models. The dynamics between the pressure command and the pressure acting on a clutch actuator

are represented by the following second order transfer function

$$\frac{p_{\star}(s)}{p_{\star,req}(s)} = \frac{1}{(\tau_{\star,1}s + 1)(\tau_{\star,2}s + 1)} \quad (3.29)$$

where  $\tau_{\star,1}$  and  $\tau_{\star,2}$  are time constants,  $p_{\star}$  is the actual clutch pressure, and  $p_{\star,req}$  is the clutch pressure request. The subscript  $\star = \{\{c, 1\}, \{c, 2\}, \{c, 3\}, \{b, 2\}\}$  is used to represent all disc-type friction elements. The clutch torques and the multi-disc brake torque are modeled as functions of the clutch pressures and slip speeds [24]:

$$T_{\star} = p_{\star} A_{\star} n_{\star} R_{\star} \mu_{\star}(\Delta\omega_{\star}) \tanh\left(\frac{\Delta\omega_{\star}}{\omega_{\star,th}}\right) \quad (3.30)$$

In this equation,  $A_{\star}$  represents the effective disc area of a friction element,  $n_{\star}$  is the number of clutch plates,  $R_{\star}$  is the effective disc radius,  $\Delta\omega_{\star}$  is the relative slip speed, and  $\omega_{\star,th}$  is a threshold speed. The coefficient of friction,  $\mu_{\star}(\Delta\omega_{\star})$ , is represented by the following expression:

$$\mu_{\star}(\Delta\omega_{\star}) = \mu_{\star,1} + \mu_{\star,2} e^{-\mu_{\star,3}|\Delta\omega_{\star}|} + \mu_{\star,4}|\Delta\omega_{\star}| \quad (3.31)$$

where  $\mu_{\star,i}$  are clutch friction coefficients. The three terms in (3.31) respectively represent the static friction, Stribeck friction and viscous friction effects [22]. The variation of clutch torque with respect to the clutch slip speed is shown in Figure 3.6 for different clutch pressures. The following slip speeds determine the direction of the torques generated by the multi-disc friction elements:

$$\Delta\omega_{c,1} = \omega_{pgs,c} - \omega_{rgs,s1} \quad (3.32)$$

$$\Delta\omega_{c,2} = \omega_{pgs,r} - \omega_{rgs,c} \quad (3.33)$$

$$\Delta\omega_{c,3} = \omega_{pgs,c} - \omega_{rgs,s2} \quad (3.34)$$

$$\Delta\omega_{b,2} = \omega_{rgs,c} \quad (3.35)$$

The band brake (B1) shows different dynamic behavior for energizing and de-energizing engagements [25]:

$$T_{b,1} = p_{b,1} A_{b,1} R_{b,1} \cdot \begin{cases} (e^{\mu_{b,1}(\Delta\omega_{b,1})\theta_{b,1}} - 1) \tanh\left(\frac{\Delta\omega_{b,1}}{\omega_{b,1,th}}\right) & \text{for energizing engagement} \\ (1 - e^{-\mu_{b,1}(\Delta\omega_{b,1})\theta_{b,1}}) \tanh\left(\frac{\Delta\omega_{b,1}}{\omega_{b,1,th}}\right) & \text{for de-energizing engagement} \end{cases} \quad (3.36)$$



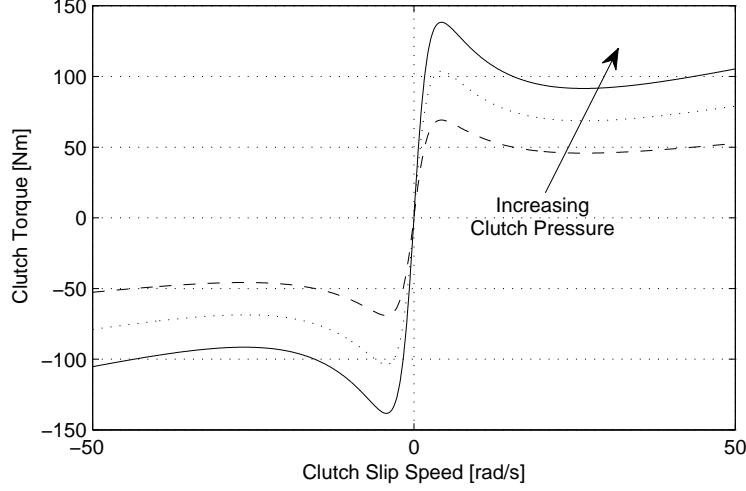


Figure 3.6: Variation of the clutch torques with slip speed and applied pressure.

$\theta_{b,1}$  is the band wrap angle,  $R_{b,1}$  is the effective band radius,  $A_{b,1}$  is the band piston area,  $\Delta\omega_{b,1} = \omega_{rgs,s2}$  is the band slip speed, and  $\omega_{b,1,th}$  is a threshold speed.

The one-way clutch (F1) only engages in the 1st gear and it allows the RGS carrier to freewheel in one direction while allowing it to transfer torque in the opposite direction. Thus, the one-way clutch dynamics can be represented as

$$T_{c,f1} = \begin{cases} 0 & \text{if } \omega_{rgs,c} > 0 \\ k_{c,f1}\theta_{rgs,c} + b_{c,f1}\omega_{rgs,c} & \text{if } \omega_{rgs,c} \leq 0 \end{cases} \quad (3.37)$$

where  $\theta_{rgs,c} = \int \omega_{rgs,c} dt$ ,  $k_{c,f1}$  is the one-way clutch stiffness, and  $b_{c,f1}$  is the one-way clutch damping coefficient.

The transmission clutch pressure commands are determined on the basis of the transmission line pressure. In this work, the transmission line pressure is assumed to be constant when the engine is running at or above idle speed. In practice, the transmission line pressure is often modified by the TCU as a function of parameters such as the engine torque request and the transmission gear.

Furthermore, the vehicle's engine start-stop functionality requires the transmission line pressure to be modified according to the state of the engine since the transmission is pressurized by an engine-driven gear pump. This phenomenon is difficult to model,

hence, it is approximated by the following conditions:

$$p_{tr} = \begin{cases} p_{tr,off} & \text{engine off} \\ f_{tr}(\omega_{ice})p_{tr,on} & \text{engine cranking} \\ p_{tr,on} & \text{engine running} \end{cases} \quad (3.38)$$

where  $p_{tr,off}$  is a small offset pressure,  $p_{tr,on}$  is the nominal transmission line pressure and  $f_{tr}(\omega_{ice})$  is a proper smoothing function. Note that the transmission line pressure also affects the behavior of the torque converter during engine start-stop. This dependence is considered in the vehicle model by multiplying the pump and turbine torques by a normalized correction term that is given by  $p_{tr}/p_{tr,on}$ .<sup>4</sup>

### 3.2.3 Electric Machines and Rear Drive

A schematic of the rear drive including the traction electric machine (EM), the motor gearbox, the rear differential, the half shafts and the rear wheels is given in Figure 3.8. The dynamics of the rear driveline can be described using a lumped model with inertias reflected to the EM output shaft:

$$\dot{\omega}_{em} = \frac{1}{J_{em} + J_{gb} + \frac{1}{\zeta_{gb}^2} J_{rd}} \left( T_{em} \eta_{gb} \eta_{rd} - T_{em,fr} - \frac{2}{\zeta_{rd} \zeta_{gb}} T_{hs,r} \right) \quad (3.39)$$

where  $J_{em}$  is the EM rotor inertia,  $J_{gb}$  is the gearbox inertia at the EM output shaft,  $J_{rd}$  is the rear differential inertia at the differential input shaft,  $\zeta_{gb}$  is the gearbox speed reduction ratio,  $\zeta_{rd}$  is the rear differential speed reduction ratio,  $\eta_{gb}$  is the mechanical efficiency of the gearbox,  $\eta_{rd}$  is the mechanical efficiency of the rear differential,  $T_{em}$  is the EM output torque, and  $T_{hs,r}$  is the reaction torque of a single half shaft on the rear axle.  $T_{em,fr}$  is a friction term that includes all spinning losses in the rear driveline including motor parasitic losses, bearing frictions and alike.  $T_{em,fr}$  is modeled by a combination of static and viscous friction components:

$$T_{em,fr} = b_{em,1} \omega_{em} + b_{em,0} \quad (3.40)$$

where  $b_{em,0}$ ,  $b_{em,1}$  are experimentally determined coefficients.

<sup>4</sup>Note that this is a crude approximation since the empirical torque converter model is only valid for engine speeds higher than the idle speed.

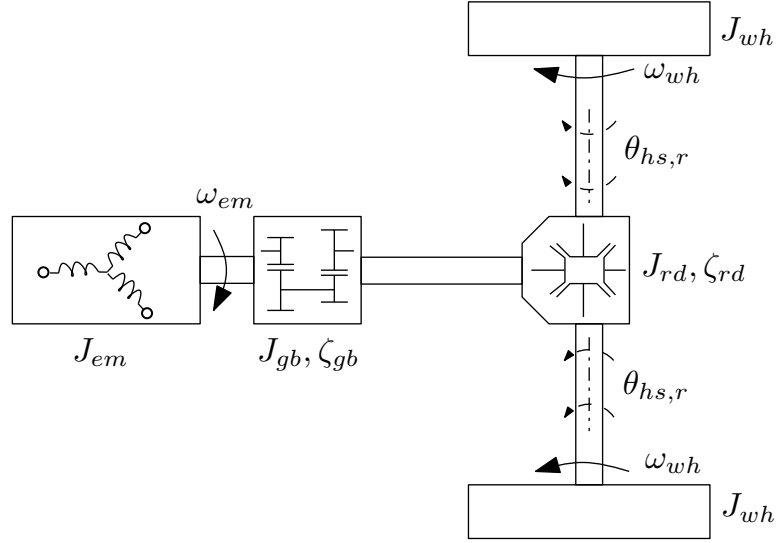


Figure 3.7: The mechanical configuration of the electrically driven rear axle of the experimental vehicle.

The mechanical behavior of the belted-starter alternator is incorporated into the engine crankshaft dynamics given by (3.3). The dynamics of the belt coupling between the engine and the BSA are neglected.

The electrical response characteristics of the electric machines are represented by simplified models similar to those used in the engine dynamics. The electric machines exhibit a short time lag between the torque request and the actual torque output that can be represented as:

$$\dot{T}_{em} = \frac{1}{\tau_{em}} (-T_{em} + T_{em,req}) \quad (3.41)$$

$$\dot{T}_{bsa} = \frac{1}{\tau_{bsa}} (-T_{bsa} + T_{bsa,req}) \quad (3.42)$$

$T_{em,req}$  and  $T_{bsa,req}$  are torque requests received by the EM and the BSA. The time constants,  $\tau_{em}$  and  $\tau_{bsa}$ , mainly result from the combined power inverter and motor torque “build-up” dynamics. These dynamics arise due to the control of the field currents and they usually reach steady state within a few motor revolutions. More

sophisticated models of electric drives are also available in the literature [3]. However, these models require the knowledge of various control variables (e.g. pulse-width modulation switching frequencies, phase voltages) and motor parameters (e.g. rotor and stator inductances and resistances) and they can not be readily implemented here.

### 3.2.4 Axles

The half shafts (or axle shafts) have non-negligible compliances that also determine the lowest resonance frequencies of the driveline [74]. A linear half-shaft model can be used to represent the half shaft torque as a function of the shaft torsion:

$$T_{hs,i} = k_{hs,i} \theta_{hs,i} + b_{hs,i} \Delta\omega_{hs,i} \quad (3.43)$$

The subscript,  $i = \{f, r\}$ , is used to refer to the front and rear axles<sup>5</sup>,  $k_{hs,i}$  is the stiffness of a single half-shaft on axle  $i$ ,  $b_{hs,i}$  is the damping coefficient of a single half-shaft on axle  $i$ ,  $\Delta\omega_{hs,i}$  is the speed difference between the two ends of a half shaft, and  $\theta_{hs,i}$  is the torsional displacement on a half-shaft.

In this work, the linear half-shaft model is extended with a lumped gear backlash model (adapted from [107]) that includes the total gear clearance of the front or rear driveline reflected to the front or rear half-shafts. In the presence of gear backlash, the half-shaft torque expression (3.43) can be modified as:

$$T_{hs,i} = k_{hs,i} (\theta_{hs,i} - \theta_{bl,i}) + b_{hs,i} (\Delta\omega_{hs,i} - \omega_{bl,i}) \quad (3.44)$$

where  $\theta_{bl,i}$  is the backlash position and  $\omega_{bl,i}$  is the backlash speed. The expressions for the half shaft torsional displacement and the relative angular speed are given as

$$\dot{\theta}_{hs,i} = \Delta\omega_{hs,i} = \begin{cases} \omega_{tr} - \omega_{wh,f}, & i = f \text{ (front axle)} \\ \frac{1}{\zeta_{gb}\zeta_{rd}} \omega_{em} - \omega_{wh,r}, & i = r \text{ (rear axle)} \end{cases} \quad (3.45)$$

<sup>5</sup>In the remainder of this chapter, the subscript  $i$  is used to differentiate between the front and rear driveline components (axles, brakes and wheels).

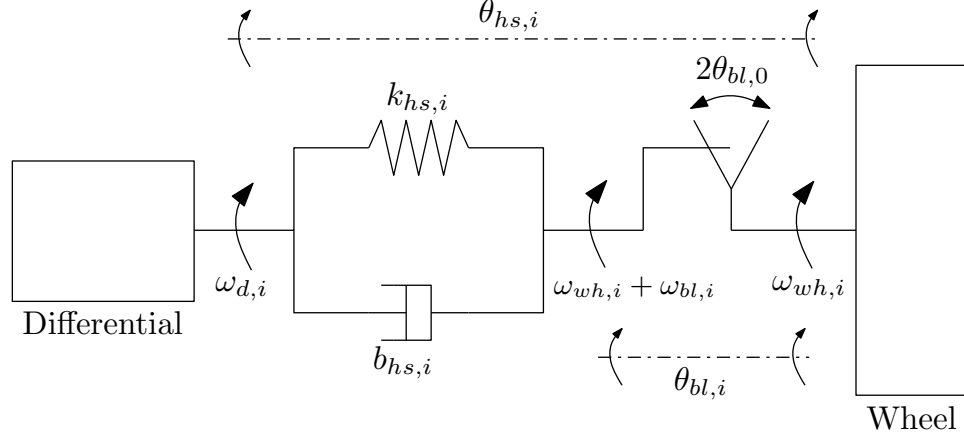


Figure 3.8: The half shaft model extended with gear backlash. Note that  $\omega_{d,i}$ , the differential output speed, is equal to  $\omega_{tr}$  for the front axle, and  $\omega_{em}/\zeta_{gb}\zeta_{rd}$  for the rear axle.

where  $\omega_{wh,i}$  is the wheel speed. The backlash speed varies as a function of the backlash position:

$$\dot{\theta}_{bl,i} = \omega_{bl,i} = \begin{cases} \frac{k_{hs,i}}{b_{hs,i}}(\theta_{hs,i} - \theta_{bl,i}) + \Delta\omega_{hs,i}, & |\theta_{bl,i}| < \theta_{bl,0} \\ \max(0, \frac{k_{hs,i}}{b_{hs,i}}(\theta_{hs,i} - \theta_{bl,i}) + \Delta\omega_{hs,i}), & \theta_{bl,i} = -\theta_{bl,0} \\ \min(0, \frac{k_{hs,i}}{b_{hs,i}}(\theta_{hs,i} - \theta_{bl,i}) + \Delta\omega_{hs,i}), & \theta_{bl,i} = \theta_{bl,0} \end{cases} \quad (3.46)$$

$\theta_{bl,i0}$  represents half of the total gear clearance in the (front or rear) driveline. This equation essentially constrains the backlash position inside a clearance region of  $2\theta_{bl,0}$ . The extended half-shaft model described by (3.44–3.46) is also graphically illustrated in Figure 3.8.

Modeling gear backlash is particularly important for the rear driveline of the test vehicle. The absence of a torque damping device in the rear driveline (such as a torque converter) aggravates drivability issues such as shunt and shuffle that are strongly influenced by gear lash.

### 3.2.5 Brakes

The test vehicle meets the driver's braking commands using a combination of conventional hydraulic braking and regenerative braking. Regenerative braking torques

are realized in the vehicle model by the mechanical transfer of negative electric motor torques through the driveline. Hydraulic braking torques are modeled using an empirically determined relationship between the brake pedal position and the hydraulic brake pressure. Using this relationship, the brake torques on the front and rear axles are obtained as

$$T_{br,i} = R_{br} p_{br}(\beta_{dr}) A_{br,i} \mu_{br} \quad (3.47)$$

where  $T_{br,i}$  is the brake torque,  $R_{br}$  is the radius of the brake disc,  $p_{br}(\beta_{dr})$  is a function that maps the driver's brake pedal position ( $\beta_{dr}$ ) to the brake line pressure,  $A_{br,i}$  is the effective brake piston area, and  $\mu_{br}$  is the brake friction coefficient of the disc brakes. The experimental vehicle incorporates disc type brakes in the front and rear axles, therefore, the front and rear brake friction coefficients are assumed to be the same.

The braking proportion between the front and rear axles (larger braking force on the front axle) is determined by the effective contact area of the hydraulic brake pistons. Equation (3.47) is an accurate representation of the braking torques assuming that all brake discs have similar frictional properties and that the anti-locking braking system (ABS) does not interfere with the driver's braking command.

### 3.2.6 Tires and Vehicle

The nonlinear tire model proposed by Pacejka [108] is used to represent the longitudinal tire dynamics. This model uses the semi-empirical "Magic Formula" to compute the tractive forces ( $F_{x,i}$ ) generated by the tires:

$$F_{x,i} = \mu_{wh} F_{z,i} \sin(C_{wh,1} \arctan(C_{wh,2} \kappa'_i - C_{wh,3}(C_{wh,2} \kappa'_i - \arctan(C_{wh,2} \kappa'_i)))) \quad (3.48)$$

The Pacejka model coefficients  $C_{wh,1}, C_{wh,2}, C_{wh,3}$  are obtained from the manufacturer's tire data. Also,  $\mu_{wh}$  is the coefficient of friction between the tires and the road surface. The vertical forces acting on the front and rear wheels ( $F_{z,f}$  and  $F_{z,r}$ ) change as a function of the vehicle acceleration and the resulting longitudinal load transfer

can be approximately represented as

$$F_{z,f} = \frac{M_{veh}g}{4} \left( 1 + K_{veh,1} \frac{a_{veh}}{g} + K_{veh,2} \right) \quad (3.49)$$

$$F_{z,r} = \frac{M_{veh}g}{4} \left( 1 - K_{veh,1} \frac{a_{veh}}{g} - K_{veh,2} \right) \quad (3.50)$$

where  $K_{veh,1}$  and  $K_{veh,2}$  are geometric vehicle properties,  $M_{veh}$  is the total mass of the vehicle,  $g$  is the gravitational acceleration, and  $a_{veh}$  is the vehicle's longitudinal acceleration.

As (3.48) indicates, the transient tire slip,  $\kappa'_i$ , has a major influence on the longitudinal tire force.  $\kappa'_i$  is a function of the longitudinal tire deflection,  $u_{wh,i}$ , which can be computed as

$$\dot{u}_{wh,i} = \begin{cases} 0 & |v_{veh}| < v_{veh,low} \wedge |\kappa'_i| > 3F_{z,i}/C_{F\kappa} \\ & \wedge (v_{s,i} + |v_{veh}|u_{wh,i}/\sigma_\kappa) u_{wh,i} < 0 \\ -v_{s,i} - \frac{1}{\sigma_\kappa}|v_{veh}|u_{wh,i} & \text{otherwise} \end{cases} \quad (3.51)$$

where the tire slip speed,  $v_{s,i}$ , is defined as

$$v_{s,i} = v_{veh} - R_{wh}\omega_{wh,i} \quad (3.52)$$

Here,  $v_{veh}$  is the vehicle's longitudinal velocity,  $v_{veh,low}$  is a threshold speed,  $\sigma_\kappa$  is the tire relaxation length,  $C_{F\kappa}$  is the longitudinal tire stiffness, and  $R_{wh}$  is the tire radius under load. The transient slip is then obtained using the following expression:

$$\kappa'_i = \frac{u_{wh,i}}{\sigma_\kappa} - \frac{b_{v,low}}{C_{F\kappa}} v_{s,i} \quad (3.53)$$

The low speed damping coefficient,  $b_{v,low}$ , can be computed using an appropriate function such as the one proposed in [108]:

$$b_{v,low} = \begin{cases} \frac{1}{2}b_{v,low,0}(1 + \cos(\pi |v_{veh}/v_{veh,low}|)) & v_{veh} \leq v_{veh,low} \\ 0 & v_{veh} > v_{veh,low} \end{cases} \quad (3.54)$$

where  $b_{v,low,0}$  is a constant damping coefficient. Using the tire tractive forces and half shaft torques, the wheel speeds are calculated from a torque balance at the wheels:

$$\dot{\omega}_{wh,i} = \frac{1}{J_{wh}} (T_{hs,i} - R_{wh}F_{x,i} - R_{wh}F_{rr,i}) \quad (3.55)$$





### 3.2.7 High Voltage Battery

The battery model has an indirect influence on vehicle drivability since the battery state-of-charge (SOC) (which is a control strategy feedback signal) affects the power-split to the actuators. In order to predict this effect, a simplified zeroth order battery model is used to estimate the battery SOC. For information on more sophisticated battery models, the reader is referred to [109].

The power supplied by the battery,  $P_{batt}$ , is given as:

$$P_{batt} = P_{acc} + \sum_k T_k \omega_k \cdot \begin{cases} \frac{1}{\eta_k(\omega_k, T_k)} & T_k \geq 0 \\ \eta_k(\omega_k, T_k) & T_k < 0 \end{cases} \quad (k = \{em, bsa\}) \quad (3.58)$$

where  $P_{acc}$  is the constant electrical load of the accessories,  $\eta_k$  is the combined energy conversion efficiency of the electric machine (EM or BSA) and its power converter.

Using the power supplied by the battery ( $P_{batt}$ ), the estimated open-circuit voltage of the battery pack ( $V_{oc}$ ), and the internal resistance of the battery pack ( $Z_{batt}$ ), the battery current and voltage can be computed as:

$$I_{batt} = \frac{V_{oc} - \sqrt{V_{oc}^2 - 4Z_{batt}P_{batt}}}{2Z_{batt}} \quad (3.59)$$

$$V_{batt} = V_{oc} - Z_{batt}I_{batt} \quad (3.60)$$

The battery internal resistance and the open circuit voltage are modeled as functions of the battery SOC and these functions change according to the sign of the battery current. Nominally, these parameters are also affected by the battery temperature. However, the dynamic simulator does not incorporate a thermal battery model, hence, the temperature dependence is neglected. Using the battery current and the estimated initial open-circuit voltage, the battery SOC ( $S_{batt}$ ) can be obtained by current integration:

$$S_{batt}(t) = S_{batt}(V_{oc}(0)) + \frac{1}{C_{batt}} \int_0^t I_{batt} dt \quad (3.61)$$

where  $C_{batt}$  is the battery energy capacity in [A.s].

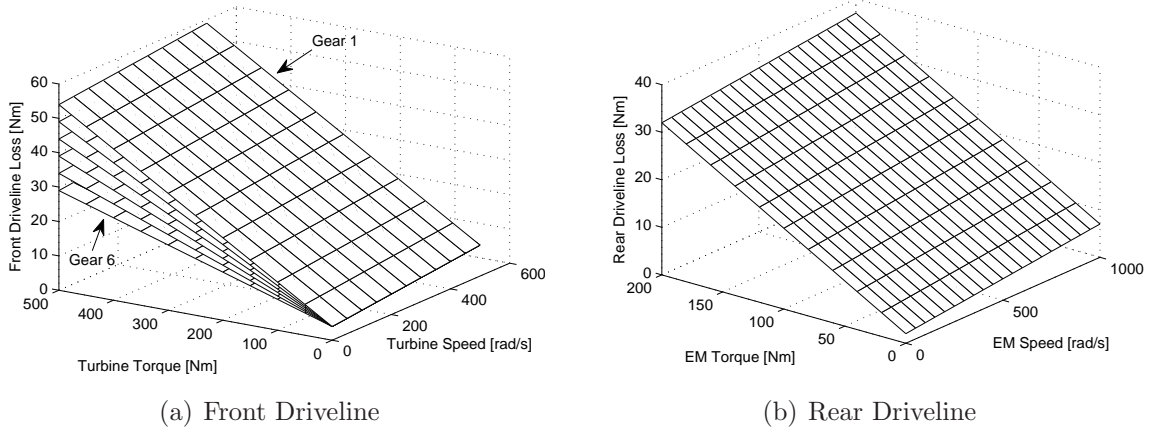


Figure 3.10: Driveline losses as functions of speed and torque.

### 3.2.8 Driveline Losses

Accurate modeling of driveline losses is crucial to achieve a good correlation between the model predictions and experimental results. Quantitatively, the most significant contribution is due to the engine friction that is given by (3.4). Other types of losses such as gear meshing losses (due to the transmission, the rear motor gearbox, the rear and front differentials), spinning losses (due to bearing frictions, clutch drag) and motor parasitic losses also influence the behavior of the model. However, these losses strongly depend on the operating conditions and are difficult to model on a component-to-component basis.

This work uses a simplified approach to modeling driveline losses by representing them as linear functions of torques and speeds. Recalling (3.15) and (3.39), all rear driveline losses are lumped to the rear gearbox input shaft, and all front driveline losses (except for the engine friction) are lumped to the transmission input shaft. The constant efficiency terms that appear in these equations represent torque-dependent driveline losses (such as gear meshing losses), and the viscous friction terms represent speed-dependent losses (spinning and motor parasitic losses).

This approach is also illustrated in Figure 3.10. While the rear driveline losses are approximated by a fixed function of motor speed and torque, the front driveline losses are approximated by a family of functions that are selected according to the transmission gear. While some of these loss functions are determined empirically, the remaining are obtained from external resources [22, 110]. Note that driveline losses can be used as tuning parameters for the vehicle model, since their values are subject to large uncertainties even when they are experimentally determined.

### 3.3 Summary

This chapter demonstrated the development of a low-frequency longitudinal dynamic HEV model that is suited for the evaluation of vehicle drivability as well as energy consumption. The vehicle model particularly focuses on the driveline dynamics while the dynamics of the hybrid powertrain actuators (the engine, the electric machines and the transmission hydraulic actuators) are highly simplified. One of the contributions of this chapter is the development of a six-speed automatic transmission that also accommodates for the transmission behavior during engine start-stop. Also, a detailed dynamic model of a through-the-road parallel HEV of the described configuration is not available in the public domain to the author's knowledge.

## CHAPTER 4

### MODEL VALIDATION

The longitudinal HEV simulation model, CX-DYN, is validated using a number of tests conducted under controlled operating conditions. The purpose of each test is to demonstrate a particular aspect of the vehicle model or to determine unknown (or uncertain) parameters of the model via empirical methods.

This chapter details these experiments and provides a comparison of the simulated vehicle states with experimental data. The simulations are conducted in an open-loop fashion, i.e., the driver model is not used in the simulator feedback loop. Instead, the control strategy torque requests recorded from actual driving conditions are directly input to the simulator and the desired output variables are generated. As discussed in Chapter 3, this is the most appropriate technique for experimental model validation, since using a driver model in the simulation loop may result in an unintended compensation of the simulator errors.

#### 4.1 Identification and Validation of Subsystem Models

Prior to validating the overall vehicle model, various tests are performed to determine important driveline parameters that are not available from component technical specifications. These tests only provide approximate values for the driveline parameters since the actual values highly depend on external factors such as the operating temperature, component wear and alike. In addition to these external factors, the linear approximations that are used to describe the component models occasionally

yield inaccurate results, since the actual parameters usually vary nonlinearly with the governing variables.

#### 4.1.1 Engine Dynamics

Accurate characterization of the engine friction is important for a driveline model. The engine friction is one of the largest mechanical losses in the driveline and its magnitude significantly affects the static behavior of the vehicle model. This effect is more pronounced at low gears since the magnitude of the engine friction, when reflected to the wheels, is greater at high gear ratios.

In this work, the engine friction is determined using a standard technique that involves linearly extrapolating the fuel consumption - engine brake torque data (obtained from manufacturer's dynamometer tests) to zero fuel consumption for a number of engine speeds.<sup>1</sup> This technique assumes that the engine friction is a static phenomenon, i.e., cyclic variations are neglected. Also, the results are only valid at nominal engine operating temperatures.

Figure 4.1(a) illustrates the engine friction identification method for various engine speeds. The friction torque is obtained using the zero crossings. Figure 4.1(b) also shows the resulting curve fit as a function of the engine speed. Although the widely accepted formula (3.4) states that the engine friction is a quadratic function of the engine speed, a linear correlation is found to be sufficient for this particular engine.

Next, an engine coast down experiment is conducted to investigate the level of agreement between the engine friction obtained from the identification method and the true friction torque acting on the engine crankshaft. Note that the true friction consists of losses other than the pure engine friction that results from the reciprocating motion of the pistons.

The experiment is conducted while the transmission is in the neutral state and the vehicle is fully stopped. The engine speed and the torque converter speed ratio obtained from the engine coast down experiment are shown in Figure 4.2.

<sup>1</sup>Recall that the engine brake torque is the reaction torque applied by a dynamometer to maintain a specific engine speed at a given engine output torque.

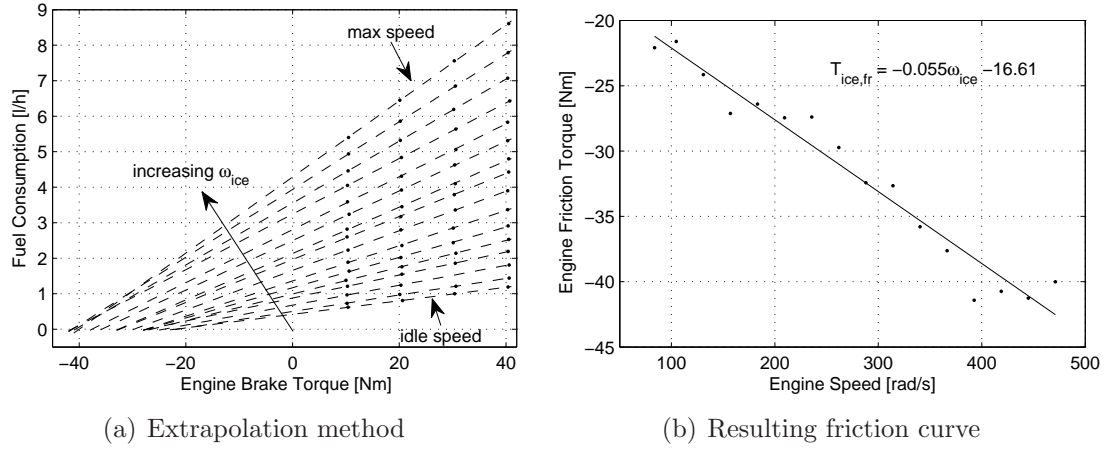


Figure 4.1: Identification of the engine friction using dynamometer data. The approximation is only valid for nominal engine temperatures.

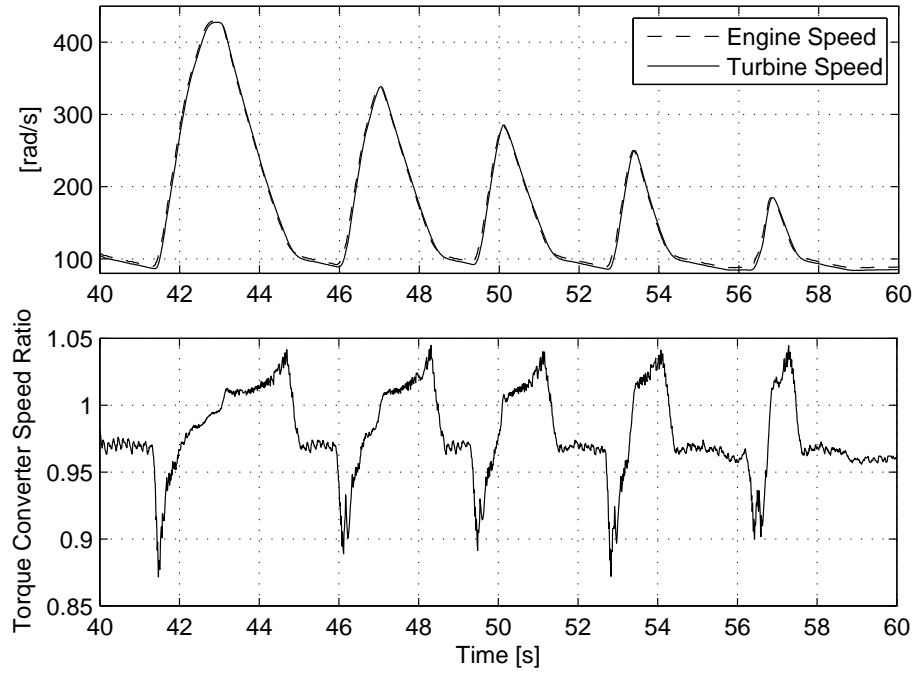


Figure 4.2: Experimental results from the engine coast down experiment. The torque converter speed ratio remains higher than the critical speed ratio during this test.

The transmission is assumed to be decoupled from the engine in the neutral state since the PGS (planetary gearset) clutches C1 and C2 are disengaged. Also, since the torque converter speed ratio is higher than the critical speed ratio ( $\gamma_c = 0.88$ ),  $T_p = T_t$  from (3.5) and (3.6). Therefore, summing (3.3) and (3.15) approximately gives:

$$(J_{ice} + J_{bsa} + J_p + J_{pgs,1})\dot{\omega}_{ice} \cong T_{ice,ind} + T_{bsa} - T_{ice,fr} - T_{tr,fr} \quad (4.1)$$

assuming that  $\omega_{ice} = \omega_t$  for the coast down portions of the experiment. This is a reasonable assumption since  $1 < \omega_t/\omega_{ice} < 1.05$  for this particular test. When the coast-down portions of Figure 4.2 are investigated, the acquired data shows that the fuel is cut off to the engine. This ensures that the only external torques acting on the system are the engine and transmission friction torques (or what is referred to above as true friction).

Using a representative value for  $T_{tr,fr}$  (obtained from [22]) and the curve fit computed for  $T_{ice,fr}$ , an estimate of the total friction is obtained. This estimate is then compared with the product of the total inertia and the engine deceleration rate. Although, the total inertia term in (4.1) is not precisely known, the inertia values obtained from external resources (such as [25], [111]) for similarly sized engines and torque converters are in agreement.

This comparison is shown in Figure 4.3. The dots represent the product of the estimated inertia and the deceleration rate of the engine from the coast down segments of Figure 4.2.<sup>2</sup> The dashed line represents the total friction torque as a function of the engine speed. Note that the coast down experiment indicates a larger friction torque that results from the unmodeled losses such as the engine accessory torque. This difference is added to the simulation model as a static loss.

The front driveline model is simulated using the determined parameters while the transmission is in the neutral state. A comparison of the experimental and simulation results for the engine speed and the torque converter speed ratio is given in Figure 4.4 for the test described in Figure 4.2. The simulated and experimental engine speed

<sup>2</sup>A total inertia of  $J_{total} = J_{ice} + J_{bsa} + J_p + J_{pgs,1} = 0.215 \text{ kg m}^2$  is used.

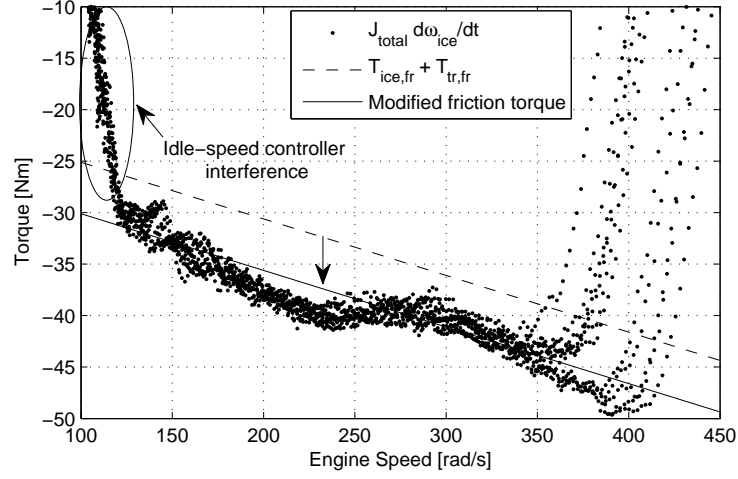


Figure 4.3: A comparison of the total friction and engine deceleration rate from the coast-down experiments.

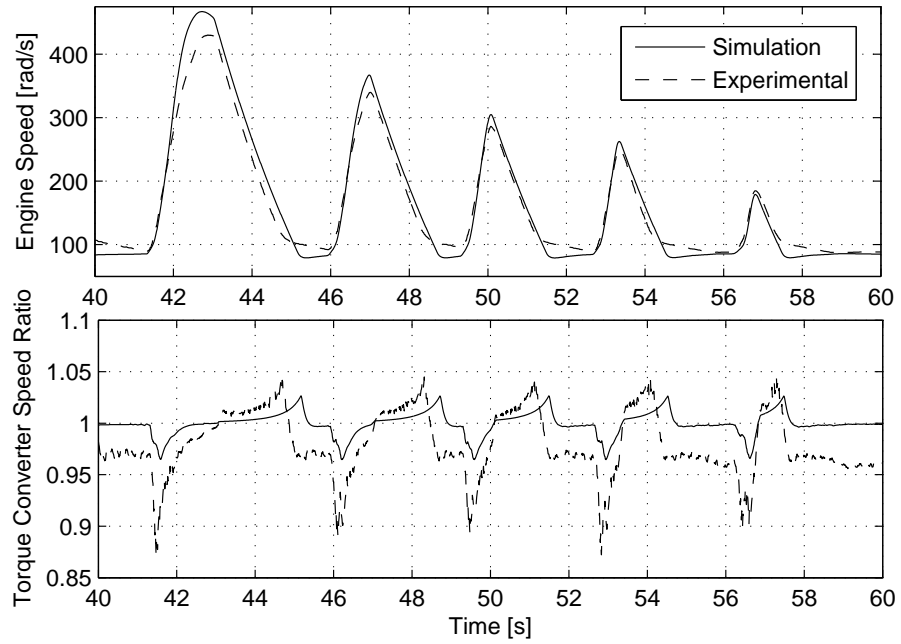


Figure 4.4: Validation of the engine and the torque converter model combined. The simulated and experimental engine speed and torque converter speed ratio are shown.



traces are in good agreement. There are slight differences below 100 rad/s due to the differences between the actual and simulated idle-speed controller behaviors. The simulated torque converter speed ratio also shows the same qualitative trend as the experimental result. The differences, that are small in magnitude, are due to the uncertainties in the torque converter model.

#### 4.1.2 Rear Driveline Dynamics

Similar tests are performed on the rear electric machine using step changes in the torque demand. The resulting EM speed is recorded. These tests are conducted while the EM and its integrated gearbox are disconnected from the rear driveline. Therefore, no mechanical load is present on the motor output shaft. The purpose of these tests is to determine the combined inertia of the EM rotor and the gearbox, the approximate EM response time constant, and the EM internal friction.

The step torque changes and the resulting EM speed are shown in Figure 4.5. Since there is no load torque on the output side, short torque pulses result in high acceleration rates. The combined rotor-gearbox inertia is estimated by taking the numerical derivatives of the EM speed during an acceleration and the EM speed during a deceleration at the same EM speed. A simple summation of the following relationships gives the desired quantity assuming that the EM friction is a single-valued function of the EM speed:

$$(J_{em} + J_{gb})\dot{\omega}_{em} \big|_{\omega_{em}=\omega_{em}(t_1)} = \eta_{gb}T_{em} - T_{em,fr} \big|_{\omega_{em}=\omega_{em}(t_1)} \quad (4.2)$$

$$-(J_{em} + J_{gb})\dot{\omega}_{em} \big|_{\omega_{em}=\omega_{em}(t_2)} = T_{em,fr} \big|_{\omega_{em}=\omega_{em}(t_2)} \quad (4.3)$$

where  $\omega_{em}(t_1)$  and  $\omega_{em}(t_2)$  are two data points with the same speed (taken at different time instances) such that  $T_{em} > 0$  at  $t = t_1$ , and  $T_{em} = 0$  at  $t = t_2$ . Since the operating speed is fixed, the friction torque cancels as a result of the summation. Therefore, for a given pair of operating points, the ratio of the EM torque to the sum of the numerical derivatives of the EM speed gives the desired inertia. Considering 3 sample data pairs, this ratio is found to be between 0.0845 – 0.0865 assuming 100%

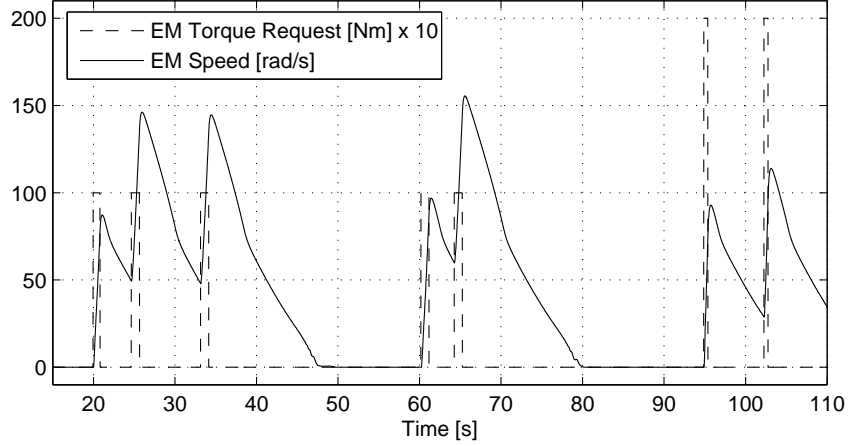


Figure 4.5: The rear EM dynamics identification experiment. A sequence of short torque pulses are applied to the EM and the resulting motor speed is recorded.

mechanical efficiency. Therefore, a mean value of  $0.085 \text{ kg m}^2$  well approximates the lumped inertia of the EM rotor and the integrated gearbox.

Once the EM inertia is obtained, the EM friction can be calculated in a straightforward manner. Using the coast down segments of the experiment, (4.3) is used to obtain the internal friction of the EM. The computed friction torque and the linear curve fit used to represent the friction torque are plotted as a functions of the motor speed in Figure 4.6. Although a linear fit does not accurately represent the behavior at higher speeds, improving the friction model would not provide a substantial benefit in terms of the overall model accuracy since the EM friction is much smaller in magnitude than the remaining driveline losses. However, it is clear that the actual EM “friction” is mostly due to the motor parasitic losses since the numerically computed friction does not change monotonically with the EM speed as shown in Figure 4.6.

The time constant of the rear EM is determined by a trial and error procedure to fit the simulated EM speed to the experimental data. The rear EM model is simulated using step changes in the torque command for the experiment given in Figure 4.5. The simulated EM speed and the experimental data are shown in Figure 4.7 for two different time constants. As shown in Figure 4.7(b), a time constant of  $\tau_{em} = 0.1 \text{ s}$

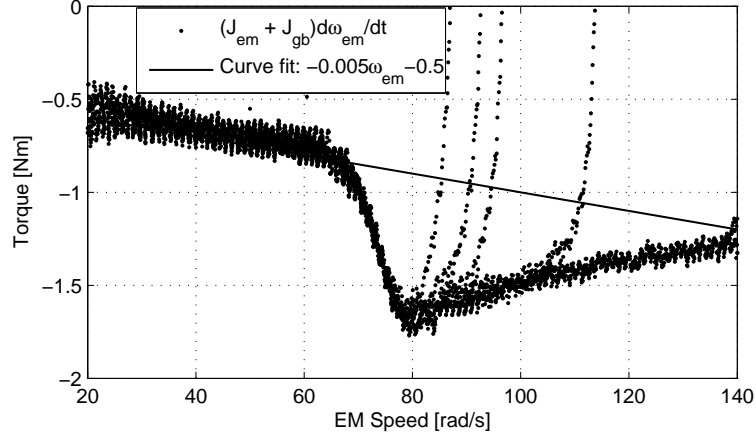


Figure 4.6: EM internal losses as a function of the EM speed obtained from the coast down tests.

better approximates the experimental data. The response delay and the mismatch of the transient responses during step torque changes ( $t = 21$  s and  $t = 26$  s) in Figure 4.7(a) disappear when a larger time constant is used. Note that assuming  $\tau_{em} = 0.1$  s is a conservative estimate for the entire speed range of operation since the motor response rate increases with the motor speed. A less conservative estimate of the time constant can be obtained by assuming that  $\tau_{em}$  changes inversely proportional with the motor speed.

Other coast-down tests are performed on the rear and front drivelines to estimate the total spinning losses in each axle. The driveline friction coefficients are adjusted based on the results of these tests. Note that all front or rear driveline spinning losses are lumped into a single linear friction term for each axle ( $T_{em,fr}$  or  $T_{tr,fr}$ ) except for the engine friction.

Experiments such as those described above not only provide a means for determining unknown driveline parameters, but they also make it possible to validate individual subsystem models prior to validating the overall vehicle model. This approach simplifies the calibration of the vehicle model since some of the uncertain parameters are individually determined (or verified) through basic experiments.

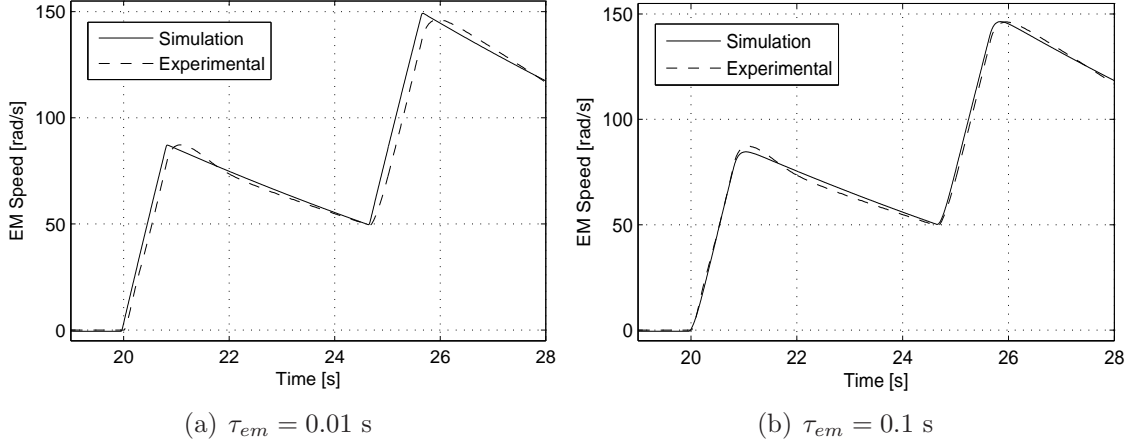


Figure 4.7: The impact of the rear electric machine time constant on the simulation results.

## 4.2 Validation of the HEV Model

The overall hybrid-electric vehicle model is validated by longitudinal driving experiments conducted on a dry asphalt surface at nearly zero road grade. Other external variables that may affect the dynamic behavior of the vehicle subsystems such as the engine coolant temperature, the transmission oil temperature and the battery temperature are maintained at their nominal operating ranges.

The variables of interest for the purpose of model validation are the vehicle acceleration, the vehicle speed, the engine speed, the transmission input and output speeds, the transmission gear, the rear electric machine speed and the wheel speeds. Also, the battery pack current and voltage are used for the validation of the battery model.

The experiments described in this section are focused primarily on low vehicle speeds. This is because dynamic events such as gear engagements, engine start-stop and pedal tip-in/tip-out result in critical disturbances when high gear ratios are present between the actuators and the wheels. As an example, the quality of a 5-6

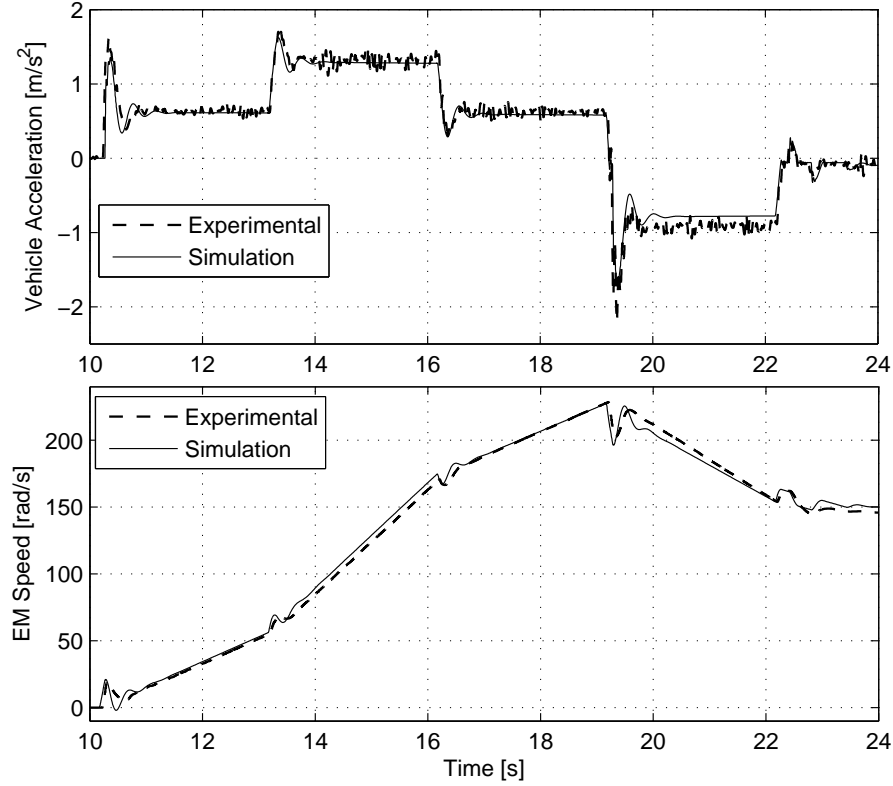


Figure 4.8: Validation of the rear driveline model. The simulated vehicle acceleration and EM speed are compared with the experimental results.

gear shift has less impact on drivability compared to a 1-2 gear shift, since the change in wheel torques is much lower in the former case.

#### 4.2.1 Electric Only Operation

The first test is conducted while the vehicle operates in electric only mode. Step torque changes are applied to the rear EM and the engine is shut off. This approach helps to minimize the dynamic coupling between the front and rear drive systems.

Figure 4.8 shows a comparison of the simulation results and experimental data for the vehicle acceleration and EM speed. There is a good correlation between the two sets of results during both transients and quasi-static operation. Some of the detailed test results are also plotted in Figure 4.9. The effect of gear backlash on pedal tip-in

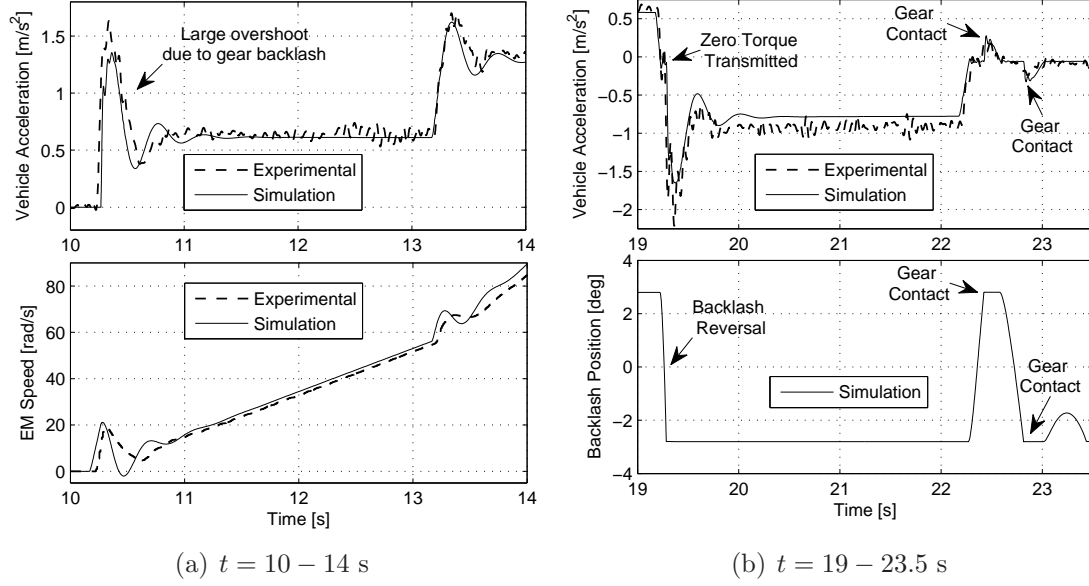


Figure 4.9: Details of the test shown in Figure 4.8. The gear backlash model accurately represents the transient effects in the rear driveline.

response from a vehicle standstill is shown in Figure 4.9(a). The first pedal tip-in at  $t = 10$  s causes a larger overshoot in vehicle acceleration compared to the second tip-in at  $t = 13$  s, although the torque steps are equal in magnitude ( $\Delta T_{em,req} = 60$  Nm). This behavior is a result of gear backlash and it is accurately captured by the simulation result.

A similar situation arises following the pedal tip-out at  $t = 19$  s as shown in Figure 4.9(b). The vehicle acceleration and the gear backlash position (only the simulation result) are plotted here. Note that the pedal tip-out at  $t = 19$  s (which is essentially a pedal tip-out followed by a negative torque demand) first causes a momentary response delay (during backlash reversal) and then a large undershoot in the vehicle acceleration. Both transients are accurately predicted by the dynamic model. Another interesting result appears when the EM torque command changes from -60 to 0 Nm shortly after  $t = 22$  s. As a result of the sign change in the half shaft torque, the gear position hits the upper and lower bounds of the gear clearance.

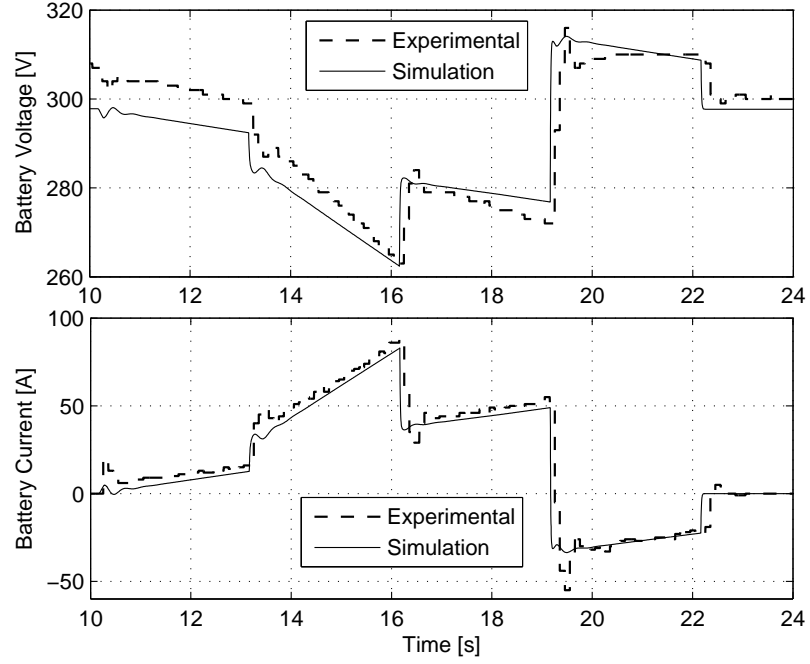


Figure 4.10: The simulated battery pack voltage and current are compared with experimental results for the test shown in Figure 4.8.

This creates two small bumps in the vehicle acceleration with opposite sign. The simulation result accurately follows the experimental data in this case.

Figure 4.10 shows another comparison of the simulation results and the experimental data for battery pack voltage and current. The simulated battery current is in agreement with the experimental data. However, the predicted battery voltage is slightly different than its experimental counterpart. Since a highly simplified battery model is used in this work, these differences are to be expected. In addition, the battery output voltage at  $t = 10$  s (with zero current) does not correspond to the open-circuit voltage of the battery, since the battery is not sufficiently relaxed prior to this experiment. This issue contributes to the existing uncertainties in the battery model. However, the same qualitative trend is observed between the two voltage traces despite the differences in magnitude. Note that the accuracy of the battery

model only affects the predicted fuel economy, and not the predicted driveline dynamic behavior. Therefore, the results obtained here are found satisfactory for the purposes of this dissertation.

### 4.2.2 Engine Only Operation

In order to validate the front driveline model, a second experiment is conducted while the vehicle is in engine only operating mode. The accelerator pedal is maintained at a nearly fixed position during this test. The indicated engine torque, which is estimated by the engine control unit, is used as an input to the vehicle simulator. The engine is initially in idle condition. During the acceleration, two gear upshifts are commanded by the transmission control unit.

The simulated vehicle states are compared with experimental data in Figures 4.11 and 4.12. The vehicle acceleration is considered again as the primary indicator of model accuracy. Other driveline states that are of interest here are the engine speed, the transmission input speed (the torque converter turbine speed), and the transmission output speed.

The simulated vehicle acceleration as well as the simulated transmission input and output speeds correlate well with the experimental data for both steady and transient accelerations. The simulated engine speed slightly overestimates the experimental data for the majority of the test. This difference is due to fact that the torque converter model parameters are adapted from another torque converter with similar dimensions [23], since the actual parameters are not available.

It is clear from Figures 4.11-4.12 that the most important transient events during the engine only operation of the test vehicle are transmission gear shifts. Other disturbances such as driveline shuffle (as a result of pedal tip-in/tip-out) are not observed in the experiments, since the excitation frequencies in the vicinity of the fundamental natural frequency of the front driveline are highly damped by the torque converter.

The 1-2 and 2-3 gear up-shifts are shown in more detail in Figure 4.13. The primary objective for the validation of gear shift transients is to capture the qualitative



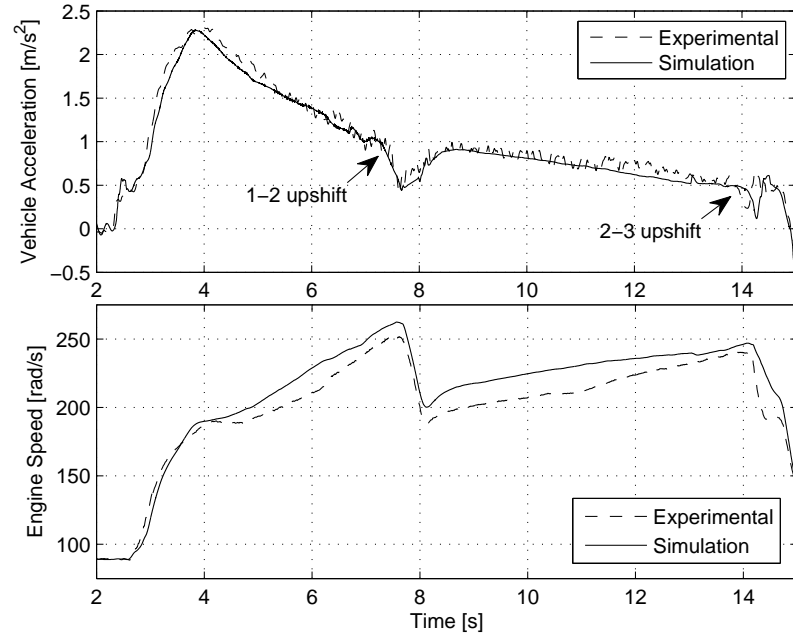


Figure 4.11: Validation of the front driveline model in engine only operation. The simulated vehicle acceleration and engine speed are compared with experimental data.

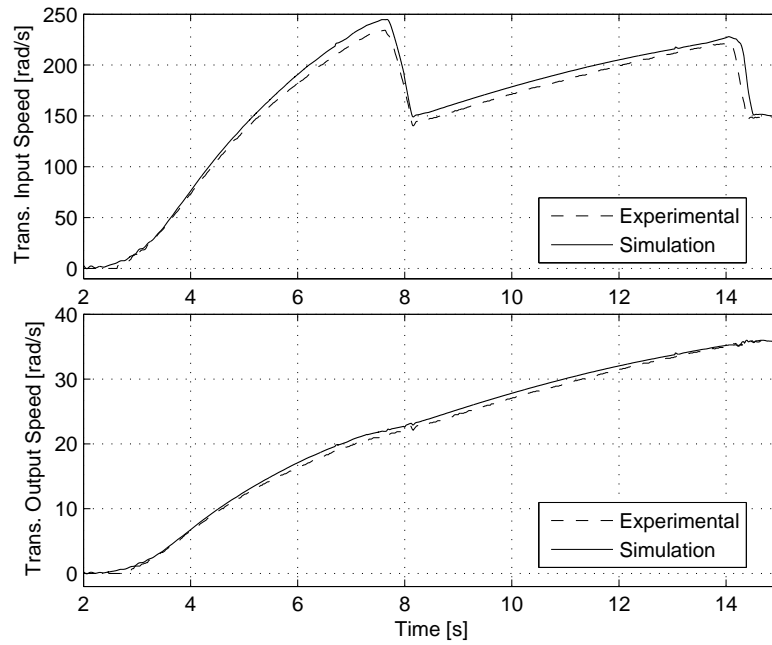


Figure 4.12: Validation of the front driveline model in engine only operation. The simulated transmission input-output speeds are compared with experimental data.

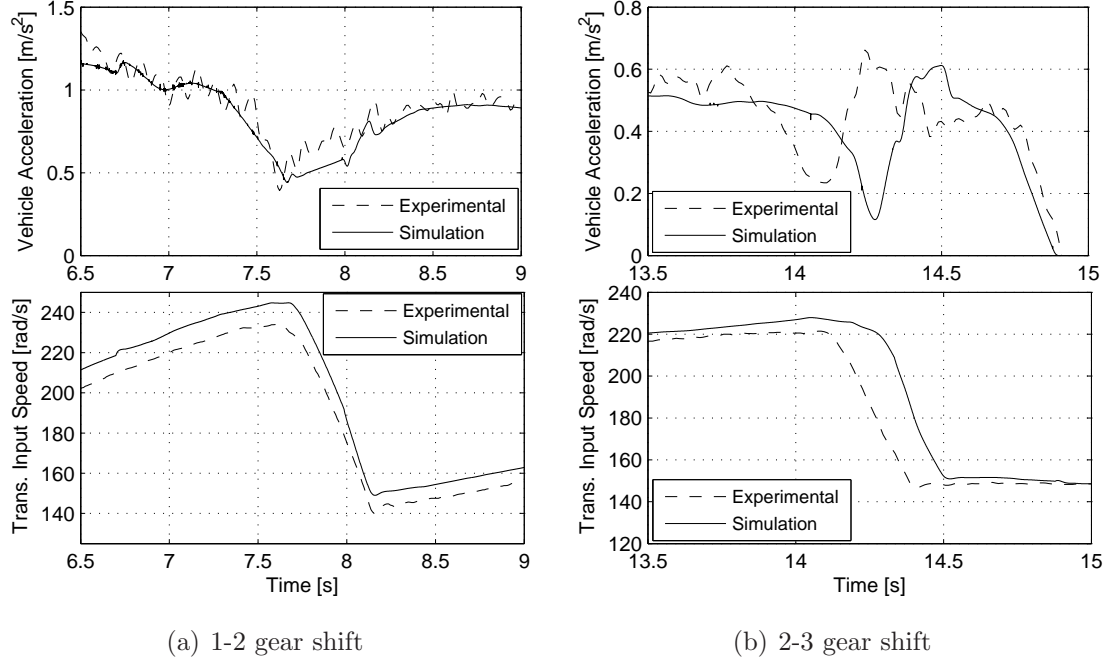


Figure 4.13: Details of the engine only operation validation test showing two gear upshifts under medium engine load.

behavior of the changes in vehicle acceleration and transmission input/output speeds.<sup>3</sup> The actual behavior is difficult to represent with high accuracy due to two reasons. First, the gear shift response largely depends on the clutch/brake pressure profiles and these profiles are not available as measurements in the test vehicle. In this work, open-loop traces are used to represent the on-coming and off-going clutch/brake pressures (see Figure 4.14). Secondly, the clutch/brake physical properties are unknown and representative values are obtained from external resources [22, 23, 25]. Note that the pressure traces are slightly calibrated to obtain the results shown in Figure 4.13. It is clearly not possible to achieve the same level of accuracy in another test that is conducted under different operating conditions (e.g. higher engine load) or one that involves a different gear shift.

<sup>3</sup>Only the details of the transmission input speed are shown here, since the transmission output speed does not have enough resolution to facilitate such comparison.

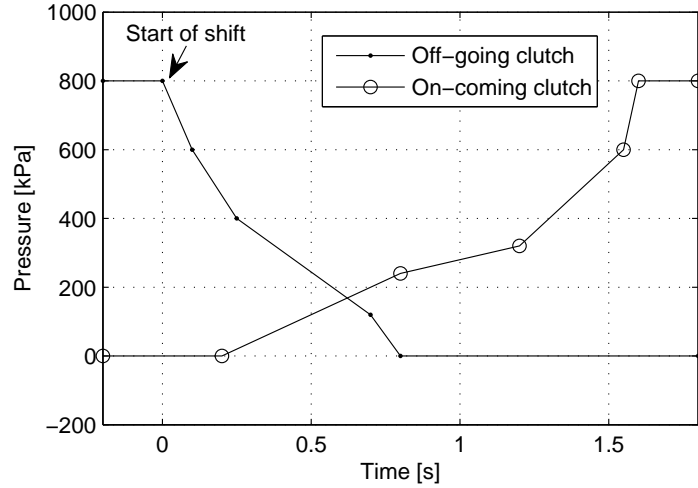


Figure 4.14: Transmission on-coming and off-going clutch pressure traces used for the validation of the front driveline model.

### 4.2.3 Hybrid Vehicle Operation

After the validation of individual subsystem and driveline models, the overall HEV model is validated during an acceleration that involves a series of operating mode changes. In this test, the vehicle is accelerated from rest using the rear EM while the engine is initially shut off. Under appropriate driving conditions, the engine is started using the belted-starter alternator. Following the engine start, the vehicle is further accelerated in the hybrid operating mode using a proper combination of the torques generated by two electric machines and the engine. This is a typical driving pattern for the test vehicle. Therefore, an accurate prediction of this pattern is particularly important from a control design standpoint.

The focus of the hybrid mode validation test is the engine start event. The engine start event, if not carefully controlled, results in a torque disturbance that occurs immediately after the first fuel injection (around the idle speed). The intensity of this torque disturbance is related to the internal states of the transmission, in particular, the speed difference between the two sides of the on-coming clutch. The control of this disturbance is the topic of Chapter 6.

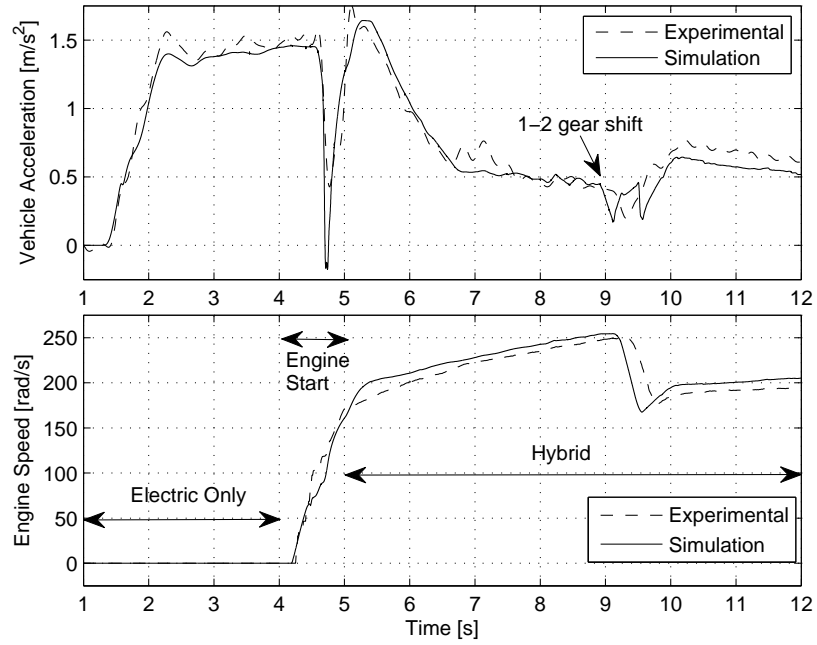


Figure 4.15: Validation of the HEV model in hybrid operation. The simulated vehicle acceleration and engine speed are compared with experimental data.

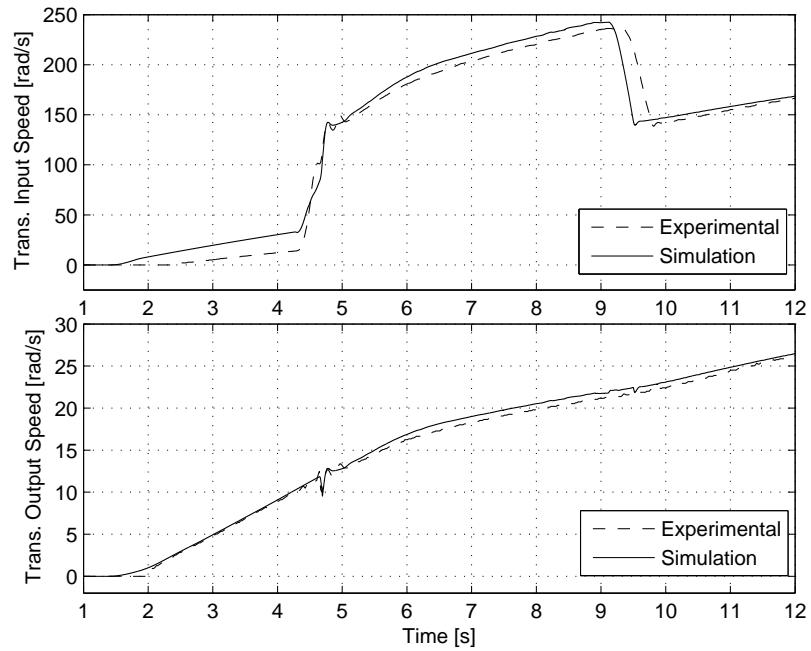


Figure 4.16: Validation of the HEV model in hybrid operation. The simulated transmission input-output speeds are compared with experimental data.

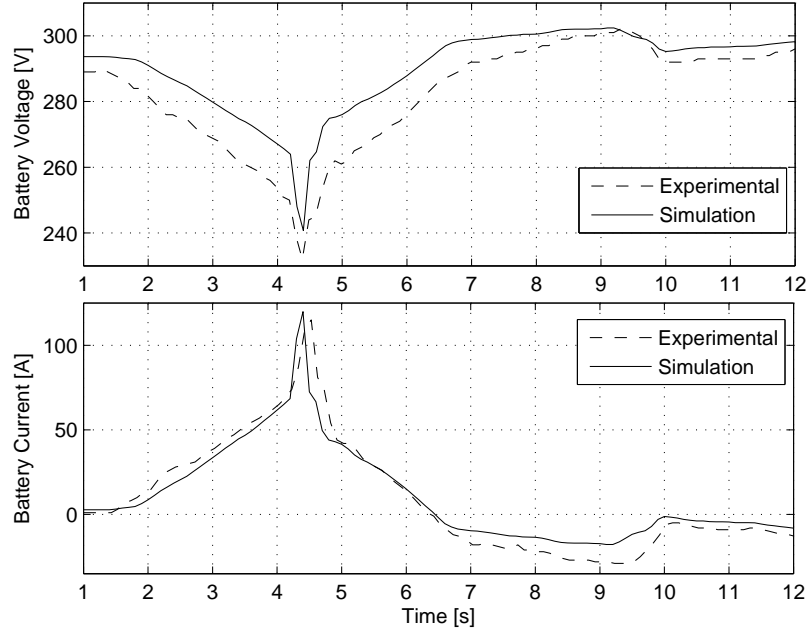


Figure 4.17: Validation of the HEV model in hybrid operation. The simulated battery pack voltage and current are compared with experimental data.

Various comparisons of the simulation results and experimental data are given in Figures 4.15–4.17 for the hybrid mode validation test. Figure 4.15 shows the vehicle acceleration and the engine speed, and Figure 4.16 shows the transmission input and output speeds. The vehicle mode changes and the start of the 1-2 gear shift are marked on Figure 4.15. The battery voltage and current are also plotted in Figure 4.17.

The results are in overall agreement, as is expected from the previous validation tests. Although the details of the gear shift event are not shown here, the simulated acceleration trace does not follow the experimental data as closely as it does in the engine only validation example (see Figure 4.13(a)). This result is not surprising since the clutch pressure profiles used in the engine only validation test are used here without any modifications. As discussed earlier, this is a crude approximation of the gear shift control algorithm. Therefore, the repeatability of this assumption is not high for the purpose of gear shift validation.

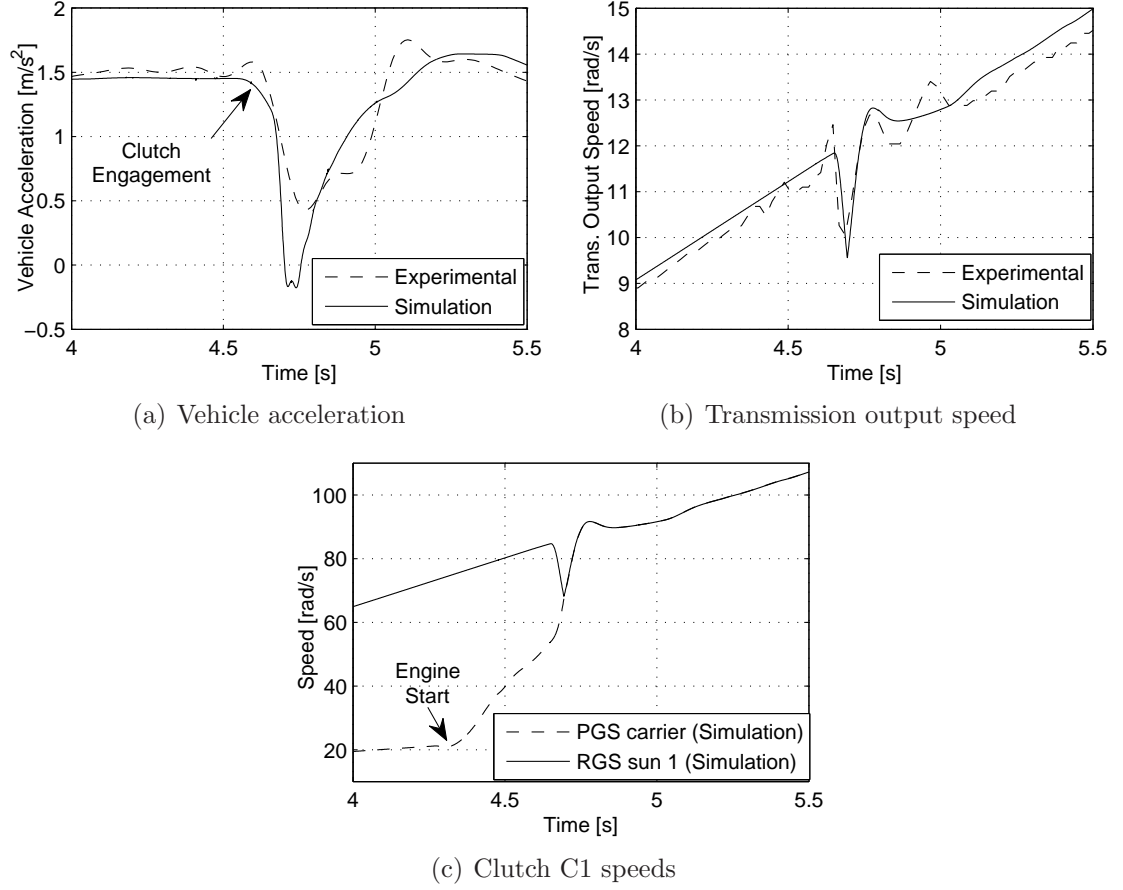


Figure 4.18: Details of the hybrid operation validation test highlighting the driveline disturbance that occurs after the engine start.

It is also worthwhile to note the transmission input speed behavior shown in Figure 4.16 during the electric only mode of the hybrid validation test. One would expect the transmission input shaft to be stationary during this phase. However, the spinning output shaft slowly drags the input side due to the effect of clutch drag. This phenomenon is modeled by introducing a small offset to the transmission oil pressure while the engine is shut-off. It is important to note that only slight changes in the transmission offset pressure would result in different transmission input speed profiles in the electric only mode. Due to the uncertainty of clutch drag, this effect is difficult to represent with a high accuracy.

The details of the engine start event are shown in Figure 4.18. The BSA starts to crank the engine approximately at  $t = 4.3$  s. At this time, the engine side torque disturbances are not transferred to the wheels, since the transmission oil pressure ( $p_{tr}$ ) is low (the torque converter and the transmission are not fully functional). Following the first fuel injection, the transmission oil pressure (also referred to as the line pressure) quickly rises to its nominal value, since the actuation mechanism activates after the engine start.<sup>4</sup> As a result, a severe torque hole occurs at  $t = 4.7$  s as shown in Figure 4.18(a). The torque disturbance may appear as a torque rise or a torque hole depending on the sign of the slip speed of the engaging clutch. The angular velocities of the input and output sides of the engaging clutch are shown in Figure 4.18(c). Only the simulation results are given here, since no speed feedback is available from the gears inside the transmission. In this case, a noticeable jerk is felt inside the cabin because of the uncontrolled engagement of the on-coming clutch.

Figure 4.18(a) indicates that the magnitude of the simulated jerk is slightly larger than the experimental result. Figure 4.18(b) confirms this observation since the simulated transmission output speed also drops more than the measured speed at  $t = 4.7$  s. However, the difference between the simulated and the actual speeds does not correlate well with the difference between the two acceleration profiles. This inconsistency is partly attributed to the effect of signal processing. The vehicle acceleration signal contains a significant amount of mid-frequency measurement noise. Therefore, the vehicle acceleration is low-pass filtered during data acquisition. As a result, some of the abrupt variations in the vehicle acceleration, such as the one shown here, are partially rejected by the low-pass filter.

Another discrepancy between the experimental data and the simulation result is observed immediately after the clutch engagement (between  $t = 4.8$  s and 5 s). The transient response of the simulated transmission output speed is highly damped as shown in Figure 4.18(b). This artificial damping is due to the use of the hyperbolic tangent function to represent the clutch torque around zero slip speed.

<sup>4</sup>The transmission line pressure is controlled by an engine driven gear pump.

### 4.3 Summary

This chapter demonstrates the experimental validation of the longitudinal HEV dynamic model developed in Chapter 3. The vehicle model is simulated under a variety of operating conditions using torque commands obtained from actual driving tests. The simulations are conducted in an open loop fashion to obtain realistic model predictions, i.e., the driver model is not used in the simulator feedback loop. The tests are performed under controlled environmental conditions.

The experiments are presented in the following order. First, the subsystem models are verified with simple experiments. Next, the front and rear driveline models are individually validated. Finally, the overall HEV model is tested in a driving scenario that includes a transition from electric only to hybrid modes. This approach simplifies the calibration of the overall vehicle model and it ensures proper operation of individual component models.

The primary goal of these experiments is to capture the qualitative dynamic behavior of the HEV driveline during low-frequency transients that result from events such as engine start, gear shifts, and pedal tip-in/tip-out. Comparisons of the simulation results and the experimental data confirm that the model accurately represents the actual vehicle behavior during transients. If required, better model accuracy can be achieved in the expense of increased model complexity. However, the results presented in this chapter are satisfactory for a control-oriented HEV model.



## CHAPTER 5

### CONTROL STRATEGY DEVELOPMENT

This chapter describes the development of a hybrid-electric vehicle control strategy for the purpose of achieving good fuel economy, satisfactory drivability and high performance. Although the described strategies are generic in nature, some of the implementation aspects are unique to the experimental vehicle in consideration. The control strategies are initially developed and tested using the dynamic vehicle simulator described in Chapter 3. They are then experimentally verified on the test vehicle. Details of the experimental verification are discussed in Chapter 7.

This chapter begins with a description of the control hardware and software. This description is followed by a detailed discussion of the control algorithms implemented onboard the vehicle. Some of the practical challenges experienced through the development stages are also highlighted.

#### 5.1 Control Systems Architecture

The control systems architecture of a hybrid-electric vehicle is fairly involved. The already complex architecture of a conventional vehicle's control system is further expanded with control units that provide the electrical powertrain with complete functionality and safety. This section briefly describes the hardware and software architectures of the experimental vehicle's control system.

### 5.1.1 Hardware Architecture

A common approach for the development of automotive control systems is to use dedicated electronic control units to manage the operations of different vehicle subsystems. A similar approach is followed in the test vehicle which results in the control software of the newly introduced subsystems to be implemented on individual control units. This approach provides two important benefits. First, the software associated with a particular subsystem can be developed and tuned independent of the remaining vehicle subsystems. Another benefit is that this type of control architecture design enables a flexible hardware configuration. For example, if the high-voltage battery pack were to be replaced with a more advanced unit, then the transition to the new system would be virtually seamless since the battery's low-level controls are implemented on a separate control unit.

A schematic that shows the interactions between the experimental vehicle's control units and the associated subsystems is given in Figure 5.1. The controllers that are introduced as a result of powertrain hybridization are interfaced with the existing control units via controller area networks (CANs). Controller area networks utilize a high-speed serial communication protocol [112] that enables reliable data transfer with high immunity to electrical noise.

As indicated in Figure 5.1, the gray highlighted blocks represent the electronic control units that are implemented by the Ohio State Challenge-X team. The vehicle control unit is a dSPACE MicroAutoBox 1401 rapid prototyping controller that uses an IBM PowerPC750 (32/64-bit architecture) microprocessor. The MicroAutoBox unit provides real-time signal monitoring and online parameter calibration capabilities via dSPACE ControlDesk software. The battery management system is implemented on a PHYTEC phyCORE development board that uses a Freescale MPC555 (32 bit) microprocessor. This control unit has limited processing capabilities compared to the vehicle's control unit and does not provide real-time memory access without third-party software support. However, the PHYTEC control unit proved to be sufficient for this particular application. Finally, the exhaust controls are implemented on

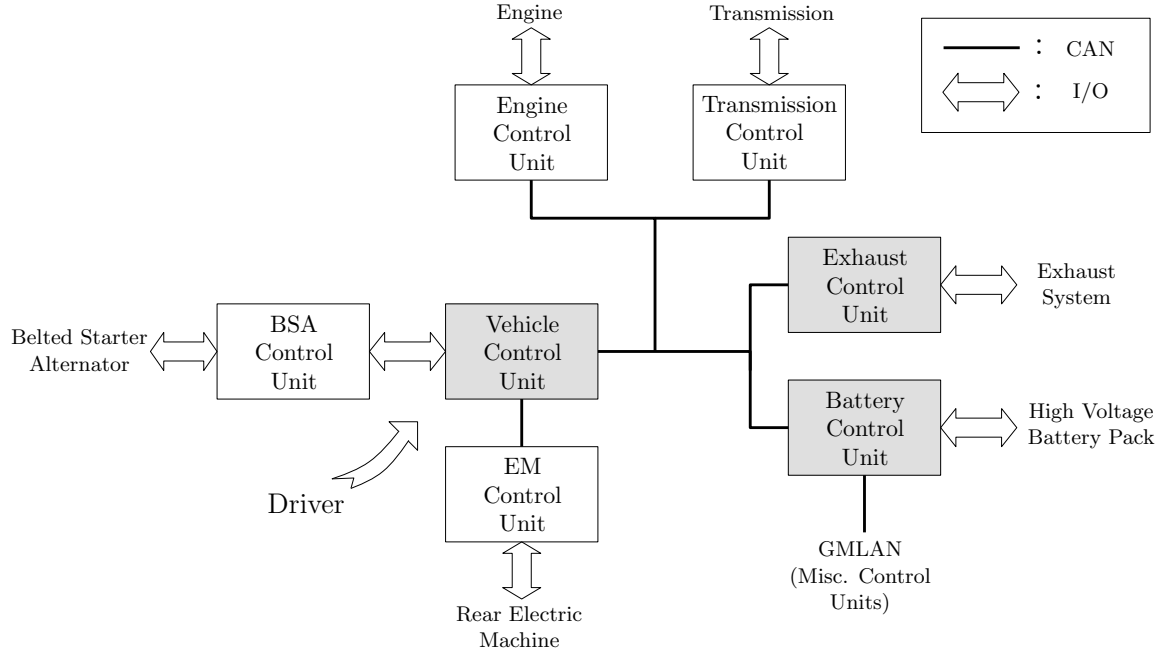


Figure 5.1: The test vehicle's control hardware architecture. The gray-highlighted blocks represent the prototype control units that are implemented by the team while others are production control units.

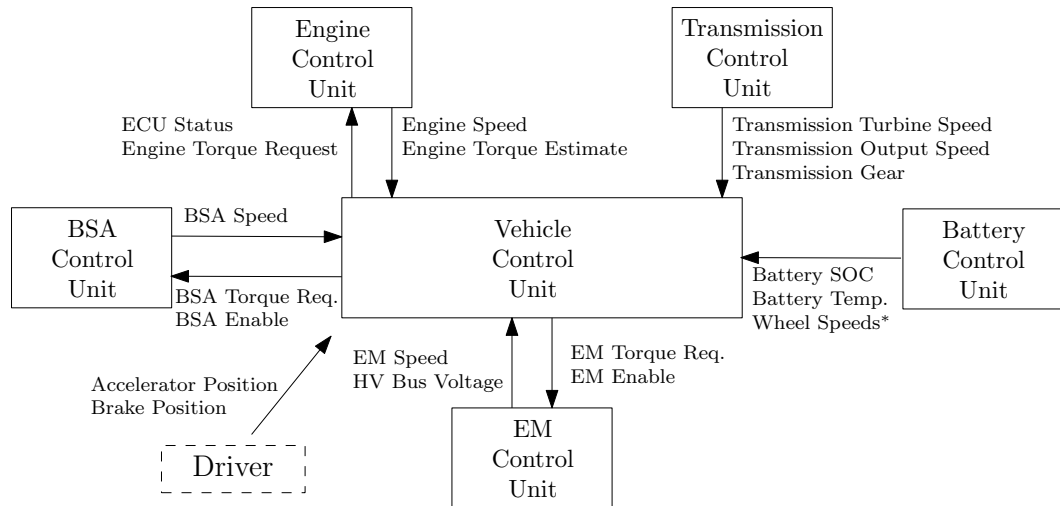


Figure 5.2: Some of the important control signals and their communication with the vehicle control unit. Note that the wheel speeds are originally transmitted by the ABS control unit and that the battery control unit acts as a gateway for communication.

a MotoTron Motohawk 80-pin ECU that is also supported by a Freescale MPC555 microprocessor. Similar to the vehicle control unit, the MotoTron system also provides real-time signal monitoring and parameter calibration capabilities via the MotoTune software.

Due to the networked nature of the control system, several feedback signals need to be transmitted from other control units to the vehicle control unit. An important subset of the control signals that are relevant to the vehicle’s high-level system operation are shown in Figure 5.2. A more thorough list of the vehicle control unit signals and their time resolutions and transmitting sources are given in Appendix A.

The vehicle’s control systems architecture has been developed in collaboration with former members of the Ohio State Challenge-X team. The primary focus of this dissertation is on the development of algorithms that manage the high-level functions of the vehicle. These algorithms are implemented on the primary vehicle control unit (see Figure 5.1).

### **5.1.2 Control Software Architecture**

The vehicle’s control system is developed in the MATLAB/Simulink environment. The standard real-time compatible Simulink blocks and embedded MATLAB code are combined into a “control model”. The control unit’s input/output and CAN communication functions are handled by a set of Simulink blocks linked to the dSPACE real-time interface (RTI). The resulting model is uploaded to the target controller via automatic code generation. Automatic code generation involves a two-step build process. First, MATLAB Real-Time Workshop converts the original control model into an equivalent C program. Then, the Microtec PowerPC compiler<sup>1</sup> converts the C program into the final Assembler code that is interpreted by the PowerPC750 microprocessor.

This implementation scheme is suitable for rapid prototyping applications such as the one described here. Also, it almost completely eliminates the need for “hand

<sup>1</sup>Different target compilers are used for battery and exhaust control units.

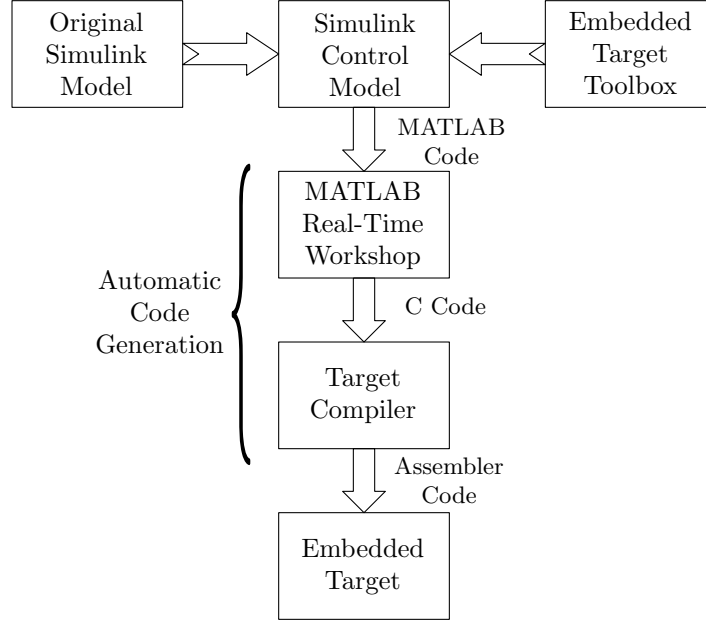


Figure 5.3: Control software development process. The embedded target toolbox and the target compiler differ based on the specific choice of the microcontroller.

coding” of the control algorithms. A schematic representation of this software development process is also given in Figure 5.3.

The HEV control strategy is implemented as a multi-rate algorithm. The update rate of a particular subset of the algorithm is selected according to the computational burden of the code segment and the dynamic variations of the relevant control variables. For instance, while operations such as driveline and engine start-stop controls require a high computational bandwidth, other operations such as temperature management can be performed at relatively lower bandwidths. As a result, the following update rates are selected for the control strategy: 0.001 s, 0.01 s, 0.1 s and 1 s.

The computational operations associated with the control strategy are handled in multiple timer tasking mode. For multi-rate systems, this mode has a significant advantage over the single timer tasking mode in that if a high priority operation interrupts a low priority operation, the low priority operation is put on hold until the

high priority operation is completed. Therefore, potential task overrun situations are nearly eliminated.

## 5.2 HEV Control Strategy

The control objectives in a hybrid-electric vehicle include but are not limited to fuel consumption minimization, emissions reduction, drivability management, state-of-health monitoring of vehicle subsystems (e.g. high voltage battery pack) and passenger and component safety assurance. The complex and often conflicting nature of these control objectives strongly necessitate the use of an elaborate control strategy that carefully utilizes the onboard energy storage systems and actuators. A practical control scheme typically incorporates multiple controllers that are designed to achieve different objectives supervised by a high level algorithm. This high level (or supervisory) controller is usually comprised of event-based or time-based conditions that coordinate component level operations.

The overall control structure of a hybrid-electric vehicle is illustrated in Figure 5.4. The data acquired from various vehicle subsystems are processed in real-time and transmitted to different layers of the control system that require this information to generate various control commands. Furthermore, the vehicle data is often used by a fault diagnostics system that supports the safety features of the vehicle. The safety tasks have a higher priority than regular control functions. Therefore, if a safety critical situation occurs then the supervisory controller interrupts normal operation and switches to a fault-tolerant operating mode.

Under normal operating conditions, the supervisory controller makes high-level decisions based on predetermined logic statements. These decisions affect the general state of the powertrain (e.g. engine on/off) and the operating mode of the vehicle (e.g. engine start, hybrid, traction control). The selected operating mode then activates a controller from a family of controllers that determines an appropriate power distribution to the actuators. This is referred to as the component level controls in Figure 5.4. The torque requests resulting from the power distribution are then sent

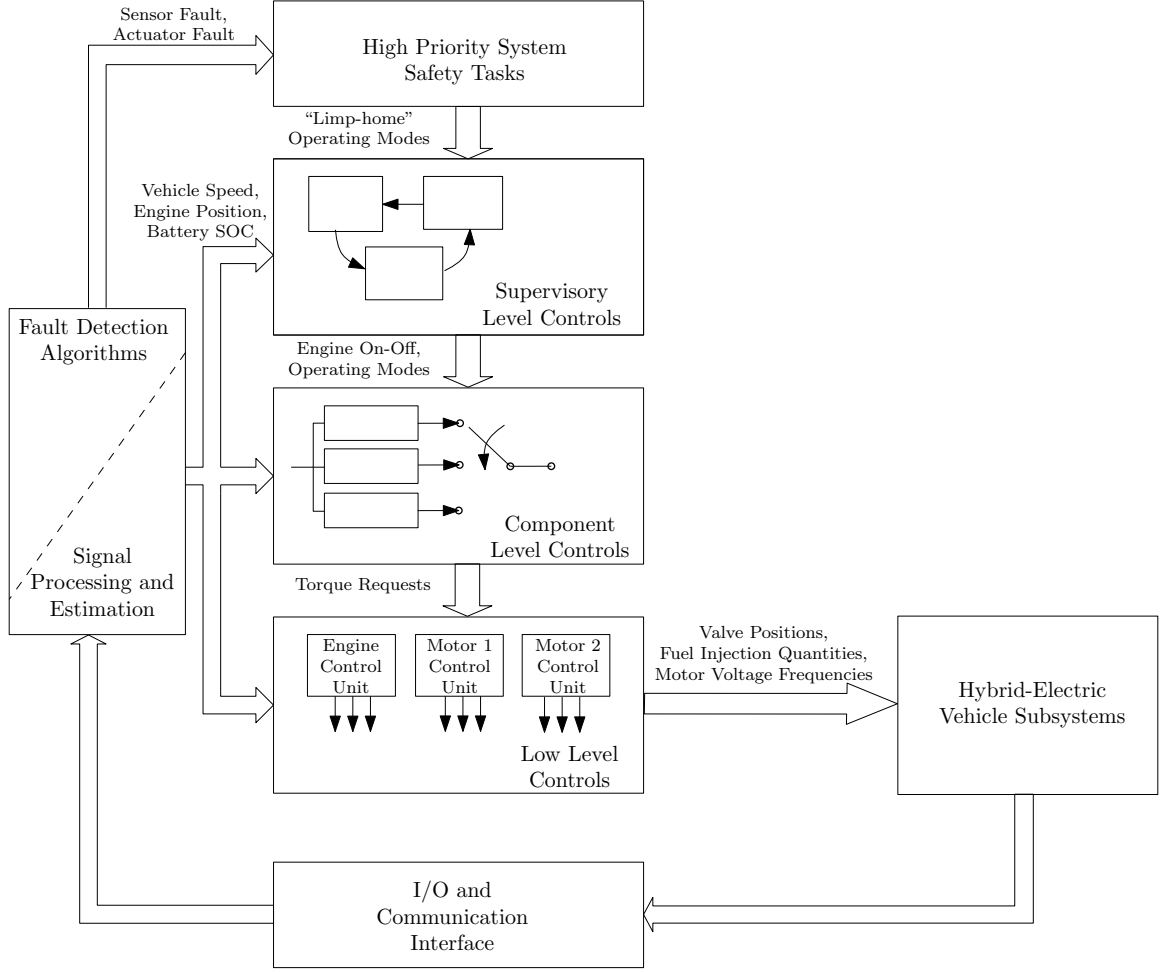


Figure 5.4: Hierarchical control systems architecture in a hybrid-electric vehicle.

to the corresponding control units (e.g. engine control unit, motor control unit) to facilitate low-level control functions. In this level, the torque requests are converted into a number of low-level actuator commands such as the fuel injection quantity and timing, the motor inverter pulse-width modulation frequency and so forth.

Among the control functions described above, this dissertation focuses on the supervisory level and component level control functions shown in Figure 5.4. The algorithms that handle the operation of these layers are discussed in the following sections.

### 5.2.1 Supervisory Level Controls

The primary functions of the vehicle’s supervisory controller are:

- Scheduling engine start-stop: Several conditions affect scheduling of the engine start-stop events to fulfill performance, fuel economy, drivability and emissions requirements. Although some of these conditions may be determined using model-based techniques, others are inevitably imposed on the control system in a rule-based fashion and are tuned to achieve desired performance metrics.
- Enabling drivability and stability specific functions: Certain vehicle functions such as traction control and driveline control require individual controllers to be activated as necessary. The supervisory controller handles these functions based on predefined transition conditions.
- Enabling driver requested control functions: If the driver manually interrupts normal operation, the supervisory controller engages the vehicle into the desired mode of operation. Cruise control is an example of such driver requested mode change.
- Ensuring safe vehicle operation: The supervisory controller reconfigures the control system if a critical powertrain fault is detected.

A finite state machine representation of the experimental vehicle’s operating modes is given in Figure 5.5. Note that the operating modes that are related to the safety features of the vehicle (such as the engine only mode) are not shown in this figure. Also, since the operations of mode 7 (traction control) and mode 8 (cruise control) are not relevant to this research, these modes are not described here.

The electric only mode is activated after the completion of the vehicle start-up sequence. Therefore, this mode has an “unconditional branch” as shown in Figure 5.5. Also, the hybrid and regenerative braking modes share a “parent” state that branches out to cruise control and traction control modes if the corresponding transition conditions are satisfied. If the controller exits one of the two modes, it defaults back to the hybrid mode.



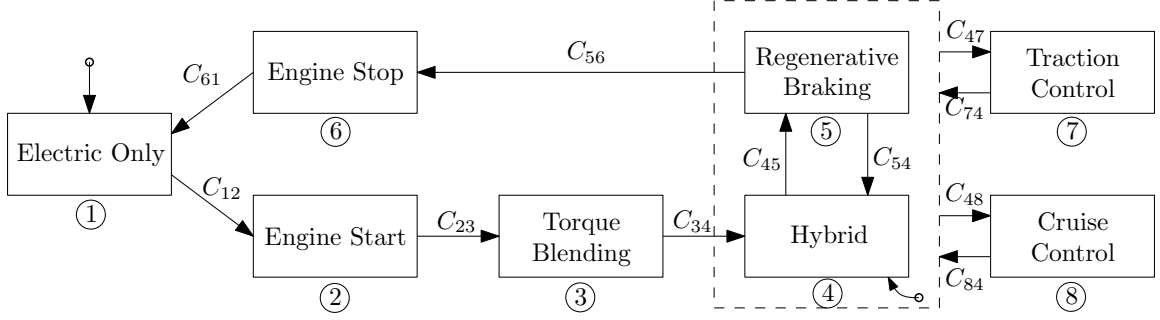


Figure 5.5: A state machine representation of the vehicle supervisory controller.

Transition Condition	Control Objectives
$C_{12} = (S_{batt} < S_{batt,min}) \vee (\omega_{tr}\zeta_{tr,1} - \omega_t < \omega_{tr,th}) \vee (P_{dr,req}^+ > P_{batt,max})$	SOC management, drivability, performance
$C_{23} = (\omega_{ice} > \omega_{ice,th,1})$	Drivability
$C_{34} = (t_{mode} > t_{mode,th,1})$	Drivability
$C_{45} = (\beta_{dr} > 0) \wedge (\alpha_{dr} = 0) \wedge (v_{veh} > v_{veh,th,1})$	SOC management, fuel economy
$C_{54} = (\alpha_{dr} > 0) \vee ((\beta_{dr} > 0) \wedge (v_{veh} \leq v_{veh,th,1})) \vee ((\beta_{dr} = 0) \wedge (S_{batt} < S_{batt,min}))$	SOC management, fuel economy
$C_{56} = (\omega_{ice} < \omega_{ice,th,2}) \wedge (S_{batt} > S_{batt,max}) \wedge ((\omega_{tr}\zeta_{tr,1} - \omega_t > \omega_{tr,th}) \vee (v_{veh} \leq v_{veh,th,2})) \wedge (T_{ice,cool} > T_{ice,cool,th})$	SOC management, fuel economy, drivability, emissions
$C_{61} = (\omega_{ice} < \omega_{ice,th,3})$	Drivability
$C_{47} =  (\omega_{wh,f}) - (\omega_{wh,r})  > \omega_{wh,th,1}$	Vehicle stability
$C_{74} =  (\omega_{wh,f}) - (\omega_{wh,r})  < \omega_{wh,th,2}$	Vehicle stability
$C_{48} = \neg C_{84} = \text{Cruise Enable}$	Driver request

Table 5.1: Some of the important transition conditions used in the supervisory controller.

The logic statements ( $C_{ij}$ ) that govern the transitions between the vehicle operating modes are listed in Table 5.1. Here,  $P_{dr,req}^+$  represents the driver's positive power request,  $P_{batt,max}$  is the maximum available battery power,  $S_{batt,min}$  and  $S_{batt,max}$  are the battery SOC lower and upper limits,  $\zeta_{tr,1}$  is the overall transmission speed reduction ratio in gear 1,  $t_{mode}$  is the time elapsed after the activation of an operating mode (reset at each instance of activation),  $\alpha_{dr}$  is the accelerator pedal position,  $\beta_{dr}$  is the brake pedal position,  $T_{ice,cool}$  is the engine coolant temperature,  $\omega_{wh,f}$  is the average speed of the front wheels, and  $\omega_{wh,r}$  is the average speed of the rear wheels. Also, the subscript “*th*” is used to represent various threshold values in Table 5.1. The remaining variables were previously defined in Chapter 3.

Although the use of an event-driven supervisory controller is required for proper vehicle operation, the transition conditions, if not carefully chosen, may cause issues for actual implementation. Some of the potential issues are illustrated in Figure 5.6 by simple examples. Figure 5.6(a) shows a case where both logic statements originating from mode 1 are satisfied simultaneously, thus resulting in a transition conflict. Figure 5.6(b) shows another case where two non-conflicting statements may cause chattering between modes 1 and 2 if the controller that is active in mode 1 acts to increase  $\omega_{ice}$  while the controller that is active in mode 2 acts in an opposite manner. Figure 5.6(c) demonstrates another situation in which the vehicle may cycle between operating modes 1, 2 and 3 if all three statements are simultaneously satisfied. It is particularly challenging to avoid these types of issues in large scaled state machines where transitions are usually governed by compounded logic statements.

The supervisory controller is implemented in the MATLAB/Stateflow environment. Stateflow provides diagnostics features to help detect issues such as transition conflicts and cyclic behavior. In this work, the supervisory controller is tested in the loop with the vehicle simulator over an extensive number of driving cycles. Combining the use of Stateflow's diagnostics features with the analysis of driving cycle simulations helped eliminate the issues described above.

In particular, the mode chattering problems are handled by introducing proper hysteresis bands between transition conditions. Potential cyclic behavior is avoided

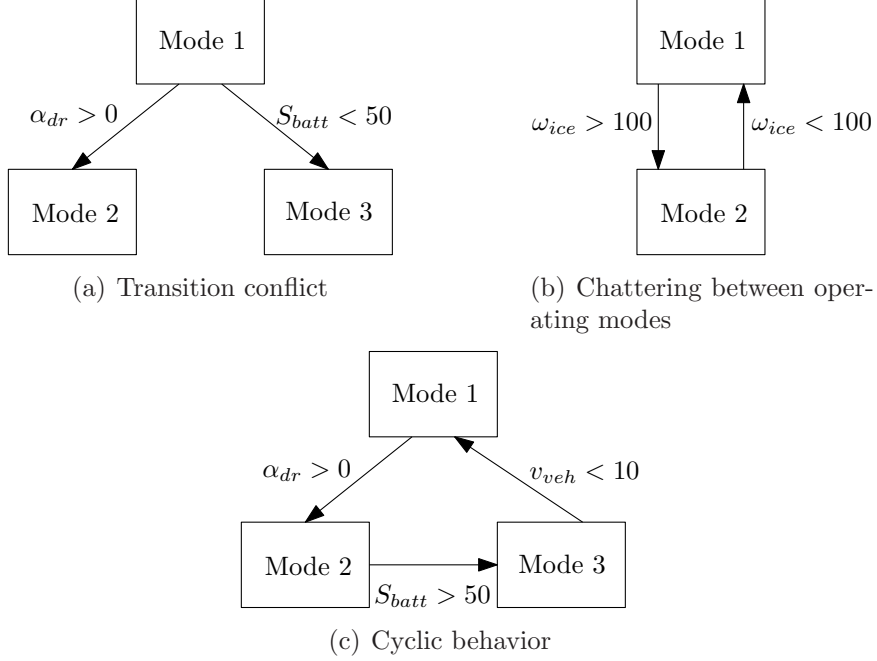


Figure 5.6: Potential issues with the implementation of control algorithms using finite state machines.

by using contradictory logic statements at the appropriate transitions. If the situation in Figure 5.6(c) is taken as an example, then a potential logic loop can be broken by augmenting the transition condition from mode 1 to mode 2 with an additional expression that involves  $v_{veh}$ :

$$C'_{12} = (\alpha_{dr} > 0) \wedge (v_{veh} > 15) \quad (5.1)$$

Here,  $C'_{12}$  represents the new transition condition from mode 1 to 2. Transition conflicts are either manually eliminated or the execution orders of the conflicting expressions are controlled by prioritizing a particular transition over others in a given operating mode.

Another method to verify that the supervisory controller is free of the types of issues discussed above is to employ a formal model checking software package. Several model checking packages such as the Symbolic Model Verifier [113] are available in the public domain. These software packages utilize sophisticated search algorithms

to debug algorithmic issues that may result in the tested software failing to meet the design requirements. However, considering the modest size of the discrete state space that is used in the design of the supervisory controller, utilizing formal software verification methods was not found to be feasible in this work.

### 5.2.2 Component Level Controls

Once the vehicle operating mode and the engine state are determined by the supervisory controller, the torque split is computed by one of a family of controllers in order to meet the objectives of that particular operating mode. In this work, this layer of control is referred to as the component level controls as previously indicated in Figure 5.4.

The primary goal is to meet the driver’s demand for acceleration and deceleration while satisfying important objectives related to fuel economy and drivability. Specifically, the driver’s accelerator and brake pedal inputs ( $\alpha_{dr}$ ,  $\beta_{dr}$ ) are combined in the control strategy with other powertrain feedback variables (such as  $\omega_{ice}$ ,  $S_{batt}$ ,  $\omega_{em}$ ) and the resulting actuator torque requests are computed ( $T_{ice,req}$ ,  $T_{em,req}$ ,  $T_{bsa,req}$ ).

Among these controllers, the operations of the electric only mode, the engine start-stop modes<sup>2</sup>, the hybrid mode and the regenerative braking mode are described in this section. The torque blending mode, which focuses on achieving drivability improvements after engine start, is a topic of the next chapter.

### Interpreting the Driver’s Power Demand

One of the critical aspects of hybrid powertrain control, particularly from a performance and drivability standpoint, is the method by which the control strategy interprets the driver’s demand for acceleration and deceleration. In the acceleration case, this relationship corresponds to a mapping between the accelerator pedal position and the torque delivered to the powertrain, or more accurately, to the wheels. A

<sup>2</sup>The engine start-stop modes are briefly mentioned here since these controllers are not an outcome of this dissertation.

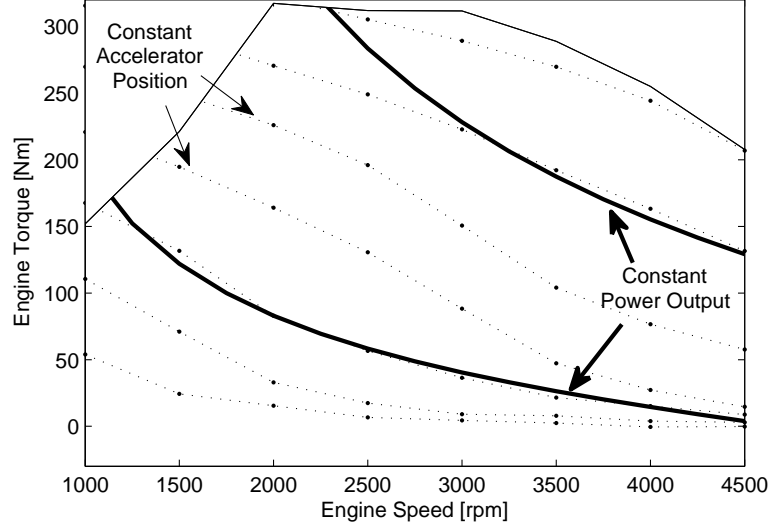


Figure 5.7: A typical accelerator pedal vs torque map for a diesel engine.

successful mapping of these parameters provides the driver with a “consistent pedal feel” for all driving conditions, hence satisfying a key drivability requirement.

In a modern conventional vehicle powered by a diesel engine, an accelerator-engine torque map is realized by calibrating the fuel injection quantity over the entire engine speed-torque range. A similar approach is used for gasoline engines equipped with electronic throttle control systems via throttle-torque maps. However, in conventional gasoline engines, the driver directly controls the throttle opening, thus the throttle-torque relationship is constrained by the physical configuration of the system.

A typical accelerator-engine torque map for a diesel engine is shown in Figure 5.7. The generic shape of this map is usually chosen to realize a driving feeling comparable to that achieved by conventional gasoline engines [34]. Figure 5.7 also reveals the fact that, at low pedal positions, a constant pedal position approximately corresponds to a constant power demand<sup>3</sup>. However, this trend is not observed at high pedal positions mainly due to the limits on the engine torque. Note that a similar conclusion was also drawn by Kim *et al.* in [61]. In fact, Kim *et al.* also emphasized the importance

<sup>3</sup>The constant power lines in Figure 5.7 are adjusted using the engine friction.

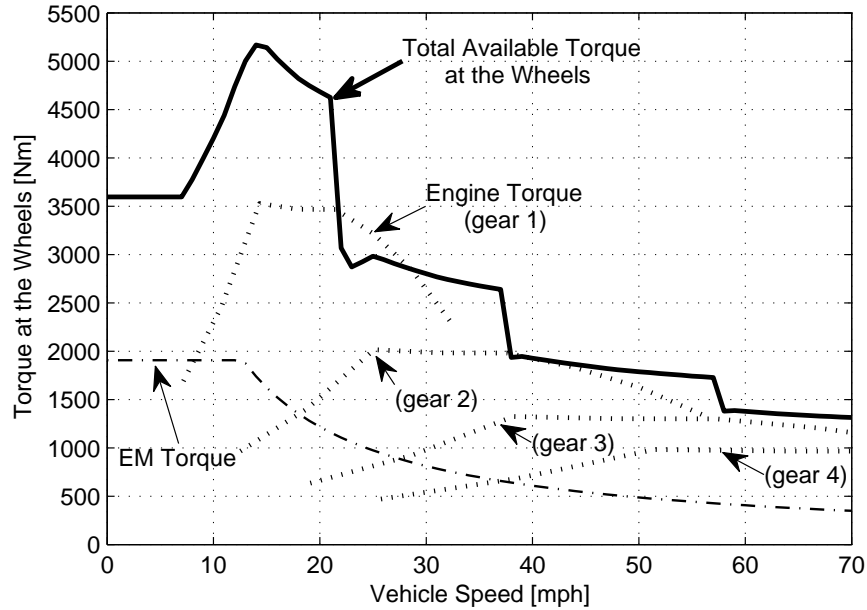


Figure 5.8: Maximum torque characteristics of an HEV. It is assumed that the transmission upshifts when the engine speed reaches 3000 rpm and that the engine is on during vehicle launch.

of modifying the accelerator map according to the transmission gear ratio in order to maintain a nearly steady power output at the wheels (for a constant accelerator pedal input) during gear shifts.

It is clear that a hybrid-electric vehicle is also expected to have a similar accelerator pedal to output power correlation. However, the situation is more complicated in the case of an HEV since there are additional actuators that contribute to the overall tractive force of the vehicle. Also, the power generated by these actuators may be coming through paths different than the power flow path of the engine, as is the case in the test vehicle. A power demand correlation that provides a consistent pedal feel regardless of the driving conditions and the state of the powertrain (engine on/off) is necessary.

In order to determine a meaningful correlation, it is important to first understand the overall torque and power characteristics of an HEV. Figure 5.8 and Figure 5.9

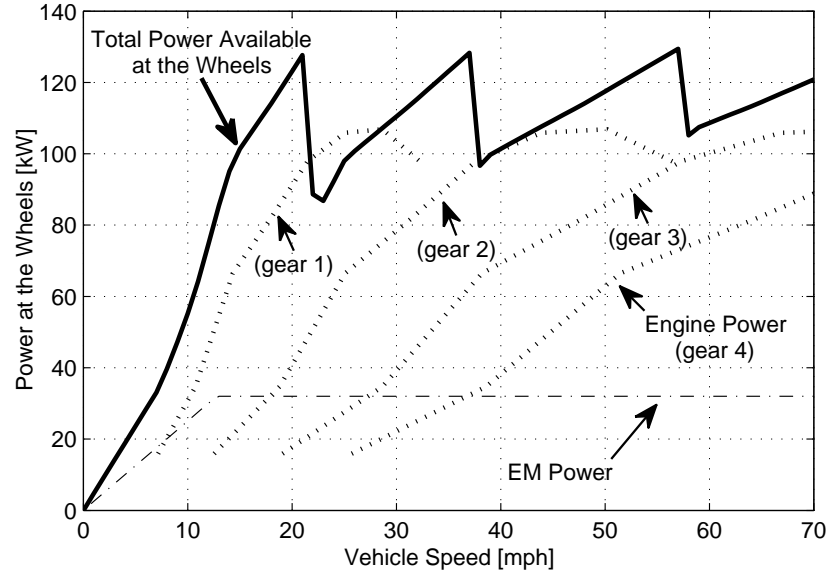


Figure 5.9: Maximum power characteristics of an HEV. The available power is calculated assuming 100% drivetrain efficiency.

illustrate the approximate torque and power available in a through-the-road parallel HEV as a function of the vehicle speed<sup>4</sup>. The bold lines represent the total power and the total torque available from the hybrid powertrain, whereas the dotted and dashed lines represent the individual contributions of the engine and the electric machine. A few points are worthwhile to note in these plots. Figure 5.8 shows that the hybrid powertrain has a large low-end torque (at low vehicle speeds) compared to a similar conventional vehicle. This torque “reserve” should be properly utilized for aggressive accelerations, however, it should also be well-balanced during normal driving conditions such that the driver does not experience abrupt torque variations as the vehicle speed changes. Secondly, the power demand expression should be robust to changes in the engine state. Clearly, removing the engine from the overall available torque expression would cause the low end torque to drop significantly (assuming that

<sup>4</sup>The plots illustrate a case relevant to the test vehicle where all the available battery power is provided to the rear electric machine. Note that this example can be easily extended to include the BSA by appropriately modifying the maximum torque characteristics of the engine.

the engine is stopped only at low vehicle speeds). Also, Figure 5.9 demonstrates that the total available power at the wheels approaches zero at low vehicle speeds, which is not the case for the available torque. Therefore, computing a torque split based solely on the available power may cause issues at low vehicle speeds. Note that this is not an issue for conventional vehicles since the engine output power is always non zero at engine speeds above the idle speed.

In this work, the following expression is used to represent the driver's positive power demand at the wheels:

$$P_{dr,req}^+ = f_{P,1}(\alpha_{dr})(\min(P_{batt,max}, \omega_{em}T_{em,max})\bar{\eta}_r + f_{P,2}(\omega_{ice})\max(\omega_{ice}, \omega_{ice,idle})T_{ice,max}(\max(\omega_{ice}, \omega_{ice,idle}))\bar{\eta}_f) \quad (5.2)$$

where  $T_{em,max}$  is the peak EM torque at low speeds,  $T_{ice,max}(\omega_{ice})$  the maximum engine torque that changes as a function of the engine speed,  $\omega_{ice,idle}$  is the engine idle speed,  $P_{batt,max}$  is the maximum available battery power, and  $\bar{\eta}_r$  and  $\bar{\eta}_f$  are approximate average values for the rear and front driveline efficiencies. Although the front driveline efficiency can not be accurately represented by a constant value due to the presence of the torque converter, this assumption ensures the continuity of the power demand during vehicle launch. Otherwise, the maximum available power from the front driveline changes abruptly during the torque converter engagement, thus resulting in poor drivability.

Equation (5.2) incorporates two calibration functions;  $f_{P,1} : \mathbb{R}_+ \rightarrow [0, 1]$  and  $f_{P,2} : \mathbb{R}_+ \rightarrow \mathbb{R}_+$ .  $f_{P,1}$  is tuned to achieve the desired pedal feeling and  $f_{P,2}$  is tuned to ensure that the driver's total power demand is not affected negatively by changes in the engine speed.<sup>5</sup> Also, note that the driver's power demand is computed assuming that the engine is always powered ( $\omega_{ice} \geq \omega_{ice,idle}$ ). This eliminates potential discontinuities that may arise due to changes in the engine state.

<sup>5</sup>For example, if  $f_{P,2} = 1$  then the driver's power demand for a fixed accelerator position would drop significantly after a gear shift (see Figure 5.9).



The power demand expression given by (5.2) is used in all operating modes of the control strategy that receive positive power requests.<sup>6</sup> It is clear that inconsistencies between the pedal position and the resulting power demand, while operating in different modes, would cause significant drivability issues.

The benefits of formulating a power demand expression that achieves good drivability have not been sufficiently emphasized by previous works on HEV control. Although similar power/torque demand expressions have been used in [8, 30, 38] to accommodate different HEV architectures, the details of these formulations have not been discussed.

### HEV Operating Modes: Electric Only

The test vehicle uses the electric only drive capability in order to achieve improved fuel economy and reduced emissions by eliminating unnecessary engine idling and reducing the engine load during vehicle launch. Since the BSA is coupled with the engine, it is unavailable as an actuator when the engine is stopped. Therefore, the rear electric machine is used to provide the test vehicle with pure electric drive functionality.

Due to a number of drivability limitations imposed by the transmission, the electric only function is mostly utilized at low vehicle speeds. Also, the use of the electric only mode becomes infeasible at high vehicle speeds since the total road load usually exceeds the available high voltage battery power (limited by approximately 35 kW) even for cruising conditions.

In the electric only mode, the positive EM torque request is computed using the following relationship:

$$T_{em,req}^+ = \min \left( \frac{P_{dr,req}^+}{(\omega_{em,lp} + 0.1)\bar{\eta}_r} + T_{em,drv}, T_{em,max} \right) \quad (5.3)$$

where  $\omega_{em,lp}$  is the EM speed signal filtered by a 4th order Butterworth low-pass filter, and  $T_{em,drv}$  is a drivability related torque adjustment. The purpose of using

<sup>6</sup>Equation (5.2) can not be directly extended to the case of regenerative braking as discussed in the following sections.

$\omega_{em,lp}$  instead of  $\omega_{em}$  is to ensure that the torque request remains unaffected by the oscillations in motor speed that arise due to the driveline dynamics.

The test vehicle utilizes the regenerative braking functionality both when the engine is running and when it is stopped. The regenerative braking torque is provided by the rear electric machine. In order to provide a uniform braking feel during deceleration, a common mathematical expression is used to compute the negative EM torques in both electric only and regenerative braking modes. The details of this expression are described later in this chapter.

The absence of a torque damping element in the rear driveline results in drivability issues when large torque gradients occur. The adverse effects of gear backlash are further aggravated by the quick response characteristics of the rear electric machine. Therefore, if the EM torque request is not properly treated during pedal tip-in and tip-out, drivability issues such as shunt (flare in the vehicle acceleration) and shuffle (driveline oscillations) occur as discussed in Chapter 2.

One possible solution is to use a low-pass filter to “smooth” the torque request. However, experimental results show that this approach leads to a slight degradation of the pedal response time. In this work, an additive torque adjustment,  $T_{em,drv}$ , is used as a means for actively damping the driveline oscillations that result from pedal tip-in and tip-out. The torque adjustment is generated by a linear compensator that uses speed feedback from the rear driveline. The control design is based on the following simplified 3<sup>rd</sup> order linear driveline model:

$$\begin{aligned} \left( J_{em} + J_{gb} + \frac{1}{\zeta_{gb}^2} J_{rd} \right) \dot{\omega}_{em} &= T_{em,req} - b_{em,1} \omega_{em} - \frac{2}{\zeta_{gb} \zeta_{rd}} T_{hs,r} \\ \dot{\theta}_{hs,r} &= \frac{1}{\zeta_{gb} \zeta_{rd}} \omega_{em} - \omega_{wh,r} \\ \left( J_{wh} + \frac{1}{2} M_{veh} R_{wh}^2 \right) \dot{\omega}_{wh,r} &= T_{hs,r} - b_{wh,r,1} \omega_{wh,r} - T_{road}(\omega_{wh,r}) \end{aligned} \quad (5.4)$$

where

$$T_{hs,r} = k_{hs,r} \theta_{hs,r} + b_{hs,r} \left( \frac{1}{\zeta_{gb} \zeta_{rd}} \omega_{em} - \omega_{wh,r} \right). \quad (5.5)$$

Since the road load,  $T_{road}(\omega_{wh,r})$ , does not have an impact on the transient behavior of the system (it can be treated as a slowly varying disturbance), it is not included

in the state space representation of the model. The remaining variables in (5.4) were previously defined in Chapter 3. A state space representation of this model can be written as:

$$\dot{x}_r(t) = A_r x_r(t) + B_r u_r(t) \quad (5.6)$$

$$y_r(t) = C_r x_r(t) \quad (5.7)$$

$$A_r = \begin{bmatrix} -\frac{\frac{2b_{hs,r}}{\zeta_{gb}^2 \zeta_{rd}^2} + b_{em,1}}{J'_{em}} & -\frac{2k_{hs,r}}{J'_{em} \zeta_{gb} \zeta_{rd}} & \frac{2b_{hs,r}}{J'_{em} \zeta_{gb} \zeta_{rd}} \\ \frac{1}{\zeta_{gb} \zeta_{rd}} & 0 & -1 \\ \frac{b_{hs,r}}{J'_{wh} \zeta_{gb} \zeta_{rd}} & \frac{k_{hs,r}}{J'_{wh}} & -\frac{b_{hs,r} + b_{wh,r,1}}{J'_{wh}} \end{bmatrix}, \quad B_r = \begin{bmatrix} \frac{1}{J'_{em}} \\ 0 \\ 0 \end{bmatrix} \quad (5.8)$$

where

$$J'_{em} = J_{em} + J_{gb} + \frac{1}{\zeta_{gb}^2} J_{rd} \quad (5.9)$$

$$J'_{wh} = J_{wh} + \frac{1}{2} M_{veh} R_{wh}^2 \quad (5.10)$$

Here, the state vector is  $x_r(t) = [\omega_{em}(t) \quad \theta_{hs,r}(t) \quad \omega_{wh,r}(t)]^T$  and the scalar control variable is  $u_r(t) = T_{em,req}(t)$ .

As for the choice of  $y_r(t)$  (hence  $C_r$ ), two possibilities are considered. The first alternative is to use the speed difference between the EM and the rear wheels as an output. However, this choice imposes the following practical drawbacks: (i) the wheel speed sensor does not provide data for speeds lower than 20 rpm,<sup>7</sup> (ii) even at higher wheel speeds, this speed difference exhibits considerable fluctuations from zero (even during cruising) due to the rear differential dynamics. However, for simulation studies, the speed difference can be used as the plant output, resulting in  $C_r = C_{hs} = [1 \quad 0 \quad -\zeta_{gb} \zeta_{rd}]$ .

Another alternative is to use the EM speed as the measured output. In fact, an experimental result shown in Figure 5.10 confirms that the EM speed has a good transient correlation with the vehicle longitudinal acceleration in the case of a severe disturbance caused by the rear electric machine. Therefore, the EM speed is used as

<sup>7</sup>Most of the severe pedal tip-in disturbances occur during vehicle take-off where  $\omega_{wh,r}(t_0) = 0$ .

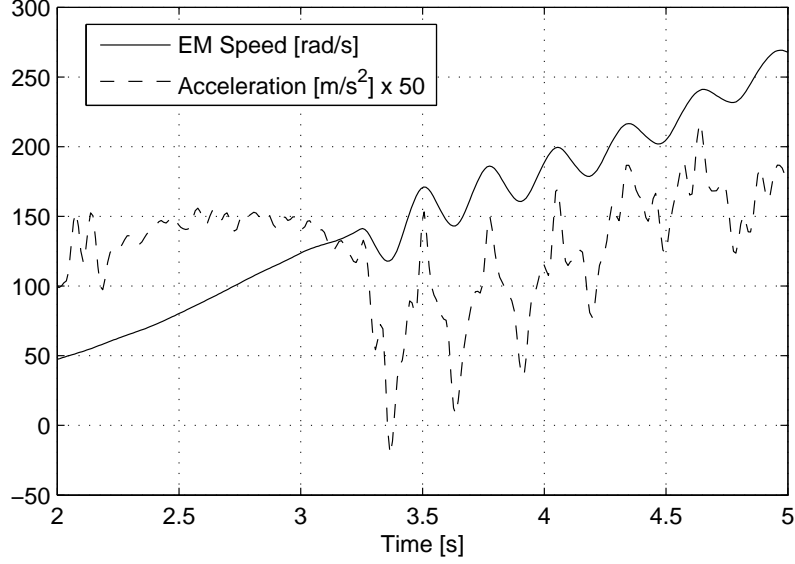


Figure 5.10: A severe EM torque disturbance (experimental) causes oscillations in the rear driveline. The EM speed is a good indicator of rear driveline disturbances.

the output for the experimental validation of this approach, resulting in  $C_r = C_{em} = [1 \ 0 \ 0]$ .

A block diagram representation of the control scheme is given in Figure 5.11. Here, the plant transfer function is represented by  $G_r(s)$  where

$$G_r(s) = C_r(sI - A_r)^{-1}B_r \quad (5.11)$$

Depending on the choice of the plant output,  $C_r$  is taken as  $C_{em}$  or  $C_{hs}$ .  $H_r(s)$  maps the actual (measured) output,  $y(t)$ , to the performance output,  $z(t)$ . If  $C_{hs}$  is used as the output matrix,  $H_r(s) = H_{hs}(s) = 1$ . However, if the EM speed is used as an output (i.e.,  $C_r = C_{em}$ ), then the performance output can be generated by applying a high-pass filter on the EM speed measurement:

$$H_r(s) = H_{em}(s) = \frac{s^2}{s^2 + 2w_{hp}s + w_{hp}^2} \quad (5.12)$$

The Bode magnitude and phase plots of the high pass filter are shown in Figure 5.12. The cutoff frequency of the filter is chosen such that the magnitude attenuation is

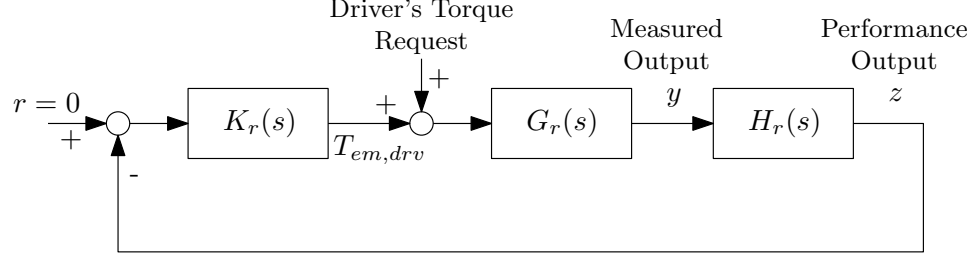


Figure 5.11: The plant-control interactions for the rear driveline active damping problem.

sufficiently high at frequencies lower than the target frequency band and that only a slight phase shift is introduced within the target frequency band. The main objective of the controller,  $K_r(s)$ , is to increase the damping ratio of the system (around the fundamental natural frequency) described by the transfer function from  $T_{em,req}$  to  $z$ . This is denoted here as the following open-loop transfer function:

$$G_{ol}(s) = G_r(s)H_r(s) \quad (5.13)$$

Given  $r = 0$  (zero speed reference), the closed loop transfer function from the driver's torque request to the performance output is the following:

$$G_d(s) = \frac{G_r(s)H_r(s)}{1 + G_r(s)H_r(s)K_r(s)} \quad (5.14)$$

A careful examination of  $G_d(s)$  suggests that the block diagram of Figure 5.11 is equivalent to the cascade connection of the open-loop transfer function and the compensator,  $K_{ol}(s)$ , as shown in Figure 5.13. Therefore, choosing  $K_r(s)$  to provide the system with active damping is equivalent to designing a filter,  $K_{ol}(s)$ , to reject the input frequencies around the natural frequency of  $G_{ol}(s)$ .<sup>8</sup> It is clear that simply choosing  $K_r(s) = K$  suffices to achieve this goal. This result is demonstrated in Figure 5.14. The Bode magnitude plots of  $G_{ol}(s)$  (using  $G_r(s) = G_{hs}(s)$  and  $H_r(s) = 1$ ),  $K_{ol}(s)$ , and  $G_d(s)$  are superposed for a particular choice of the feedback gain

<sup>8</sup>Note that a similar result is obtained by choosing  $G_r(s) = G_{em}(s)$  and  $H_r(s) = H_{em}(s)$ .

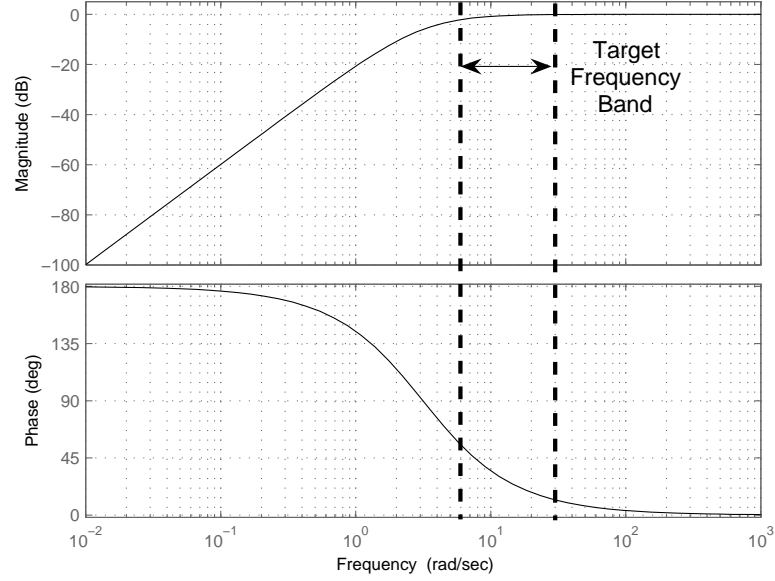


Figure 5.12: The Bode magnitude-phase plot of  $H_{em}(s)$ . The targeted driveline oscillations lie in the 1-5 Hz frequency band.

( $K = 5$ ). Note that the peak magnitude of  $G_{ol}(s)$  around the natural frequency is significantly reduced when the band-reject filter is introduced by a proper choice of  $K$ . Increasing the feedback gain increases the attenuation at the natural frequency while also distorting the response at lower frequencies.

The active damping control scheme is implemented on the nonlinear dynamic HEV simulator described in Chapter 3 using the half-shaft speed difference as a measurement. The HEV simulator incorporates additional dynamics such as gear backlash and detailed tire behavior that are not captured by the control model given in (5.4).

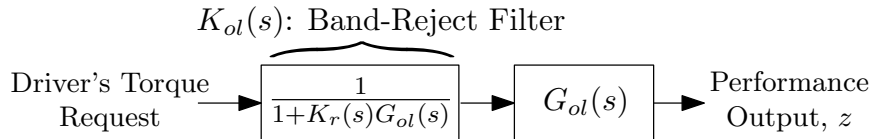


Figure 5.13: The open-loop equivalent of the control scheme shown in Figure 5.11.

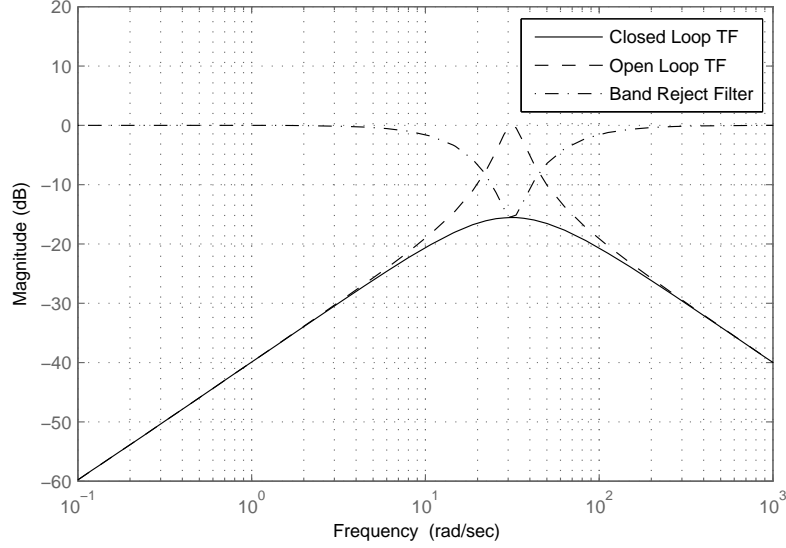


Figure 5.14: The Bode magnitude plots of  $G_d(s)$ ,  $G_{ol}(s)$ , and  $K_{ol}(s)$ .

A comparison of the EM speed and the vehicle acceleration with and without active driveline damping is given in Figure 5.15. The driver's torque request is modeled as a step change of 50 Nm in magnitude that engages at  $t = 0$  s and then disengages at  $t = 2.4$  s. Initially, the driveline backlash causes large oscillations in the vehicle acceleration due to the sudden gear engagement after a brief period of no gear contact. This is denoted as the backlash effect in Figure 5.15(a). In the case of pedal tip-out, the disturbance is less severe since the gears are already in contact. Clearly, the driveline disturbances are reduced in both cases when the active damping controller is active. However, the controller performance slightly degrades when the backlash position,  $\theta_{bl,r}$ , traverses the gear clearance,  $\theta_{bl,r0}$  at  $t = 0$  s.

The experimental validation of the proposed active damping controller is also demonstrated in Chapter 7 using only the EM speed as a measurement.

### HEV Operating Modes: Engine Start/Stop

Different than a conventional vehicle, a hybrid-electric vehicle frequently uses the engine start-stop functions. The use of a high power belted-starter alternator makes

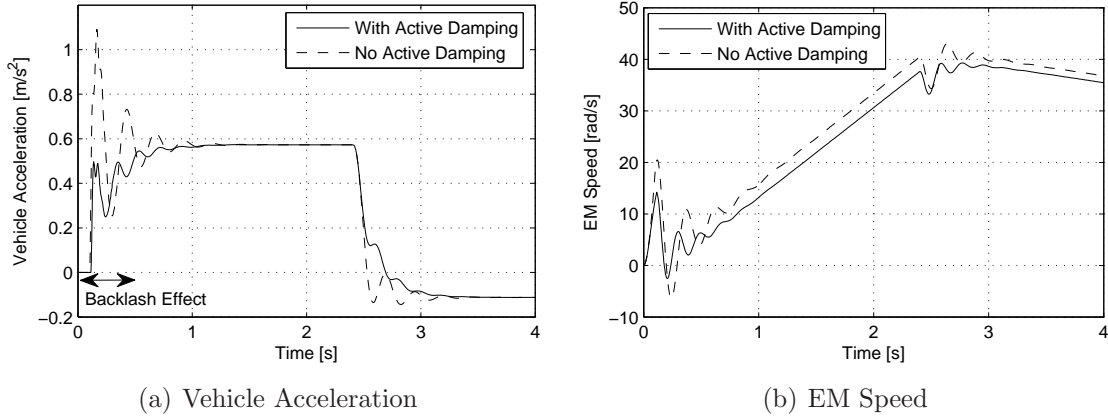


Figure 5.15: A comparison of pedal tip-in and tip-out responses with and without active driveline damping. Note that the driveline backlash causes a large overshoot in the vehicle acceleration following pedal tip-in when the controller is not used.

it possible to start the engine within 0.3 s in the test vehicle. When this capability is properly utilized, the engine can be started under normal driving conditions without disrupting the power flow to the wheels.

The main goal of the engine start event is to quickly bring the engine up to a desired operating speed<sup>9</sup> by using minimum actuator effort and without causing excessive vibrations. This problem is treated as a linear optimization problem by Canova *et al.* in [114]. In this work, a linear quadratic regulator is used in combination with a feed-forward controller to follow a prescribed engine speed trace during the engine start event. This control method is also implemented in the test vehicle. Note that the rear electric machine is also used during the engine start phase. The EM torque is computed using (5.3) in order to satisfy the driver's power request.

The engine stop can be controlled similar to the engine start. However, unlike the engine start event where the primary goal is to quickly reach a target speed, the main objective here is to smoothly stop the engine. Therefore, the engine stop time can be traded off for better drivability. Particular emphasis should be placed on the controller performance at low engine speeds if the transmission carries the engine

<sup>9</sup>The engine idle speed is used as the target speed for the test vehicle.



pulsations to the wheels. In the experimental vehicle, simply cutting off the fuel injection to the engine results in an acceptable performance. Therefore, a detailed engine stop strategy is not utilized.

In the experimental vehicle, the engine start event does not create major longitudinal disturbances until the engine nears the idle speed. This is because the transmission pressure (and the torque converter pressure) builds up around the idle speed immediately after the first fuel injection. Note that the gear pump that supplies pressure to the transmission is driven by the engine. Therefore, the engine start event mainly influences the vertical vibrational characteristics of the vehicle since the engine start pulsations are transmitted to the chassis via the engine mounts. However, the main drivability issue is that following the engine start phase, a change in the internal dynamics of the transmission (due to the sudden pressure increase) results in driveline disturbances. This issue may become more severe as a result of the controller transfer that occurs after the engine start. A control scheme that addresses these difficulties is the subject of the next chapter.

## **HEV Operating Modes: Hybrid**

The hybrid operating mode is initiated after the engine start event. In this mode, the control strategy has the ability to use the the engine and the two electric machines in combination to satisfy the driver's power request. This mode is active for the majority of vehicle's normal operating conditions. Therefore, the performance of the controller that is active in the hybrid operating mode greatly influences the overall performance of the vehicle.

Among the practically feasible optimization techniques, the Equivalent (fuel) Consumption Minimization Strategy (ECMS) [8] is used in this dissertation for the implementation of the hybrid operating mode. A review of this control technique along with some remarks regarding its practical implementation follow next.

### Equivalent Consumption Minimization Strategy: An Overview

The primary objective of the ECMS is to find a local minimum for an equivalent fuel metric while also satisfying a number of equality and inequality constraints. These constraints are imposed by the driver's power demand, the actuator torque limitations, and the high voltage battery's power and energy capacity limitations.

For the experimental vehicle's hybrid architecture, the global HEV energy optimization problem involves finding a control policy that minimizes the fuel consumption over the entire trip:

$$\mathcal{J}_{[t_0, t_f]} = \int_{t_0}^{t_f} \dot{m}_{ice,f}(t) dt \quad (5.15)$$

The optimal control policy is subject to (5.2) as well as the following inequality constraints for all  $t$ :

$$\begin{aligned} S_{batt,min} &< S_{batt}(t) < S_{batt,max} \\ P_{batt,min}(t) &< P_{batt}(t) < P_{batt,max}(t) \\ 0 &< T_{ice,req}(t) < T_{ice,max}(t) \\ T_{em,min}(t) &< T_{em,req}(t) < T_{em,max}(t) \\ T_{bsa,min}(t) &< T_{bsa,req}(t) < T_{bsa,max}(t). \end{aligned} \quad (5.16)$$

In this formulation,  $t_0$  and  $t_f$  represent the start and end times of the trip,  $P_{batt,min}$  is the maximum available battery power under charging,  $T_{ice,max}$ ,  $T_{em,max}$ ,  $T_{bsa,max}$  are the maximum ICE, EM and BSA torques, and  $T_{em,min}$ ,  $T_{bsa,min}$  are the minimum (regenerative) EM and BSA torques. An expression for  $P_{batt}$  was previously given in (3.58). Note that the constraints that arise from the actuator operating speeds and the power converter operating voltages are not included in (5.16). However, these constraints should be also taken into consideration during implementation.

Equation (5.15) assumes that a perfectly charge sustaining strategy is desirable, i.e.,  $S_{batt}(t_0) = S_{batt}(t_f)$ . Therefore, the cost incurred by possible variations between the initial and the terminal battery SOC is not included in (5.15).

Since the solution of the global optimization problem requires *a priori* knowledge of the entire driving cycle, a local criterion is necessary to convert (5.15) into a

local optimization problem that has a tractable solution for real-time implementation. Using the ECMS framework, this problem can be written as:

$$\mathcal{J}_{ECMS}(t) = \dot{m}_{ice,f}(t) + s(t) \sum_i \dot{m}_{i,eqf}(t) \quad (5.17)$$

$$u_{ECMS}(t) = \underset{u \in \mathcal{U}}{\operatorname{argmin}} \mathcal{J}_{ECMS}(t) \quad (5.18)$$

where  $i \in \{bsa, em\}$  and

$$u_{ECMS}(t) = \{T_{ice,req}^*(t), T_{em,req}^*(t), T_{bsa,req}^*(t)\} \quad (5.19)$$

$$\dot{m}_{i,eqf}(t) = \frac{1}{Q_{lhv}} \cdot \begin{cases} \frac{1}{\eta_i(T_{i,req}(t), \omega_i(t))} T_{i,req}(t) \omega_i(t), & T_{i,req}(t) > 0 \\ \eta_i(T_{i,req}(t), \omega_i(t)) T_{i,req}(t) \omega_i(t), & T_{i,req}(t) < 0 \end{cases} \quad (5.20)$$

$u_{ECMS}(t)$  is the local solution obtained using ECMS that is subject to (5.2) and (5.16). The superscript, \*, represents the optimum values of the torque requests computed by minimizing  $\mathcal{J}_{ECMS}(t)$ . Also,  $\dot{m}_{i,eqf}(t)$  are the individual equivalent fuel consumption contributions of the electric machines,  $Q_{lhv}$  is the lower heating value of the diesel fuel, and  $s(t)$  is the equivalence factor between the energy consumption of the electric machines and the fuel (or energy) consumption of the engine.

In order to converge to the globally optimal solution using ECMS, the equivalence factor function,  $s(t)$ , should be carefully selected. From a practical standpoint, a large value of  $s(t)$  penalizes the electrical energy use resulting in a higher engine fuel consumption, while a small value of  $s(t)$  promotes the battery use resulting in a depletion of the battery SOC. Assigning the equivalence factor to a fixed value or a static function does not suffice to achieve good fuel economy, since the changes in the driving cycle characteristics, battery SOC and direction of electrical currents all affect the “optimum” value of  $s(t)$ .

Other formulations have been proposed to facilitate the computation of the equivalent electrical fuel consumption, and consequently, the equivalence factor. For an HEV architecture that uses an engine and a single electric machine (the “two-way

split” case), Musardo *et al.* [30] proposed the following  $\dot{m}_{eqf}(t)$  formulation:

$$\dot{m}_{eqf}(t) = \frac{P_{em}(t)}{Q_{lhv}} \left( \left( \frac{1 + \text{sign}(P_{em})}{2} \right) s_{dis} \frac{1}{\eta_{batt}(P_{em}(t))\eta_{em}(P_{em}(t))} + \left( \frac{1 - \text{sign}(P_{em})}{2} \right) s_{ch} \eta_{batt}(P_{em}(t))\eta_{em}(P_{em}(t)) \right) \quad (5.21)$$

where  $s_{dis}$ ,  $s_{ch}$  are the two equivalence factors for battery discharging and charging,  $P_{em}$  is the power output of the electric machine, and  $\eta_{batt}$  is the battery efficiency. In this work, Musardo *et al.* rightly point out that the discharge (and charge) equivalence factor(s) essentially correspond to the average tank-to-battery (and “virtual” battery-to-tank) energy conversion efficiencies proposed by Paganelli *et al.* [8] for the two-way split case. For the two-way split architecture given in [30], these relationships can be written as:

$$s_{dis} = \frac{1}{\bar{\eta}_{tank \rightarrow batt}} = \frac{1}{\bar{\eta}_{ice,ch} \bar{\eta}_{belt,ch} \bar{\eta}_{em,ch} \bar{\eta}_{batt,ch}} \quad (5.22)$$

$$s_{ch} = \bar{\eta}_{batt \rightarrow tank} = \frac{\bar{\eta}_{belt,dis} \bar{\eta}_{em,dis} \bar{\eta}_{batt,dis}}{\bar{\eta}_{ice,dis}} \quad (5.23)$$

where  $\bar{\eta}_{\star,dis}$  and  $\bar{\eta}_{\star,ch}$  are the average discharge and charge efficiencies of the component  $\star$  for the two-way architecture investigated in [30]. This is an intuitively appealing definition of the equivalence factor, since the electrical energy available onboard ultimately comes from the fuel tank. Therefore, the equivalence factor between the two forms of energy should incorporate losses that occur during this energy conversion in a charge-sustaining hybrid vehicle.<sup>10</sup>

There are some notable differences between the equivalent fuel expressions given for the two-way split case (5.21) and the three-way split case (5.20). In the three-way split case, two electric machines exist within the power flow path between the fuel tank and the battery pack. Therefore, the implementation of the idea described by (5.21–5.23) requires several equivalence factors to be defined and individually optimized for a number of driving cycles. This situation is demonstrated in Figure 5.16. Sections

<sup>10</sup>Note that the definition of the equivalence factor would be different in the case of a plug-in hybrid vehicle since all the battery energy does not necessarily come from the fuel tank.

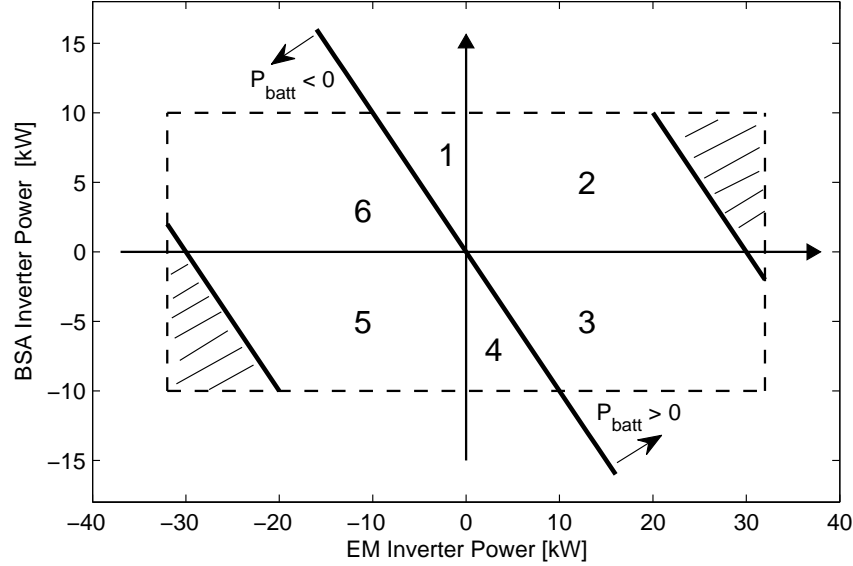


Figure 5.16: The average tank-to-battery and battery-to-tank energy conversion efficiencies take on different forms inside the numbered sections. This also requires that different equivalence factor formulations be used for different sections.

numbered 1 through 6 are divided in such a way that the EM inverter power, the BSA inverter power and the total battery power have different signs. This implies that for each of the sections 1 through 6, a different equivalence factor should be used if an idea similar to (5.21) is to be used. Note that the shaded regions are not admissible due to the battery power limitations.

In this work, an average equivalence factor,  $s(t)$ , is used to account for all the regions shown in Figure 5.16. In fact, this approach is preferred even for the two-way split case if the control strategy is intended for real-time operation. In the case of actual implementation, an online driving cycle estimation scheme is usually used to update the equivalence factor in order to achieve a near-optimum performance for a variety of driving cycles. Examples of driving pattern recognition techniques are given in [30] for a two-way split architecture, and in [115] for a three-way split architecture.

Another difference between (5.21) and (5.20) is that, for the three-way split case, the battery's energy conversion efficiency is included in the equivalence factor. This

assumption is necessary since the sign of either the EM torque or the BSA torque does not individually determine the direction of the battery current in the three-way split case (see Figure 5.16). Therefore, appropriately incorporating the battery efficiency into (5.20) would greatly complicate the equivalent fuel expression without providing a substantial practical benefit. Note that this is not applicable for the two-way split case (5.21) since the sign of  $P_{em}$  alone determines the direction of the battery current.

If the driving cycle is known *a priori*, the battery SOC can be maintained within a desired operating range by proper calibration of  $s(t)$ . In addition, a terminal constraint such as  $S_{batt}(t_f) = S_{batt}(t_0)$  can be satisfied. However, in the absence of such information, an equivalence factor correction function must be used to regulate the battery SOC. In this work, the nominal battery SOC operating range is determined to be between 50% and 80%. These limits are selected in order to reduce the rate of battery aging and to maintain the battery voltage within the EM and BSA inverter voltage limits for normal operating conditions. The SOC correction function,  $f_{SOC}$ , is multiplied by the nominal equivalence factor,  $s$ :

$$s_{act}(t) = f_{SOC}(S_{batt}(t)) s(t) \quad (5.24)$$

Here,  $s_{act}$  represents the actual equivalence factor used by ECMS during real-time implementation. Typically, the SOC correction function assumes a form similar to a proportional-integral (PI) controller [30, 115]. In this work, the following function is used for SOC based equivalence factor correction:

$$f_{SOC}(S_{batt}(t)) = \left( 1 + \left( \frac{S_{batt,ave} - S_{batt}(t)}{S_{batt,ave} - S_{batt,min}} \right)^{2n_{SOC}+1} \right) \cdot \left( 1 + \tanh \left( \frac{f_{SOC,I}(S_{batt}(t))}{S_{batt,th}} \right) \right) \quad (5.25)$$

$$f_{SOC,I}(S_{batt}(t)) = 0.99 f_{SOC,I}(t - \Delta T) + 0.01(S_{batt,ave} - S_{batt}(t)) \quad (5.26)$$

Using the battery SOC limits given above,  $S_{batt,ave} = 65\%$ ,  $S_{batt,max} = 80\%$ , and  $S_{batt,min} = 50\%$ . Also,  $\Delta T$  is the sampling time used to update the ECMS,  $n_{SOC} \in \mathbb{Z}^+$  is a suitable function order, and  $S_{batt,th}$  is the tolerance of the hyperbolic tangent function. Note that  $f_{SOC}$  is composed of two subfunctions where the first function

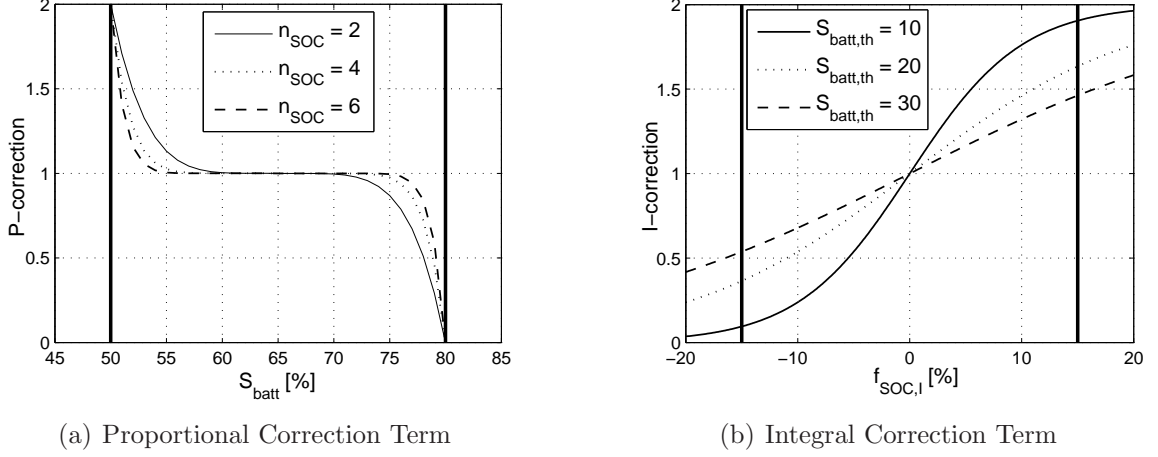


Figure 5.17: Variations of the proportional and integral SOC correction subfunctions with respect to SOC deviation from nominal and its weighted moving average.

represents the P-correction term (tuned by  $n_{SOC}$ ) and the second function represents the I-correction term (tuned by  $S_{batt,th}$ ). The integral correction term incorporates a weighted moving average function ( $f_{SOC,I}$ ) instead of a conventional integrator. The purpose of using a moving average function is to ensure that the effects of past deviations from  $S_{batt,ave}$  are eventually “washed away” from the current integral correction term as indicated in [115].

Figure 5.17 shows the variations of the SOC correction functions for different values of  $n_{SOC}$  and  $S_{batt,th}$ . The battery operating range is marked with bold vertical lines in both figures. The objective of the proportional correction term is to maintain the battery SOC between  $S_{batt,min}$  and  $S_{batt,max}$ . Figure 5.17(a) shows that this is achieved by applying an aggressive correction factor near the boundaries. In this work,  $n_{SOC} = 4$  is selected. Furthermore, the objective of the integral term is to ensure that the mean value of the battery SOC does not significantly deviate from  $S_{batt,ave}$  over a driving cycle. It is important that this function does not change the value of the nominal equivalence factor considerably during normal operating conditions. Using a value of  $S_{batt,th} = 30\%$  achieves this objective without overcorrecting the equivalence factor as shown in Figure 5.17(b).

Although, the SOC correction function slightly degrades the performance of ECMS as reported in [30], the use of this function is inevitable for real-time implementation. Clearly, proper calibration of  $f_{SOC}$  reduces the degradation in fuel economy. Note that in addition to impacting the fuel consumption, the SOC correction term also affects vehicle drivability. The drivability aspect is discussed later in this section.

### **ECMS: Implementation Considerations**

The equivalent consumption minimization strategy is an effective control algorithm for fuel consumption optimization. However, there are some difficulties with regard to its practical implementation. These difficulties mainly arise due to (i) the computational limitations of electronic control units, (ii) the drivability issues that result from the fundamental nature of an energy management strategy, i.e. an energy-optimal power distribution computed by ECMS in no way assures good vehicle drivability. A discussion of these issues follows next.

**Computational Issues:** There are two methods for implementing ECMS in an embedded control environment. The first method involves converting the ECMS algorithm into a high dimensional look-up table. This is achieved by pre-computing possible power/torque splits over a discretized space of input variables. The input variables in the case of the test vehicle are the driver's accelerator input ( $\alpha_{dr}$ ), the battery SOC ( $S_{batt}$ ), the engine speed ( $\omega_{ice}$ ), the EM speed ( $\omega_{em}$ ), the transmission gear ratio ( $\zeta_{tr}$ ), and the actual fuel equivalence factor ( $s_{act}$ ). The resulting torque/power split values are then stored in the controller's flash memory. During real-time implementation, the intermediate data points are either interpolated or the nearest stored values are selected. This process is also illustrated in Figure 5.18.

The look-up table method suffers from a number of issues. Once the look-up table is created, it is not possible to calibrate the control strategy unless a new look-up table is generated using a new set of calibration parameters. This may be a time-consuming process if the size of the discrete state space is too large. The look-up table implementation method is also subject to interpolation issues. Interpolating



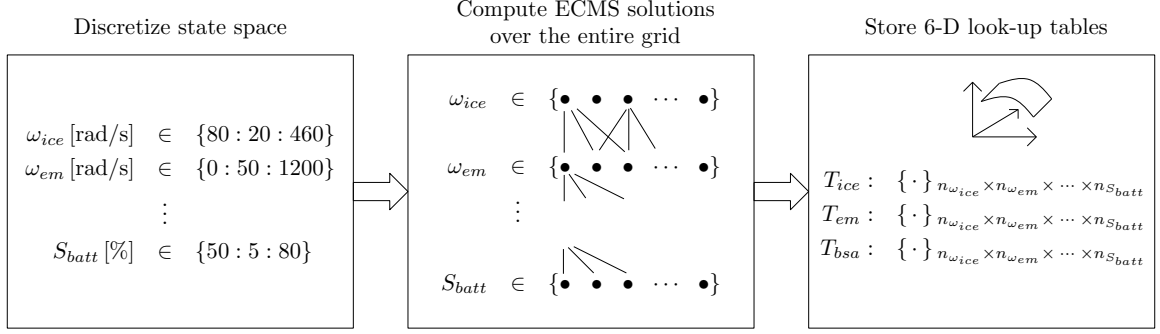


Figure 5.18: The ECMS look-up table generation process.

between two data points in a six-dimensional look-up table may result in inaccurate approximations. Another major limitation is the substantial memory requirement of the resulting look-up table. Usually only a small portion of a control unit's flash memory is allocated for data storage, and this memory may be insufficient if a fine grid resolution is required for the look-up table.

Another implementation method is to run the ECMS code directly on the embedded controller. The main drawback in this case is the limited computational power of the control unit. Even when a powerful rapid-prototyping controller (such as the dSPACE control unit) is used, performing a “brute-force” search over all allowable torque splits for the lowest fuel consumption is usually not possible within a reasonable update rate (50-100 ms). This computational difficulty is evident from the ECMS pseudo-code given in Table 5.2. At every sampling instant, two for loops are executed. The inner loop that computes the equivalent fuel consumption for a candidate torque split is executed  $M \times N$  times, where  $M$  and  $N$  are the number of grid points for the EM and BSA torques, respectively. This causes a significant computational burden on the embedded control unit.

In order to overcome this difficulty, a local search technique is employed in this work for real-time implementation. This technique uses the fact that the driver's power demand is continuous and it changes smoothly between the control strategy

```

Compute  $P_{dr,req}^+$  using (5.2)
M = length( $T_{em,min} : T_{em,step} : T_{em,max}$ )
N = length( $T_{bsa,min} : T_{bsa,step} : T_{bsa,max}$ )
for  $1 \leq i \leq M$ 
    for  $1 \leq j \leq N$ 
        Check  $|P_{batt}(P_{em}(i), P_{bsa}(j))| < P_{batt,max}$  (if not  $\rightarrow$  end loop)
        Choose  $T_{ice}(i, j)$  to satisfy  $P_{dr,req}^+$ 
        Compute  $\mathcal{J}_{ECMS}(i, j)$  using (5.17)
    end
end
 $(i^*, j^*) = \text{index}(\min(\mathcal{J}_{ECMS}(i, j)))$ 
return  $(T_{ice}(i^*, j^*), T_{em}(i^*), T_{bsa}(j^*))$ 

```

Table 5.2: The three-way split ECMS pseudo-code. (Some of the algorithm details are not shown here.)

updates.<sup>11</sup> Using this knowledge, the majority of the candidate torque splits can be eliminated from the fuel minimization search at any given time, since these points are not reachable due to the power demand constraint. This idea leads to the use of a “box” that confines the ECMS search space to a neighborhood of the current operating point. This concept is illustrated in Figure 5.19. Figure 5.19(a) shows the inputs and outputs of the original ECMS algorithm as well as the corresponding search space. Using the local search technique, this space is reduced to the neighborhood shown in Figure 5.19(b). This strategy also requires torque feedback from the previous operating point such that the local search neighborhood can be determined.

<sup>11</sup>An update rate of 100 ms is sufficient for proper operation of ECMS.

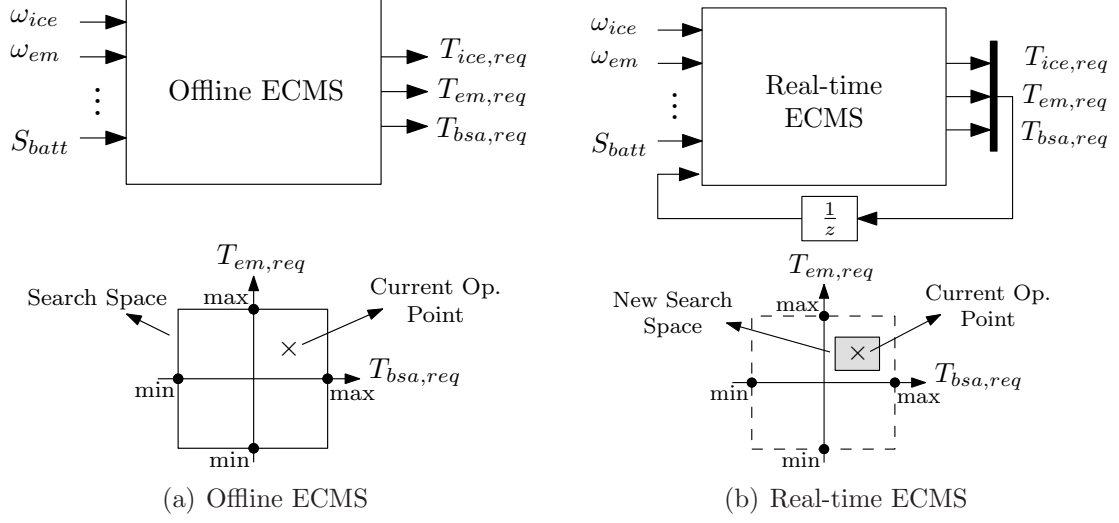


Figure 5.19: A comparison of the conventional ECMS and the version used for real-time implementation.

This approach has a number of benefits as well as some drawbacks. In addition to improving the computational time, the local search method also reduces the possibility of torque chattering.<sup>12</sup> Also, the local search technique provides a means for initializing ECMS which is advantageous in the case of a controller transfer. The mode transition aspects of the control strategy are explained in detail in the next chapter. The drawbacks of the local search technique are particularly related to how the “box size” is calibrated. If the ratio of the search box size to the ECMS sampling rate is too small then this not only deteriorates the fuel economy but it also introduces a time lag between the driver’s accelerator input and the resulting torque requests generated by ECMS. For most driving conditions, a choice of  $\pm 25$  Nm for  $T_{em,req}$  and  $\pm 10$  Nm for  $T_{bsa,req}$  gives an acceptable performance using an update rate of  $\Delta T = 100$  ms. The size of the local search space can be adjusted online if performance improvements are needed. A potential method is to relate the gradient of the

<sup>12</sup>Although, the torque chattering issue is reduced by means of the local search technique, it is not completely eliminated. This topic is further discussed later in this chapter.

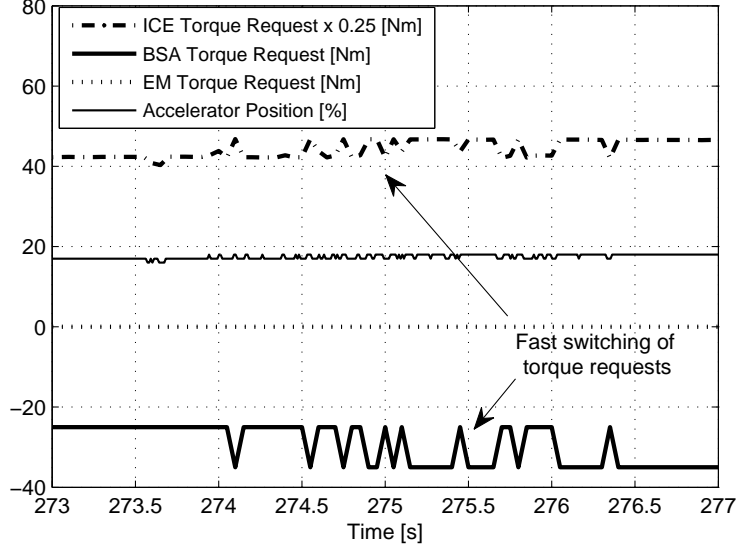


Figure 5.20: Rapid switching between torque requests during the ECMS operation.

accelerator pedal input (or the rate of change of  $P_{dr,req}^+$ ) to the size of the local search space, such that a higher power gradient results in a larger search neighborhood.

**Drivability Issues:** As described in Chapter 2, the behavior of an HEV control strategy may lead to drivability issues that are not seen in conventional vehicles. Some of the issues that are specific to the implementation of ECMS are discussed next and potential solution methods are proposed.

- *High-frequency switching of torque requests:* The ECMS cost function incorporates a low gradient around the local minimum for steady operating conditions such as cruising. This causes undesired switching between torque requests if slight changes in the operating conditions are introduced between consecutive samples. This situation is demonstrated by an experimental result in Figure 5.20. Although the driver maintains a nearly constant accelerator pedal position, the optimum torque split undergoes a rapid switching between two grid points. The switching frequency increases as the ECMS update rate is increased. The cycling situation usually disappears when one of the input variables (usually  $\alpha_{dr}$ ) sufficiently varies from its current value.

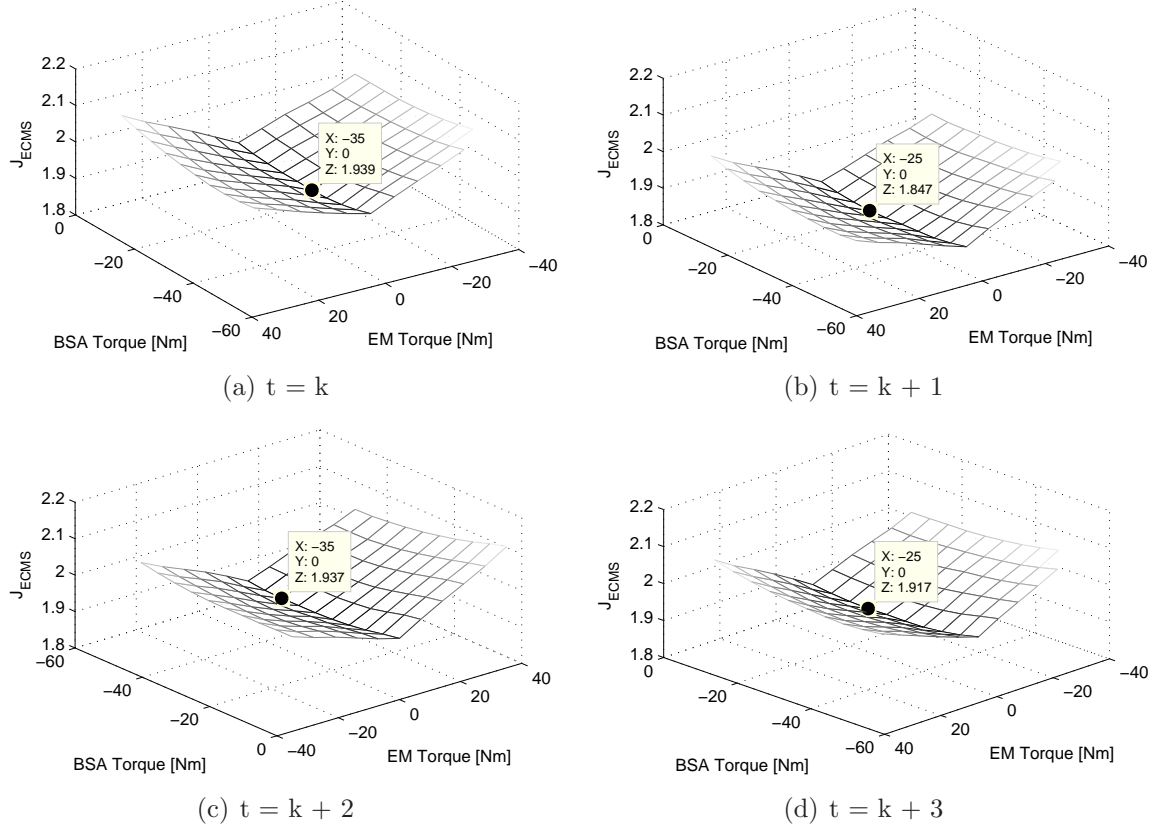


Figure 5.21: Variation of the ECMS cost function for four consecutive samples. The bold dot represents the minimum value of the cost function in each case.

In order to study this problem in more detail, the ECMS cost function is plotted as a function of the EM and BSA torques during the fast switching event in Figure 5.21. Note that the ICE torque is obtained as a result of the power demand constraint and it is not shown here. A constrained search space with magnitudes  $\pm 35$  Nm for the EM torque and  $\pm 25$  Nm for the BSA torque is used. The search region moves relative to the previous operating point.

Figure 5.21(a) through 5.21(d) show the variations of the cost function for four consecutive operating points. Clearly, the cost function has a low sensitivity to changes

in the BSA torque. As a result, the minimum of the cost function is located at different points of the grid, although the cost function hardly changes from one time instant to another. This causes the torque chattering problem shown in Figure 5.20.

To resolve this issue, the following sensitivity functions are used to modify the nominal ECMS solution:

$$\Omega_{T_{em} \rightarrow \mathcal{J}_{ECMS}} = \left| \frac{\mathcal{J}_{ECMS}(k) - \mathcal{J}_{ECMS}(k-1)}{T_{em,req}(k) - T_{em,req}(k-1)} \right| \quad (5.27)$$

$$\Omega_{T_{bsa} \rightarrow \mathcal{J}_{ECMS}} = \left| \frac{\mathcal{J}_{ECMS}(k) - \mathcal{J}_{ECMS}(k-1)}{T_{bsa,req}(k) - T_{bsa,req}(k-1)} \right| \quad (5.28)$$

Here, the index  $k$  represents the current control strategy operating point. The values of the sensitivity functions are compared with two threshold values,  $\Omega_{T_{em} \rightarrow \mathcal{J}_{ECMS},th}$  and  $\Omega_{T_{bsa} \rightarrow \mathcal{J}_{ECMS},th}$ . If either one of the sensitivity terms has a value lower than the corresponding threshold then that particular torque split is discarded and sub-optimal solutions are sought. If no other solutions are found then the torque split from the previous time step is held as the current value of the torque split.

At the expense of the additional calibration burden introduced by the sensitivity function thresholds, the rapid torque switching issue can be largely eliminated. However, the torque profiles generated as a result of using (5.27) and (5.28) are sensitive to specific threshold values. If a threshold value is selected too high then the torque split remains at its previous value longer than it should, thus resulting in a mismatch between  $\alpha_{dr}$  and the corrected torque split. Therefore, these thresholds should be selected sufficiently low to ensure that further drivability issues are not introduced.

- *Pedal sensitivity:* Improper calibration of the SOC correction function (5.25) may cause ECMS to generate torque splits that result in an undesired pedal sensitivity issue at low battery SOC. This situation is illustrated in Figure 5.22. Figure 5.22(a) demonstrates the case in which a pedal tip-in causes a torque hole (appears as a small drop in the engine speed) due to the large negative BSA torque applied immediately after take-off. The battery SOC is equal to 54% in this case. Figure 5.22(b) shows a similar take-off situation at a higher battery SOC. Here, the magnitude of the

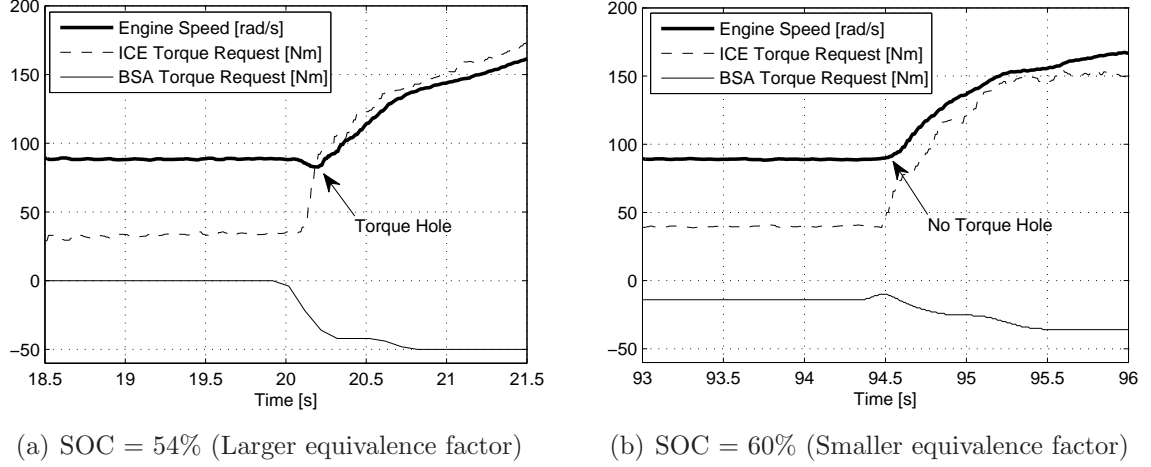


Figure 5.22: A comparison of pedal tip-in responses at different battery SOC levels. A torque hole is present for the case of SOC = 54% due to the poor calibration of the SOC correction function (5.25).

BSA torque is lower than the previous case, hence, the torque hole issue is no longer present. Note that the engine torque profiles are similar in both cases.

The root cause of the pedal sensitivity issue is obvious when Figure 5.17 is carefully investigated. If the SOC correction function is calibrated using a small  $n_{SOC}$  or  $S_{batt,th}$  then the equivalence factor is excessively penalized for small SOC deviations from  $S_{batt,ave}$ . This problem is fixed by properly calibrating the SOC correction function.

- *Actuator bandwidth issues:* The electric machines and the engine have different dynamic response characteristics. Although the electric machines offer important benefits for driveline control as a result of their fast response characteristics, this feature may also cause unexpected pedal response if the torque requests are not properly synchronized in the hybrid operating mode. A potential solution is to artificially “slow down” the response of the electric actuators such that all torque requests are realized simultaneously at the wheels. For this purpose, the BSA and EM torque requests are low-pass filtered in hybrid mode such that the engine’s dynamic response is compatible with those of the electric machines.

- *Control integration issues:* Integrating production control units and custom implemented controllers (such as the vehicle control unit) brings some challenges in terms of the implementation of ECMS. Drivability problems may arise due to the interactions between the vehicle control unit (VCU), the engine control unit (ECU) and the transmission control unit (TCU). An illustrative example is the engine idling condition. During the engine idle, ECMS often computes the following torque split if the battery SOC is low and  $\alpha_{dr} = 0$ :

$$\begin{aligned} T_{ice,req} &= T_{ECMS}(\omega_{ice,idle}) \\ T_{bsa,req} &= -T_{ECMS}(\omega_{ice,idle}) \\ T_{em,req} &= 0 \end{aligned} \tag{5.29}$$

where  $T_{ECMS}(\omega_{ice,idle})$  is a positive torque request computed by ECMS when the engine is idling. This is a result of the fact that the actual equivalence factor becomes large when the battery SOC is low, resulting in  $\sum_i \dot{m}_{i,eqf}$  to dominate the expression for  $\mathcal{J}_{ECMS}$  (see (5.17)). Therefore, a negative torque request that minimizes the ECMS cost function is given to the BSA. In order to meet the power demand ( $P_{dr,req}^+ = 0$ ),  $T_{ice,req}$  is chosen to be equal to  $T_{bsa,req}$  and opposite in sign. Although this torque split appears to be reasonable, an interruption from the ECU idle-speed controller changes this result.

This situation is demonstrated by an experimental result in Figure 5.23. The idle-speed controller attempts to compensate for the BSA torque since the ECU perceives the BSA torque as a disturbance. Therefore, the “conflict” between the ECMS and the existing idle-speed controller results in a poor idle quality. To overcome this issue, the engine torque request is multiplied by a correction function that is only active at low engine speeds:

$$f_{ice,idle}(\alpha_{dr}) = \begin{cases} 20\alpha_{dr} & \alpha_{dr} \leq 0.05 \\ 1 & \alpha_{dr} > 0.05 \end{cases} \tag{5.30}$$

Another control integration related issue occurs during transmission gear shifting. During an upshift event, the TCU requests a reduction in engine torque (see (3.1))



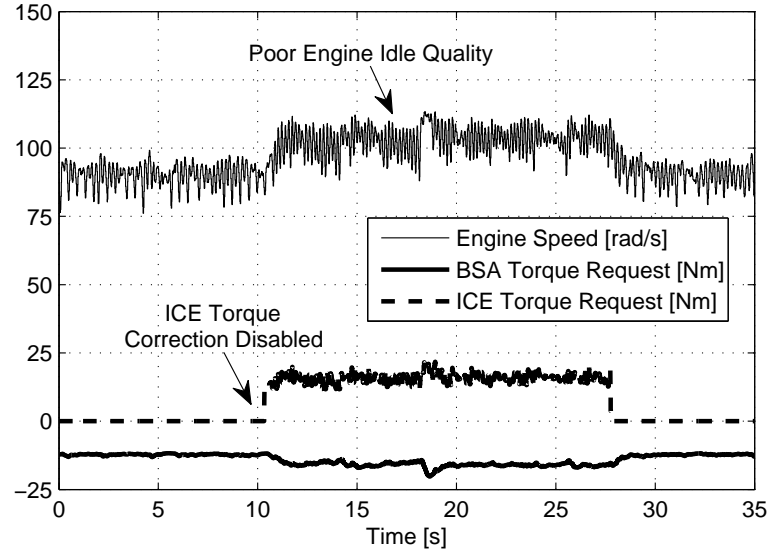


Figure 5.23: Poor engine idle quality resulting from the uncorrected ECMS engine torque request.

to limit the reaction torques acting on the engaging friction elements during the speed synchronization phase. The engine torque request that results from a TCU interruption during the 1-2 gear shift is shown in Figure 5.24. Clearly, such a torque reduction is not applied to the BSA by the TCU, and hence, a drivability issue would be expected during gear shifts. However, this situation does not create a major practical issue in the test vehicle since the BSA is used mostly for battery charging. However, if a large traction electric machine is used on the input side of the transmission, the ECMS torque split should be modified to account for this effect during gear shifts.

In conclusion, the control system should be designed, from early stages, with the knowledge that a high-level control algorithm such as ECMS is present in the system. Due to the use of available production control units, this was not possible in the experimental vehicle. Therefore, certain modifications are made to ensure that ECMS works harmoniously with the existing control system. Note that the drivability issues

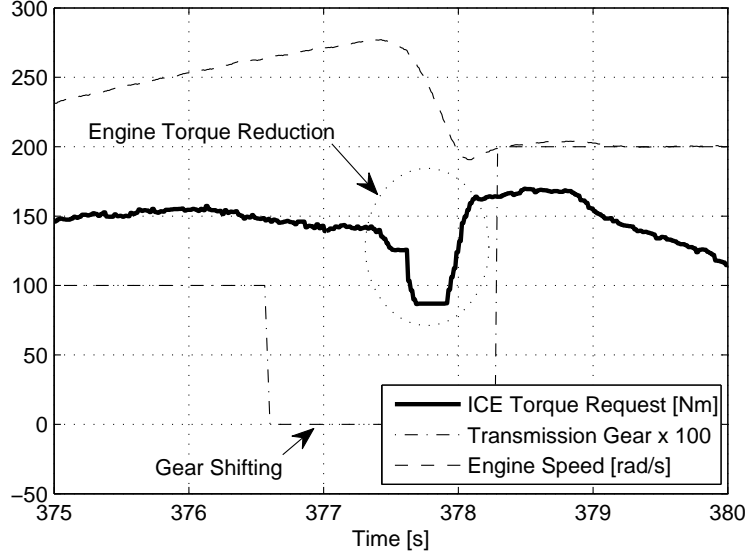


Figure 5.24: Engine torque reduction requested by the TCU during a 1-2 gear shift.

discussed above are specific to the HEV architecture investigated in this research. Different types of issues may arise when the ECMS is applied to different vehicle platforms.

### HEV Operating Modes: Regenerative Braking

Regenerative braking helps recuperate part of the kinetic energy that is normally lost during mechanical braking. The experimental vehicle always utilizes a combination of mechanical and electrical (regenerative) braking functions. The objective of the regenerative braking portion is to maximize the energy recuperation without adversely affecting drivability.

In contrast to the definition of the driver's request for positive power (when  $\alpha_{dr} > 0$ ), braking should be perceived as a torque request at the wheels. This is necessary to achieve a braking feel similar to a conventional vehicle. The brake torque equation (3.47) supports this conclusion. This equation states that the brake pedal position ( $\beta_{dr}$ ) is approximately linearly proportional to the brake line pressure ( $p_{br}$ ) and similarly, the mechanical braking torque  $T_{br}$  changes linearly with  $p_{br}$  (assuming a

constant friction coefficient). Therefore, a change in the brake pedal position linearly affects the mechanical braking torque at the wheels.

Since the vehicle's mechanical braking system is not modified for hybrid operation, it is necessary to introduce the regenerative braking torque such that a uniform braking feeling is achieved independent from the vehicle speed. Also, it is important prevent the battery from being overcharged in the regenerative braking mode. To meet these objectives, the following expression is used<sup>13</sup>:

$$T_{em,req}^- = \beta_{dr} \max \left( \frac{P_{batt,min}}{(\omega_{em,lp} + 0.1)}, T_{em,rgn} \right) f_{em,rgn,1}(\omega_{em,lp}) f_{em,rgn,2}(S_{batt}) \quad (5.31)$$

where  $T_{em,req}^-$  is the negative EM torque request and  $T_{em,rgn}$  is the regenerative braking torque limit used for low vehicle speeds ( $|T_{em,rgn}| < |T_{em,min}|$ ).  $f_{em,rgn,i} : \mathbb{R}_+ \rightarrow [0, 1]$  (where  $i \in \{1, 2\}$ ) are the following functions:

$$f_{em,rgn,1}(\omega_{em,lp}) = \tanh \left( \frac{\omega_{em,lp}}{\omega_{em,rgn,th}} \right) \quad (5.32)$$

$$f_{em,rgn,2}(S_{batt}) = \frac{1 - \tanh(S_{batt} - S_{batt,max})}{2} \quad (5.33)$$

where  $\omega_{em,rgn,th}$  is a threshold speed. Note that (5.31) does not incorporate the energy conversion efficiency of the EM and its inverter. This is because  $P_{batt,min}$  is chosen to be significantly lower than the actual battery power limit due to the restrictions on the maximum allowable inverter voltage. Therefore, including  $\eta_{em}$  into (5.31) is not necessary for the calculation of the maximum regenerative braking torque.

A graphical interpretation of this expression is also given in Figure 5.25. Figure 5.25(a) shows a comparison of the available regenerative braking torque and the maximum torque calculated according to (5.31). The maximum available torque is attenuated at low vehicle speeds in order to achieve a consistent braking feel. This restriction results in the shaded region of Figure 5.25(b) to be discarded for energy recuperation in order to improve drivability. However, this does not cause a significant degradation in fuel economy since the power available for regenerative braking is already limited at low vehicle speeds.

<sup>13</sup>As mentioned earlier, (5.31) is used in both regenerative braking and electric only modes.

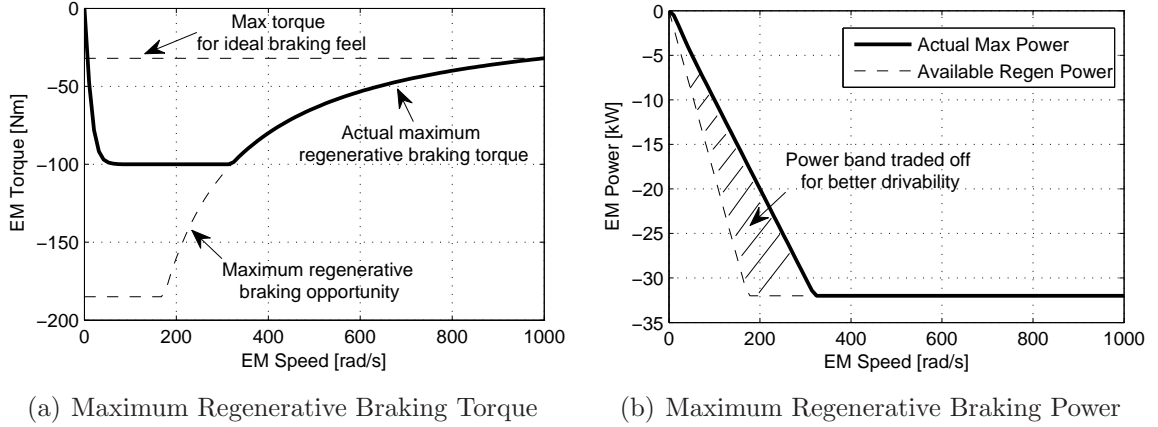


Figure 5.25: A comparison of the actual and the maximum available regenerative braking torque and power. A portion of the available regenerative braking power is discarded to achieve better drivability.

### 5.3 Summary

This chapter described the development of a control strategy for the OSU experimental hybrid-electric vehicle. The discussion focused on the supervisory and component level control functions of the vehicle. The main objective of the proposed controllers is to achieve improvements in fuel economy while maintaining good drivability. This objective is met by the control strategy by first converting the accelerator/brake pedal position into a power/torque demand, then determining the suitable vehicle operating mode, and finally computing a torque split to achieve the control objectives defined in a particular operating mode.

Some of the contributions of this chapter are as follows: (i) an expression that maps the accelerator position to a power demand is proposed for a parallel HEV to achieve a consistent accelerator pedal feel independent of the vehicle operating conditions, (ii) an active driveline damping strategy is developed to improve pedal tip-in/tip-out response during electric launch, (iii) the implementation aspects of the three-way split ECMS are investigated from computational and drivability viewpoints and various techniques are proposed to improve drivability during the hybrid operating mode.

## CHAPTER 6

### CONTROL OF SYSTEMS WITH MODE SWITCHING INDUCED TRANSIENTS

An HEV is a hybrid dynamical system because of the switching in system behavior due to events such as engine start-stop, and because of the use of multiple control algorithms to manage different vehicle functions. The hybrid nature of the plant and the control algorithms were previously discussed in Chapter 3 and Chapter 5.

One of the practical challenges for the control of systems of the above type, also known as switched dynamic systems, is the lack of a systematic method to reduce the adverse effects of switching-induced transients. In this chapter, a model-based control technique is developed to address the problem of achieving seamless transitions between the operating modes of a switched system. The technique presented here can be viewed as an extension of the classical notion of bumpless transfer. An illustrative simulation example that focuses on engine start related HEV drivability issues is given to show the effectiveness of this approach. The experimental verification of this method on the test vehicle is also discussed in Chapter 7.

#### 6.1 Problem Formulation

The focus of the proposed technique is a class of switched dynamical systems described by state-dependent differential equations with  $m$  modes denoted by

$$\Sigma = \bigcup_{i=1}^m \Sigma_i, \quad (6.1)$$

where each  $\Sigma_i$  denotes a mode of the system and is given by the six-tuple

$$\Sigma_i : \{\mathcal{X}_i, \mathcal{P}_i, \mathcal{U}_i, \mathcal{F}_i, \mathcal{T}_i^j, \mathcal{S}_i^j\} \quad (6.2)$$

where  $\mathcal{X}_i \subset \mathbb{R}^{n_i}$  is the associated state space,

$$\mathcal{P}_i = \{\mathcal{P}_i^0, \mathcal{P}_i^1, \dots, \mathcal{P}_i^{d_i}\} \quad (6.3)$$

such that  $\bigcup_{k=0}^{d_i} \mathcal{P}_i^k = \mathcal{X}_i$  are  $d_i + 1$  partitions of  $\mathcal{X}_i$ ,

$$\mathcal{U}_i = \{u_i^0, u_i^1, \dots, u_i^{d_i}\} \quad (6.4)$$

are the  $d_i + 1$  controllers on the corresponding partitions where  $u_i^k : \mathbb{R} \times \mathcal{X}_i \rightarrow \mathbb{R}^{p_i}$ ,  $\mathcal{F}_i : \mathbb{R} \times \mathcal{X}_i \times \mathcal{U}_i \rightarrow \mathbb{R}^{n_i}$  is the associated  $\mathcal{C}^\infty$  vector field on  $\mathcal{X}_i$ . The presentation of this approach is restricted to the case where each mode may only transition to at most one other mode. Therefore, the number of partitions is restricted to be either 1 or 2.  $\mathcal{S}_i^j \subset \mathcal{X}_i$  is the switching set in which the transition rule  $\mathcal{T}_i^j : \mathcal{X}_i \rightarrow \mathcal{X}_j$  is applied which takes the state from mode  $i$  to mode  $j$ . Similar notations are used in [67] and [116] to describe hybrid system models. The notation used here is specialized to suit the methodology used for control design.

Associated with each mode is the cost  $\mathcal{J}_i^j : \mathcal{S}_i^j \rightarrow \mathbb{R}_+$  of transitioning from mode  $i$  to mode  $j$ . Note that it may be the case that  $\mathcal{S}_i^j$  is given by the system's dynamics (consider the case of clutch slip-stick dynamics) or it may be the case that  $\mathcal{S}_i^j$  may be chosen (consider the case of a gearshift map). If  $\mathcal{S}_i^j$  is not dependent on the system's dynamics then it becomes a control variable since the value of the cost  $\mathcal{J}_i^j$  is affected by a specific choice of  $\mathcal{S}_i^j$ .

Figure 6.1 shows an abstraction of the class of systems under consideration.<sup>1</sup> As an example, the state trajectory originating from  $\mathcal{P}_i^0$  experiences a mode transition after reaching the switching set  $\mathcal{S}_i^j$  that is located in  $\mathcal{P}_i^1$ . If a state jump occurs,  $\mathcal{T}_i^j$  maps  $\mathcal{X}_i$  to  $\mathcal{X}_j$ . As a result of the mode change, the new vector field  $\mathcal{F}_j$  governs the evolution of  $\mathcal{X}_j$  in mode  $j$ .

<sup>1</sup>In fact, the abstraction in Figure 6.1 represents a broader class of systems than that investigated in this research. Note that mode  $i$  is allowed to transition to multiple modes through  $\mathcal{S}_i^k$  and  $\mathcal{S}_i^l$ .

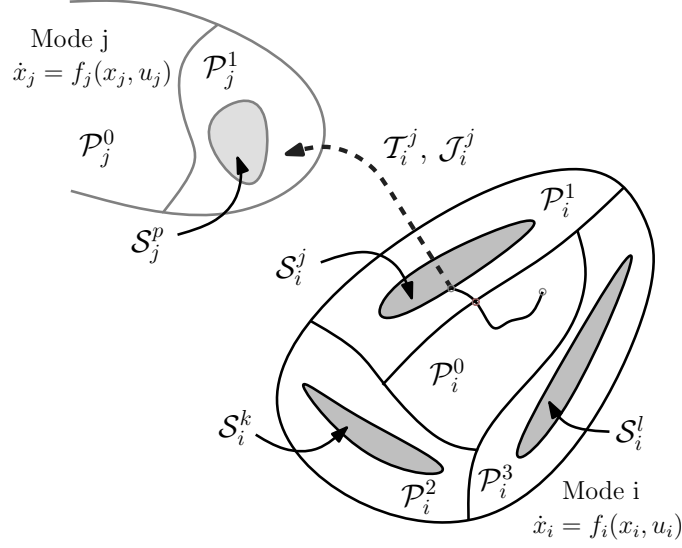


Figure 6.1: An abstraction of the modeling formalism that represents the switched hybrid systems of interest.

The following assumptions are made about the properties of the switched dynamic systems studied in this research:

- Each mode's vector field is affine in control. (i.e.  $\mathcal{F}_i : f_i(x_i) + g_i(x_i) u_i^k$  for all  $i, k$ ).
- The control inputs  $\mathcal{U}_i$  are bounded.
- The number of system modes  $m$  is finite.
- The mode transitions are well separated in time (i.e. the system does not exhibit Zeno behavior [117]).
- The state space partitions are chosen such that each partition may allow for a transition to at most one other mode.
- The switched dynamic system is deterministic.

## 6.2 Proposed Solution Method

With the class of systems detailed, the primary objective of the proposed control design technique can be stated as follows.

**Problem Statement:** Achieve seamless (low-cost) transitions for the given class of switched hybrid systems.

As the problem statement indicates, the essence of the control strategy is to design controllers such that the cost associated with transitioning,  $\mathcal{J}_i^j$ , is minimized. The approach involves two pieces. In the first piece, if it is the case that  $\mathcal{S}_i^j$  may be chosen, the switching set should be chosen such that  $\|\mathcal{J}_i^j(\mathcal{S}_i^j)\|$  is minimized, where  $\|\cdot\|$  is a suitable norm. In the second piece,  $\mathcal{X}_i$  is partitioned and controllers are designed for each partition. The partitioning and controller design is to be done such that as the state approaches  $\mathcal{S}_i^j$  (where transitioning is imminent) the state is steered to a location in  $\mathcal{S}_i^j$  with low cost. Away from the partitions that contain switching sets, a controller may be designed to achieve any suitable control objective.

The proposed method focuses on a *preemptive* control approach to avoid undesired transitions. A common approach, however, is to suppress the adverse effects of a mode transition after the transition occurs (see [118] for example).

In this work, controllers that are in effect inside the edge partitions are designed using linearizing control laws. A block diagram representation of the plant-control interactions is given in Figure 6.2. In this approach, the problem of achieving low-cost transitions is formulated as a regulation problem. A linear transformation,  $H_i : x_i \mapsto H_i x_i$ , gives the performance output  $z_i$  that is to be regulated. The resulting control input is composed of a feed-forward linearizing component ( $\bar{u}_i^k$ ) and a linear feedback component (with output feedback gain matrix  $K_i$ ) that may be chosen by pole placement to achieve desired performance and to provide robustness in the presence of model uncertainties. Note that other control techniques may also be used to achieve the mode transition objective given by  $\mathcal{J}_i^j$ .



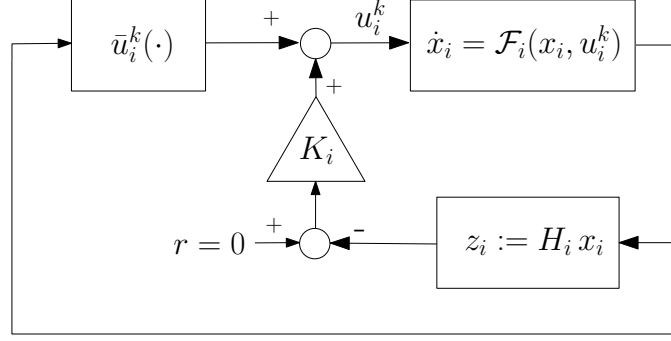


Figure 6.2: A block diagram representation of the controllers that are in effect inside the edge partitions.

Details of the control design are given in Section 6.4 for a simplified HEV electric launch control application.

### 6.3 Potential Applications of the Proposed Control Method

A wide variety of real-world applications can be addressed using the proposed method. The control of HEV drivelines is chosen as an area of application since this is the main topic of this dissertation. The following are other potential applications for which the proposed method will be an effective tool in designing controllers to improve transient performance during mode switching:

1. The regulation of mode-transitions for multi-mode combustion engines [5];
2. the control of cylinder de-activation for displacement-on-demand engines [119];
3. the control of gear shifting in automated manual transmissions [6]; and
4. the control of soft-landing in variable valve actuated (camless) engines [7].

The method proposed in this dissertation is essentially a generalization and formalization of some of the above successful approaches to ensuring seamless transitions.

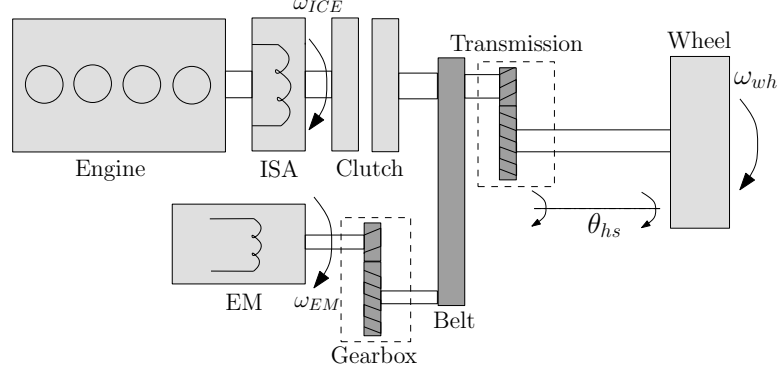


Figure 6.3: Simplified driveline model for the HEV launch example.

## 6.4 An Illustrative Example: Control of HEV Launch

The main objective during HEV electric launch is to achieve a smooth and quick mode transition between electric only and hybrid operating modes. The model validation results given in Section 4.2.3 clearly demonstrate that if this transition is not carefully controlled, it results in undesired driveline disturbances. The proposed control design method offers a systematic approach for improving drivability during this transition.

For the preliminary analysis of this problem, a simplified model of a parallel HEV drivetrain is used (see Figure 6.3). Although the simplified drivetrain configuration does not fully correspond to the configuration of the experimental vehicle, the basic dynamical interactions and the nature of the switchings in plant model are common in both cases.

The HEV driveline given in Figure 6.3 consists of an ICE and a traction EM that are coupled prior to the transmission to deliver the desired propulsion torque. During launch, the ICE is initially decoupled from the driveline and the vehicle is launched solely by the EM. When appropriate, the ICE is started via an integrated starter alternator (ISA) and a dry clutch engages the ICE to the driveline. Clutch engagement transitions the vehicle into the parallel hybrid operating mode.

### 6.4.1 Hybrid Model of HEV Launch

In order to facilitate the design of controllers that are in effect in different phases of system operation, a hybrid model of the simplified drivetrain is derived. The details of the derivation are not given here since this control model is a simplified version of the component models described in Chapter 3.

In this example, the state variables are chosen as  $x_1, x_2 := (\omega_{em}, \omega_{ice}, \omega_{wh}, \theta_{hs})'$  and  $x_3 := (\omega_{ice}, \omega_{wh}, \theta_{hs})'$ . The number of DOFs is reduced to three in the parallel hybrid mode since the ICE speed and the EM speed are kinematically constrained. The dimensions of the input spaces for each mode are all two.

The overall hybrid control model is described by the following vector fields:

$$\mathcal{F}_1 = \begin{cases} \dot{\omega}_{em} = \frac{1}{J_{em,1}} (T_{em} - b_{em}\omega_{em} - (\zeta_{gb}\zeta_{tr})^{-1} (k_{hs}\theta_{hs} + b_{hs}((\zeta_{gb}\zeta_{tr})^{-1}\omega_{em} - \omega_{wh}))) \\ \dot{\omega}_{ice} = \frac{1}{J_{ice,1}} (T_{ice} - b_{ice}\omega_{ice}) \\ \dot{\omega}_{wh} = \frac{1}{J_{wh,1}} (k_{hs}\theta_{hs} + b_{hs}((\zeta_{gb}\zeta_{tr})^{-1}\omega_{em} - \omega_{wh}) - C_{aero}\omega_{wh}^2 - C_{rr}) \\ \dot{\theta}_{hs} = (\zeta_{gb}\zeta_{tr})^{-1} \omega_{em} - \omega_{wh} \end{cases} \quad (6.5)$$

$$\mathcal{F}_2 = \begin{cases} \dot{\omega}_{em} = \frac{1}{J_{em,1}} (T_{em} - b_{em}\omega_{em} - (\zeta_{gb}\zeta_{tr})^{-1} (k_{hs}\theta_{hs} + b_{hs}((\zeta_{gb}\zeta_{tr})^{-1}\omega_{em} - \omega_{wh}))) \\ \quad + \frac{1}{\zeta_{gb}} (2\mu_{dc} R_{dc} A_{dc} p_{dc} \tanh(\frac{1}{\epsilon}(\omega_{ice} - \frac{1}{\zeta_{gb}}\omega_{em}))) \\ \dot{\omega}_{ice} = \frac{1}{J_{ice,1}} (T_{ice} - b_{ice}\omega_{ice} - 2\mu_{dc} R_{dc} A_{dc} p_{dc} \tanh(\frac{1}{\epsilon}(\omega_{ice} - \frac{1}{\zeta_{gb}}\omega_{em}))) \\ \dot{\omega}_{wh} = \frac{1}{J_{wh,1}} (k_{hs}\theta_{hs} + b_{hs}((\zeta_{gb}\zeta_{tr})^{-1}\omega_{em} - \omega_{wh}) - C_{aero}\omega_{wh}^2 - C_{rr}) \\ \dot{\theta}_{hs} = (\zeta_{gb}\zeta_{tr})^{-1} \omega_{em} - \omega_{wh} \end{cases} \quad (6.6)$$

$$\mathcal{F}_3 = \begin{cases} \dot{\omega}_{ice} = \frac{1}{J_{ice,2}} (T_{ice} + \zeta_{gb}T_{em} - (b_{em}\zeta_{gb}^2 + b_{ice})\omega_{ice} \\ \quad - \frac{1}{\zeta_{tr}} (k_{hs}\theta_{hs} + b_{hs}((\zeta_{tr})^{-1}\omega_{ice} - \omega_{wh}))) \\ \dot{\omega}_{wh} = \frac{1}{J_{wh,1}} (k_{hs}\theta_{hs} + b_{hs}((\zeta_{tr})^{-1}\omega_{ice} - \omega_{wh}) - C_{aero}\omega_{wh}^2 - C_{rr}) \\ \dot{\theta}_{hs} = (\zeta_{tr})^{-1} \omega_{ice} - \omega_{wh} \end{cases} \quad (6.7)$$

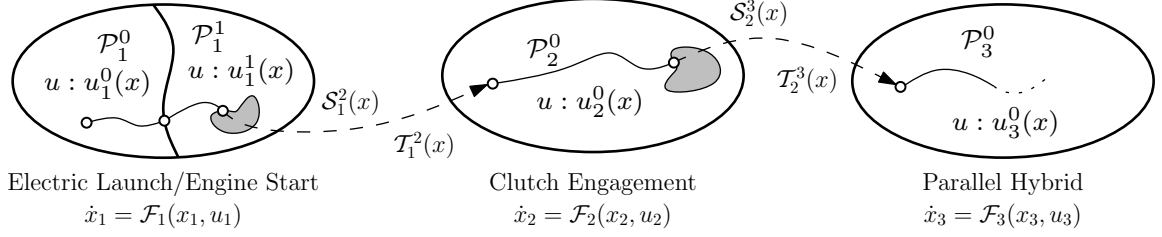


Figure 6.4: A hybrid model of the mode traversals for the HEV launch problem.

Here,  $J_{ice,1}$  is the combined inertia of the ISA, the engine and the input side of the dry clutch,  $J_{ice,2}$  is the combined inertia of all the pre-transmission components on the engine shaft,  $J_{em,1}$  is the combined inertia of the rotor, the motor gearbox and the transmission at the motor shaft,  $J_{wh,1}$  is the sum of the wheel inertias and the vehicle effective inertia,  $C_{aero}$  is the aerodynamic road load coefficient,  $C_{rr}$  is the constant rolling resistance load,  $\mu_{dc}$  is the friction coefficient of the dry clutch,  $R_{dc}$  is the effective radius of the dry clutch,  $A_{dc}$  is the effective area of the dry clutch,  $p_{dc}$  is the pressure applied to the dry clutch, and  $\epsilon = 0.1$ . Other variables represent the same quantities as in Chapter 3.

The only nonlinearity (aside from the aerodynamic load) in the hybrid driveline model is due to the engagement dynamics of the dry clutch. In order to satisfy the assumption on the smoothness of vector fields, the hyperbolic tangent function is used to represent the clutch nonlinearity about zero slip speed. Also, note that the ICE and ISA torques are combined into  $T_{ice}$  since the actuator dynamics are ignored in the control model. However, the resulting  $T_{ice}$  is constrained by different torque limits in different phases of operation.

A graphical illustration of the various system phases is given in Figure 6.4. The electric only and engine start operating phases have the same vector field, only the governing control laws are different. Therefore, they are considered as a single mode that contains two state space partitions. The clutch engagement and parallel hybrid phases have distinct vector fields and are represented by system modes 2 and 3.

In this example, the state space partitions are chosen as

$$\begin{aligned}
\mathcal{P}_1^0 &:= \{x \in \mathcal{X}_1 \mid \omega_{wh} < \omega_{wh,th} \quad \wedge \quad \omega_{ice} = 0\} & (\text{"ICE off"}) \\
\mathcal{P}_1^1 &:= \{x \in \mathcal{X}_1 \mid \omega_{wh} \geq \omega_{wh,th} \quad \vee \quad \omega_{ice} > 0\} & (\text{"ICE on"}) \\
\mathcal{P}_2^0 &:= \{x \in \mathcal{X}_2\}, \quad \mathcal{P}_3^0 := \{x \in \mathcal{X}_3\} & (\text{trivial partitions})
\end{aligned} \tag{6.8}$$

where  $\omega_{wh,th}$  is a threshold speed. The engine start condition is chosen such that it only has a dependence on the vehicle speed (hence on  $\omega_{wh}$ ). The clutch slip speed,  $\Delta\omega_{dc} := \zeta_{gb}^{-1}\omega_{em} - \omega_{ice}$ , is used to define the switching sets,

$$\begin{aligned}
\mathcal{S}_1^2 &:= \{x \in \mathcal{X}_1 \mid |\Delta\omega_{dc}| \leq \Delta\omega_{dc,th}\} & (\text{"slip speed below threshold"}) \\
\mathcal{S}_2^3 &:= \{x \in \mathcal{X}_2 \mid |\Delta\omega_{dc}| < \epsilon\} & (\text{"clutched locked up"})
\end{aligned} \tag{6.9}$$

where  $\Delta\omega_{dc,th}$  is a (constant) threshold speed for  $\Delta\omega_{dc}$ . Choice of  $\mathcal{S}_1^2$  is arbitrary since the beginning of the clutch engagement can be freely determined. However,  $\mathcal{S}_2^3$  depends on the internal dynamics of the system and it cannot be arbitrarily selected. The transition maps are linear and are given by  $\mathcal{T}_1^2 : x \mapsto x$  and  $\mathcal{T}_2^3 : x \mapsto Tx$  where

$$T := \begin{bmatrix} \zeta_{gb}^{-1} & 0 & 0 & 0 \\ 0 & 0 & 1 & 0 \\ 0 & 0 & 0 & 1 \end{bmatrix}. \tag{6.10}$$

The cost functions associated with switching are

$$\mathcal{J}_1^2(x_1) := |\Delta\omega_{dc}| \tag{6.11a}$$

$$\mathcal{J}_2^3(x_2) := w_1 |\Delta\omega_{dc}| + w_2 |\Delta\omega_{hs}| \tag{6.11b}$$

where  $w_1$  and  $w_2$  are the weights associated with  $\mathcal{J}_2^3$  and  $\Delta\omega_{hs} := (\zeta_{gb}\zeta_{tr})^{-1}\omega_{em} - \omega_{wh}$  is the half-shaft deflection rate. Once the system is expressed using the formalism introduced earlier, the control problem for good drivability simplifies to designing controllers to minimize  $\mathcal{J}_1^2$  and  $\mathcal{J}_2^3$ . Minimizing  $\mathcal{J}_1^2$  ensures rapid convergence of ICE and clutch speeds, while minimizing  $\mathcal{J}_2^3$  ensures that the clutch speeds are fully synchronized and that the downstream driveline torque is steady at the end of the engagement. Note that the control problem involves improving drivability by minimizing vibrational disturbances and the engagement time. The selection of torques in preparation for the transition only minimally affects fuel consumption since the transition preparation takes only seconds.

### 6.4.2 Control Design

The chief requirement of the control design is to seamlessly transfer from an open-loop controller that is active during electric-only mode to an energy management controller that is active during parallel-hybrid mode. In this example, a simplified form of the open-loop controller described in Section 5.2.2 is used to manage the electric only phase. Also, a two-way split ECMS is used to compute the torque requests in parallel hybrid operating mode.

The remaining controllers are designed to minimize selected mode transition cost functions,  $\mathcal{J}_i^k$ . The approach taken here is to formulate these cost minimization problems as regulation problems (see Figure 6.2). These controllers are described next.

#### Engine Start Phase

Conventional ICE start strategies are often designed to bring the ICE up to a specified idle speed [64]. The goal here is to minimize  $\mathcal{J}_1^2$ , the speed difference between the ICE crankshaft and the transmission input shaft prior to the clutch engagement while also ensuring a fast response. The performance output (relative degree one) and its derivative are given as

$$\begin{aligned} z_1 &= \Delta\omega_{dc} = \begin{bmatrix} \zeta_{gb}^{-1} & -1 & 0 & 0 \end{bmatrix} x_1 \\ \dot{z}_1 &= \Delta\dot{\omega}_{dc} = f_1(x_1) + g_1 u_1 \end{aligned} \quad (6.12)$$

where

$$\begin{aligned} f_1(x_1) &= \left( \frac{-b_{em}}{J_{em,1}} - \frac{b_{hs}}{\zeta_{tr}^2 \zeta_{gb}^2 J_{em,1}} \right) \Delta\omega_{dc} + \left( \frac{-b_{em}}{J_{em,1}} - \frac{b_{hs}}{\zeta_{tr}^2 \zeta_{gb}^2 J_{em,1}} + \frac{b_{ice}}{J_{ice,1}} \right) \omega_{ice} \\ &\quad + \left( \frac{b_{hs}}{\zeta_{gb}^2 \zeta_{tr} J_{em,1}} \right) \omega_{wh} + \left( -\frac{k_{hs}}{\zeta_{gb}^2 \zeta_{tr} J_{em,1}} \right) \theta_{hs} \\ g_1 &= \begin{bmatrix} \frac{1}{J_{em,1} \zeta_{gb}} & \frac{-1}{J_{ice,1}} \end{bmatrix} \\ u_1 &= \begin{bmatrix} T_{em} & T_{ice} \end{bmatrix}' \end{aligned} \quad (6.13)$$

Since the ICE and driveline dynamics are decoupled in this phase, the EM torque may be chosen similar to the electric-only phase to fulfill the driver's power demand. This

constraint also reduces the control problem into a single input-single output problem. The combination of ISA and ICE torques (treated as a single input,  $T_{ice}$ ) can be used to render  $\Delta\omega_{dc} = 0$  asymptotically stable using the following control law:

$$(u_1)_{2,1} = T_{ice} = -J_{ice,1} \left( - \left( \frac{-b_{em}}{J_{em,1}} - \frac{b_{hs}}{\zeta_{tr}^2 \zeta_{gb}^2 J_{em,1}} + \frac{b_{ice}}{J_{ice,1}} \right) \omega_{ice} - \frac{b_{hs}}{\zeta_{gb}^2 \zeta_{tr} J_{em,1}} \omega_{wh} + \frac{k_{hs}}{\zeta_{gb}^2 \zeta_{tr} J_{em,1}} \theta_{hs} - \frac{1}{J_{em,1} \zeta_{gb}} T_{em} \right) \quad (6.14)$$

### Clutch Engagement Phase

The objective of the clutch engagement is to match quickly the ICE speed to the transmission input speed without inducing undesirable vibrations. The objective function expressed in (6.11) can be written in terms of two outputs. Two performance outputs of relative degree one are defined,  $z_2 = [ \Delta\omega_{dc} \quad \Delta\omega_{hs} ]'$ , where

$$\begin{aligned} z_2 &= \begin{bmatrix} \zeta_{gb}^{-1} & -1 & 0 & 0 \\ (\zeta_{gb} \zeta_{tr})^{-1} & 0 & -1 & 0 \end{bmatrix} x_2 \\ \dot{z}_2 &= f_2(x_2, p_{dc}) + g_2 u_2 \end{aligned} \quad (6.15)$$

where

$$\begin{aligned} (f_2)_{1,1} &= - \left( \frac{1}{\zeta_{gb}^2 J_{em,1}} + \frac{1}{J_{ice,1}} \right) T_{dc}(p_{dc}, x_2) - \frac{b_{ice}}{J_{ice,1}} \Delta\omega_{dc} \\ &\quad + \left( \frac{b_{ice} \zeta_{tr}}{J_{ice,1}} - \frac{b_{em} \zeta_{tr}}{J_{em,1}} - \frac{b_{hs}}{\zeta_{tr} \zeta_{gb}^2 J_{em,1}} \right) \Delta\omega_{hs} + \frac{k_{hs}}{\zeta_{tr} \zeta_{gb}^2 J_{em,1}} \theta_{hs} \\ (f_2)_{2,1} &= \frac{1}{J_{em,1} \zeta_{tr} \zeta_{gb}^2} T_{dc}(p_{dc}, x_2) + \frac{1}{J_{wh,1}} (C_{aero} \omega_{wh}^2 + C_{rr}) \\ &\quad + \left( -\frac{b_{em}}{J_{em,1}} - \frac{b_{hs}}{\zeta_{tr}^2 \zeta_{gb}^2 J_{em,1}} + \frac{b_{hs}}{J_{wh,1}} \right) \Delta\omega_{hs} - \frac{b_{em}}{J_{em,1}} \omega_{wh} \\ &\quad - \left( \frac{k_{hs}}{\zeta_{tr}^2 \zeta_{gb}^2 J_{em,1}} + \frac{k_{hs}}{J_{wh}} \right) \theta_{hs} \\ g_2 &= \begin{bmatrix} (J_{em,1} \zeta_{gb})^{-1} & -(J_{ice,1})^{-1} \\ (\zeta_{tr} \zeta_{gb} J_{em,1})^{-1} & 0 \end{bmatrix} \end{aligned} \quad (6.16)$$

The nonlinear clutch torque is  $T_{dc}(p_{dc}, x_2) = 2\mu_{dc} R_{dc} A_{dc} p_{dc} \tanh\left(\frac{1}{\epsilon}(\omega_{ice} - \frac{1}{\zeta_{gb}} \omega_{em})\right)$ , and  $u_2 = u_1$ . It is assumed that the hydraulic clutch pressure,  $p_{dc}$ , is measured or

that the commanded value is known. Note that the clutch pressure is not considered a control variable and is simply treated as a known disturbance. In this control scheme,  $T_{em}$  is used to render the shaft torsion  $\Delta\omega_{hs} = 0$  asymptotically stable and  $T_{ice}$  is used to control the engine speed during clutch engagement. The multi input multi output control problem is decoupled such that  $T_{em}$  is used to render the shaft torsion  $\Delta\omega_{hs} = 0$  asymptotically stable, and then the engine torque  $T_{ice}$  is used to render asymptotically stable the ‘back-stepped dynamics’, which include the clutch slip speed  $\Delta\omega_{dc}$  and a linearizing control law plus linear state feedback. The resulting control laws are given by

$$(u_2)_{1,1} = T_{em} = -J_{ice,1} \left( \frac{b_{em}}{J_{em,1}} \omega_{wh} + \left( \frac{k_{hs}}{J_{em,1} \zeta_{tr}^2 \zeta_{gb}^2} + \frac{k_{hs}}{J_{wh,1}} \right) \theta_{hs} - \frac{1}{J_{em,1} \zeta_{tr} \zeta_{gb}^2} T_{dc} - \frac{1}{J_{wh,1}} (C_{aero} \omega_{wh}^2 + C_{rr}) \right) \quad (6.17)$$

$$(u_2)_{2,1} = T_{ice} = -J_{ice,1} \left( - \left( \frac{b_{ice} \zeta_{tr}}{J_{ice,1}} - \frac{b_{em} \zeta_{tr}}{J_{em,1}} - \frac{b_{hs}}{\zeta_{tr} \zeta_{gb}^2 J_{em,1}} \right) \Delta\omega_{hs} - \frac{k_{hs}}{\zeta_{tr} \zeta_{gb}^2 J_{em,1}} \theta_{hs} + \left( \frac{1}{\zeta_{gb}^2 J_{em,1}} + \frac{1}{J_{ice,1}} \right) T_{dc} - \frac{1}{J_{em,1} \zeta_{gb}} T_{em} \right) \quad (6.18)$$

### Parallel Hybrid Phase

When the vehicle enters the parallel-hybrid mode, the control is given by the ECMS algorithm. Since the purpose of this example is to maintain good drivability, the main function of ECMS is to fulfill the driver’s torque request. This requirement is imposed by the following constraint:

$$T_{dr,req} := \zeta_{gb} T_{em} + T_{ice} = (b_{ice} + \zeta_{em}^2 b_{em}) \omega_{ice} + \frac{1}{\zeta_{tr}} (C_{aero} \omega_{wh}^2 + C_{rr}) + J_{wh,1} f(\alpha_{dr}) \quad (6.19)$$

Here,  $T_{dr,req}$  is the torque required to fulfill the driver’s pedal request, and  $f(\cdot) : \mathbb{R} \rightarrow \mathbb{R}$  is a mapping between  $\alpha_{dr}$  and the demand for vehicle acceleration. This equation constrains one of the control inputs in (6.19). The remaining control input can be



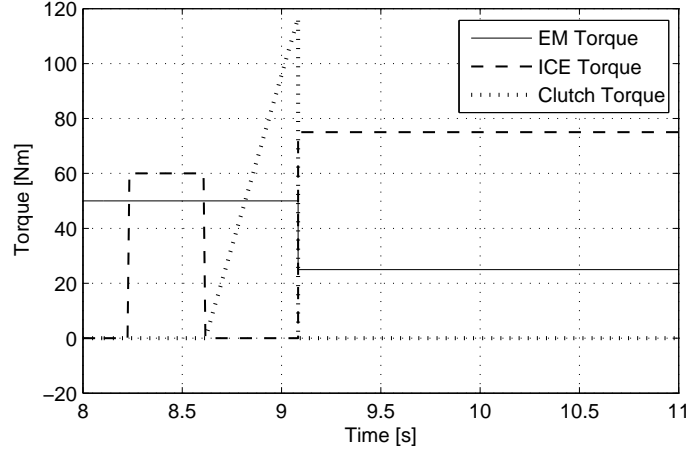


Figure 6.5: External torques acting on the system during the transition from electric only to parallel hybrid mode using open-loop control. Note that the ICE torque is a combination of the ISA and ICE torque requests.

chosen such that the fuel consumption is locally minimized (see Section 5.2.2). However, since the fuel consumption is not part of the control objective in this example, one of the control inputs can be arbitrarily selected.

#### 6.4.3 Simulation Results

As mentioned earlier, most HEV control strategies are based on minimizing the fuel consumption and rarely consider the drivability effects of the choice of control. Such an energy management strategy is used here to provide a basis for comparison. The simulations are performed assuming a constant torque request from the driver.

The energy management strategy used for comparison uses an open-loop torque profile for each actuator. The torque profiles include step changes to maintain a fixed pre-transmission torque such that the driver's power request is always satisfied (see Figure 6.5). Clearly, this strategy does not consider the internal dynamics of the system. Simulation results from this strategy are given in Figure 6.6. A significant amount of disturbance is evident in the acceleration profile as seen in the lower plot. Note that the clutch engagement was set to begin at idle speed. The result of the

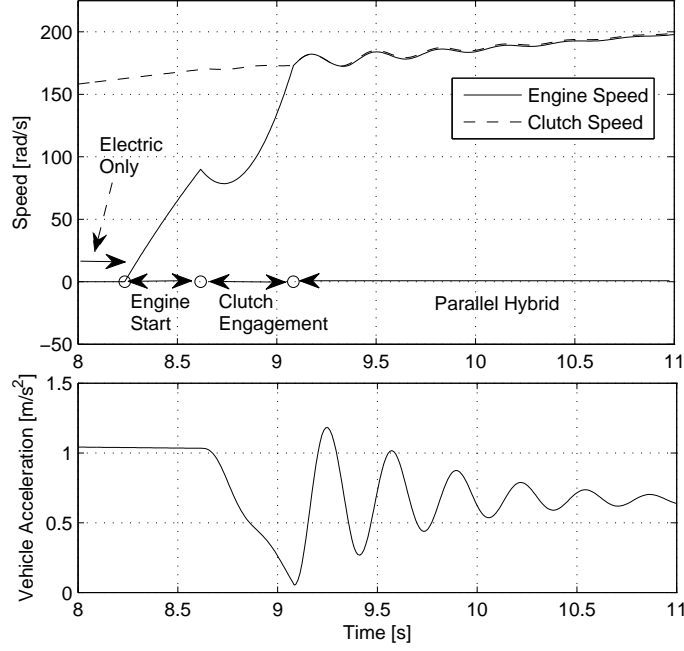


Figure 6.6: Simulated engine and clutch speeds and vehicle acceleration during the transition from electric only to parallel hybrid mode using open-loop control.

simulation illustrates that, without proper control, the mode changes would be easily noticed by the driver.

A mode change with good drivability can be realized using the control design proposed in Section 6.4.2. Figure 6.7 gives the engine and transmission input (or clutch) speeds during the transition. Although the mode transition is completed in a slightly longer duration (approximately 1.5 s) than the previous case (approximately 1 s), the longitudinal vibrations in vehicle acceleration are mostly suppressed as can be seen in the lower plot of Figure 6.7.<sup>2</sup> Note that the control law proposed in (6.18)

<sup>2</sup>A small disturbance is visible in the vehicle acceleration when the proposed control method is used. This result is due to the clutch lock-up discontinuity.

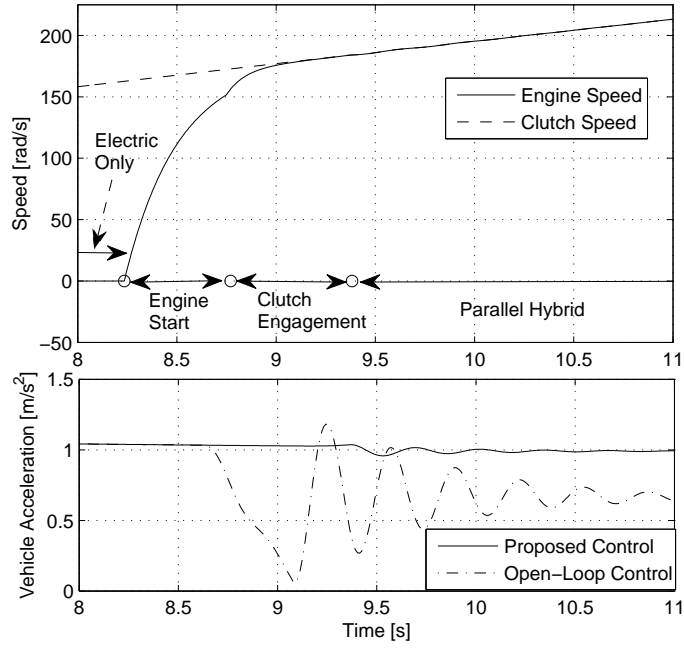


Figure 6.7: Simulated engine and clutch speeds and vehicle acceleration during the transition from electric only to parallel hybrid mode using the proposed control design.

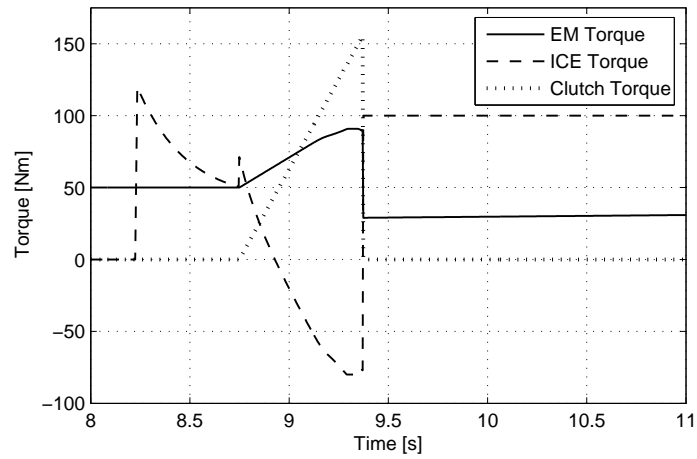


Figure 6.8: Simulated external torques during the transition from electric only to parallel hybrid mode using the proposed control design.

is slightly modified using proportional output feedback such that

$$(u'_2)_{2,1} = -J_{ice,1} \left( - (k_2)_{2,1} \Delta\omega_{dc} - \left( \frac{b_{ice}\zeta_{tr}}{J_{ice,1}} - \frac{b_{em}\zeta_{tr}}{J_{em,1}} - \frac{b_{hs}}{\zeta_{tr}\zeta_{gb}^2 J_{em,1}} \right) \Delta\omega_{hs} \right. \\ \left. - \frac{k_{hs}}{\zeta_{tr}\zeta_{gb}^2 J_{em,1}} \theta_{hs} + \left( \frac{1}{\zeta_{gb}^2 J_{em,1}} + \frac{1}{J_{ice,1}} \right) T_{dc} - \frac{1}{J_{em,1}\zeta_{gb}} T_{em} \right) \quad (6.20)$$

which allows the closed-loop response of  $\Delta\omega_c$  to be tuned using  $(k_2)_{2,1} > 0$ .

Figure 6.8 also shows the actuator torques requested by this controller. The gain  $(k_2)_{2,1}$  was chosen such that magnitude of the torque requests were within reasonable limits. Note that sudden changes in torque requests do not create undesired transients (e.g. when the parallel hybrid mode is first activated) as long as they satisfy the torque constraint given by (6.19). This is because the actuator dynamics are not modeled in this example, i.e. all actuators have infinite response bandwidth.

### Robustness Analysis

The results discussed above are valid when perfect knowledge of the plant model is assumed. This is obviously not the case in real-life applications. To investigate the effects of variations in plant dynamics, additive uncertainties are introduced to some of the system parameters that are used in the control laws given in Section 6.4.2. The numerical values of the uncertainties are given in Table 6.1. The focus here is on the parameters that are most likely to experience variations due to changes in the environmental conditions (e.g. clutch friction coefficient), or those that are not constant or not accurately known in reality (e.g. engine inertia, half shaft damping and stiffness coefficients). The specific numerical values are chosen according to the expected bounds on parameter variations.

Since the control design presented in Section 6.4.2 mostly relies on feedforward cancelation of the plant dynamics, using the same control laws does not provide satisfactory results in the presence of plant uncertainty, particularly in the clutch engagement phase. Therefore, the control laws that are active in this phase are modified as follows:

Parameter	$\Delta\mu_{dc}$	$\Delta b_{ice}$	$\Delta b_{hs}$	$\Delta k_{hs}$	$\Delta J_{ice,1}$	$\Delta J_{wh,1}$
Uncertainty [%]	25	25	50	25	25	10

Table 6.1: Numerical values of the parameter uncertainties used for controller robustness analysis.

$$(u_2'')_{1,1} = -J_{ice,1} \left( - (k_2)_{1,1} \Delta\omega_{hs} + \frac{b_{em}}{J_{em,1}} \omega_{wh} + \left( \frac{k_{hs}}{J_{em,1} \zeta_{tr}^2 \zeta_{gb}^2} + \frac{k_{hs}}{J_{wh,1}} \right) \theta_{hs} \right. \\ \left. - \frac{1}{J_{em,1} \zeta_{tr} \zeta_{gb}^2} T'_{dc} - \frac{1}{J_{wh,1}} (C_{aero} \omega_{wh}^2 + C_{rr}) \right) \quad (6.21)$$

$$(u_2'')_{2,1} = -J_{ice,1} \left( - (k_2)_{2,1} \Delta\omega_{dc} - \left( \frac{b_{ice} \zeta_{tr}}{J_{ice,1}} - \frac{b_{em} \zeta_{tr}}{J_{em,1}} - \frac{b_{hs}}{\zeta_{tr} \zeta_{gb}^2 J_{em,1}} \right) \Delta\omega_{hs} \right. \\ \left. - \frac{k_{hs}}{\zeta_{tr} \zeta_{gb}^2 J_{em,1}} \theta_{hs} + \left( \frac{1}{\zeta_{gb}^2 J_{em,1}} + \frac{1}{J_{ice,1}} \right) T'_{dc} - \frac{1}{J_{em,1} \zeta_{gb}} T_{em} \right) \quad (6.22)$$

where  $(k_2)_{1,1} > 0$  is a feedback gain, and  $T'_{dc} = 2\mu_{dc} R_{dc} A_{dc} p_{dc} \tanh\left(\frac{1}{\epsilon'}(\omega_{ice} - \frac{1}{\zeta_{gb}}\omega_{em})\right)$ . Note that the only differences are the addition of the feedback term  $(k_1)_{2,1}\Delta\omega_{dc}$  in (6.21), and the use of the modified clutch torque expression (only used in the control laws) with  $\epsilon'$  such that  $\epsilon' \gg \epsilon$ . The main function of the output feedback term in (6.21) is to dissipate the adverse effects of the uncertainty in the half shaft stiffness coefficient. The modified clutch torque expression helps reject the clutch disturbance when the clutch friction coefficient is not accurately known. Otherwise, both actuators attempt to overcorrect for the clutch disturbance since the friction coefficient is overestimated.

Also, note that the actuator limits are constrained in this case such that  $|T_{ice}| < 80 \text{ Nm}$  and  $|T_{em}| < 150 \text{ Nm}$ .<sup>3</sup> The numerical values of these limits are chosen in accordance with the peak torque capabilities of the electric machines that are used in the experimental vehicle.

<sup>3</sup>The saturation limits for  $T_{ice}$  are selected according to the ISA torque limits.

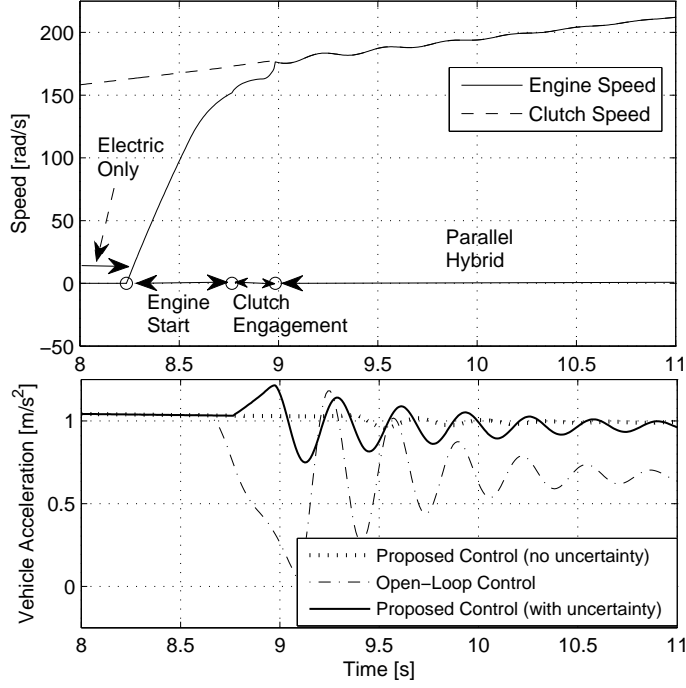


Figure 6.9: Top plot shows the simulated engine and clutch speeds using the revised control laws in the presence of model uncertainty. Lower plot shows a comparison of the vehicle accelerations for the three cases considered here.

The results are shown in Figure 6.9. The controller that uses the revised control laws achieves an acceptable performance in the presence of model uncertainty. The constrained torque requests are also shown in Figure 6.10. It is concluded that the magnitudes of the uncertainties in  $k_{hs}$  and  $\mu_{dc}$  have the largest impact on the controller performance. Especially proper calibration of  $\epsilon'$  is crucial to successfully compensate for the clutch disturbance. Larger values of  $\epsilon'$  result in smoother clutch engagements as shown in Figure 6.11.

#### 6.4.4 Remarks on the Closed-Loop Stability of the Switched System

Although a formal proof for the closed-loop stability of the switched dynamic system is not given here, a few remarks should be made regarding this topic.

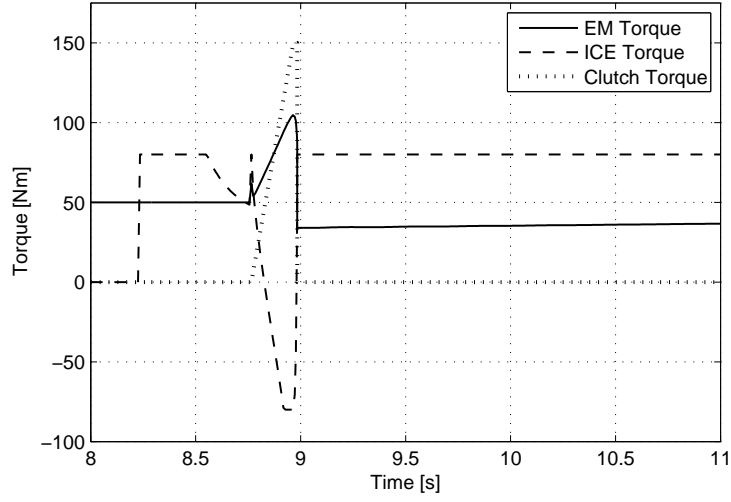


Figure 6.10: External torques acting on the system in the presence of model uncertainty and actuator torque limitations.

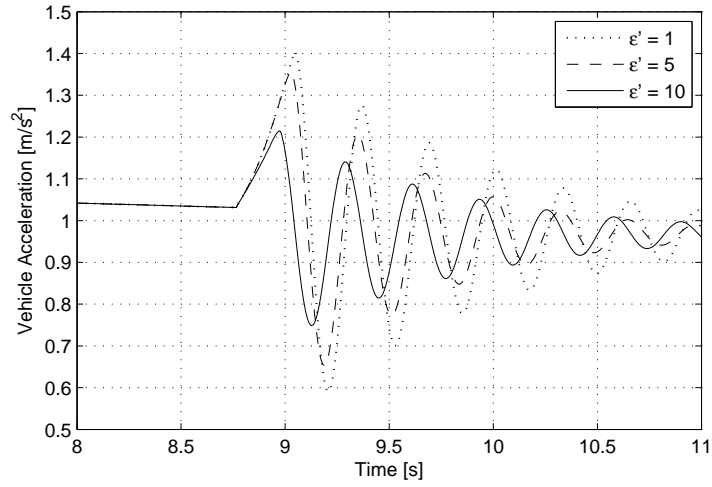


Figure 6.11: The effect of clutch torque tolerance  $\epsilon'$  (used in the control law) on the simulation result when the clutch friction coefficient is not accurately known.

The proposed control design method is based on linearizing control laws that result in asymptotically stable output dynamics for each mode of operation. However, it is clearly known that the stability of the individual system modes does not imply the stability of the overall switched dynamic system [4]. In order to ensure the stability of the closed-loop system in a Lyapunov sense, the dwell time approach described in [4] can be utilized. This approach requires the switching signals to be restricted in a way such that the interval between consecutive switching times is no smaller than the so-called dwell time,  $\tau_s$ . As an example, suppose that the switched system has two modes where  $\Sigma_1$  is active in  $[t_0, t_1)$  and  $\Sigma_2$  is active in  $[t_1, t_2)$ . Also, assume that there exist Lyapunov functions  $V_i$  and positive constants  $a_i, b_i, c_i$  (where  $i = \{1, 2\}$ ) that satisfy

$$a_i|x|^2 \leq V_i(x) \leq b_i|x|^2 \quad (6.23)$$

$$\dot{V}_i(x) \leq -c_i|x|^2 \quad (6.24)$$

If a sufficiently large dwell time can be found for all possible switching pairs that satisfy

$$V_1(t_2) \leq \frac{b_1 b_2}{a_1 a_2} e^{-\left(\frac{c_1}{b_1} + \frac{c_2}{b_2}\right)\tau_s} V_1(t_0) \quad (6.25)$$

then the switched dynamic system (assuming that the individual subsystems that are linearized by the controller are also asymptotically stable) is globally asymptotically stable.<sup>4</sup> Therefore, ensuring stability in this case requires the use of a similar argument based on multiple Lyapunov functions to obtain an average dwell time for the closed-loop switched dynamic system. The detailed proof of this statement is left as future work.

## 6.5 Summary

The sketch of a framework for the systematic design of hybrid controllers is presented for a class of switched hybrid dynamical systems. The dynamics of this class of switched systems are described by a combination of smooth and discrete dynamics.

<sup>4</sup>See [4] for a detailed derivation of this result.



The switching conditions are assumed to be functions of the state only. A key feature of the control design methodology is the change of control action in a neighborhood of the switching set where transition to another mode is imminent.

The proposed approach is shown to be effective in addressing the hybrid nature of a simplified HEV driveline. Simulation results confirmed that mode transitions that result in good drivability can be realized using the proposed controller when compared to a heuristic control technique. The experimental verification of the proposed control method is also discussed in Chapter 7.

## CHAPTER 7

### EXPERIMENTAL VERIFICATION OF CONTROL STRATEGIES

This chapter describes the experimental verification of the control strategies developed in Chapters 5 and 6 on the OSU hybrid-electric vehicle. The results highlight mainly the improvements in vehicle drivability. Additionally, some general results are presented to demonstrate proper functionality of the hybrid powertrain, the overall vehicle performance and the fuel consumption over selected driving cycles.

#### 7.1 Electric Only Mode: Active Damping Controller

As described in Section 5.2.2, using an active damping strategy is essential to reduce the drivability problems associated with pedal tip-in/tip-out during the electric only operating mode. The lack of a torque coupler results in an underdamped (rear) driveline that is prone to issues such as shunt and shuffle when large torque gradients occur. The presence of gear backlash further aggravates these problems as demonstrated in Section 4.2.1.

In this section, two control strategies are implemented to address these issues. The first strategy is an output feedback controller that is active when the gears are in full contact, i.e. when there is no sign change in the rear driveline torque. This is also the model-based controller proposed in Section 5.2.2. The second strategy incorporates a combination of feedback and feedforward controls. The main function of the feedforward part is to reduce the disturbances caused by gear backlash, therefore, it is only active when there is a sign change in the rear driveline torque. This approach

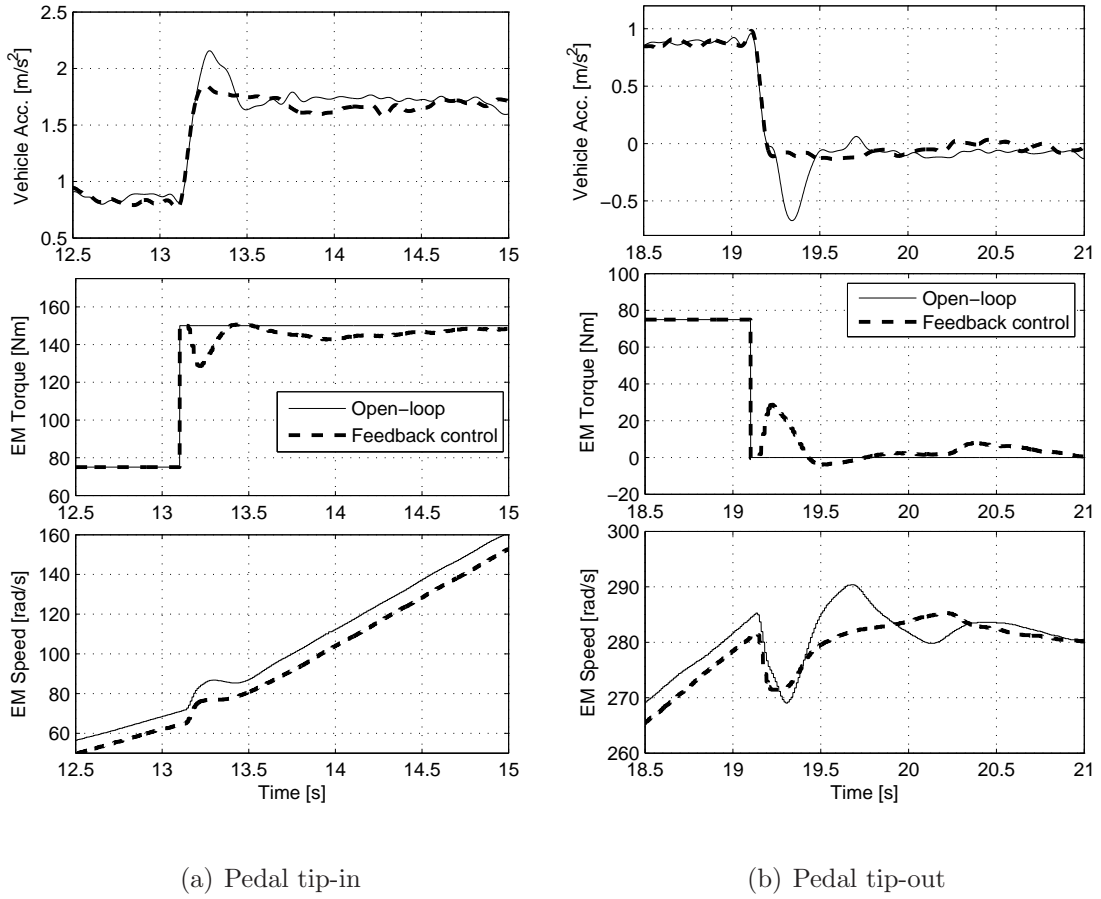


Figure 7.1: Experimental validation of the feedback controller during pedal tip-in and tip-out. The test vehicle is in electric only operating mode.

is analogous to the switching controller proposed in [120] where different controllers are active in the gear contact phase and in the backlash phase.

The performance of the feedback controller is evaluated by a pedal tip-in/tip-out maneuver while the driving gears are in contact. This test involves a step change in  $T_{em,req}$  from 75 Nm to 150 Nm followed by a tip-out maneuver that reduces  $T_{em,req}$  from 75 Nm to 0 Nm. Figure 7.1 summarizes the results of this test for both maneuvers. The overshoot in vehicle acceleration resulting from the pedal tip-in (or undershoot for the tip-out) is successfully damped using speed feedback from the rear

electric machine. The effectiveness of the controller is also evident from the initial EM speed transients; the low-frequency oscillations in  $\omega_{em}$  are smaller in magnitude when the feedback controller is used. Note that the controller gain is slightly reduced here in comparison to the initial design (from  $K = 5$  to  $K = 3$ ). The controller torque requests are shown in the middle plots of Figures 7.1(a) and 7.1(b).

Despite the satisfactory controller performance achieved in this case, one can conclude that the driveline disturbances resulting from pedal tip-in/tip-out, even when feedback control is not used, are not severe as long as the gears are in full contact. A second experiment is performed to demonstrate the impact of backlash reversal on the controller performance. The vehicle is launched in electric only mode by applying a step change in torque request from 0 Nm to 75 Nm. In this test, the performances of three control strategies (open-loop control, feedback control, and combined feedback and feedforward controls) are compared for the same maneuver. The results of these tests are depicted in Figure 7.2.

Clearly, the pedal tip-in disturbance is severe in the case of open-loop control; the vehicle acceleration reaches 2 m/s<sup>2</sup> from standstill within 0.1 s. Such a large rate of change in vehicle acceleration results in poor drivability. Figure 7.2 also indicates that, following the acceleration overshoot, a small torque hole appears at  $t = 10.6$  s. When the feedback controller is used, only partial improvements in drivability are achieved in the presence of gear backlash. The overshoot in vehicle acceleration is slightly reduced, however, the initial jerk remains unimproved.

It is concluded that a feedforward controller is needed to address this issue, i.e. the problem of smoothly traversing gear backlash. In this work, a combined feedforward and feedback control law of the following form is used:

$$T'_{em,req} = \begin{cases} (T_{bl,0} - T_{bl,1}) \exp(-t_{bl}/\tau_{bl}) + T_{bl,1} & t_{bl} \leq 3\tau_{bl} \\ T_{em,req} + K\omega_{em,hp} & t_{bl} > 3\tau_{bl} \end{cases} \quad (7.1)$$

where  $T'_{em,req}$  is the adjusted EM torque request,  $T_{bl,0}$  and  $T_{bl,1}$  are torque requests such that  $T_{bl,0}$  is equal to the initial value of  $T_{em,req}$  and  $T_{bl,1}$  is chosen such that  $T_{bl,1} = 0.2 T_{bl,0}$ .  $t_{bl}$  is the time elapsed after pedal tip-in ( $t_{bl}$  is triggered when  $T_{em,req}$  changes direction). An important calibration parameter in (7.1) is  $3\tau_{bl}$ , or what is

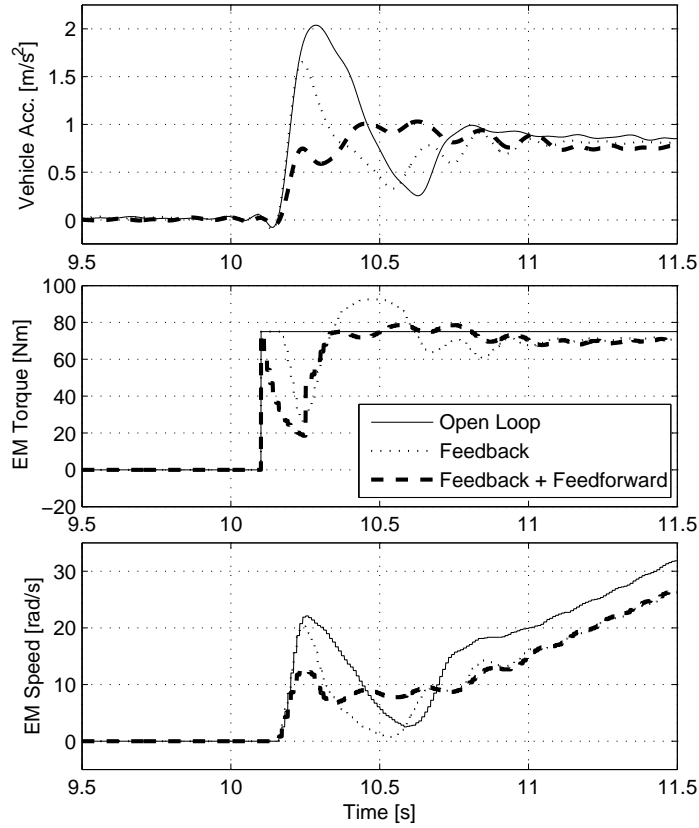


Figure 7.2: Controller performances when there is a change in backlash direction.

referred to here as the backlash fill time. In this work, the backlash fill time is selected according to the simulation predictions given in Figure 7.3. This plot shows the simulated backlash fill time as a function of the torque applied to traverse full gear clearance,  $2\theta_{bl,0}$ . As expected, the backlash fill time changes inversely proportional to the torque request. Since the decay rate of the backlash fill time becomes relatively steady for torque requests larger than 20 Nm, a value of  $3\tau_{bl} = 0.15$  s is sufficient to traverse full gear backlash. Therefore,  $\tau_{bl} = 0.05$  s is selected for the feedforward controller. Note that traversing the backlash faster than 0.15 s does not degrade

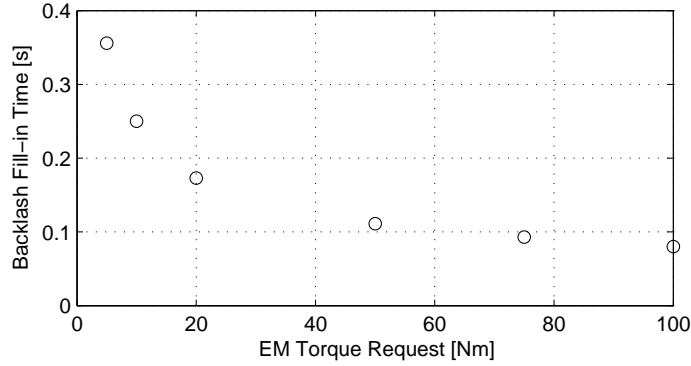


Figure 7.3: Simulated backlash fill time as a function of the EM torque request.

the controller performance significantly.<sup>1</sup> Therefore, choosing a conservative value is more suitable for actual implementation.

The motivation for using a relatively simple feedforward controller for backlash compensation is due to the fact that the backlash position can not be measured. Although certain techniques are available to estimate backlash position [107], this topic is beyond the scope of this research.

Overall, the performance of the switched controller is superior to that of the feedback controller when gear backlash is present. Figure 7.2 indicates that by using the switched controller the acceleration overshoot is completely eliminated. Note that the feedforward controller's primary function is to enable soft landing of the driving gear since the acceleration overshoot is mainly caused by a sudden impact of the gears during the initial engagement.

The controller torque requests for the three cases investigated here are also given in the middle plot of Figure 7.2 to facilitate easy comparison of the controller behaviors. The lower plot shows the differences between the EM speed transient responses. This plot also confirms the conclusions derived so far about the performances achievable by these three controllers.

<sup>1</sup>If the backlash is traversed quicker, then the drive shaft will simply be pre-loaded for a brief period of time.

## 7.2 HEV Control Strategy: In-Vehicle Validation

This section demonstrates the performance and overall behavior of the proposed multi-mode HEV control strategy in actual driving conditions. The results presented here serve as a validation of the control strategies (supervisory and component level) developed in Chapter 5. The presentation focuses on high-level results that represent the low-frequency ( $< 1$  Hz) dynamic behavior of the vehicle.

### 7.2.1 Test 1: Investigation of Control Strategy Behavior

The first experiment is conducted over a short driving segment that is representative of a combination of urban and highway driving conditions. The purposes of this test are to verify proper functionality of the hybrid powertrain and to analyze the qualitative behavior of the control strategy in different sections of the driving pattern.

The vehicle speed and the engine speed acquired from this test are shown in Figure 7.4. The vehicle speed trace is divided into a number of sections and the control strategy operating modes that are triggered during this test are marked on the upper plot in Figure 7.4.<sup>2</sup> The actuator torque requests, driver's accelerator and brake pedal requests and the resulting vehicle acceleration (obtained from the chassis accelerometer) are given in Figure 7.5. Also, Figure 7.6 shows the battery current, battery voltage, estimated battery SOC and the ECMS equivalence factor.

Initially, the vehicle starts from a standstill while the engine is shut off. This results in a zero diesel fuel consumption until  $t = 4$  s since the vehicle operates in zero-emissions (or electric only) mode. The torque request given to the rear electric machine (computed using (5.3)) is shown in the upper plot of Figure 7.5. After the vehicle launch, the engine is started using the BSA, thus engaging the vehicle into hybrid operating mode. In this case, the engine is started at a low vehicle speed in order to ensure proper synchronization of the internal transmission speeds during the

<sup>2</sup>Transitional modes such as engine start/stop are not shown here.

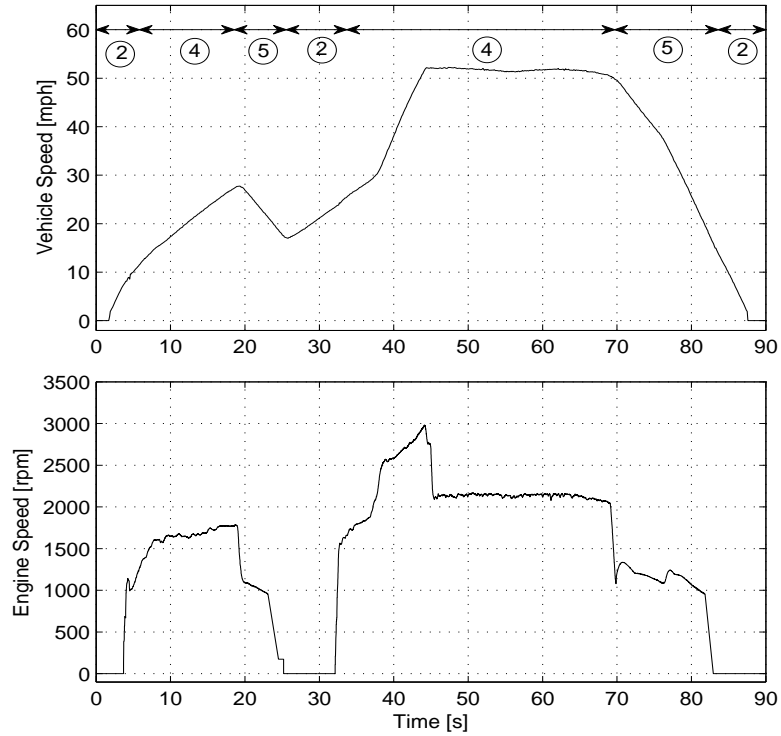


Figure 7.4: Vehicle speed and engine speed acquired during the control strategy verification test. Following the convention in Figure 5.5, test sections are labeled such that 2, 4 and 5 represent the electric only, hybrid and regenerative braking modes respectively.

mode change. Note that rear EM continues to provide the necessary tractive torque during the engine start event.

While operating in hybrid mode, the test vehicle is first accelerated until a brake request is received from the driver at  $t = 19$  s. The three-way split ECMS, previously described in Chapter 5, is functional between  $t = 5$  s and  $t = 19$  s. Within this time window, the ECMS primarily uses the engine to provide the driver's power request after a brief period of EM torque assist between  $t = 5$  s and  $t = 8$  s (see Figure 7.5). An important result should be noted from the vehicle acceleration in the lower plot of Figure 7.5. Despite the change of operating modes, the vehicle acceleration is consistent with what is expected from a conventional vehicle during an acceleration



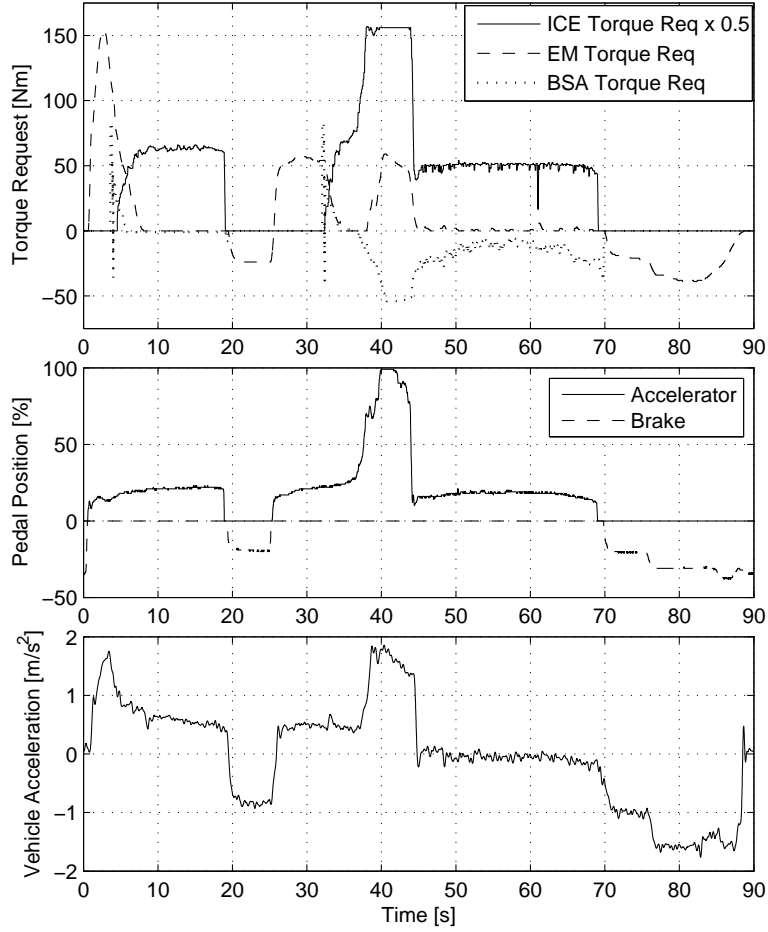


Figure 7.5: Actuator torque requests, driver's pedal positions and vehicle acceleration obtained during the control strategy verification test.

from standstill.<sup>3</sup> This is a result of the use of the power demand expression (5.2) for both electric only and hybrid operating modes. In other words, the driver's power request is fulfilled regardless of the operating state of the engine; a highly desirable drivability feature for hybrid-electric vehicles.

As a result of the braking request at  $t = 19$  s, the supervisory controller triggers the regenerative braking, engine stop and electric only modes, respectively. Since the

<sup>3</sup>Although, expected vehicle acceleration is a subjective measure, a desired acceleration trace (for fixed accelerator input) typically incorporates an initial target peak acceleration followed by a gradual decrease as the vehicle speed increases. See [121] for a qualitative example.

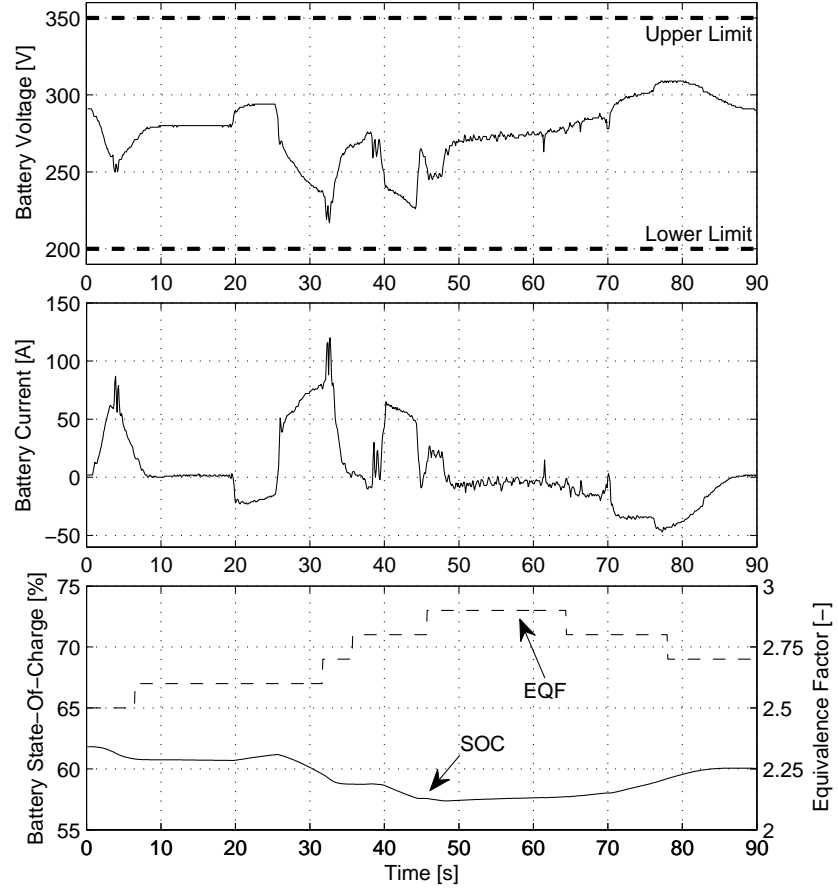


Figure 7.6: Battery voltage, battery current (positive currents indicate battery discharge), estimated battery SOC, and the ECMS equivalence factor obtained during the control strategy verification test.

engine is stopped while the transmission is in third gear, the electric only function is used more extensively and without jeopardizing drivability due to the high vehicle speed. This is possible because of the low gear ratio between the transmission input and output shafts, which allows the engaging clutch speeds to remain synchronized for a longer period of time compared to the case of the first or the second gear.

Shortly after the engine start at  $t = 32$  s, the vehicle is accelerated to a highway speed and maintained at a nearly fixed speed until  $t = 70$  s. During the acceleration,

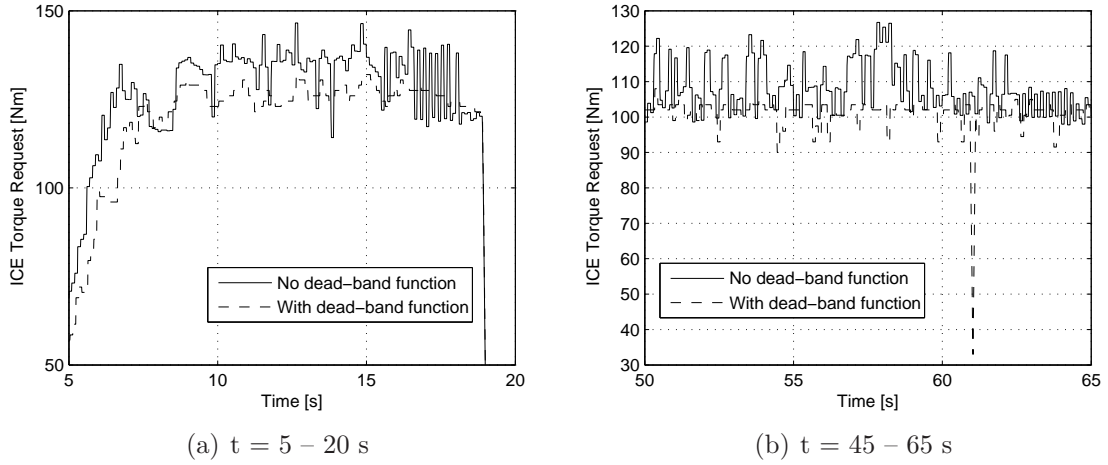


Figure 7.7: Effectiveness of the dead-band function in reducing torque chattering.

ECMS uses the traction EM to provide torque assist to the engine. When the vehicle reaches a highway speed, ECMS uses the BSA to charge the high-voltage battery.

Note that the engine torque request given by ECMS during the highway portion of the test contains a small amount of high frequency ripple as well as a brief torque spike at  $t = 61$  s. This situation typically occurs when a constant pedal request is received from the driver under steady operating conditions such as cruising. As described in Chapter 5, a dead-band function is used to limit the amount of torque chattering in these situations. Figure 7.7 shows the effectiveness of this approach. Here, the engine torque requests recorded from two sections of the test are compared with the engine torque requests generated by ECMS without the use of the dead-band function.<sup>4</sup> The results clearly demonstrate that the dead-band function reduces the amount of torque chattering.

After the highway portion of the test, the vehicle is gradually decelerated as a result of the driver's brake request. The regenerative braking mode is engaged at  $t = 70$  s, and the engine is shut off at  $t = 82$  s which enables the electric only mode. The

<sup>4</sup>The latter result is obtained by simulating the control strategy using the feedback signals recorded from the same experiment.

negative EM torque request is computed using the mapping function given by (5.31) in both operating modes. As shown in the upper plot of Figure 7.5, the EM torque request is gradually reduced to zero as the vehicle approaches zero speed. This is necessary to avoid braking related drivability problems at low vehicle speeds.

Another important objective of the control strategy is to ensure proper operation of the electrical powertrain. This includes maintaining the battery SOC within a desired range and respecting voltage and current limitations imposed by the motor inverters and the battery. The upper plot of Figure 7.6 indicates that the battery voltage is maintained within safe operating limits. The lower plot shows that the battery SOC is sustained within the desired range of 50 – 80%. The variation of the ECMS equivalence factor is also shown on the same plot. The nominal value of the equivalence factor is adjusted using the SOC correction function (5.25).

The middle plot of Figure 7.6 shows the variation of the battery current with time. Due to the instantaneous battery power limit (approximately 35 kW), the maximum allowable battery charge and discharge currents are also limited. However, the instantaneous charge current limit of the battery does not pose a practical constraint on the control strategy, since the upper voltage limit of the EM inverter has a higher priority in the case of charging. However, the power limit of the battery under discharging often becomes a constraining factor. To ensure proper battery and inverter operation, the torque request to the rear electric machine is limited accordingly.

### 7.2.2 Test 2: Fuel Economy Comparison

The second experiment of this section is conducted over a 20 min driving cycle to evaluate the fuel consumption of the test vehicle using the multi-mode HEV control strategy. The details of the test cycle are given in Appendix B. Two tests are performed over the same driving cycle under warm engine operating conditions.<sup>5</sup> The first test facilitates a benchmark comparison using an engine only strategy that commands a small BSA torque to offset the electrical accessory power (less than 1

<sup>5</sup>The consistency of the driving conditions between two tests is high as verified by the driving cycle statistics in Appendix B.

Test Case	Power Rating [kW]	Diesel Fuel Consumption [MPG]	Gasoline Equivalent Fuel Consumption [MPGGE]	Corrected Fuel Consumption [MPGGE]	Improvement [%]
Baseline Vehicle (City)	138	N/A	17	17	0
Test Vehicle (Engine Only)	110	20.6	20.2	22.1	30.0
Test Vehicle (Hybrid)	145	24.1	23.7	23.7	39.4

Table 7.1: A comparison of the fuel consumptions obtained from the test vehicle (using different control strategies) and the fuel consumption of the baseline vehicle over the urban driving schedule.

kW). The second test features the multi-mode HEV control strategy described in Chapter 5.

The fuel economy results obtained from the test vehicle are summarized in Table 7.1. Also included in this table is the Environmental Protection Agency reported fuel economy estimate (for city driving) for the baseline 2005 Chevrolet Equinox according to 2008 regulations [122]. The fuel economies are compared using three measures: diesel fuel consumption in miles per gallon (MPG), gasoline equivalent fuel consumption in miles per gallon gasoline equivalent (MPGGE), and the vehicle weight corrected gasoline equivalent fuel consumption (for the engine only case). The last item is not a standard fuel economy measure and it is introduced here to facilitate a fair comparison between the engine only strategy and the proposed control strategy. The vehicle weight correction factor  $\gamma_{wc}$  is calculated using the following expression:

$$\gamma_{wc} = \frac{\int_{t_0}^{t_f} (F_{aero}(v_{veh}) + F_{rr}(M'_{veh}) + F_{inertia}(M'_{veh}, a_{veh})) v_{veh} dt}{\int_{t_0}^{t_f} (F_{aero}(v_{veh}) + F_{rr}(M_{veh}) + F_{inertia}(M_{veh}, a_{veh})) v_{veh} dt} \quad (7.2)$$

where the aerodynamic drag, rolling resistance and vehicle inertia forces are given as

$$\begin{aligned} F_{aero}(v_{veh}) &= \frac{1}{2} \rho_a C_d A_{veh} v_{veh}^2 \\ F_{rr}(M_{veh}) &= M_{veh} g C_{rr,0} \\ F_{inertia}(M_{veh}, a_{veh}) &= M_{veh} a_{veh}. \end{aligned} \quad (7.3)$$

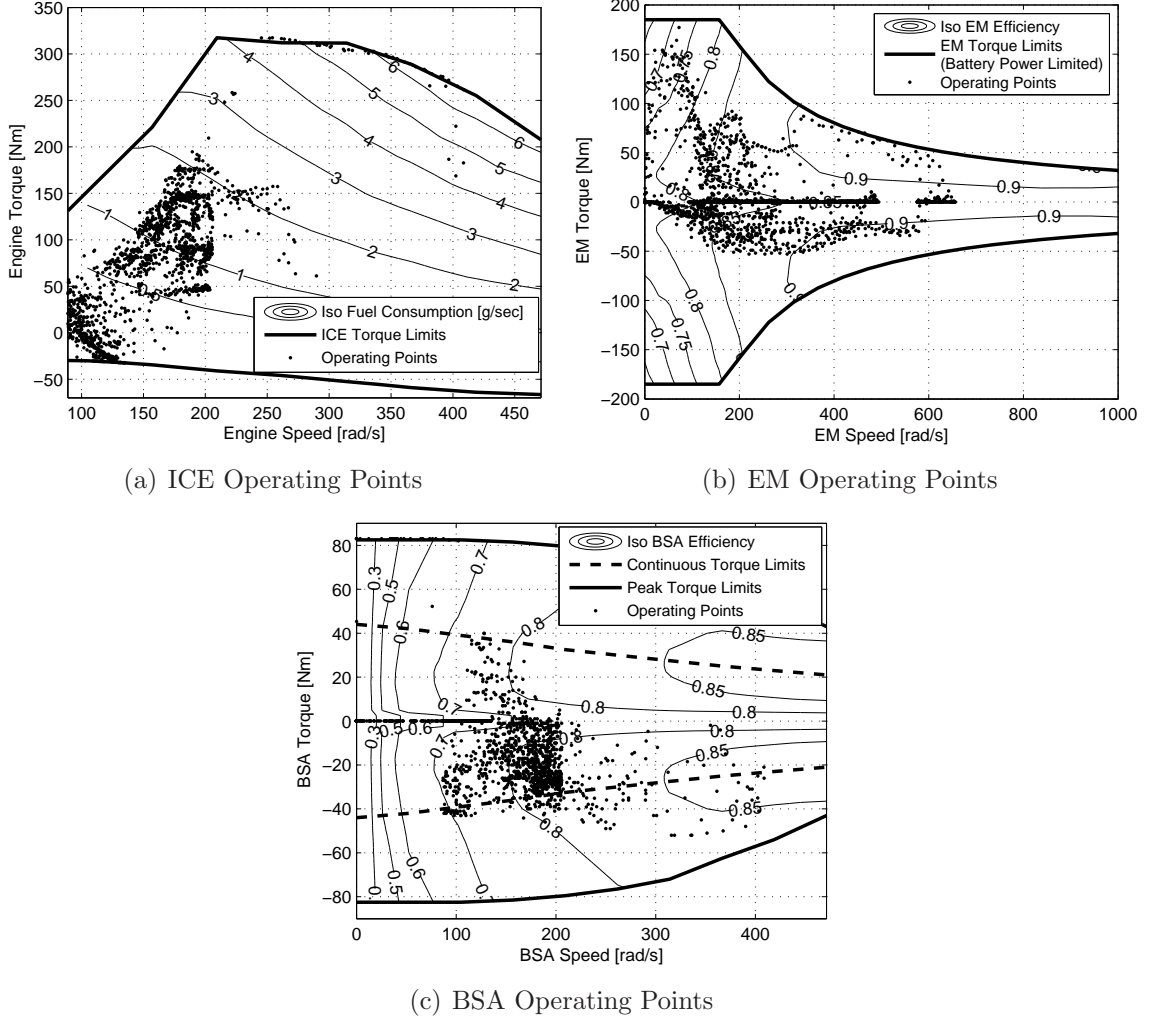


Figure 7.8: Operating points of the actuators on the speed-torque plane.

$M'_{veh}$  is an estimate of the test vehicle mass for the diesel only vehicle configuration (excluding the weight of the hybrid powertrain components). In this case,  $M_{veh} = 2050$  kg and  $M'_{veh} = 1800$  kg are used to represent the actual and corrected vehicle masses (both including the weight of the driver). For the test cycle investigated here,  $\gamma_{wc} = 0.914$ . The corrected fuel consumption for the engine only configuration is then simply the product of  $\gamma_{wc}$  and the gasoline equivalent MPG.

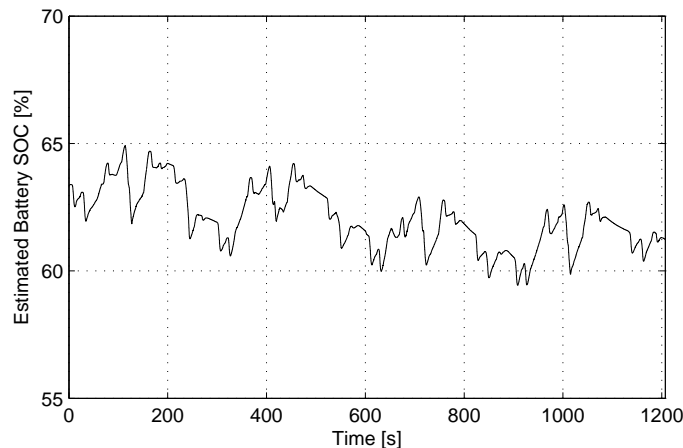


Figure 7.9: The estimated battery SOC during the fuel economy test.

The fuel economy results given in Table 7.1 suggest that the HEV control strategy helps to achieve a 39.4% improvement over the baseline vehicle in urban driving conditions.<sup>6</sup> However, one must note that the majority of the fuel savings is due to the use of a downsized high-efficiency diesel engine. This conclusion, although mostly true, is also slightly misleading. The diesel only configuration is capable of generating 110 kW of peak power, whereas the hybrid configuration can deliver up to 145 kW power during peak conditions. This implies that the latter configuration provides significant advantages in terms of performance and fuel economy for aggressive driving cycles.

Figure 7.8 shows the operating points of the actuators on their respective speed-torque planes. A few points are worthwhile to note regarding the motor (EM and BSA) specifications given in Figure 7.8. The EM torque limits at medium and high speeds are determined by the maximum high-voltage battery power. The EM efficiency curves represent the combined efficiencies of the inverter and the rear electric machine. The BSA torque limits are given by two curves that represent continuous (dashed line) and peak (solid line) torque limits of the motor. Also note that

<sup>6</sup>Appendix B confirms the high statistical correlation between the characteristics of the standard urban driving schedule and the given test cycle.

the BSA efficiency curves are scaled from a standard electric machine map since the actual efficiency data is not available for the BSA.

As shown in Figure 7.8(a), the engine operating points are concentrated in the low speed region because of the nature of the driving cycle. Large torque requests at low engine speeds are mostly avoided (due to the poor engine efficiency) as a result of the electric launch functionality of the test vehicle. Figure 7.8(b) shows that the hybrid control strategy primarily uses the EM for (i) low speed traction, (ii) regenerative braking, (iii) torque assist to the engine during periods of high power demand. Also, note that the regenerative braking torques are gradually reduced as the vehicle approaches zero speed. This is a result of the drivability modification introduced by (5.31). The BSA is used primarily for battery charging as depicted in Figure 7.8(c). There are only a limited number of operating conditions for which the BSA is used for torque assist to the engine. Note that a few data points are located outside the BSA continuous torque limit. However, since the peak torque limit is also permitted for brief instances of operation (up to 10-15 seconds), this does not pose a concern for the safety of the component.

Finally, Figure 7.9 shows the estimated battery SOC obtained from the fuel economy test.<sup>7</sup> The control strategy successfully maintains the battery SOC within the desired limits. Although there is a slight trend of decrease during the first half of the driving cycle, the battery SOC is maintained above 60% during the second half of the cycle with the aid of the SOC correction function given in (5.25).

### 7.3 Control of HEV Launch

The challenges associated with enabling a smooth launch for a HEV are introduced in Chapter 6 using a simplified driveline example. In this section, the hybrid control design given in Section 6.4 is revised for the test vehicle and the results obtained from the experimental verification of this technique are presented.

<sup>7</sup>The battery SOC is computed by an adaptive estimation technique using battery current, voltage and temperature. The details of the estimation algorithm are beyond the scope of this research.



Despite the similarities between the dynamics of the simplified driveline example of Section 6.4 and the dynamics of the test vehicle, the latter case presents more complexities. The test vehicle incorporates additional DOFs in the driveline. Also, the differences between the actuator torque requests and the actual torque outputs should be taken into consideration in the control design. These differences are more evident at the engine torque input channel and they are mainly caused by the unmodeled engine dynamics and the torque disturbances that are generated by the engine control unit during the engine start event.

The mode traversals of the test vehicle during HEV launch can be represented by the mode diagram given in Figure 6.4. The vector fields that describe the dynamics of the hybrid phases as well as the switching sets and the transition maps are given in Appendix C. Note that the model is valid under the assumption that the transmission engages in first gear after the engine start.

### **7.3.1 Control Design**

The controllers that are in effect during various phases of vehicle operation are designed using the information obtained from the hybrid system model given in Appendix C. These controllers are described next.

#### **Engine Start Phase**

The control objective in the engine start phase is different for the test vehicle than the control objective given in the simulation example. The goal in this case is to start the engine rapidly, rather than to minimize the speed difference between the transmission input shaft and the engine crankshaft. Therefore, the control problem

can be reformulated as follows:

$$\begin{aligned}
\mathcal{J}_1^2 &= \int_{t_0}^{t_f} 1 \cdot dt \\
|T_{bsa,req}| &< T_{bsa,max}(\omega_{ice}) \\
|T_{em,req}| &< T_{em,max}(\omega_{em}) \\
\omega_{ice}(t_f) &> \omega_{ice,idle} \\
P_{dr,req}^+ &= T_{em,req}\omega_{em}\bar{\eta}_r + T_{bsa,req}\omega_{ice}\bar{\eta}_f
\end{aligned} \tag{7.4}$$

where  $t_0$  and  $t_f$  are the start and end times of the engine start phase. This control problem has the following trivial solution since the engine dynamics are decoupled<sup>8</sup> from the dynamics of the driveline during the engine start event:

$$\begin{aligned}
T_{bsa,req} &= T_{bsa,max}(\omega_{ice}) \\
T_{em,req} &= \min \left( \frac{1}{\omega_{em,lp}\bar{\eta}_r} P_{dr,req}^+, T_{em,max} \right) \\
T_{ice,req} &= 0.
\end{aligned} \tag{7.5}$$

Note that the solution for  $T_{bsa,req}$  is different than that proposed by Canova *et al.* in [114]. This is because the traditional engine start problem investigated in [114] is a trajectory following problem, whereas the control objective in this case simply involves the minimization of the engine start time.

## Clutch Engagement Phase

The primary focus of control design for HEV launch is the clutch engagement phase, or the torque blending phase as referred to in Figure 5.5. The main objectives here are to reject the disturbance generated by the engaging clutch and to ensure that the torque transfer between the rear and front drive systems is done smoothly. The second objective requires taking into consideration the engine dynamics that were previously ignored in the simulation example. Therefore, the transition cost for

<sup>8</sup>Note that the transmission does not have sufficient internal pressure during the engine start event to be able to transmit torque disturbances from the engine to the wheels. Therefore,  $\bar{\eta}_f \approx 0$  during the engine start.

the clutch engagement phase is defined as follows:

$$\mathcal{J}_2^3 = w_1 |\Delta\omega_{hs,f}| + w_2 |\Delta\omega_{hs,r}| \quad (7.6)$$

where  $\Delta\omega_{hs,f}$  and  $\Delta\omega_{hs,r}$  were previously defined in (3.45). Note that the power demand constraint and the actuator torque constraints (not restated here) should be also respected by the control law. The following control law is used to achieve these objectives in the clutch engagement phase:

$$\begin{aligned} T_{bsa,req} &= -\frac{R_{pgs,r}}{R_{pgs,r} + R_{pgs,s}}(T_{c,1,th} + b_{c,1}|\Delta\omega_{c,1}|)\tanh\left(\frac{\Delta\omega_{c,1}}{\epsilon'}\right) \\ T_{em,req} &= \frac{P_{dr,req}^+ - T_{ice}\omega_{ice}\bar{\eta}_f}{\bar{\eta}_r\omega_{em,lp}} + (k_2)_{2,1}\left(\omega_{tr} - \frac{1}{R_{wh}}v_{veh}\right) \\ T_{ice,req} &= \frac{1}{\bar{\eta}_f\omega_{ice}}P_{dr,req}^+ + b_{ice,1}\omega_{ice} + b_{ice,0}. \end{aligned} \quad (7.7)$$

where  $T_{c,1,th} = p_{c,1,th}A_{c,1}n_{c,1}R_{c,1}\mu_{c,1}$  and  $p_{c,1,th}$  represents the estimated pressure acting on clutch C1 immediately after the engine start. Here, a feedforward control law, that aims to counteract the disturbance caused by the engaging clutch C1, is used to compute the BSA torque request. Based on a similar idea suggested in Section 6.4.2 (robustness analysis), the clutch torque tolerance  $\epsilon'$  is kept relatively large to take into account possible uncertainties in the actual clutch torque.

The ICE torque request is calculated based on the driver's power demand. The internal engine friction is also included in the control law. The EM torque request consists of a feedforward and a feedback term. The feedforward term aims to compensate for the engine's inability to quickly satisfy the driver's power demand after the engine start phase.<sup>9</sup> The objective of the feedback term, tuned by  $(k_2)_{2,1}$ , is to provide active damping to further reduce the driveline vibrations caused by the abrupt clutch engagement. Although, the second term in the cost function (7.6) is not explicitly addressed by the controller, ensuring that the EM torque request smoothly changes during the clutch engagement phase suffices to achieve this goal. For this purpose,

<sup>9</sup>The feedforward part of the EM torque request is a function of the actual engine torque ( $T_{ice}$ ) rather than the engine torque request. The hybrid system model in Appendix C includes  $T_{ice}$  as a state.

the feedback gain,  $(k_2)_{2,1}$ , is properly tuned to avoid excessive excitation of the rear driveline dynamics.

## Parallel Hybrid Phase

In this phase, the control is given by the equivalent fuel consumption minimization strategy. An important benefit of the implementation scheme described in Section 5.2.2 (see Figure 5.19(b)), which is also utilized here, is the control strategy's capability to properly initialize after the mode transition. The controller initializes using torque requests from the last control update, i.e., using the last output of the clutch engagement controller. This eliminates the need for a bumpless transfer scheme, since the control signal does not experience large changes while switching from clutch engagement to hybrid mode.

### 7.3.2 Experimental Results

Next, a comparison of the proposed control strategy and an open-loop, heuristic control strategy that was used in early phases of the project is given. The control variable that has the largest impact on the mode transition quality is the vehicle speed during the engine start. Therefore, the vehicle speed threshold that triggers the mode transition sequence is varied throughout the experiments. The tests are performed while the transmission is in first gear. Also, the accelerator pedal is maintained at a nearly fixed position.

Figure 7.10 shows the results of using the open-loop strategy of switching from engine start to hybrid mode at different vehicle speeds. The mode transition disturbance becomes more severe as the vehicle speed switching threshold is increased. In fact, when the experiments are repeated for lower speed thresholds (not shown here), the vehicle undergoes a jerk in the forward direction (a torque flare). Also, the magnitude of the torque flare increases as the switching speed threshold is decreased.

As discussed earlier, the root cause of the driveline disturbance is the abrupt engagement of the on-coming clutch due to the unsynchronized speeds between the

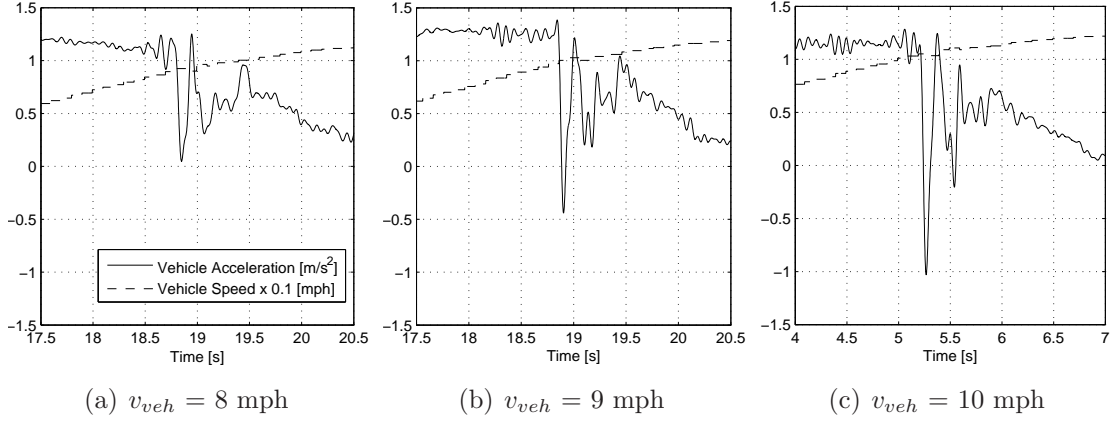


Figure 7.10: The driveline disturbance during the mode transition using the open-loop control strategy at different vehicle speeds.

input and output sides of the clutch element. Although experimental data from internal transmission speeds is not available, this phenomenon was previously illustrated using a simulation result in Figure 4.18.

Using the control strategy proposed in Section 7.3.1, the mode transition quality is significantly improved. A comparison of the results obtained from the open-loop strategy and the proposed approach is given in Figures 7.11 and 7.12. Figure 7.11 shows the comparison of vehicle acceleration and driveline speeds, and Figure 7.12 shows the actuator torque requests given by the controllers. Note that the mode transition sequence is triggered at the same vehicle speed for both experiments.

First, the behavior of the open-loop strategy is discussed. The open-loop strategy gradually reduces the EM torque request (as a function of time) between the engine start and hybrid modes, while the ICE is coming up to speed. The engine start BSA controller is the same as that proposed in [63]. The ECMS mode is activated (without using the initialization scheme discussed earlier) immediately after the engine start event. Such a strategy clearly does not consider the changes in the internal dynamics of the system, hence, it is prone to drivability issues. The results shown in Figure 7.11(a) confirm this conclusion. Despite the attempt to smoothly blend the

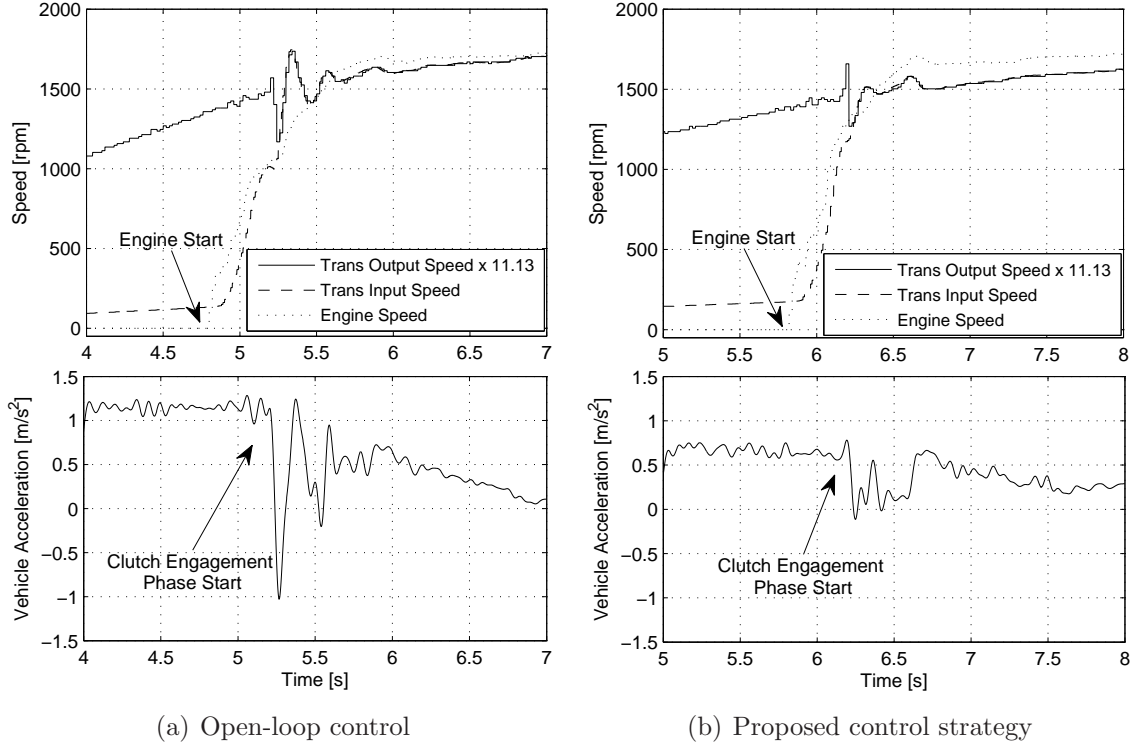


Figure 7.11: A comparison of driveline speeds and vehicle acceleration using the described controllers. In both cases, the mode transition sequence is triggered at  $v_{veh} = 10$  mph.

torque requests between the engine start and hybrid modes (see Figure 7.12(a)), the vehicle acceleration undergoes a critical disturbance at  $t = 5.2$  s, following the engine start phase. A detailed explanation of this phenomenon can be given by analyzing the driveline speeds in the upper plot of Figure 7.11(a). Prior to the end of the engine start event, the BSA torque request is gradually reduced to zero (see lower plot of Figure 7.12(a)) in order to track a specified engine speed reference trace. This is the traditional engine start scheme of [63] and is not well suited to the problem in consideration. As a result, the rate of increase in the engine speed slows down towards the end of the engine start phase. Since the engine crankshaft “drags” the torque converter turbine side due to increasing transmission line pressure, the turbine speed follows a similar trajectory as the engine speed (with a time lag) between  $t = 4.9$  s

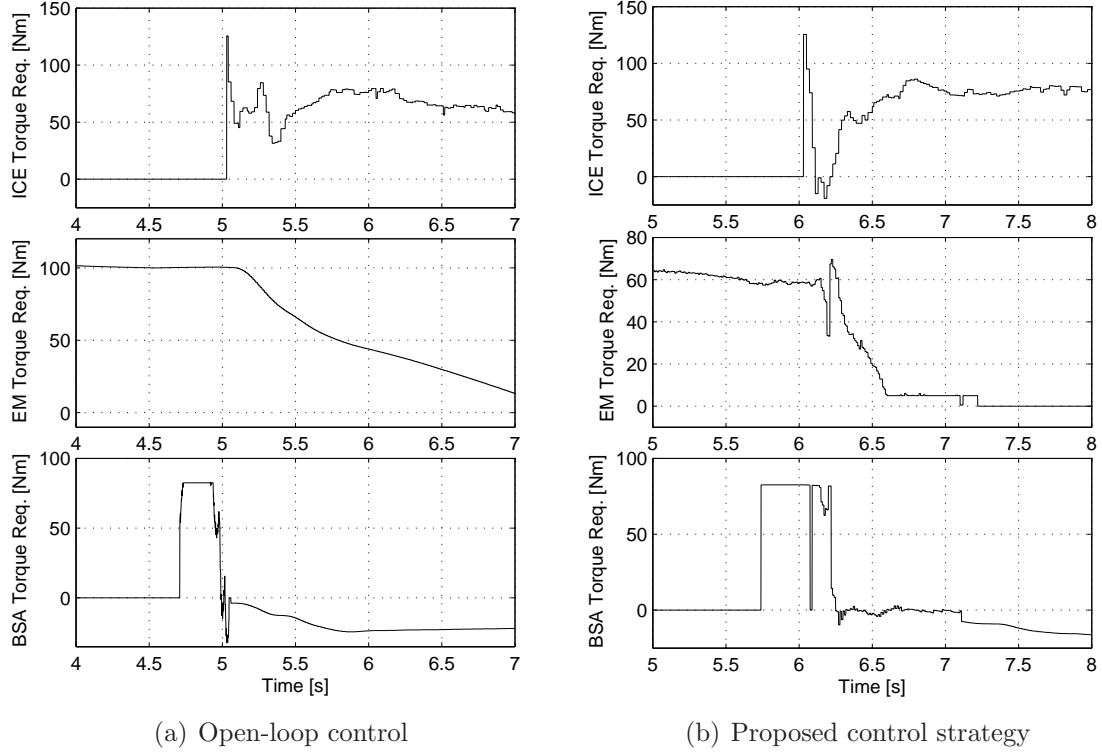


Figure 7.12: A comparison of the actuator torque requests given by the described controllers. In both cases, the mode transition sequence is triggered at  $v_{veh} = 10$  mph.

and 5.2 s. Therefore, the transmission enters the clutch engagement phase, for which there is no special control action in the open-loop strategy case, in an unsynchronized state. This causes the clutch engagement to occur abruptly and without any torque compensation from the BSA, since the ECMS mode is immediately activated. The resulting disturbance appears as a torque hole followed by shuffle vibrations with a damped natural frequency of  $\sim 5$  Hz. The disturbance is evident from the transients in the transmission output speed and the vehicle acceleration.

Next, the behavior of the proposed control strategy is analyzed. Due to the reasons discussed above, the engine start controller commands the maximum BSA torque as shown in Figure 7.12(b). This causes the transmission input and output speeds to be better synchronized at the beginning of the clutch engagement phase,

when compared to the open-loop strategy case. In addition, the feedforward torque compensation provided by the BSA helps to improve the driveline response during the clutch engagement phase. The EM torque controller performs two functions. The first one, realized by the feedforward part, is to smoothly transfer between two controllers that are active in the engine start and hybrid phases. The transfer is done in accordance with the estimated dynamics of the engine. The second one, realized by the feedback part, is to provide active damping during the clutch engagement phase. The feedback part contributes to the slight oscillation in the torque request at  $t = 6.2$  s (see middle plot of Figure 7.12(b)). The EM feedback gain is selected as  $(k_2)_{2,1} = 10$ .

The resulting controller performance is shown in Figure 7.11(b). The torque hole is largely improved and the magnitude of oscillations in the transmission output speed is smaller than in the previous case. A comparison of the transmission input and output speeds between Figures 7.11(a) and 7.11(b) confirms that the transmission speed synchronization occurs more smoothly in the latter case.

Note that the engine torque signal shown in Figure 7.12 is obtained from the ECU, and it represents the final torque request to the engine including both the idle-speed controller torque request (which appears as a short torque spike in both plots) and the actual engine torque request. Therefore, some uncertainty is present between the torque request given by the controller and the final torque request realized by the ECU. This is one of the factors that make the engine less favorable to use for the control of driveline transients in the test vehicle.

It is important to verify the consistency of the performance obtained by using the proposed control scheme. Therefore, experiments similar to those shown in Figure 7.10 are also conducted using the proposed control method. The results are demonstrated in Figure 7.13. Clearly, the driveline disturbances are reduced for all vehicle speed thresholds when compared to the results shown in Figure 7.10. However, as expected, the value of the speed threshold still impacts the quality of the mode transition.



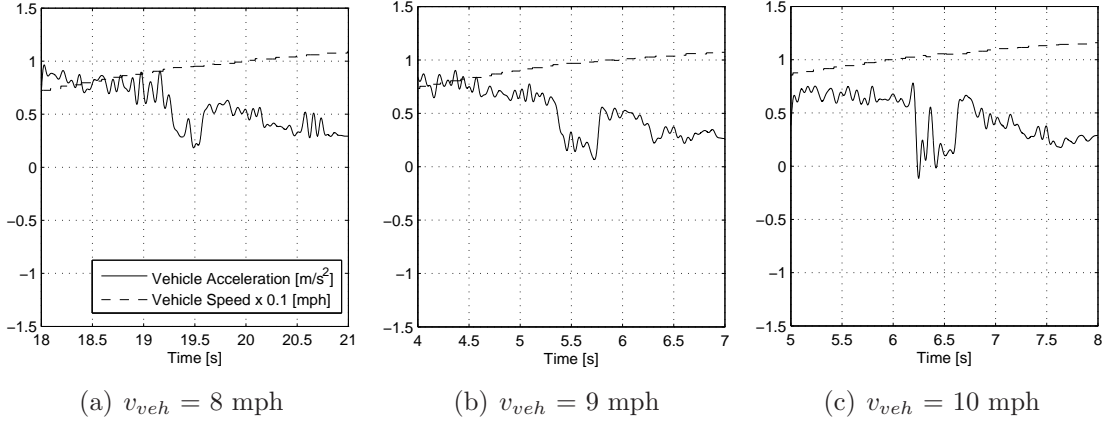


Figure 7.13: The driveline disturbance during the mode transition using the proposed control strategy at different vehicle speeds.

It is important to note two major limitations on the controller performance. The first one is the inability to adjust the transmission line pressure (or more accurately, the pressure acting on clutch C1) during the transition from engine start to hybrid phase.<sup>10</sup> Therefore, further improvements on the mode transition quality require electronic control of the transmission line pressure. A second limitation arises due to the lack of complete access to the engine and transmission control algorithms. If these algorithms were accessible, one could achieve even further improvements by modifying the fuel injection strategy during the engine start phase, and by adjusting the clutch pressure commands during the clutch engagement phase.

## 7.4 Summary

This chapter demonstrated the experimental verification of the control strategies described in Chapters 5 and 6. First, the performance of the rear driveline active damping controller is evaluated for two test cases. It is shown that the feedback controller is effective in damping driveline vibrations when the driving gears are in

<sup>10</sup>Note that the transmission pressure is regulated by a mechanical pump that is driven by the engine.

contact, however, a feedforward controller is necessary to smoothly traverse the gear backlash. Next, the performance of the multi-mode HEV control strategy described in Chapter 5 is evaluated by two experiments. The first experiment is conducted over a short driving segment that includes a combination of urban and highway driving conditions. It is shown that the control strategy successfully performs the desired hybrid functions with good drivability while respecting the safe operating limits of the electric powertrain subsystems. The second experiment is performed on a real-world driving schedule for the purpose of evaluating the fuel economy of the test vehicle. Using the multi-mode control strategy, the test vehicle achieved an estimated 39% improvement in fuel economy in urban driving conditions compared to the baseline vehicle.

Finally, the mode-transition control scheme presented in Chapter 6 is experimentally verified. Due to the differences between the dynamics of the simulation example of Section 6.4 and the dynamics of the test vehicle, some control design modifications were required. The revised control design is implemented and compared with an open-loop switching strategy. The results of the proposed control scheme showed significant improvements over the open-loop strategy for different vehicle speeds.

## CHAPTER 8

### CONCLUSIONS AND FUTURE WORK

#### 8.1 Conclusions

This dissertation discusses two important aspects of the hybrid-electric vehicle development process: modeling and control design. The first part of this work is dedicated to the development and validation of a dynamic HEV model that is capable of predicting vehicle dynamic responses in the low-to-mid frequency region. The experimental results given in Chapter 4 confirm the fidelity of the model for a variety of operating conditions. The second part of this dissertation focuses on control development. In particular, a multi-mode control strategy that strives to achieve improvements in fuel economy and drivability is developed and implemented on the test vehicle. The results obtained during the control development process reveal the importance of ensuring seamless mode transitions under normal driving conditions. This is the motivation behind the approach described in Chapter 6, a control design technique that addresses the problem of mode-switching induced transients in a class of switched dynamic systems. The proposed approach is first illustrated using a simulation example, and later experimentally verified for the case of HEV launch. A summary of the steps that lead to the acquisition of the results in this dissertation is given next.

One of the initial goals of this research was to identify the sources of drivability problems that are characteristic to HEVs. For this purpose, a low-frequency dynamic

model that represents the architecture of the experimental vehicle was built. A challenge here was to determine the appropriate detail for the model, since the simulator only needed to accurately predict vehicle responses up to 10 Hz. Therefore, any additional detail would only increase the computational complexity of the model without providing significant benefits for control design and model accuracy. After the development of the model, the preliminary simulation results showed that the transmission behavior has the largest impact on driveline responses that affect drivability. As a result, the transmission model was further refined. Following the initial calibration of the model via basic experiments, a number of test cases were specified and the data obtained from experiments were compared with simulation results. The resulting degree of agreement between the simulations and the experiments is found to be satisfactory for cases involving electric only, engine only and hybrid vehicle operation.

The initial stages of control design were conducted in parallel with model development. Therefore, the observations made by analyzing the simulation results were well-incorporated into the control design process. This is an important aspect of the design approach, since a good understanding of the driveline behavior is central to the development of controllers with drivability considerations. As described in Chapter 5, the design of a HEV control strategy is viewed as a three-step process: (i) converting the accelerator/brake pedal position into a power/torque demand, (ii) determining the suitable vehicle operating mode, (iii) computing a torque split in order to achieve the control objectives defined in a particular operating mode. The equivalent consumption minimization strategy is implemented in the hybrid phase of the multi-mode control strategy. Various implementation and drivability considerations of the control strategy are investigated and reported in Chapter 5. The main practical challenge here was to integrate the existing control units into a new networked control structure supervised by the hybrid energy management strategy.

The multi-mode structure of the control strategy is mainly required to accommodate the engine start-stop function. However, a drawback of using a multi-mode (or hybrid) control architecture is the difficulty of maintaining a consistent drive quality

independent of the driving conditions. A control technique that addresses this problem is described in Chapter 6. The presented formulation allows to generalize the technique to a broader class of systems that satisfy similar properties as the HEV system. The key idea of the design procedure is based on changing the control action in order to minimize a specified transitioning cost as the state trajectory approaches a switching set. Potential areas of application and a simulation example that illustrates the steps of the proposed approach are also given in Chapter 6.

Experimental verification of the control strategies is demonstrated in Chapter 7. First, the rear driveline active damping controller is tested using step changes in torque demand. It is concluded that the feedback controller is effective in damping driveline vibrations when the gears are in contact, however, a feedforward controller is necessary to smoothly traverse gear backlash. Second, the performance of the HEV control strategy is evaluated by experiments. The first experiment is conducted over a short driving segment that triggers a number of vehicle operating modes. It is shown that the control strategy successfully performs the desired hybrid functions with good drivability while respecting the safe operating limits of the electric powertrain subsystems. The second experiment is performed on a real-world driving schedule with the purpose of evaluating the fuel economy of the test vehicle. Using the multi-mode control strategy, the test vehicle achieved an estimated 39% improvement in fuel economy in urban driving conditions compared to the baseline vehicle. Finally, the experimental verification of the mode transition control technique is given. The results confirm that the proposed approach reduces the driveline disturbances that occur during a transition from electric only to hybrid mode, when compared to an open-loop strategy that was used in the earlier stages of this research.

## 8.2 Future Work

The control of hybrid-electric vehicle drivelines is an active research topic, and many areas of future improvement are possible. A number of these research directions are discussed next.

**ECMS improvements:** Two potential research directions are proposed in this area for future study. The first topic involves determining the optimum transmission gear ratio using the equivalent consumption minimization strategy. The traditional formulation of ECMS is aimed at finding a torque split that locally minimizes the equivalent fuel consumption. However, the transmission gear ratio is another control variable that significantly affects the fuel economy. Therefore, the combined control of the actuator torques and the transmission gear ratio is necessary to utilize the true fuel economy potential of the hybrid powertrain.

Another improvement opportunity should be noted regarding the numerical implementation method of ECMS. In this research, ECMS is implemented using a constrained search method that computes the solution with best possible fuel economy within a neighborhood of the current operating point. However, despite the use of large quantization intervals, the algorithm is still time consuming to compute even when a rapid-prototyping controller is used. Therefore, the use of a gradient-based numerical search technique is desirable to find the local minimum of the cost function. In this scheme, the constrained search method proposed in this work may prove to be beneficial for guaranteeing the convexity of the cost function about the current operating point.

**Pedal tip-in/tip-out:** The control design presented in Section 5.2.2 is a preliminary approach for the active damping of rear driveline vibrations. Other design techniques are available in the literature, however, they are mostly focused on the active damping of conventional drivetrains [58,59]. However, the problem is not identical in the case of electric (or hybrid) vehicles, since electric machines and ICEs have different dynamic response characteristics. In the test vehicle, gear backlash also largely contributes to the magnitude of driveline oscillations when there are sign changes in the EM torque request.<sup>1</sup> Therefore, the nonlinear structure of gear backlash should be exploited in the model-based control design. For this purpose, (nonlinear) frequency domain

<sup>1</sup>Note that changes in the torque direction commonly occur in electric (or hybrid) vehicles due to the regenerative braking functionality. However, this is not the case for conventional vehicles.

control techniques such as the describing function method or the circle criterion, or an observer-based switched controller may be used.

**Torque fill-in during gear shifts:** As discussed in Section 2.4, gear shifts in automatic transmissions cause the so-called shift shock problem, which is characterized by a momentary loss of the drivetrain torque. The availability of redundant actuators in HEVs makes it possible overcome gear shift related drivability problems. For this purpose, an open-loop torque fill-in strategy is proposed in [54] to reduce gear shift disturbances in a parallel HEV. However, model-based techniques for the control of gear-shifts using electric motor torque assist are not currently available to the author's knowledge. This is a promising area of research, since the gear shift problem still involves many challenges especially under high engine loads.

**Control of seamless mode transitions:** The control development framework described in Chapter 6 is still in a preliminary stage. Further research is required to develop effective strategies for the design of partition controllers and to ensure their robustness to model uncertainty. Also, extensions of the approach to the case where a system mode may transition to multiple modes are highly desirable. Another potential research topic is demonstrating applications of the proposed framework other than the HEV control application. A good example is the control of transitions in multi-mode combustion engines.

## APPENDIX A

### VEHICLE CONTROL UNIT SIGNALS

Important control signals that are received and transmitted by the vehicle control unit are listed in Table A.1 along with the sources/destinations and the time resolutions of the signals. Note that this list does not contain the signals that support the control of auxiliary systems such as the engine cooling system.

The following acronyms are used to represent the electronic control units onboard the test vehicle: ECU for the engine control unit, TCU for the transmission control unit, MCU for the rear electric machine control unit, SACU for the belted-starter alternator control unit, BCU for the battery control unit, and ABCU for the anti-locking braking system control unit. Also, PWM stands for pulse-width modulation. The time resolutions of the signals are specified such that the slower of the transmitting/receiving module (which may be different in the case of CAN signals) is selected. For example, if the TCU relays the transmission output speed every 20 ms, and the vehicle control unit receives it every 10 ms, the actual time resolution is 20 ms.



	Signal	Source/Destination	Time Resolution
<b>Received</b>	Accelerator Pedal Position	Analog	1 ms
	Brake Pedal Position	Analog	1 ms
	Battery Current	CAN (BCU)	100 ms
	Battery SOC	CAN (BCU)	100 ms
	Battery Temperature	CAN (BCU)	100 ms
	BSA Speed	PWM (SACU)	1 ms
	EM Inverter Active	CAN (MCU)	100 ms
	EM Inverter Temperature	CAN (MCU)	1000 ms
	EM Inverter Voltage	CAN (MCU)	100 ms
	EM Speed	CAN (MCU)	10 ms
	EM Temperature	CAN (MCU)	1000 ms
	Engine Actual Torque	CAN (ECU)	10 ms
	Engine Coolant Temperature	CAN (ECU)	1000 ms
	Engine Speed	CAN (ECU)	10 ms
	Transmission Gear	CAN (TCU)	100 ms
	Transmission Input Speed	CAN (TCU)	10 ms
	Transmission Oil Temperature	CAN (TCU)	1000 ms
	Transmission Output Speed	CAN (TCU)	20 ms
	Vehicle Acceleration	Analog	1 ms
	Vehicle Key Start	Analog	1 ms
	Vehicle Speed	CAN (ECU)	100 ms
	Wheel Speeds	CAN (ABCU)	100 ms
<b>Transmitted</b>	BSA Inverter Enable	Digital	10 ms
	BSA Torque Request	Analog	1 ms
	DC-DC Converter Enable	Digital	10 ms
	ECU Enable	Digital	1 ms
	EM Inverter Enable	Digital	10 ms
	EM Torque Request	CAN (MCU)	10 ms
	Engine Torque Request	Analog	10 ms
	Vehicle Mode	CAN (BCU)	10 ms

Table A.1: Vehicle control unit signal information.

## APPENDIX B

### DRIVING CYCLE FOR FUEL ECONOMY EVALUATION

Figure B.1 shows the driving cycle used in Chapter 7 for the evaluation of the actual fuel economy obtained from the test vehicle. This cycle is generated by repeating a 300 s driving pattern for four consecutive times. The cycle does not include any significant variations in the road grade.

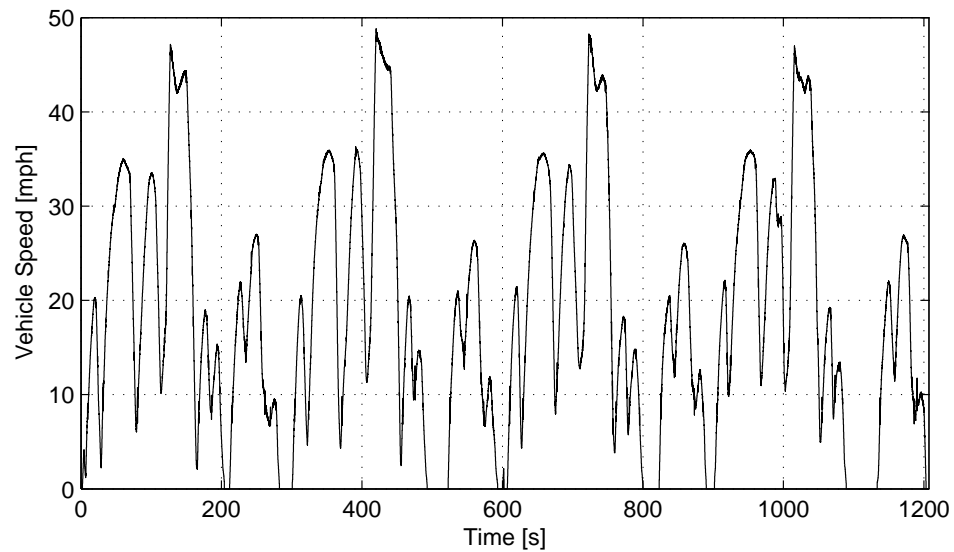


Figure B.1: A real-world driving cycle used to evaluate the fuel economy of the test vehicle.

Also, Table B.1 shows a comparison of important driving cycle statistics for selected standard US driving schedules (FUDS, FHDS, US06) and the two test cycles

that are used to compute the fuel economies of the test vehicle under the action of different control strategies. Note that it is crucial to replicate the control strategy test cycles as closely as possible for accurate comparison of the fuel economies. This goal is achieved as seen from the comparison of driving cycle statistics given in Table B.1 for the two test cycles. Furthermore, it is shown that both test cycles closely resemble the Federal Urban Driving Schedule (FUDS) as far as the driving statistics are concerned. For this reason, the fuel economy comparisons in Chapter 7 are made in reference to the urban driving schedule.

<b>Driving Cycle</b>	<b>Average Speed [mph]</b>	<b>RMS Acceleration [m/s<sup>2</sup>]</b>	<b>Percentage of Idle Time [%]</b>
FUDS (Urban)	19.6	0.68	19.5
FHDS (Highway)	48.3	0.31	0.6
US06 (High Acceleration)	48.4	1.06	8.0
Test Cycle (Engine Only)	18.7	0.73	13.4
Test Cycle (Hybrid Strategy)	18.5	0.72	12.7

Table B.1: Driving cycle statistics.

## APPENDIX C

### HYBRID MODEL OF THE TEST VEHICLE

Following the notation of Figure 6.4, a simplified hybrid model of the test vehicle is developed to represent the transition from electric only mode to hybrid mode.

The state variables are chosen as

$$\begin{aligned} x_1 &= (\omega_{em}, \omega_{ice}, \omega_t, v_{veh}, \theta_{hs,r})' \\ x_2 &= (\omega_{em}, \omega_{ice}, \omega_t, v_{veh}, \theta_{hs,r}, \theta_{hs,f}, \omega_{tr}, T_{ice})' \\ x_3 &= (\omega_{em}, \omega_{ice}, \omega_t, v_{veh}, \theta_{hs,r}, \theta_{hs,f}, T_{ice})' \end{aligned} \quad (C.1)$$

Also, the control variables in each operating mode are  $u_1 = (T_{em,req}, T_{bsa,req})'$ , and  $u_2, u_3 = (T_{bsa,req}, T_{em,req}, T_{ice,req})'$ . The overall hybrid control model of the test vehicle during vehicle launch can be described by the following vector fields:

$$\mathcal{F}_1(x_1, u_1) = \begin{cases} \dot{\omega}_{em} = \frac{1}{J_{em,1}} \left( T_{em,req} \bar{\eta}_r - b_{em} \omega_{em} - \frac{2}{\zeta_{gb} \zeta_{rd}} T_{hs,r} \right) \\ \dot{\omega}_{ice} = \frac{1}{J_{ice,1}} (T_{bsa,req} - b_{ice,1} \omega_{ice} - b_{ice,0} - T_{p,1}) \\ \dot{\omega}_t = \frac{1}{J_{pgs,1}} (T_{t,1} \bar{\eta}_f - b_{t,1} \omega_t) \\ \dot{v}_{veh} = \frac{1}{M_{veh,1}} \left( \frac{2}{R_{wh}} T_{hs,r} - F_{road} \right) \\ \dot{\theta}_{hs,r} = \frac{1}{\zeta_{gb} \zeta_{rd}} \omega_{em} - \frac{1}{R_{wh}} v_{veh} \end{cases} \quad (C.2)$$

$$\mathcal{F}_2(x_2, u_2) = \begin{cases} \dot{\omega}_{em} = \frac{1}{J_{em,1}} \left( T_{em,req} \bar{\eta}_r - b_{em} \omega_{em} - \frac{2}{\zeta_{gb} \zeta_{rd}} T_{hs,r} \right) \\ \dot{\omega}_{ice} = \frac{1}{J_{ice,1}} (T_{bsa,req} + T_{ice} - b_{ice,1} \omega_{ice} - b_{ice,0} - T_{p,2}) \\ \dot{\omega}_t = \frac{1}{J_{t,2}} \left( T_{t,2} \bar{\eta}_f - b_{t,1} \omega_t - \frac{R_{pgs,r}}{2R_{pgs,c}} T_{c,1} \right) \\ \dot{v}_{veh} = \frac{1}{M_{veh,1}} \left( \frac{2}{R_{wh}} T_{hs,r} + \frac{2}{R_{wh}} T_{hs,f} - F_{road} \right) \\ \dot{\theta}_{hs,r} = \frac{1}{\zeta_{gb} \zeta_{rd}} \omega_{em} - \frac{1}{R_{wh}} v_{veh} \\ \dot{\theta}_{hs,f} = \omega_{tr} - \frac{1}{R_{wh}} v_{veh} \\ \dot{\omega}_{tr} = \frac{1}{J_{tr,2}} \left( \frac{R_{rgs,r}}{R_{rgs,s1}} T_{c,1} - \frac{2}{\zeta_{cg} \zeta_{fd}} T_{hs,f} \right) \\ \dot{T}_{ice} = \frac{1}{\tau_{ice}} (T_{ice,req} - T_{ice}) \end{cases} \quad (C.3)$$

$$\mathcal{F}_3(x_3, u_3) = \begin{cases} \dot{\omega}_{em} = \frac{1}{J_{em,1}} \left( T_{em,req} \bar{\eta}_r - b_{em} \omega_{em} - \frac{2}{\zeta_{gb} \zeta_{rd}} T_{hs,r} \right) \\ \dot{\omega}_{ice} = \frac{1}{J_{ice,1}} (T_{bsa,req} + T_{ice} - b_{ice,1} \omega_{ice} - b_{ice,0} - T_{p,2}) \\ \dot{\omega}_t = \frac{1}{J_{t,3}} \left( T_{t,2} \bar{\eta}_f - b_{t,1} \omega_t - \frac{2}{\zeta_{tr,1} \zeta_{cg} \zeta_{fd}} T_{hs,f} \right) \\ \dot{v}_{veh} = \frac{1}{M_{veh,1}} \left( \frac{2}{R_{wh}} T_{hs,r} + \frac{2}{R_{wh}} T_{hs,f} - F_{road} \right) \\ \dot{\theta}_{hs,r} = \frac{1}{\zeta_{gb} \zeta_{rd}} \omega_{em} - \frac{1}{R_{wh}} v_{veh} \\ \dot{\theta}_{hs,f} = \omega_{tr} - \frac{1}{R_{wh}} v_{veh} \\ \dot{T}_{ice} = \frac{1}{\tau_{ice}} (T_{ice,req} - T_{ice}) \end{cases} \quad (C.4)$$

where the first gear ratio is

$$\zeta_{tr,1} = \frac{2R_{pgs,c}R_{rgs,r}}{R_{pgs,r}R_{rgs,s1}}. \quad (C.5)$$

The driveline torques and the road load can be written as

$$\begin{aligned}
T_{hs,r} &= k_{hs,r} \theta_{hs,r} + b_{hs,r} \left( \frac{1}{\zeta_{gb}\zeta_{rd}} \omega_{em} - \frac{1}{R_{wh}} v_{veh} \right) \\
T_{hs,f} &= k_{hs,f} \theta_{hs,f} + b_{hs,f} \left( \omega_{tr} - \frac{1}{R_{wh}} v_{veh} \right) \\
T_{p,1} &= C_{tc,1} \omega_{ice}^2 + C_{tc,2} \omega_{ice} \omega_t + C_{tc,3} \omega_t^2 \\
T_{p,2} &= C_{tc,4} \omega_{ice}^2 + C_{tc,5} \omega_{ice} \omega_t + C_{tc,6} \omega_t^2 \\
T_{t,1} &= C_{tc,7} \omega_{ice}^2 + C_{tc,8} \omega_{ice} \omega_t + C_{tc,9} \omega_t^2 \\
T_{t,2} &= T_{p,2} \\
T_{c,1} &= (p_{c,1} A_{c,1} n_{c,1} R_{c,1} \mu_{c,1} + b_{c,1} |\Delta \omega_{c,1}|) \tanh \left( \frac{\Delta \omega_{c,1}}{\epsilon} \right) \\
F_{road} &= \frac{1}{2} \rho_a C_d A_{veh} v_{veh}^2 + M_{veh} g C_{rr,0}.
\end{aligned} \tag{C.6}$$

Note that the clutch slip speed is a function of the state variables

$$\Delta \omega_{c,1} = \frac{R_{pgs,r}}{2R_{pgs,c}} \omega_t - \frac{R_{rgs,r} \zeta_{cg} \zeta_{fd}}{R_{rgs,s1}} \omega_{tr}. \tag{C.7}$$

Also, the combined inertias are

$$\begin{aligned}
J_{em,1} &= J_{em} + J_{gb} + \frac{1}{J_{gb}^2} J_{rd} \\
J_{ice,1} &= J_{ice} + J_{bsa} + J_p \\
M_{veh,1} &= M_{veh} + \frac{4J_{wh}}{R_{wh}^2} \\
J_{t,2} &= J_{pgs,1} + \frac{R_{pgs,r}^2}{4} \left( \frac{n_{pgs,p} J_{pgs,p}}{R_{pgs,p}^2} + \frac{J_{pgs,c}}{2R_{pgs,c}^2} \right) \\
J_{tr,2} &= \zeta_{cg} \zeta_{fd} \left( \frac{n_{rgs,p1}}{n_{rgs,p2}} J_{rgs,4} + R_{rgs,r}^2 \left( \frac{R_{rgs,p2}}{R_{rgs,c2} R_{rgs,s1}^2} J_{rgs,2} \right. \right. \\
&\quad \left. \left. + n_{pgs,p1} \left( \frac{J_{rgs,p2}}{R_{rgs,p2}^2} + \frac{J_{rgs,3}}{R_{rgs,s2}^2 n_{rgs,p2}} + \frac{J_{rgs,p1}}{R_{rgs,p1}^2} \right) \right) \right) \\
J_{t,3} &= J_{t,2} + \frac{1}{\zeta_{tr,1}^2 \zeta_{cg} \zeta_{fd}} J_{tr,2}.
\end{aligned} \tag{C.8}$$

The remaining parameters were previously defined in Chapter 3. The hybrid model assumes that the transmission engages in first gear after the engine start phase.

Also, the torque converter is assumed to work in the torque multiplication mode ( $\omega_t/\omega_{ice} < \gamma_c$ ) during the engine start phase, and in the torque coupling mode during the clutch engagement and parallel hybrid phases ( $\gamma_c \leq \omega_t/\omega_{ice} < 1$ ).

In this case, the state space partitions are chosen as

$$\begin{aligned}\mathcal{P}_1^0 &:= \{x \in \mathcal{X}_1 \mid v_{veh} < v_{veh,th} \quad \wedge \quad \omega_{ice} = 0\} && \text{("engine off")} \\ \mathcal{P}_1^1 &:= \{x \in \mathcal{X}_1 \mid v_{veh} \geq v_{veh,th} \quad \vee \quad \omega_{ice} > 0\} && \text{("engine starting")} \\ \mathcal{P}_2^0 &:= \{x \in \mathcal{X}_2\}, \quad \mathcal{P}_3^0 := \{x \in \mathcal{X}_3\} && \text{(trivial partitions)}\end{aligned} \tag{C.9}$$

where  $v_{veh,th}$  is a threshold speed. The switching sets depend on the internal dynamics of the system:

$$\begin{aligned}\mathcal{S}_1^2 &:= \{x \in \mathcal{X}_1 \mid \omega_{ice} > \omega_{ice,idle}\} && \text{("engine started")} \\ \mathcal{S}_2^3 &:= \{x \in \mathcal{X}_2 \mid |\Delta\omega_{c,1}| < \epsilon\} && \text{("clutched locked up")}\end{aligned} \tag{C.10}$$

The transition from mode 1 to mode 2 does not cause any discontinuous jumps in  $x_1$ . However, additional states are introduced as a result of the transition. The transition map from mode 2 to mode 3 is given by  $\mathcal{T}_2^3 : x \mapsto Tx$  where

$$T := \begin{bmatrix} 1 & 0 & 0 & 0 & 0 & 0 & 0 & 0 \\ 0 & 1 & 0 & 0 & 0 & 0 & 0 & 0 \\ 0 & 0 & 0 & 0 & 0 & 0 & \zeta_{tr,1}\zeta_{cg}\zeta_{fd} & 0 \\ 0 & 0 & 0 & 1 & 0 & 0 & 0 & 0 \\ 0 & 0 & 0 & 0 & 1 & 0 & 0 & 0 \\ 0 & 0 & 0 & 0 & 0 & 1 & 0 & 0 \\ 0 & 0 & 0 & 0 & 0 & 0 & 0 & 1 \end{bmatrix}. \tag{C.11}$$

## BIBLIOGRAPHY

- [1] U.S. Energy Information Administration. The Annual Energy Review. Technical report, 2006. (Available at <http://www.eia.doe.gov/aer/>).
- [2] F. Porsche. The first hybrid vehicle built in 1898. (Available at <http://www.hybrid-vehicle.org/hybrid-vehicle-porsche.html>).
- [3] John M. Miller. *Propulsion systems for hybrid vehicles*. IEE Power & Energy Series 45. The Institution of Electrical Engineers, 2004.
- [4] D. Liberzon. *Switching in Systems and Control*. Systems and Control: Foundations and Applications. Birkhauser, Boston, MA, 2003.
- [5] M.J. Roelle, G. M. Shaver, and J. C. Gerdes. Tackling the transition: A multi-mode combustion model of SI and HCCI for mode transition control. In *Proceedings of the IMECE*, number 62188, 2004.
- [6] L. Glielmo, L. Iannelli, V. Vacca, and F. Vasca. Gearshift control for automated manual transmissions. *IEEE/ASME Transactions on Mechatronics*, 11(1):17–26, 2006.
- [7] A. Scacchioli. *Hybrid Regulation of Electromagnetic Valves in Automotive Systems*. PhD thesis, University of L’Aquila, Italy, 2005.
- [8] G. Paganelli, G. Ercole, A. Brahma, Y. Guezennec, and G. Rizzoni. A general formulation for the instantaneous control of the power split in charge-sustaining hybrid electric vehicles. In *Proceedings of the 5th Intl. Symposium on Advanced Vehicle Control*, pages 73–80, 2000.
- [9] J. M. Miller. Hybrid electric vehicle propulsion system architectures of the e-CVT type. *IEEE Transactions on Power Electronics*, 21(3):756–767, 2006.
- [10] C. Schyr and K. Gschweitl. Model-based development and calibration of hybrid powertrains. In *SAE Proceedings*, number 2007-01-0285.



- [11] T. Markel, A. Brooker, T. Hendricks, V. Johnson, K. Kelly, B. Kramer, M. O’Keefe, S. Sprik, and K. Wipke. ADVISOR: a systems analysis tool for advanced vehicle modeling. *Journal of Power Sources*, 110(2):255–66, 2002.
- [12] A. Rousseau, P. Sharer, S. Pagerit, and M. Duoba. Integrating data, performing quality assurance, and validating the vehicle model for the 2004 Prius using PSAT. In *SAE Proceedings*, number 2006-01-0667.
- [13] G. Rizzoni, L. Guzzella, and B. M. Baumann. Unified modeling of hybrid electric vehicle drivetrains. *IEEE/ASME Transactions on Mechatronics*, 4(3):246–257, 1999.
- [14] K. L. Butler, M. Ehsani, and P. Kamath. A MATLAB-based modeling and simulation package for electric and hybrid electric vehicle design. *IEEE Transactions on Vehicular Technology*, 48(6):1770–78, 1999.
- [15] B.K. Powell, K.E. Bailey, and S.R. Cikanek. Dynamic modeling and control of hybrid electric vehicle powertrain systems. *IEEE Control Systems Magazine*, 18(5):17–33, 1998.
- [16] C. Lo, Y. Luan, E. D. Tate, and T. H. Zarger. A simulation model for the saturn VUE green line hybrid vehicle. In *SAE Proceedings*, number 2006-01-0441.
- [17] F. U. Syed, M. L. Kuang, J. Czubay, and H. Ying. Derivation and experimental validation of a power-split hybrid electric vehicle model. *IEEE Transactions on Vehicular Technology*, 55(6):1731–1747, 2006.
- [18] C. C. Lin, Z. Filipi, Y. Wang, L. Louca, H. Peng, D. Assanis, and J. Stein. Integrated, feed-forward hybrid electric vehicle simulation in SIMULINK and its use for power management studies. In *SAE Proceedings*, number 2001-01-1334, 2001.
- [19] The Mathworks Inc. Simdriveline 1.4 toolbox. (Available at <http://www.mathworks.com/products/simdrive/>).
- [20] M. Amrhein and P.T. Krein. Dynamic simulation for analysis of hybrid electric vehicle system and subsystem interactions, including power electronics. *IEEE Transactions on Vehicular Technology*, 54(3):825–836, 2005.
- [21] P. Waltermann. Modelling and control of the longitudinal and lateral dynamics of a series hybrid vehicle. In *Proceedings of the IEEE International Conference on Control Applications*, pages 191–198, 1996.
- [22] J. Deur, J. Asgari, and D. Hrovat. Modeling and analysis of automatic transmission engagement dynamics-nonlinear case including validation. *Journal of Dynamic Systems, Measurement, and Control*, 128:251–262, 2006.

- [23] Dong-Il Cho. *Nonlinear Control Methods for Automotive Powertrain Systems*. PhD thesis, Massachusetts Institute of Technology (MIT), 1987.
- [24] Q. Zheng. *Modeling and Control of Powertrains with Stepped Automatic Transmissions*. PhD thesis, The Ohio State University, 1999.
- [25] Y. Fujii, W.E. Tobler, E.M. Clausing, T. W. Megli, and M. Haghighooie. Application of dynamic band brake model for enhanced drivetrain simulation. *Proceedings of the IMechE Part D, Journal of Automobile Engineering*, 216(11):873–881, 2002.
- [26] C. C. Lin, H. Peng, and J. W. Grizzle. Power management strategy for a parallel hybrid electric truck. *IEEE Transactions on Control Systems Technology*, 11(6):839–49, 2003.
- [27] A. Sciarretta, M. Back, and L. Guzzella. Optimal control of parallel hybrid electric vehicles. *IEEE Transactions on Control Systems Technology*, 12:352–63, 2004.
- [28] S. Jeon, S. Jo, Y. Park, and J. Lee. Multi-mode driving control of a parallel hybrid electric vehicle using driving pattern recognition. *Journal of Dynamic Systems, Measurement, and Control*, 124(1):141–49, 2002.
- [29] K. Koprubasi, J. M. Morbitzer, E. R. Westervelt, and G. Rizzoni. Toward a framework for the hybrid control of a multi-mode hybrid-electric driveline. In *Proceedings of the American Control Conference*, pages 3296–3301, 2006.
- [30] C. Musardo, G. Rizzoni, Y. Guezennec, and B. Staccia. A-ECMS: An adaptive algorithm for hybrid electric vehicle energy management. *European Journal of Control*, 11(4-5), 2005. Fundamental Issues in Control, Special Issue.
- [31] Y. Zhu, Y. Chen, G. Tian, H. Wu, and Q. Chen. A four-step method to design an energy management strategy for hybrid vehicles. In *Proceedings of the American Control Conference*, volume 1, pages 156–61, 2004.
- [32] N. J. Schouten, M. A. Salman, and N. A. Kheir. Fuzzy logic control for parallel hybrid vehicles. *IEEE Transactions on Control Systems Technology*, 10:460–68, 2002.
- [33] M. L. Kuang, C. A. Ochocinski, D. Mack, and J. W. Anthony. Controller and control method for a hybrid electric vehicle powertrain. *US Patent 7,210,546*, 2007.
- [34] M. Jankovic and B. K. Powell. Hybrid powertrain controller. *US Patent 6,164,400*, 2000.

- [35] H. Ueda. Drive control of hybrid electric vehicle. *US Patent 7,057,304 B2*, 2006.
- [36] P. Pisu, K. Koprubasi, and G. Rizzoni. Energy management and driveability control problems for hybrid electric vehicles. In *Proceedings of the IEEE International Conference on Decision and Control / European Control Conference*, pages 1824–30, 2005.
- [37] V. H. Johnson, K. B. Kipke, and D. J. Rausen. HEV control strategy for real-time optimization of fuel economy and emissions. In *SAE Proceedings*, number 2000-01-1543.
- [38] C.C. Lin, H. Peng, and J.W. Grizzle. A stochastic control strategy for hybrid electric vehicles. In *Proceedings of the American Control Conference*, volume 5, pages 4710–15, 2004.
- [39] E. D. Tate, J. W. Grizzle, and H. Peng. Shortest path stochastic control for hybrid electric vehicles. *International Journal of Robust and Nonlinear Control*. published online Dec 5, 2007.
- [40] X. Wei, L. Guzzella, V. I. Utkin, and G. Rizzoni. Model-based fuel optimal control of hybrid electric vehicle using variable structure control systems. *Journal of Dynamic Systems, Measurement, and Control*, 129(1):13–19, 2007.
- [41] P. Pisu and G. Rizzoni. H-inf control for hybrid electric vehicles. In *Proceedings of the 43rd IEEE Conference on Decision and Control*, volume 4, pages 3497–502, 2004.
- [42] M. Koot, J.T.B.A. Kessels, B. de Jager, W.P.M.H. Heemels, P.P.J. van den Bosch, and M. Steinbuch. Energy management strategies for vehicular electric power systems. *IEEE Transactions on Vehicular Technology*, 54(3):771–782, 2005.
- [43] A. Sciarretta and L. Guzzella. Control of hybrid electric vehicles. *IEEE Control Systems Magazine*, 27(2):60–70, 2007.
- [44] L. Guzzella and A. Amstutz. Control of diesel engines. *IEEE Control Systems Magazine*, 18:53–71, 1998.
- [45] P. Schoeggl, E. Ramschak, and E. Bogner. On-board optimization of driveability character depending on driver style by using a new closed loop approach. In *SAE Proceedings*, number 2001-01-0556.
- [46] A.P. Cann, A. W. Salmoni, P. Vi, and T.R. Eger. An exploratory study of whole-body vibration exposure and dose while operating heavy equipment in

- the construction industry. *Journal of Applied Occupational and Environmental Hygiene*, 18(12):999–1005, 2003.
- [47] Z. Sun and K. Hebbale. Challenges and opportunities in automotive transmission control. In *Proceedings of the American Control Conference*, pages 3284–89, 2005.
  - [48] Y. Saitou, K. Ooshima, I. Hirose, and M. Tanaka. System for controlling torque reduction at shifting for automatic transmission. *US Patent 6,991,583 B2*, 2006.
  - [49] K. Hebbale and C.K. Kao. Adaptive control of shifts in automatic transmissions. In *Proceedings of the ASME Conference on Advanced Automotive Technologies*, pages 171–182, 1995.
  - [50] H-D. Lee, S-K. Sul, H-S. Cho, and J-M. Lee. Advanced gear-shifting and clutching strategy for a parallel-hybrid vehicle. *IEEE Industry Applications Magazine*, 6(6):26–32, 2000.
  - [51] J. M. Slicker. Design of robust vehicle launch control system. *IEEE Transactions on Control Systems Technology*, 4:326–335, 1996.
  - [52] P. Dolcini, H. Bechart, and C. Canudas de Wit. Observer-based optimal control of dry clutch engagement. In *Proceedings of the IEEE International Conference on Decision and Control / European Control Conference*, pages 440–445, 2005.
  - [53] M. Pettersson and Nielsen L. Gear shifting by engine control. *IEEE Transactions on Control Systems Technology*, 8(3):495–507, 2000.
  - [54] R. C. Baraszu and S. R. Cikanek. Torque fill-in for an automated shift manual transmission in a parallel hybrid electric vehicle. In *Proceedings of the American Control Conference*, volume 2, pages 1431–36, 2002.
  - [55] M. Pettersson. *Driveline Modeling and Control*. PhD thesis, Linköping University, Linköping, Sweden, 1996.
  - [56] S. Johansson, E. Langjord, and S. Pettersson. Objective evaluation of shunt and shuffle in vehicle powertrains. In *Proceedings of the International Symposium on Advanced Vehicle Control*, 2004.
  - [57] I.-J. Ha, A.K. Tugcu, and N.M. Boustany. Feedback linearizing control of vehicle longitudinal acceleration. *IEEE Transactions on Automatic Control*, 34(7):689–698, 1989.
  - [58] D. Lefebvre, P. Chevrel, and S. Richard. An H-infinity-based control design methodology dedicated to the active control of vehicle longitudinal oscillations. *IEEE Transactions on Control Systems Technology*, 11(6):948–956, 2003.

- [59] J. Baumann, A. Swarnakar, and U. Kiencke. A robust controller design for anti-jerking. In *SAE Proceedings*, number 2005-01-0041.
- [60] N. Amann, J. Bocker, and F. Prenner. Active damping of drive train oscillations for an electrically driven vehicle. *IEEE/ASME Transactions on Mechatronics*, 9(4):697–700, 2004.
- [61] D. Kim, H. Peng, S. Bai, and J. M. Maguire. Control of integrated powertrain with electronic throttle and automatic transmission. *IEEE Transactions on Control Systems Technology*, 15(3):474–482, 2007.
- [62] M. L. Kuang. An investigation of engine start-stop NVH in a power split powertrain hybrid electric vehicle. In *SAE Proceedings*, number 2006-01-1500, 2006.
- [63] M. Canova, K. Sevel, Y. Guezennec, and S. Yurkovich. Control of the start/stop of a diesel engine in a parallel HEV: Modeling and experiments. In *Proceedings of the IMECE*, number 15611, 2006.
- [64] R. Beck, F. Richert, A. Bollig, D. Abel, S. Saenger, K. Neil, T. Scholt, and K.-E. Noreikat. Model predictive control of a parallel hybrid vehicle drivetrain. In *Proceedings of the IEEE International Conference on Decision and Control / European Control Conference*, pages 2670–75, 2005.
- [65] K. Koprubasi, E. R. Westervelt, and G. Rizzoni. Toward the systematic design of controllers for smooth hybrid electric vehicle mode changes. In *Proceedings of the American Control Conference*, 2007.
- [66] X. Wei. *Modeling and Control of A Hybrid Electric Drivetrain for Optimal Fuel Economy, Performance and Driveability*. PhD thesis, The Ohio State University, Columbus, 2004.
- [67] J. Lygeros, K. H. Johansson, S. N. Simic, J. Zhang, and S. S. Sastry. Dynamical properties of hybrid automata. *IEEE Transactions on Automatic Control*, 48(1):2–17, 2003.
- [68] M.S. Branicky. Multiple Lyapunov functions and other analysis tools for switched and hybrid systems. *IEEE Transactions on Automatic Control*, 43(4):475–82, 1998.
- [69] H. Ye, A.N. Michel, and L. Hou. Stability theory for hybrid dynamical systems. *IEEE Transactions on Automatic Control*, 43(4):461–74, 1998.
- [70] M.S. Branicky, V.S. Borkar, and S.K. Mitter. A unified framework for hybrid control: model and optimal control theory. *IEEE Transactions on Automatic Control*, 43(1):31–45, 1998.

- [71] C.J. Tomlin, J. Lygeros, and S. Sastry. A game theoretic approach to controller design for hybrid systems. *Proceedings of the IEEE*, 88(7):949–70, 2000.
- [72] D. Liberzon and A. S. Morse. Basic problems in stability and design of switched systems. *IEEE Control Systems Magazine*, 19(5):59–70, 1999.
- [73] R. A. Decarlo, M. S. Branicky, S. Pettersson, and B. Lennartson. Perspectives and results on the stability and stabilizability of hybrid systems. *Proceedings of the IEEE*, 88(7):1069–82, 2000.
- [74] S. Pettersson and B. Lennartson. LMI for stability and robustness of hybrid systems. In *Proceedings of the American Control Conference*, volume 3, pages 1714–18, 1997.
- [75] M. Margaliot and D. Liberzon. Lie-algebraic stability conditions for nonlinear switched systems and differential inclusions. *Systems and Control Letters*, 55:8–16, 2006.
- [76] J. P. Hespanha. Uniform stability of switched linear systems: extensions of LaSalle’s invariance principle. *IEEE Transactions on Automatic Control*, 49(4):470–82, 2004.
- [77] R. N. Shorten and K. S. Narendra. Necessary and sufficient conditions for the existence of a common quadratic Lyapunov function for m-stable second order linear time-invariant systems. In *Proceedings of the American Control Conference*, pages 1410–14, 1999.
- [78] J. P. Hespanha and A. S. Morse. Stability of switched systems with average dwell-time. In *Proceedings of the 38th Conference on Decision and Control*, pages 2655–60, 1999.
- [79] D. Liberzon, J. P. Hespanha, and A. S. Morse. Stability of switched systems: a Lie-algebraic condition. *Systems and Control Letters*, 37:117–22, 1999.
- [80] J. P. Hespanha and A. S. Morse. Switching between stabilizing controllers. *Automatica*, 38(11):1905–17, November 2002.
- [81] M. Wicks, P. Peleties, and R. DeCarlo. Switched controller synthesis for the quadratic stabilization of a pair of unstable linear systems. *European Journal of Control*, 4:140–47, 1998.
- [82] P. Riedinger, F. Kratz, C. Iung, and C. Zanne. Linear quadratic optimization for hybrid systems. In *Proceedings of the 38th IEEE Conference on Decision and Control*, pages 3059–64, 1999.

- [83] M. Egerstedt, P. Ogren, O. Shakernia, and J. Lygeros. Toward optimal control of switched linear systems. In *Proceedings of the 39th IEEE Conference on Decision and Control*, volume 1, pages 587–92, 2000.
- [84] H. J. Sussmann. A maximum principle for hybrid optimal control problems. In *Proceedings of the Conference on Decision and Control*, pages 425–30, 1999.
- [85] M.L. Bujorianu and J. Lygeros. General stochastic hybrid systems: modelling and optimal control. In *Proceedings of the 43rd IEEE Conference on Decision and Control*, volume 2, pages 1872–77, 2004.
- [86] L. Shi, A. Abate, and S. Sastry. Optimal control for a class of stochastic hybrid systems. In *Proceedings of the 43rd IEEE Conference on Decision and Control*, volume 2, pages 1842–47, 2004.
- [87] A. Bemporad and M. Morari. Control of systems integrating logic, dynamics, and constraints. *Automatica*, 35(3):407–27, 1999.
- [88] N. H. McClamroch and I. Kolmanovsky. Performance benefits of hybrid control design for linear and nonlinear systems. *Proceedings of the IEEE*, 88(7):1083–96, 2000.
- [89] F. Borrelli, A. Bemporad, M. Fodor, and D. Hrovat. An MPC/hybrid system approach to traction control. *IEEE Transactions on Control Systems Technology*, 14(3):541–52, 2006.
- [90] S. C. Bengea. *Optimal Control of Switched Hybrid Systems with Applications to the Control of Hybrid Electric Vehicles*. PhD thesis, Purdue University, August 2004.
- [91] M. Baotic, M. Vasak, M. Morari, and N. Peric. Hybrid system theory based optimal control of an electronic throttle. In *Proceedings of the American Control Conference*, volume 6, pages 5209–14, 2003.
- [92] A. Balluchi, L. Benvenuti, M. D. Di Benedetto, C. Pinello, and Sangiovanni-Vincentelli A. L. Automotive engine control and hybrid systems: Challenges and opportunities. *Proceedings of the IEEE*, 88(7):888–912, 2000.
- [93] R. Hanus, M. Kinnaert, and J. L. Henrotte. Conditioning technique, a general anti-windup and bumpless transfer method. *Automatica*, 23:729–39, 1987.
- [94] P.J. Campo, M. Morari, and C. N. Nett. Multivariable anti-windup and bumpless transfer: A general theory. In *Proceedings of the American Control Conference*, pages 1706–11, 1989.



- [95] M.V. Kothare, P.J. Campo, M. Morari, and N. Nett. A unified framework for the study of anti-windup designs. *Automatica*, 30(12):1869–1883, 1994.
- [96] Y. Peng, D. Vrancic, and R. Hanus. Anti-windup, bumpless, and conditioned transfer techniques for PID controllers. *IEEE Control Systems Magazine*, 16:48–57, 1996.
- [97] M.C. Turner and D.J. Walker. Linear quadratic bumpless transfer. *Automatica*, 36(8):1089–101, 2000.
- [98] L. Zaccarian and A. R. Teel. The L-2 bumpless transfer problem for linear plants: Its definition and solution. *Automatica*, 41:1273–80, 2005.
- [99] K. Zheng, A-H. Lee, J. Bentsman, and C.W. Taft. Steady-state bumpless transfer under controller uncertainty using the state/output feedback topology. *IEEE Transactions on Control Systems Technology*, 14(1):3–17, 2006.
- [100] Challenge-X competition official web site. *www.challengeX.org*.
- [101] K. Koprubasi, E. R. Westervelt, G. Rizzoni, E. Galvagno, and M. Velardocchia. Experimental validation of a model for the control of drivability in a hybrid-electric vehicle. In *Proceedings of the IMECE*, number 41489, 2007.
- [102] A. J. Kotwicki. Dynamic model for torque converter equipped vehicles. In *SAE Proceedings*, number 820393, 1982.
- [103] D. Hrovat and W. E. Tobler. Bond graph modeling and computer simulation of automotive torque converter. *Journal of Franklin Institute*, 319:93–114, 1985.
- [104] P. A. G. Lepelletier. Multispeed automatic transmission for automobile vehicles. *US Patent 5,106,352*, 1992.
- [105] S. Kasuya, T. Taniguchi, K. Tsukamoto, M. Hayabuchi, M. Nishida, A. Suzuki, and H. Niki. AISIN AW new high torque capacity six-speed automatic transmission for FWD vehicles. In *SAE Proceedings*, number 2005-01-1020.
- [106] N. Katou, T. Taniguchi, K. Tsukamoto, M. Hayabuchi, M. Nishida, and A. Katou. AISIN AW new six-speed automatic transmission for FWD vehicles. In *SAE Proceedings*, number 2004-01-0651.
- [107] A. Lagerberg and B. Egardt. Backlash estimation with application to automotive powertrains. *IEEE Transactions on Control Systems Technology*, 15(3):483–493, 2007.
- [108] H. B. Pacejka. *Tyre and Vehicle Dynamics*. Butterworth-Heinemann, 2002.



- [109] R. Bornatico, A. Storti, A. Zappavigna, L. Mandrioli, Y. Guezennec, and G. Rizzoni. NiMH battery characterization and state-of-charge estimation for HEV applications. In *Proceedings of the IMECE*, number 42484, 2007.
- [110] M. A. Kluger and D. M. Long. An overview of current automatic, manual and continuously variable transmission efficiencies and their projected future improvements. In *SAE Proceedings*, number 1999-01-1259.
- [111] B. Pohl. Transient torque converter performance, testing, simulation and reverse engineering. In *SAE Proceedings*, number 2003-01-0249.
- [112] Robert Bosch GmbH. CAN specification v 2.0. Technical report, 1991. Available at <http://www.semiconductors.bosch.de/pdf/can2spec.pdf>.
- [113] Carnegie Mellon University. Symbolic Model Verifier (SMV). Available at <http://www-2.cs.cmu.edu/~modelcheck/smv.html>.
- [114] M. Canova, Y. Guezennec, and S. Yurkovich. On the control of the start/stop dynamics in a hybrid electric vehicle. *Journal of Dynamic Systems, Measurement, and Control*. Review pending.
- [115] B. Gu. Supervisory control strategy development for a hybrid-electric vehicle. Master's thesis, Graduate School of The Ohio State University, 2006.
- [116] A. Van der Schaft. *An introduction to hybrid dynamical systems*. Springer-Verlag, 2000.
- [117] J. Zhang, K.H. Johansson, J. Lygeros, and S. Sastry. Zeno hybrid systems. *International Journal of Robust and Nonlinear Control*, 11(5):435–51, 2001.
- [118] D. D. Hrovat, J. Asgari, and M. G. Fodor. Vehicle shift quality using a supplemental torque source. *US Patent 6,193,628*, 2001.
- [119] J. Michelini and C. Glugla. Control system design for steady state operation and mode switching of an engine with cylinder deactivation. In *Proceedings of the American Control Conference*, pages 3125–29, 2003.
- [120] A. Lagerberg and B. S. Egardt. Evaluation and control strategies for automotive powertrains with backlash. 2002.
- [121] A. F. A. Serrarens. *Coordinated Control of The Zero Inertia Powertrain*. PhD thesis, Technische Universiteit Eindhoven, 2001.
- [122] Environmental Protection Agency. Fuel economy estimates for the 2005 Chevrolet Equinox. Available at <http://www.fueleconomy.gov/feg/noframes/21374.shtml>.